Static and Dynamic Analysis of Twist Drills Subjected to Cutting Loads

Sagar Chandrakant Kadam

A Thesis

In

The Department

Of

Mechanical and Industrial Engineering

Presented in Partial Fulfillment of the Requirements

for the Degree of Master of Applied Science at

Concordia University

Montréal, Québec,

Canada

January 2007

Your file Votre référence
ISBN: 978-0-494-34628-0
Our file Notre référence
ISBN: 978-0-494-34628-0

ABSTRACT

Static and Dynamic Analysis of Twist Drills Subjected to Cutting Loads

Sagar Chandrakant Kadam

Continuous models for a fluted twist drill are developed to study its static and dynamic bending characteristics.

The static model is numerically simulated within Matlab for point loads at the free end of a twist drill. The bending curves are plotted and the bending stiffness of a twist drill is estimated. Effect of orientation of the spirally fluted cross-section at the fixed end on end deflection is studied. Characteristic bending curves for one pitch length of drill are plotted and region of minimum deflection is identified.

Dynamic model is numerically simulated in Matlab over a range of rotating speeds and the first two natural frequencies and corresponding mode shapes are identified for the twist drill.

New formulation for estimation of work stiffness is proposed considering the interaction of drill with the hole-wall. A new lumped mass model for studying lateral vibration behavior of the twist drill is developed using this work stiffness. The bending stiffness and fundamental natural frequency estimated using continuous models above and work stiffness calculated using proposed formulation are used in this new model. This model is numerically simulated in Matlab for different set of parameters and drill orbital motions

are obtained. Results are analyzed to study the influence of various parameters on dynamics of drill and an explanation is given for generation of lobed holes and drill wandering phenomenon and surface roughness.

Torsional stiffness of set of twist drills in clockwise and counter clockwise directions are measured experimentally in order to verify the stiffness symmetry.

Appearance of cutting resistance when direction of twist coincides with the direction of cutting leads to periodic change in torsional stiffness of the twist drill during actual drilling. Lumped mass model is developed wherein the effect of this periodic change in torsional stiffness on torsional vibration is studied. Numerical simulations are carried out in Matlab for stiffness change of bilinear and combined linear and half sinusoidal nature.

Lateral deflection of drill against hole wall is always associated with a small amount of angular twist. Lumped mass model to study bending-torsional coupling is developed. Numerical simulations are carried out in Matlab and results are compared with results for uncoupled torsional model.

ACKNOWLEDGEMENTS

I sincerely wish to express my gratitude and appreciation to my thesis supervisor Dr. Rama B. Bhat for his continuous encouragement, enthusiastic assistance and precious guidance throughout the course of my thesis work.

I would like to thank the technical support staff in Mechanical and Industrial Engineering Department John Elliot, Brian Cooper and Brad Luckhart for their assistance in preparation of my experimental work.

My special thanks are due to K. V. Nagrajan and my other colleagues and friends Suresh, Vaibhav, Ashish, Saurabha, Anand, Nandu, Adarsh, Gary and Shankar for their valuable advice and moral support at various stages of my research.

I am grateful to my parents, brothers, sisters and Rajindi for showering me with affection, blessings and wishes all the time. Experience of enormous energy, strength and optimism all the time, I believe, originated from the blessings of Mata Tulja Bhavani and lead me to this stage.

TABLE OF CONTENTS

LIST OF FIGURES XI-XXI

LIST OF SYMBOLS XXII-XXVI

CHAPTER 1 1-20

INTRODUCTION

1.1. Drilling Operation 1

1.2. Drilling Machine and Drill 3

1.3. Literature Survey 7

1.4. Objectives of Thesis 17

1.5. Organization of Thesis 19

CHAPTER 2 21-49

CONTINUOUS MODEL - STATIC BENDING CHARACTERISTICS OF TWIST DRILLS

2.1. Introduction 21

2.2. Moment of Inertia Formulation for Fluted Cutting Tools 22

2.3. Bending Deflection of Beam with Rectangular Cross-section 26

2.4. Bending Characteristics of Twist Drills 28

2.5. Simulation Results and Interpretations 32

2.6. Significance of Phase Angle for Drilling using Twist Drills 46

2.7. Summary 49

CHAPTER 3 50-62

CONTINUOUS MODEL - EULER-BERNOULLI BEAM EQUATION APPLIED TO TWIST DRILLS

3.1. Introduction 50

3.2. Continuous Form of Equation of Motion for Twist Drills 51

3.3. Simulation Results 56-62

3.3.1. Identification of Natural Frequencies 56

3.3.2. Identification of Mode Shapes 58

3.4. Summary 62

CHAPTER 4 63-157

LUMPED MASS MODEL - ORBITAL DYNAMICS OF TWIST DRILLS

4.1. Introduction 63

4.2. Description of Mathematical Model 66

4.3. New Formulation for Work Stiffness (K_W) 68

4.4. Formulation of Equation of Motion 72

4.5. Calculation of Basic Simulation Parameters 81-86

4.5.1. Drill Torsional Stiffness (K_t) 82

4.5.2. Drill Lateral Stiffness (K_d) 82

4.5.3. Work Stiffness (K_w) 83

4.5.4. Drill Natural Frequency (ω_n) 84

4.5.5. Other Parameters 85

4.5.6. Final Simulation Parameters 86

4.6. Simulation Results 87-157

4.6.1. Effect of Change in Unbalanced Force Components 88

4.6.2. Effect of Change in Force Amplitude Modulation Factor 101

4.6.3. Combined Effect of Unbalance Force Components and Amplitude Modulation Factors 112

4.6.4. Observations – 1 117

4.6.5. Validation of Results - 1 118

4.6.6. Effect of Change in Forcing Frequency 122

4.6.6.1. Observations - 2 131

4.6.6.2. Observations - 3 136

4.6.6.3. Observations - 4 151

4.6.7. Validation of Results - 2 153

4.7. Summary 157

CHAPTER 5 158-171

EXPERIMENTAL INVESTIGATION OF TORSIONAL STIFFNESS SYMMETRY OF TWIST DRILLS

5.1. Introduction 158

5.2. Experimental Set-up 159

5.3. Test Results and Conclusion 164

5.4. Summary 171

CHAPTER 6 172-194

LUMPED MASS MODEL – BENDING TORSIONAL COUPLING DYNAMICS OF TWIST DRILLS

6.1. Introduction 172

6.2. Non-Linear Torsional Stiffness Models 174-176

6.2.1. Bilinear Torsional Stiffness 174

6.2.2. Combined Linear Sinusoidal Torsional Stiffness 176

6.3. Discrete Model - Nonlinear Torsional Stiffness 178

6.4. Simulation Results 1 179

6.5. Discrete Model for Bending-Torsional Coupling 183

6.6. Simulation Results 2 186

6.7. Observations 195

6.8. Summary 197

CHAPTER 7 198-201

CONCLUSIONS AND FUTURE RECOMMENDATIONS

7.1. Summary and Conclusions 198

7.2. Recommendations for Future Work 201

LIST OF REFERENCES 202-206

LIST OF FIGURES

Figure 1.1	Schematic of Bench Press and Radial Arm Drilling Machine [1]	4
Figure 1.2	Twist Drill Geometry [2]	5
Figure 2.1	Schematic of Twist Drill Cross-section	22
Figure 2.2	Schematic of Beam Cross-section and Axes System	26
Figure 2.3	Schematic of Twist Drill Cross-section and Axes System	28
Figure 2.4	Deflection Curves for Rectangular Strip Placed Vertically	34
Figure 2.5	Deflection Curves for Rectangular Strip Placed Horizontally	34
Figure 2.6	Deflection Curves for Twist Drill (Φ = 0 degree)	35
Figure 2.7	Deflection Curves for Twist Drill (Φ = 45 degree)	35
Figure 2.8	Deflection Curves for Twist Drill (Φ = 90 degree)	36
Figure 2.9	Deflection Curves for Twist Drill (Φ = 135 degree)	36
Figure 2.10	Deflection Curves for Twist Drill (Φ = 180 degree)	37
Figure 2.11	Area Moment of Inertia Variations along the Length of Twist Drill	38
Figure 2.12	Deflection Curve for Twist Drill (Φ = 0 degree)	38
Figure 2.13	Deflection Curve for Rectangular Strip Placed Vertically	39
Figure 2.14	Slope Variation Curve for Rectangular Strip Placed Vertically	40
Figure 2.15	Slope Variation Curve for Twist Drill (Φ = 0 degree)	40
Figure 2.16	Curvature Variation Curve for Rectangular Strip Placed Vertically	41

Figure 2.17	Curvature Variation Curve for Twist Drill (Φ = 0 degree)	41
Figure 2.18	End Deflection Variation with Phase Angle (Pitch = 80 mm)	42
Figure 2.19	End Deflection Variation with Phase Angle (Pitch = 64 mm)	43
Figure 2.20	End Deflection Variation with Phase Angle (Pitch = 60 mm)	43
Figure 2.21	End Deflection Variation with Phase Angle (Pitch = 56mm)	44
Figure 2.22	End Deflection Variation with Phase Angle (Pitch = 52mm)	44
Figure 2.23	End Deflection Variation with Phase Angle (Pitch = 48 mm)	45
Figure 2.24	End Deflection Variation with Phase Angle (Pitch = 32 mm)	45
Figure 2.25	Schematic of Cross-section at Drill Tip	46
Figure 2.26	Variation of Phage Angle for Different Lengths of Twist Drill	47
Figure 2.27	Characteristic End Deflection Curve for Twist drill	48
Figure 3.1	Displacement Amplitude v/s Forcing Frequency	57
Figure 3.2	First Mode Shape for Twist Drill (D = 13.0 mm, L = 100.0 mm)	59
Figure 3.3	Second Mode Shape for Twist Drill (D = 13.0 mm, L = 100.0 mm)	59
Figure 3.4	Analytical Mode Shapes for fluted micro-drill [7] (Ds = 1.0 mm, Ls = 3.0 mm, D = 0.3 mm, L = 5.5 mm)	60
Figure 3.5	Experimental Mode Shapes for Twist Drill [21] (D = 19.05 mm, L = 305 mm)	61
Figure 4.1	Schematic of Drill-Hole Wall Interface	66
Figure 4.2	Schematic of Lumped Mass Model and Axes System	66
Figure 4.3	Cutting Lips Orientation- Top View	68

Figure 4.4	Cutting Lips in Displaced Position	68
Figure 4.5.1	Cutting forces and torques on a twist drill	72
Figure 4.5.2	Free Body Diagram for Drill's Displaced Position	72
Figure 4.6	Trajectory of Drill Centerline (F_i = 0.2 N)	89
Figure 4.7	Trajectory of Drill Centerline on Time Scale (F_i = 0.2 N)	89
Figure 4.8	Locus of Outermost Point of Cutting Lip (F_i = 0.2 N)	90
Figure 4.9	Locus of Outermost Point of Cutting Lip on Time Scale (F_i = 0.2 N)	90
Figure 4.10	Trajectory of Drill Centerline (F_i = 0.5 N)	91
Figure 4.11	Trajectory of Drill Centerline on Time Scale (F_i = 0.5 N)	91
Figure 4.12	Locus of Outermost Point of Cutting Lip (F_i = 0.5 N)	92
Figure 4.13	Locus of Outermost Point of Cutting Lip on Time Scale (F_i = 0.5 N)	92
Figure 4.14	Trajectory of Drill Centerline (F_i = 1.0 N)	93
Figure 4.15	Trajectory of Drill Centerline on Time Scale (F_i = 1.0 N)	93
Figure 4.16	Locus of Outermost Point of Cutting Lip (F_i = 1.0 N)	94
Figure 4.17	Locus of Outermost Point of Cutting Lip on Time Scale (F_i = 1.0 N)	94
Figure 4.18	Trajectory of Drill Centerline (F_i = 1.5 N)	95
Figure 4.19	Trajectory of Drill Centerline on Time Scale (F_i = 1.5 N)	95

Figure 4.20	Locus of Outermost Point of Cutting Lip (F_i = 1.5 N)	96
Figure 4.21	Locus of Outermost Point of Cutting Lip on Time Scale (F_i =1.5 N)	96
Figure 4.22	Trajectory of Drill Centerline (F_i = 2.0 N)	97
Figure 4.23	Trajectory of Drill Centerline on Time Scale (F_i = 2.0 N)	97
Figure 4.24	Locus of Outermost Point of Cutting Lip (F_i = 2.0 N)	98
Figure 4.25	Locus of Outermost Point of Cutting Lip on Time Scale (F_i = 2.0 N)	98
Figure 4.26	Trajectory of Drill Centerline (F_i = 3.0 N)	99
Figure 4.27	Trajectory of Drill Centerline on Time Scale (F_i = 3.0 N)	99
Figure 4.28	Locus of Outermost Point of Cutting Lip (F_i = 3.0 N)	100
Figure 4.29	Locus of Outermost Point of Cutting Lip on Time Scale (F_i = 3.0 N)	100
Figure 4.30	Trajectory of Drill Centerline (λ= 1)	102
Figure 4.31	Trajectory of Drill Centerline on Time Scale (λ = 1)	102
Figure 4.32	Locus of Outermost Point of Cutting Lip (λ = 1)	103
Figure 4.33	Locus of Outermost Point of Cutting Lip on Time Scale (λ = 1)	103
Figure 4.34	Trajectory of Drill Centerline (λ = 2)	104
Figure 4.35	Trajectory of Drill Centerline on Time Scale (λ = 2)	104
Figure 4.36	Locus of Outermost Point of Cutting Lip (λ = 2)	105

Figure 4.37	Locus of Outermost Point of Cutting Lip on Time Scale ($\lambda = 2$)	105
Figure 4.38	Trajectory of Drill Centerline ($\lambda = 3$)	106
Figure 4.39	Trajectory of Drill Centerline on Time Scale ($\lambda = 3$)	106
Figure 4.40	Locus of Outermost Point of Cutting Lip ($\lambda = 3$)	107
Figure 4.41	Locus of Outermost Point of Cutting Lip on Time Scale ($\lambda = 3$)	107
Figure 4.42	Trajectory of Drill Centerline ($\lambda = 4$)	108
Figure 4.43	Trajectory of Drill Centerline on Time Scale ($\lambda = 4$)	108
Figure 4.44	Locus of Outermost Point of Cutting Lip ($\lambda = 4$)	109
Figure 4.45	Locus of Outermost Point of Cutting Lip on Time Scale ($\lambda = 4$)	109
Figure 4.46	Trajectory of Drill Centerline ($\lambda = 5$)	110
Figure 4.47	Trajectory of Drill Centerline on Time Scale ($\lambda = 5$)	110
Figure 4.48	Locus of Outermost Point of Cutting Lip ($\lambda = 5$)	111
Figure 4.49	Locus of Outermost Point of Cutting Lip on Time Scale ($\lambda = 5$)	111
Figure 4.50	Trajectory of Drill Centerline ($\lambda = 3$, $F_i = 0.4$ N)	113
Figure 4.51	Trajectory of Drill Centerline on Time Scale ($\lambda = 3$, $F_i = 0.4$ N)	113
Figure 4.52	Locus of Outermost Point of Cutting Lip ($\lambda = 3$, $F_i = 0.4$ N)	114
Figure 4.53	Locus of Outermost Point of Cutting Lip on Time Scale ($\lambda = 3$, $F_i = 0.4$ N)	114

Figure 4.54	Trajectory of Drill Centerline ($\lambda = 3$, $F_i = 0.7$ N)	115
Figure 4.55	Locus of Outermost Point of Cutting Lip ($\lambda = 3$, $F_i = 0.7$ N)	115
Figure 4.56	Trajectory of Drill Centerline ($\lambda = 3$, $F_i = 1.0$ N)	116
Figure 4.57	Locus of Outermost Point of Cutting Lip ($\lambda = 3$, $F_i = 1.0$ N)	116
Figure 4.58	Simulated and Experimental Hole Profiles [12]	118
Figure 4.59	Predicted 3-Lobed Hole Profile [17]	119
Figure 4.60	Experimental 3-Lobed Hole profile [17]	120
Figure 4.61	Measured Profile and Photograph of 3-Lobed Hole [17]	121
Figure 4.62	Trajectory of Drill Centerline (N = 100 rpm)	123
Figure 4.63	Locus of Outermost Point of Cutting Lip (N = 100 rpm)	124
Figure 4.64	Locus of Outermost Point of Cutting Lip on Time Scale (N = 100 rpm)	124
Figure 4.65	Trajectory of Drill Centerline (N = 300 rpm)	125
Figure 4.66	Locus of Outermost Point of Cutting Lip (N = 300 rpm)	126
Figure 4.67	Locus of Outermost Point of Cutting Lip on Time Scale (N = 300 rpm)	126
Figure 4.68	Trajectory of Drill Centerline (N = 500 rpm)	127
Figure 4.69	Locus of Outermost Point of Cutting Lip (N = 500 rpm)	128
Figure 4.70	Locus of Outermost Point of Cutting Lip on Time Scale (N = 500 rpm)	128
Figure 4.71	Trajectory of drill centerline (N = 1000 rpm)	129
Figure 4.72	Locus of Outermost Point of Cutting Lip (N = 1000 rpm)	130

Figure 4.73	Locus of Outermost Point of Cutting Lip on Time Scale (N = 1000 rpm)	130
Figure 4.74	Trajectory of Drill Centerline (N =3000 rpm)	132
Figure 4.75	Locus of Outermost Point of Cutting Lip (N = 3000 rpm)	133
Figure 4.76	Locus of Outermost Point of Cutting Lip on Time Scale (N = 3000 rpm)	133
Figure 4.77	Trajectory of Drill Centerline (N = 6000 rpm)	134
Figure 4.78	Locus of Outermost Point of Cutting Lip (N = 6000 rpm)	135
Figure 4.79	Locus of Outermost Point of Cutting Lip on Time Scale (N = 6000 rpm)	135
Figure 4.80	Trajectory of Drill Centerline (N = 10000 rpm)	137
Figure 4.81	Locus of Outermost Point of Cutting Lip (N = 10000 rpm)	138
Figure 4.82	Locus of Outermost Point of Cutting Lip on Time Scale (N =10000 rpm)	138
Figure 4.83	Trajectory of Drill Centerline (N = 14000 rpm)	139
Figure 4.84	Locus of Outermost Point of Cutting Lip (N = 14000 rpm)	140
Figure 4.85	Locus of Outermost Point of Cutting Lip on Time Scale (N = 14000 rpm)	140
Figure 4.85.1	Circular Orbit (N = 14000 rpm, τ = 10-20)	140
Figure 4.85.2	Circular Orbit (N = 14000 rpm, τ = 40-50)	141
Figure 4.85.3	Three Lobed Orbit (N = 14000 rpm, τ = 20-30)	142
Figure 4.85.4	Three Lobed Orbit (N = 14000 rpm, τ = 70-80)	142
Figure 4.85.5	Elliptical Orbit (N = 14000 rpm, τ = 30-40)	143

Figure 4.85.6	Elliptical Orbit (N = 14000 rpm, τ = 50-60)	143
Figure 4.85.7	Elliptical Orbit (N = 14000 rpm, τ = 60-70)	144
Figure 4.85.8	Elliptical Orbit (N = 14000 rpm, τ = 80-90)	144
Figure 4.86	Trajectory of Drill Centerline (N = 18000 rpm)	145
Figure 4.87	Trajectory of Drill Centerline on Time Scale (N = 18000 rpm)	145
Figure 4.88	Locus of Outermost Point of Cutting Lip (N = 18000 rpm)	146
Figure 4.89	Locus of Outermost Point of Cutting Lip on Time Scale (N = 18000 rpm)	146
Figure 4.90	Trajectory of Drill Centerline (N = 18000 rpm)	147
Figure 4.91	Trajectory of Drill Centerline on Time Scale (N = 25000 rpm)	147
Figure 4.92	Locus of Outermost Point of Cutting Lip (N = 25000 rpm)	148
Figure 4.93	Locus of Outermost Point of Cutting Lip on Time Scale (N = 25000 rpm)	148
Figure 4.94	Trajectory of Drill Centerline (N = 20000 rpm)	149
Figure 4.95	Locus of Outermost Point of Cutting Lip (N = 20000 rpm)	150
Figure 4.96	Three-Lobed Orbit (N = 20000 rpm, τ = 50-60)	150
Figure 4.97	Experimental Three-Lobed Orbit [9]	153
Figure 4.98	Experimental Three-Lobed Orbit [9]	154
Figure 4.99	Experimental Elliptical Orbit [9]	154
Figure 4.100	Drill Orbits Predicted Using Finite Element [9]	155
Figure 4.101	Experimental Elliptical Orbit [9]	156
Figure 5.1	Torsion Test on UTM (D = 12.7 mm, Cutting Direction)	161

Figure 5.2	Torsion Test Fixture Components (Cutting and Opposite Directions)	162
Figure 5.3	Test Set –up for Torsion Test on Twist Drills	163
Figure 5.4	Twist Drills Tested on Torsion Test Fixture	163
Figure 5.5	Plot of Torque v/s Twist angle (D = 10.5 mm, Cutting Direction)	166
Figure 5.6	Plot of Torque v/s Twist angle (D = 10.5 mm, Opposite Cutting Direction)	166
Figure 5.7	Plot of Torque v/s Twist angle (D = 11.0 mm, Cutting Direction)	167
Figure 5.8	Plot of Torque v/s Twist angle (D = 11.0 mm, Opposite Cutting Direction)	167
Figure 5.9	Plot of Torque v/s Twist angle (D = 12.0 mm, Cutting Direction)	168
Figure 5.10	Plot of Torque v/s Twist angle (D = 12.0 mm, Opposite Cutting Direction)	168
Figure 5.11	Plot of Torque v/s Twist angle (D = 13.0 mm, Cutting Direction)	169
Figure 5.12	Plot of Torque v/s Twist angle (D = 13.0 mm, Opposite Cutting Direction)	169
Figure 5.13	Plot of Torque v/s Twist Angle (UTM Test, D = 12.7 mm)	170
Figure 6.1	Schematic of Drill Torsional Stiffness in Cutting Direction	175
Figure 6.2	System Torsional Stiffness v/s Time (N = 100 rpm)	176

Figure 6.3	System Torsional Stiffness v/s Time (N = 100 rpm)	177
Figure 6.4	Torque v/s Time –Type A (N = 100 rpm)	179
Figure 6.5	Torque v/s Time – Type B (N = 100 rpm)	180
Figure 6.6	Angular Displacement v/s Time	181
	(Torque Type A, Stiffness Linear, N = 100 rpm)	
Figure 6.7	Figure 6.7: Angular Displacement v/s Time	181
	(Torque Type A, Stiffness Non-Linear, N = 100 rpm)	
Figure 6.8	Angular Displacement v/s Time	182
	(Torque Type B, Stiffness Linear, N = 100 rpm)	
Figure 6.9	Angular Displacement v/s Time	182
	(Torque Type B, Stiffness Non-Linear, N = 100 rpm)	
Figure 6.10	Trajectory of Drill Centerline (N = 100 rpm, F_i = 0.2 N, λ = 1)	186
Figure 6.11	Locus of Outermost Point of Cutting Lip	186
	(N = 100 rpm, F_i = 0.2 N, λ = 1)	
Figure 6.12	Angular Displacement v/s Time without Coupling	187
	(Torque Type A, Stiffness Non-Linear, N = 100 rpm)	
Figure 6.13	Angular Displacement v/s Time with Coupling	187
	(Torque Type A, Stiffness Non-Linear, N = 100 rpm)	
Figure 6.14	Coupled and Uncoupled Angular Displacements Overlapped	188
	(N = 100 rpm, F_i = 0.2 N, λ = 1)	
Figure 6.15	Trajectory of Drill Centerline	190
	(N = 200 rpm, F_i = 0.3 N, λ = 1.5)	

Figure 6.16	Locus of Outermost Point of Cutting Lip (N = 200 rpm, F_i = 0.3 N, λ = 1.5)	190
Figure 6.17	Coupled and Uncoupled Angular Displacements Overlapped (N = 200 rpm, F_i = 0.3 N, λ = 1.5)	191
Figure 6.18	Trajectory of Drill Centerline (N = 200 rpm, F_i = 0.2 N, λ = 2)	192
Figure 6.19	Locus of Outermost Point of Cutting Lip (N = 200 rpm, F_i = 0.2 N, λ = 2)	192
Figure 6.20	Coupled and Uncoupled Angular Displacements Overlapped, (N = 200 rpm, F_i = 0.2 N, λ = 2)	193
Figure 6.21	Coupled and Uncoupled Angular Displacements Overlapped (N = 200 rpm, F_i = 0.2 N, λ = 3)	194
Figure 6.22	Schematic of Bending-Torsion Coupling	196

LIST OF SYMBOLS

Notation	Description	Unit
b	Web Thickness of Drill	m, mm
C_d	Linear Damping Coefficient	$\frac{Ns}{m}$
D, Ds	Diameter of Drill, Shank Diameter	m, mm
E	Modulus of Elasticity	$\frac{N}{m^2}$
f	Harmonic Force	N
f_b	Tensile or Compressive Stress in Extreme Fiber of Beam	$\frac{N}{m^2}$
F	Force Amplitude or Point Load	N
$F_{bx}*$, $F_{by}*$	Basile's Harmonic Forcing Functions in X and Y Directions in Non-dimensional form [13]	_
F_f	Frictional Force	N
F_{imbx}, F_{imby}	Amplitudes of Basile's Harmonic Forcing Functions in X and Y directions	N
F_{ix}, F_{iy}	Harmonic Forcing Functions in X and Y Directions Before Non-dimensionalization	N
F_r	Reaction Force	N
F_x, F_y	Force in X direction, Force in Y direction	N

G	Numerical Constant	-
H, H_θ	Heaviside Unit-Step Functions	_
I_{uu}	Principal Area Moments of Inertias of Twist Drill about Axis UU	m^4
I_{uv}	Product Area Moments of Inertias of Twist Drill	m^4
I_{vv}	Principal Area Moments of Inertias of Twist Drill about Axis VV	m^4
I_{ww}	Polar Area Moments of Inertias of Twist Drill	m^4
I_{xx}	Polar Area Moments of Inertias of Twist Drill	m^4
I_{yy}	Principal Area Moments of Inertias of Twist Drill about Axis YY	m^4
$I_{yy}(x)$	Principal Area Moments of Inertias about Axis YY at Distance 'x' from Fixed End of Drill	m^4
I_{zy}	Product Area Moments of Inertias of Twist Drill	m^4
I_{zz}	Principal Area Moments of Inertias of Twist Drill about Axis ZZ	m^4
$I_{zz}(x)$	Principal Area Moments of Inertias about Axis ZZ at Distance 'x' from Fixed End of Drill	m^4
J	Mass Moment of Inertia of Twist Drill	kg- m^2

k	Non-dimensional Stiffness	–
K_c	Torsional Stiffness Added for Cutting Resistance	$\frac{Nm}{rad}$
K_d	Drill Bending Stiffness	$\frac{N}{m}$
K_s	System Torsional Stiffness for Drill and Work-Piece Together	$\frac{Nm}{rad}$
K_{sc}	System Torsional Stiffness for Drill and Work-Piece in Cutting Direction	$\frac{Nm}{rad}$
K_{snc}	System Torsional Stiffness for Drill and Work-Piece in Non-Cutting Direction	$\frac{Nm}{rad}$
K_t	Drill Torsional Stiffness	$\frac{N}{m}$
K_w	Work Stiffness	$\frac{N}{m}$
L, Ls	Length of Drill, Shank Length	m, mm
m, M	Mass Per Unit Length of Twist Drill, Lumped Mass	$\frac{kg}{m}$, kg
M_b	Bending Moment	Nm
n	Number of Flutes	–
N	Rotational Speed	rpm
P	Pitch of Twist Drill	m, mm
Q	Constant $\left(I_{yy} - I_{zz}\right)$	m^4

r, R	Radius of Twist Drill, Radius of Drilled Hole	m, mm
S	Displacement of Drill Center	m, mm
t	Time	sec
T	Cutting Torque	Nm
u, v, w	Cartesian Coordinates in Twisted Frames	m
U-V-W	Cartesian Coordinate System for Twisted Frame	_
x, y, z	Cartesian Coordinates in Inertial Frames (Ch. 2)	m
	Non-dimensional Displacements (Ch. 4)	_
X-Y-Z	Cartesian Coordinate System for Inertial Frame	_
α	Stiffness Ratio	_
β	Angle of Twist Per Unit Length	$\frac{rad}{m}$
δ	Radial Clearance (R – r)	m, mm ,μm
δ_{max}	Deflection of Drill Tip	m, mm
θ	Angle Between Inertial Frame and Twisted Frame (Ch 1)	rad
	Angular Co-ordinate for Torsion of Twist Drill (Ch 6)	
θ_c	Angular Displacement Component for Coupling	rad
λ	Amplitude Modulation Factor	_
μ_x, μ_y, μ	Coefficient of Friction in X and Y Directions	_

ξ	Damping Ratio	_
ρ	Frequency Ratio	-
τ	Non-dimensional Time	_
Φ	Phase Angle	rad, degree
φ	Instantaneous Position Angle	rad, degree
ψ	Displacement Induced Twist	rad, degree
ω, ω_n	Angular Velocity of Twist Drill, Natural Frequency	Hz, $\frac{\text{rad}}{\text{s}}$

CHAPTER 1

INTRODUCTION

1.1 Drilling Operation

Metal cutting operations are widely used in manufacturing and turning, milling, and drilling are the three most widely used among them. Drilling is the most versatile cutting operation and can be used on variety of machine tools such as lathes, milling machines, boring machines, machining centers, radial drilling machines, special purpose machines and hand drills.

Important applications of drilling are found in manufacturing industries viz. automotive, aerospace, machine tool and computer hardware. In all metal cutting operations the hole manufacturing contributes roughly up to 60%, out of which 20% share goes to conventional drilling using twist drill. Drilling is a complex operation due to the fluted geometry of the twist drill and complex design of drill tip. Because of these characteristics drilling remains a poorly understood manufacturing operation despite wide applications in industry.

The precision manufacturer prefers the CNC controlled machines and process monitoring is vital to achieve required accuracy. Drilling performance can be defined either in terms of tool life or hole quality. Drilling performance depends on tool geometry, process parameters and drill bit vibration. In the presence of drill bit vibration the performance is

deteriorated and leads to out of round holes and poor surface finish. Excessive drilling vibration can also lead to burred holes and tool breakage. Hence vibration analysis is essential to define the parameters influencing drilling errors such as shape, size, location, straightness and surface roughness, all of which are primary measures for defining drilling accuracy.

1.2 Drilling Machine and Drill

Depending upon design and construction features, drilling machines are classified into different types.

Drilling machine used for light hole making operations with v-belt and stepped pulley type spindle drive mechanism and manually adjustable work table and the whole machine mounted on a bench is called Bench Press.

Another most popular type of drilling machine is Radial Arm Drilling Machine. It is comparatively rigid machine tool and it has large radial arm which supports the spindle, the gear drive mechanism and drive motor. Vertical Pillar acts as supporting structure and guide surface for movements of radial arm and it also has drive mechanism for the vertical and swing movements of the radial arm. Radial arm has guideways for sliding motion of spindle head in horizontal direction. Some have spindle head that can swivel around two axes facilitating drilling of inclined holes, with one of these axes horizontal running parallel to the center line of the radial arm and another perpendicular to it. It has heavy foundation and large fixed work table for mounting heavy work pieces. Schematic of Bench Press and Radial Arm Drilling Machine are shown in figure 1.1.

Other machine tools specially designed for drilling long holes with horizontal spindle are called Deep Hole Drilling Machine, or Gun Drilling Machine depending upon the application.

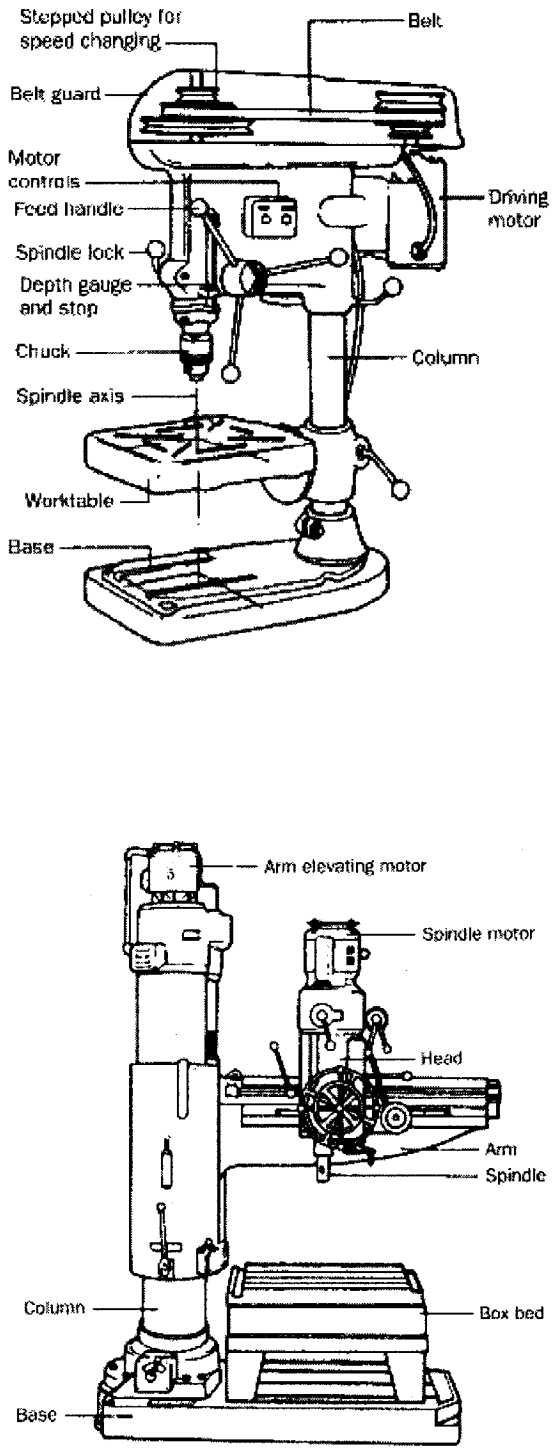

Figure 1.1: Schematic diagram of a Bench Press and Radial Arm Drilling Machine [1]

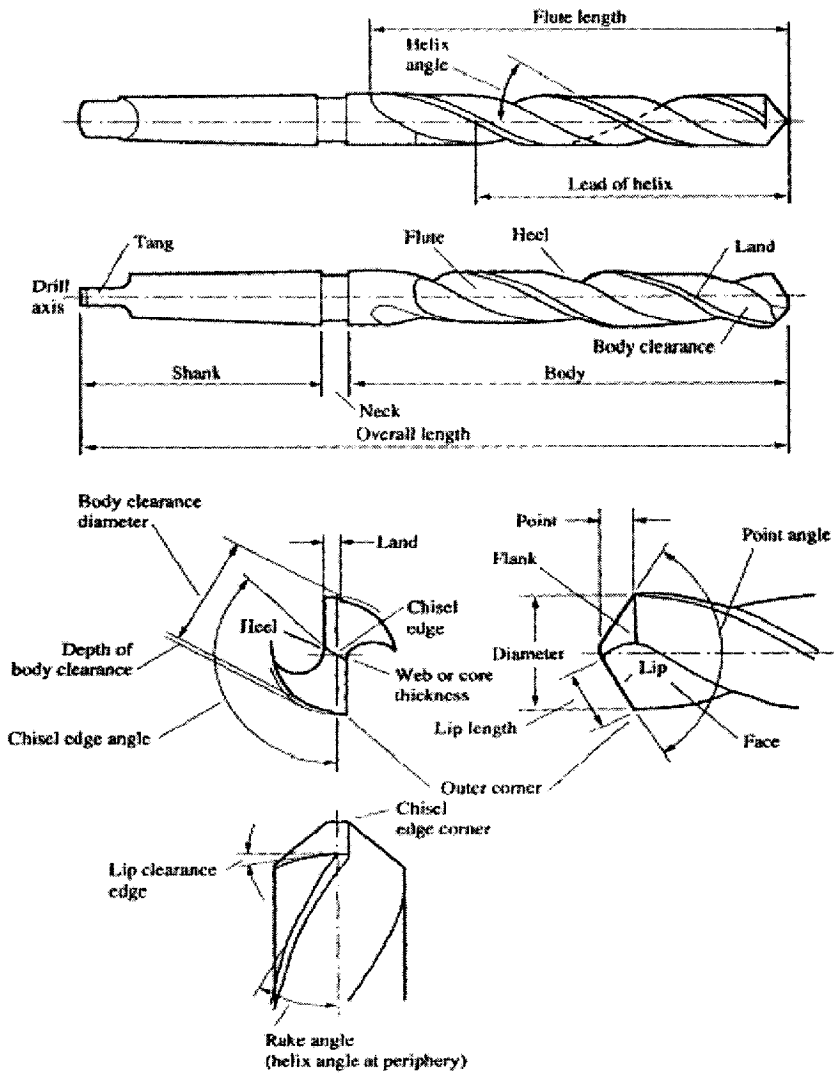

Figure 1.2: Twist Drill Geometry [2]

Like drilling machine, drills are also classified into different types. Most popular type is the Twist Drill. It is named so because of its spirally fluted body giving rise to typical drill geometry. Better understanding of drilling process requires good understanding of drill geometry. Cutting lips, chisel edge angle, web thickness, helix angle, land width, point angle, rake angle and body clearance are the most important elements of drill geometry. Drill geometry is shown in figure 1.2 above.

Body of the drill is cylindrical with two semicircular helical flutes ground on periphery. Cylindrical surface is relieved to avoid full surface contact with hole wall. Precisely ground land runs helically along the sides of flutes. Land controls the size of the drilled hole. The tip of the drill is ground conically which leads to formation of two straight cutting lips of equal length. Cutting lips do the actual cutting whereas the chisel edge displaces the metal by extrusion action. Accuracy of the point angle at drill tip affects the relative lengths and heights of cutting lips which have large impact on cutting efficiency. Chips produced at the cutting lips slide upward through the flutes and the cutting fluid is discharged at cutting site through the flute.

1.3 Literature Survey

Production of precise holes with minimum errors in shape, size, location, straightness and surface finish is of utmost importance in view of increased demand for high accuracy and high productivity from industries. As discussed earlier the hole-quality is influenced by several factors such as tool geometry, process parameters, dynamics of drill and supporting machine tool structure, thermodynamic and material properties of drill and supporting machine tool structure and also the mechanics of cutting at the drill tip. Because of the vast applications of drilling, slight enhancement in performance of the drilling process has huge savings in manufacturing costs and reduces final product prices. Researchers have always tried to refine the understanding of the metal cutting processes with developments in basic sciences and advanced computing, measurement and control technologies in order to achieve perfection in drilling and other machining applications.

C. Sujatha, S. V. Muthukrishna [2] have presented the finite element model to study the lateral, angular and axial deflections of twist drill. The model incorporates all details of the drill geometry. They presented the results of the model and explained the effect of helix angle, point angle, chisel angle, diametrical clearance etc. on the deflections of the twist drill. The results of this extensive static analysis were used to optimize the design of drill.

D. M. Rincon, A. G. Ulsoy [3] have studied the effect of drill geometry, gyroscopic moments and rotary inertia on lateral vibration of drill. They found that although gyroscopic moments and rotary inertia are not that significant as to affect the natural

frequency of drill, number of flutes has impact on it. Higher the number of flutes, stiffer the drill becomes and leads to increase in natural frequency.

B. W. Huang [4] proposed a time dependent vibration model to study the effects of rotational speed, pre-twist angle and upward thrust on the amplitude response and natural frequency of the drill.

B. Dawson, W. Carnegie [5] studied the modal curves of the pre-twisted beam so as to study the effects of factors such as pre-twist angle, size of cross-section, aerodynamic effects etc. Theoretical mode shapes are studied for rectangular cross-section beams with emphasis on effect of width-depth ratio, pre-twist angle and results are validated by comparison with those from experiments.

O. Tekinalp, A. G. Ulsoy [6] developed a model based on Euler-Bernoulli Beam Theory to analyze the effects of various geometrical parameters of twist drill, cutting torques and forces, thrust forces etc. Equation of motion is solved by finite element technique and the results are compared with known analytical, experimental and numerical results. Effects of cross-sectional properties, helix angle on lateral stability of drill are studied.

B. W. Huang [7] applied the same model to micro-drilling operation. Thrust force was subject of concern for micro-drilling. Variation in natural frequencies of micro-drill with different thrust forces was studied. It was found that natural frequency decreases with

increase in thrust force up to a critical thrust force and drill becomes unstable for higher values.

A. C. Wijeyewickrema and L. M. Keer [8] have proposed a continuous model representing a pre-twisted drill subjected to a thrust load. Model incorporates the effects of rotary inertia, gyroscopic moments and shear deformation on transverse dynamic motion of the twist drill. Finite element method is used to obtain the critical speeds and critical thrust forces for different helix angles.

New model is developed on similar lines as explained above again by A. C. Wijeyewickrema, L. M. Keer and K. F. Ehman [9] for analysis of wandering motion observed in micro-drilling of electronic circuit boards. For micro-drills the aspect ratio is greater than twenty. Results of the finite element model are validated experimentally.

S. J. Lee, K. F. Eman and S. M. Wu [10] discussed the wandering phenomenon which is analyzed by other researchers as described above.

Dynamics of initial penetration of a drill are very important as it has profound impact on the hole quality and geometrical errors. Reference [11] by Y. Gong, C. Lin, and K. F. Ehmann is an effort to establish dynamic force models (thrust, torque and radial) for twist drill for drill's major and secondary cutting edges and for indentation zone, based on the understanding of the mechanics of cutting at these locations. Dynamic chip thickness variations due to drill grinding errors and lateral deflections are formulated and

corresponding formulations for dynamic chip areas at chisel edge and major cutting edge are also formulated.

Y. Gong, C. Lin, and K. F. Ehmann [12] formulated a complete model for drill skidding and wandering. Model incorporates both transverse and angular motions of drill tip. Drill is simplified as pre-twisted beam acted upon by axial thrust and unbalanced radial force at the drill tip. Continuous forms of governing equations of motion are developed and solved using finite element methods. For drill skidding, wandering and stable cutting, different boundary conditions are applied. Numerical results are verified by experiments. Explanation for generation of odd numbered polygonal holes is presented in mathematical form.

S. A. Basile [13] developed a 2-D model for drill rotating in a oversize hole and introduced the concept of work stiffness and included its effect by considering a system stiffness as bilinear spring. The model identified various factors affecting drill performance such as rotational speed, damping coefficient, drill-wall clearance, force amplitude modulation factor etc.

A. Poustie, Z. Katz [14] carried out the experiments on radial drilling machine in order to study the drill wandering and hole location errors. Deflection measurements were done on disc attached to the drill at some distance from tip allowing drilling up to 7 mm depth using infra-red sensor system. Experimental orbit clearly depicts the hole location error as a result of initial wandering and spindle alignment errors.

K. Gupta, O. B. Ozdoganlar, S. G. Kapoor, R. E. Devor [15] have studied the effect of the drill alignment error on drill dynamics. Analytical model presented was validated by experiments done on the aircraft extension drill. The model predicted the radial forces and corresponding lateral vibrations which were in agreement with the experimental values.

K. Gupta, O. B. Ozdoganlar, S. G. Kapoor and R. E. Devor [16] proposed a comprehensive hole profile prediction model which combines the effects of drill alignment errors, drill wandering and drill margin-hole wall interaction. Results of the model are validated experimentally.

P. V. Bayly, M. T. Lamar and S. G. Calvert [17] proposed quasi-static model to explain the phenomenon of regenerative vibration in presence of cutting and rubbing forces on similar line as in [8, 9 and 10]. Inertia and damping effects are neglected at low speeds. Whirling oscillations at odd integer multiple of the rotational frequency are observed. Analytical results are validated experimentally.

P. G. Reinhall and D. W. Storti [18] have used most simplistic approach to model a drill penetrating a circular hole in a thin plate. Drill trajectories are plotted for the case of no material removal and numerical methods are used to include the effect of metal cutting on walls of the hole.

C. H. Kahng and I. Ham [19] did theoretical and experimental investigation of influence of centering and pilot holes on roundness errors, parallelism errors and surface roughness and effectiveness of subsequent reaming and boring operations.

D. F. Galloway [20] provided a most extensive discussion on the effects of drill shape especially the elements like point angle, relief angle, relative lip height and many other parameters on drill life, drilling forces and drilling accuracy. Seven appendices in the paper provide valuable information on material properties, drill nomenclature, drill grinding parameters, theory of regenerative chatter, theoretical analysis of hole size variation and drill path during drilling. In addition to that expert comments of some other researchers on various issues discussed in paper are also presented.

At the start of the drilling operation drill rotates freely and drill tip has no constraints which resembles the fixed-free boundary condition of a cantilever beam. When at the start of penetration drill touches the surface of work it resembles the fixed-pinned boundary conditions. Finally when drill tip enters completely in the work-piece it can be assumed as fixed-fixed boundary condition. M. Kohring and C. Johnson [21] have done modal analysis for all these boundary constraints. Bending and torsional modes, natural frequencies and damping factors are determined.

A. G. Ulsoy [22] presented a lumped parameter model for transverse vibration of a twist drill to incorporate the effects of drill sizes, speed and feed of drilling. Model also

considers the centrifugal effect. He found out that the fundamental frequency decreases with the increase in the speed of the drill.

At the start of drilling operation drill tip deflects in elliptical orbit in addition to the drill rotation and is characterized as whirling vibration. H. Fujii, E. Marui, S. Ema [23] discussed the regenerative effect at the major cutting edge which is source of energy for this kind of vibration while the chisel edge is acting as a damper. In second part [24] they investigated the effect of drill's geometrical parameters on initial excitation of whirling vibration. Detailed explanation is given for role of chisel edge and flank surface in determining the amplitude of vibration. In third part [25] effect of presence of pilot hole on whirling vibration was theoretically studied. It was deduced that odd numbered polygonal holes can be an outcome of regenerative effect by virtue of which the low frequency vibration is caused which is well below the natural frequency of the system. Cutting forces vary from the mean values because of variation in dynamic chip load in the presence of lateral deflection of drill tip due to vibration. Drill bit vibration deteriorates the drilling performance, and the fluctuations in axial thrust, radial forces and torque are indicators of the presence of vibration. D. M. Rincon, A. G. Ulsoy [26] have proposed the analytical model for prediction of radial and thrust forces and torque.

E. B. Magrab and D. E. Gilsinn [27] have modeled the twist drill as pre-twisted Euler beam under the action of axial thrust and clamped at both end. Set of equations of motion is solved using Galerkin procedure. Natural frequencies, mode shapes and buckling loads are calculated for different combinations of geometrical parameters of a drill. Mode

shape revealed presence of complex out of plane motion which can be a cause for production of out of round holes.

Y. S. Tarng and T. C. Li [28] and E. Marui, S. Ema [29] proposed methods for detection and suppression of chatter vibration evident in deep-hole drilling because the lateral stiffness and damping are markedly lower. Chatter is detected by monitoring the variations in the thrust forces and torque. Earlier researchers used spindle speed change method using observed chatter frequency as basis for selection of new frequency to suppress chatter. Later researchers used the impact type damper for suppressing the chatter completely, which some times can not be suppressed by changing the cutting conditions.

The long drills exhibit whirling vibration as explained in [23, 24 and 25]. Another kind of vibration is called drill chatter. H. Fujii, E. Marui, S. Ema [30] presented the experimental analysis for chatter vibration. Parameters investigated are the frequency, amplitude, initiation boundary of chatter. Unstable range of chatter is found out for different sets of parameters. Experimental results revealed that chatter frequency is equal to drills first natural frequency for the condition of drill tip supported in machined hole.

A. Askari, E. Stone [31] have discussed the effects of friction on both the regenerative and non-regenerative chatter observed in drilling. The one-dimensional model explains the excitation of the torsional-axial mode and its interaction with the nonlinear frictional forces.

A. G. Rehorn, J. Jiang, P. E. Orban and E. Bordatchev [32] investigated the structural dynamics of the high-precision machine tools. Impact testing and modal analysis is done to check change in dynamic response of spindle after adding cutter. Also the investigation results suggest that for precise applications dynamics of drive spindle should be considered to seek improved performance. The model is also useful for tool condition monitoring.

W. C. Chen [33] has discussed the drill design method based on finite element analysis to find optimum drill geometry of the twist drill. Two dimensional and three dimensional finite element analysis is applied to study the effect of various drill geometry features on the drill's torsional rigidity. Three dimensional analysis results demonstrating the effect of helix angle on lateral, angular and axial drill deformations are of great significance.

In case of twisted beams a static torque causes axial deformation whereas axial thrust produces twist in the beam. This phenomenon is called torsional-axial coupling. P. V. Bayly, S. A. Metzler, A. J. Schaut, K. A. Young [34] tried to explain the torsional chatter in drilling by torsional-axial coupling. Results are validated by numerical and experimental analysis.

D. H. Hodges [35] used principle of virtual work to formulate equilibrium equation for static torsional deformation of pre-twisted beams. He deduced that pre-twisted beam untwists under the action of tensile loads.

T. Arvajeh, F. Ismail [36] have studied both bending and torsional chatter in an integrated way. Time domain simulation model presented combines the effect of both torsional and bending. Effect of drill length on both types of chatter is comparatively studied. Results of simulations and experiments for two different length drill are presented and discussed.

A. J. Schaut, D. N. Dilley, P. V. Bayly [37] have proposed a model which uses spring supported end conditions unlike many other models which used either fixed type or pinned type end condition. Spring supported end condition is more representative of the actual drill- workpiece interaction. Paper also explains the chisel point effect on chatter frequency through the experimental results.

K. V. Nagrajan [38] extensively studied the model proposed by S. A. Basile in [13]. He plotted drill orbits for different simulation parameters to validate the model proposed by S.A. Basile. He compared the orbital motion plotted using finite element analysis of drill-spindle assembly with the experimental orbits obtained from tests done on bench press for free rotation of drill.

1.4 Objectives of the Thesis

In the previous section, a literature review was carried out in order to understand the approaches used by different researchers for investigation of factors causing inaccuracies in drilled holes.

Two most important approaches are discrete analysis and continuous analysis. Continuous models always give better approximation of actual drilling inaccuracies but it is also true that discrete models can also be equally effective in simulating the actual drilling process if simulation parameters are selected properly and assumptions about boundary constraints and excitation forces are made based on sound practical or experimental data.

Some researchers preferred to study selectively various stages of drilling viz. skidding, wandering and stable cutting, whereas other preferred integrated study which is rather complex. Some models studied bending, torsion and axial vibration separately whereas other models studied them in integrated manner.

The first objective of the thesis is to thoroughly investigate the lumped mass model for bending vibration of the drill presented in reference [13], calculate analytically or experimentally the simulation parameters, refine the concept of boundary constraints and ultimately build a new lumped mass model to simulate the actual drilling operation more precisely and fully understand the cause of the most common drilling errors based on the critical analysis of the simulation results.

The second objective of the thesis is to develop a continuous model for twist drill as a cantilever with point load acting at unconstrained drill tip to study the static bending characteristics of twist drill, to understand the significance of different geometrical parameters in bending behavior and stiffness of twist drill.

The third objective of the thesis is to develop a continuous model for twist drill as a cantilever with point load acting at unconstrained drill tip to study the dynamic bending characteristics of twist drill and to identify the first two natural frequencies and mode shapes of twist drill.

The fourth objective of the thesis is to carry out experimental measurements of torsional stiffness of twist drills in clockwise and anti clockwise direction in order to verify the stiffness asymmetry.

The fifth objective of the thesis is to investigate the effect of the cutting resistance on torsional behavior of twist drill when the drill is cutting through the work-piece material and to develop a simple discrete torsional model considering time dependent periodic variations in magnitude of the torsional stiffness of twist drill when cutting through the work-piece material.

The final objective of the thesis is to develop a lumped mass model to study the Bending-Torsional Coupling and to study the significance of this coupling on torsional and bending vibrations of twist drill.

1.5 Organization of the Thesis

In Chapter 1, an introduction to the drilling operation, the drilling machine and the twist drill design is given. Survey of past research work on the topic of twist drill vibration is presented briefly and objective of thesis is defined.

In Chapter 2, the continuous model to study the static bending characteristics of twist drill as a cantilever beam with point load acting at unconstrained drill tip is presented. Model is simulated in Matlab to understand the significance of different geometrical parameters in bending behavior and stiffness of twist drill.

In Chapter 3, the continuous model to study the dynamic bending characteristics of twist drill as a cantilever with point load acting at unconstrained drill tip is presented. Model is simulated in Matlab to identify the first two natural frequencies and mode shapes of twist drill.

In chapter 4, the lumped mass model for bending vibration of drill described in reference [13], boundary constraint formulation and forcing function are investigated. The new concept of boundary constraint is described and new formulation of work stiffness proposed. Finally modified lumped mass model considering new work stiffness concept is presented.

Model is simulated in Matlab and results predicting the drill orbits for different sets of parameters are presented followed by the explanation for the most common drilling errors based on the analysis of the simulation results.

In chapter 5, experimental investigations are done to verify to verify the symmetry in torsional stiffness of twist drills in clockwise and anti clockwise direction.

In chapter 6, the simple discrete torsional model is developed considering time dependent cyclic variations of the torsional stiffness of twist drill because of the of the cutting resistance coming in to picture as a result of torsional vibration of drill tip when cutting through the work-piece material. Model is simulated in Matlab to study the effect of this non-linear torsional stiffness on torsional response for harmonic torque imbalance. Another lumped mass model to study the Bending-Torsional Coupling is developed and the significance of this coupling on torsional vibration of twist drill is studied.

In Chapter 7, conclusions and recommendations for future work are presented.

CHAPTER 2

CONTINUOUS MODEL - STATIC BENDING CHARACTERISTICS OF TWIST DRILLS

2.1 Introduction

Different modeling efforts for lateral vibration analysis of twist drill demands thorough understanding of bending characteristic of fluted or twisted beams similar to twist drill. Generalized formulation for moment of inertia calculation of fluted structures is presented. Moment of Inertia formulae for two, three and four fluted drills are derived.

Moment of inertia of twist drill varies continuously as we move from tip of the drill to the fixed end. The bisymmetric cross-section of drill changes its angular orientation with respect to the direction of unbalanced cutting force which is assumed to act perpendicular to cutting lips as we move along the length of the drill. Bending equation for uniform beams is modified by replacing the constant moment of inertia term with varying values which are functions of length and twist angle along the twist drill. Second order differential equation obtained is solved numerically using boundary value problem solver in Matlab. Drill is considered as a cantilever beam with point load at the tip and corresponding boundary conditions are used. Full length of drill is assumed to be fluted, ignoring the cylindrical shank of drill and drill is assumed to be made by uniformly twisting the strip of rectangular cross-section.

2.2 Moment of Inertia Formulation for Fluted Cutting Tools

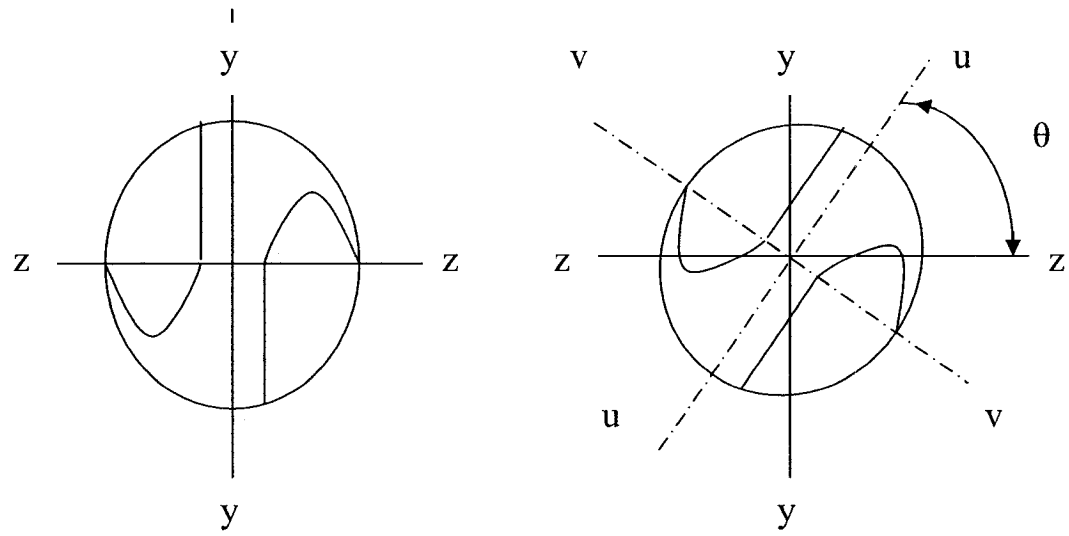

Figure 2.1: Schematic of Twist Drill Cross-section

Cross-section of the twist drill is as shown in figure 2.1. Suppose axes system YY-ZZ is fixed on the drill and drill cross-section perpendicular to drill center line lies in plane YZ (Inertial Frame). The unbalanced cutting force acts perpendicular to axis YY which is again axis of bi-symmetry. As said before cross-section changes its orientation by an angle 'θ' degree along length. Consider that new displaced axes system UU and VV (Twisted Frame) is placed at an angle of 'θ' with respect to the fixed axes system YY-ZZ such that the axis UU lies along axis bi-symmetry running parallel to two cutting lips. Suppose I_{zz}, I_{yy} and I_{uu}, I_{vv} are area moments of inertias of the cross-section corresponding to the fixed axes system, and displaced axes system, respectively. Now applying transformation principle we can define new coordinates in displaced axes system UU –VV as follows,

$$u = z \cdot \cos\theta + y \cdot \sin\theta$$
$$v = y \cdot \cos\theta - z \cdot \sin\theta \qquad \textbf{Equation 2.1}$$

From definitions of moment of inertia and product moment of inertia, we can write,

$$I_{uu} = \int v^2 \cdot dA$$
$$I_{vv} = \int u^2 \cdot dA \qquad \textbf{Equation 2.2}$$
$$I_{uv} = \int u \cdot v \cdot dA$$

Substituting equation 2.1 in 2.2, we get,

$$I_{uu} = I_{zz} \cdot \cos^2\theta + I_{yy} \cdot \sin^2\theta - 2 \cdot I_{zy} \cdot \sin\theta \cdot \cos\theta$$
$$I_{vv} = I_{zz} \cdot \sin^2\theta + I_{yy} \cdot \cos^2\theta + 2 \cdot I_{zy} \cdot \sin\theta \cdot \cos\theta \qquad \textbf{Equation 2.3}$$
$$I_{uv} = \left(I_{zz} - I_{yy}\right) \cdot \sin\theta \cdot \cos\theta + I_{zy} \cdot \left(\cos^2\theta - \sin^2\theta\right)$$

Rewriting in matrix form,

$$\begin{bmatrix} I_{uu} & I_{uv} \\ I_{uv} & I_{vv} \end{bmatrix} = \begin{bmatrix} \cos\theta & \sin\theta \\ -\sin\theta & \cos\theta \end{bmatrix}^T \cdot \begin{bmatrix} I_{zz} & I_{zy} \\ I_{zy} & I_{yy} \end{bmatrix} \cdot \begin{bmatrix} \cos\theta & \sin\theta \\ -\sin\theta & \cos\theta \end{bmatrix}$$

Equation 2.4

Above formulation can be applied to multi fluted cutting tools such as twist drill as follows. Consider a twist drill with 'n' number of flutes. Let us divide the total cross

section in 'n' symmetric sectors. Let I_{zz}, I_{yy} and I_{zy} are area moments of inertias and product moment of inertia of individual sector about the principal axes. Now the moment of inertia properties of whole cross section of a twist drill with 'n' number of flutes can be calculated from the following generalized formula [3].

$$\begin{bmatrix} I_{uu} & I_{uv} \\ I_{uv} & I_{vv} \end{bmatrix} = \sum_{i=1}^{n} \left\{ \begin{bmatrix} \cos\theta_i & \sin\theta_i \\ -\sin\theta_i & \cos\theta_i \end{bmatrix}^T \cdot \begin{bmatrix} I_{zz} & I_{zy} \\ I_{zy} & I_{yy} \end{bmatrix} \cdot \begin{bmatrix} \cos\theta_i & \sin\theta_i \\ -\sin\theta_i & \cos\theta_i \end{bmatrix} \right\}$$

Equation 2.5

where,

$$\theta_i = \frac{2 \cdot \pi \cdot i}{n}$$ **Equation 2.6**

If I_{zz} and I_{yy} are principal moments of inertias in above formulation, then the principal product moment of inertia

$$I_{zy} = 0$$

Hence we can write following generalized formulation for moments of inertias of multi fluted twist drills in terms of principal moments of inertias I_{pzz}, I_{pyy}

$$\begin{bmatrix} I_{puu} & 0 \\ 0 & I_{pvv} \end{bmatrix} = \sum_{i=1}^{n} \left\{ \begin{bmatrix} \cos\theta_i & \sin\theta_i \\ -\sin\theta_i & \cos\theta_i \end{bmatrix}^T \cdot \begin{bmatrix} I_{pzz} & 0 \\ 0 & I_{pyy} \end{bmatrix} \cdot \begin{bmatrix} \cos\theta_i & \sin\theta_i \\ -\sin\theta_i & \cos\theta_i \end{bmatrix} \right\}$$

Equation 2.7

For two, three and four fluted twist drills following simplified formulae are derived respectively [3].

$$\begin{bmatrix} I_{puu} & 0 \\ 0 & I_{pvv} \end{bmatrix} = \begin{bmatrix} 2 \cdot I_{pzz} & 0 \\ 0 & 2 \cdot I_{pyy} \end{bmatrix} \qquad 2 - \text{flutes}$$

$$\begin{bmatrix} I_{puu} & 0 \\ 0 & I_{pvv} \end{bmatrix} = \begin{bmatrix} \frac{3}{2} \cdot I_{pzz} + \frac{3}{2} \cdot I_{pyy} & 0 \\ 0 & \frac{3}{2} \cdot I_{pzz} + \frac{3}{2} \cdot I_{pyy} \end{bmatrix} \qquad 3 - \text{flutes}$$

$$\begin{bmatrix} I_{puu} & 0 \\ 0 & I_{pvv} \end{bmatrix} = \begin{bmatrix} 2 \cdot I_{pzz} + 2 \cdot I_{pyy} & 0 \\ 0 & 2 \cdot I_{pzz} + 2 \cdot I_{pyy} \end{bmatrix} \qquad 4 - \text{flutes}$$

Equation 2.8

2.3 Bending Deflection of Beam with Rectangular Cross-section

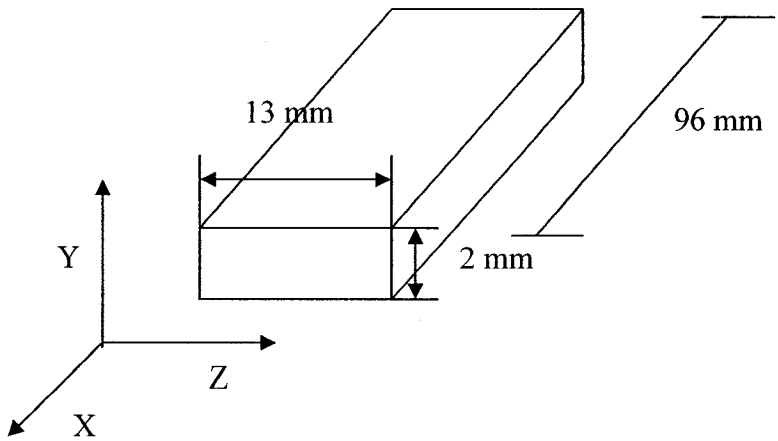

Figure 2.2: Schematic of Beam Cross-section and Axes System

Deflection of cantilever beam with point load at free end is given by

$$\delta_{max} = \frac{F \cdot L^3}{3 \cdot E \cdot I} \qquad \textbf{Equation 2.9}$$

Assuming standard drill geometry and the following numerical values

F	=	1.0 N		(Force)
L	=	0.096 m		(Length)
E	=	$210.0 \times 10^9 \frac{N}{m^2}$		(Modulus of Elasticity)
D	=	13.0 mm		(Diameter)
b	=	2.0 mm		(Web Thickness)
I_{zz}	=	8.0×10^{-12}	m^4	(Moment of Inertia)
I_{yy}	=	357.0×10^{-12}	m^4	(Moment of Inertia)

The bending deflection of a beam with rectangular cross-section normal to the width of the section i.e. about axis of symmetry parallel to axis ZZ (Figure 2.2)

$$\delta_{max} = \quad -1.7554 \times 10^{-4}\ m$$

The bending deflection of a beam with rectangular cross-section parallel to the width of the section i.e. about axis of symmetry parallel to axis YY (Figure 2.2)

$$\delta_{max} = \quad -3.9337 \times 10^{-6}\ m$$

2.4 Bending Characteristics of Twist Drill

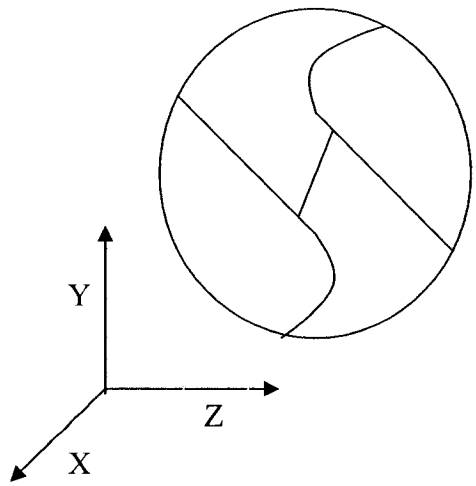

Figure 2.3: Schematic of Twist Drill Cross-section and Axes System

Generalized bending equations for uniform beams can be written as follows [40]

$$E\frac{d^2y}{dx^2} = \frac{M_b}{I_{zz}(x)} \quad \text{and} \quad E\frac{d^2y}{dx^2} = \frac{f_b}{y} \qquad \textbf{Equation 2.10}$$

where,

$$\frac{1}{R} = \frac{d^2y}{dx^2} \qquad \textbf{Equation 2.11}$$

M_b = Bending Moment

f_b = Tensile or compressive stress in extreme fiber of beam

y = Distance of extreme fiber from neutral axis of beam

Hence,

$$\frac{M_b}{I_{zz}(x)} = \frac{f_b}{y} = \frac{E}{R}$$ **Equation 2.12**

Let 'P' be the pitch of the twist drill. Twist angle per unit length 'β' is given by,

$$\beta = \frac{2 \cdot \pi}{P}$$ **Equation 2.13**

The area moments of inertias $I_{zz}(x)$ and $I_{yy}(x)$ for twist drills change along length and are functions of twist angle per unit length 'β' and coordinate 'x'.

By following the same steps followed for deriving equation 2.7 the equations for the area moments of inertias $I_{zz}(x)$ and $I_{yy}(x)$ at any point along 'x' are given by [3].

$$I_{zz}(x) = I_{zz} \cdot \cos^2(\beta \cdot x) + I_{yy} \cdot \sin^2(\beta \cdot x)$$
$$I_{yy}(x) = I_{yy} \cdot \cos^2(\beta \cdot x) + I_{zz} \cdot \sin^2(\beta \cdot x)$$ **Equation 2.14**

Applying above formulation of area moment of inertia bending equation for twist drill fixed at shank and point load 'F' acting at tip is given by,

$$\frac{d^2y}{dx^2} = \frac{F \cdot (L - x)}{E \cdot I_{zz}(x)}$$ **Equation 2.15**

In order to get the deflection curve this equation is solved numerically using the boundary value problem solver in Matlab. The following four Boundary Conditions (BCs) for cantilever beam are used.

A] At fixed end i.e. at $\mathbf{x = 0}$

$$y = 0, \qquad \frac{dy}{dx} = 0$$

B] At free end i.e. at $\mathbf{x = L}$

$$\frac{d^2y}{dx^2} = 0, \qquad \frac{d^3y}{dx^3} = F$$ **Equation 2.16**

Equation 2.15 will use the first three boundary conditions. The equation 2.15 is differentiated once to obtain following equation.

$$\frac{d^3y}{dx^3} = \frac{F}{E} \cdot \left\{ \frac{d}{dx} \left[\frac{L - x}{I_{zz}(x)} \right] \right\}$$

$$\frac{d^3y}{dx^3} = \frac{F}{E} \left[\frac{G \cdot (L - x) \cdot \sin(2 \cdot \beta \cdot x) - \left(I_{zz} \cdot \cos^2(\beta \cdot x) + I_{yy} \cdot \sin^2(\beta \cdot x) \right)}{\left(I_{zz} \cdot \cos^2(\beta \cdot x) + I_{yy} \cdot \sin^2(\beta \cdot x) \right)^2} \right]$$

Equation 2.17

where,

G = Numerical Constant which appears after differentiation using Maple

(For twist drill of D = 13 mm, L = 96 mm, b = 2 mm)

$$= \quad 0.5 \times \quad 0.1370519859 \times 10^{-7} \qquad (P = 32 \text{ mm})$$

$$= \quad 0.5 \times \quad 0.913679906 \times 10^{-7} \qquad (P = 48 \text{ mm})$$

$$= \quad 0.5 \times \quad 0.783153906 \times 10^{-7} \qquad (P = 56 \text{ mm})$$

$$= \quad 0.5 \times \quad 0.84339689 \times 10^{-7} \qquad (P = 52 \text{ mm})$$

$$= \quad 0.5 \times \quad 0.730944204 \times 10^{-7} \qquad (P = 60 \text{ mm})$$

$$= \quad 0.5 \times \quad 0.685260104 \times 10^{-7} \qquad (P = 64 \text{ mm})$$

$$= \quad 0.5 \times \quad 0.548207804 \times 10^{-7} \qquad (P = 80 \text{ mm})$$

The fourth boundary condition can be applied to equation 2.17 above.

2.5 Simulation Results and Interpretations

The third order differential equation (Equation 2.17) is solved numerically in Matlab to get the deflection vector for whole length of drill. Deflection vector so obtained is plotted with respect to length vector of the twisted beam to get the deflection curve. The influence of fluted geometry on the deflection of a beam is evident from the nature of the deflection curves as seen in the different simulation results presented below. Deflection curves are plotted for beam with rectangular cross-section about axis of symmetry parallel to axis ZZ and axis YY (Figure 2.2) for comparison purpose.

After comparing the deflection curves for untwisted strip of uniform rectangular cross-section along length (figures 2.4, 2.5) with the deflection curves for twisted beam with identical cross-section (figures 2.6 to 2.10), it is found that slope and curvature variations along the length of the beam follows different trend as compared to untwisted beam of uniform rectangular cross-section. Hence slope and curvature variation trends are studied by plotting the variations with respect to length of the twisted beam for both untwisted beam of uniform cross-section and twist drill. Slope and curvature variation plots and corresponding deflection curve plots for beam length equal to twice the pitch are also presented below (figures 2.12 to 2.17).

In figures 2.6 to 2.10 it is observed that end deflection is function of phase angle. Phase angle 'Φ' is the angle between the axis of bi-symmetry at the tip and at the fixed end. So if the point-load at the tip of drill is in vertical direction and for given length of a drill the orientation of axis of bi-symmetry is horizontal then phase angle is considered equal to

zero. If the phase angle is changed in steps from 0 degree to 180 degree corresponding end deflection values also change as shown in figures 2.6 to 2.10 presented below. Variation of end deflection of the twisted beam is studied by changing value of phase angle 'Φ' over a range of '0-180' degree and for different pitch values between 32 mm and 80 mm (figures 2.18 to 2.24).

Deflection of the twist drill is found to be grater than the deflection calculated using empirical formula for rectangular cross-section beam when load acting parallel to the width of the section and it is found to be less than that when load acting normal to the width of the section. The end deflections obtained by solving the continuous bending model for the rectangular cross-section beam when load acting parallel to the width of the section and normal to the width of the section are compared with the respective end deflection calculated using empirical formulae. These results are found to be identical. Thus the reliability of the numerical results obtained for the continuous bending model for the actual case of twist drill is validated.

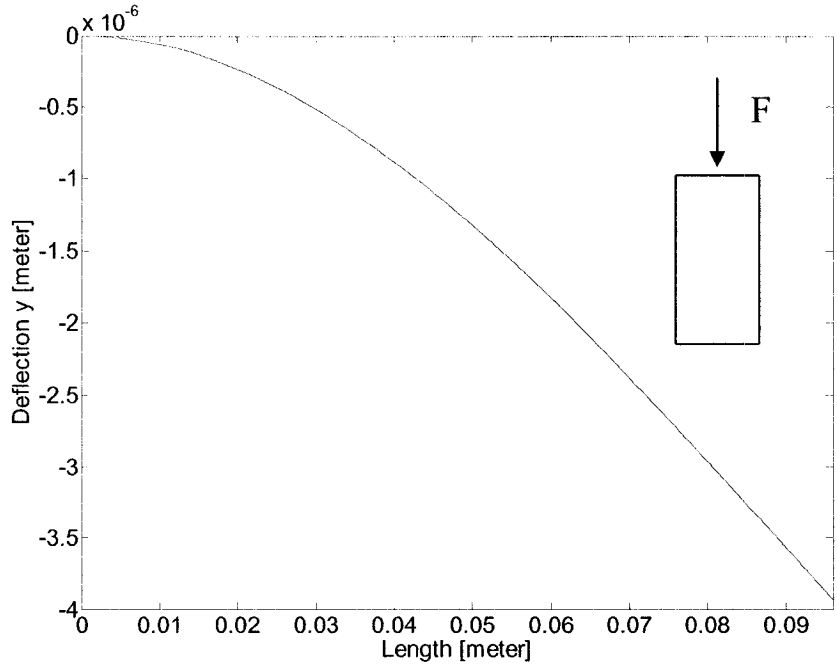

Figure 2.4: Deflection Curves for Rectangular Strip Placed Vertically
(Deflection at free end = - 3.9337 $\times 10^{-6}$ m = = - 0.0039337 mm)

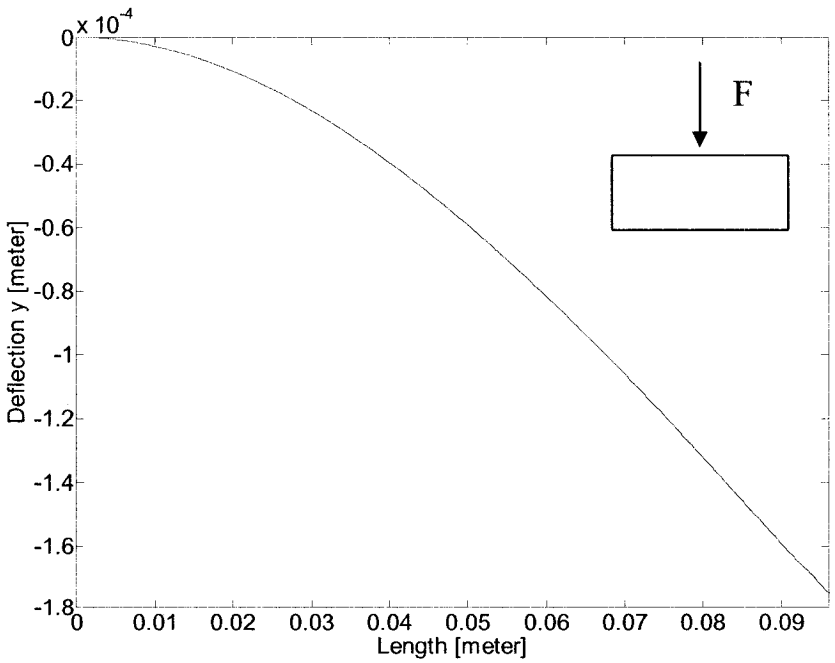

Figure 2.5: Deflection Curves for Rectangular Strip Placed Horizontally
(Deflection at free end = - 1.7554 $\times$ 10^{-4} m = - 0.175542 mm)

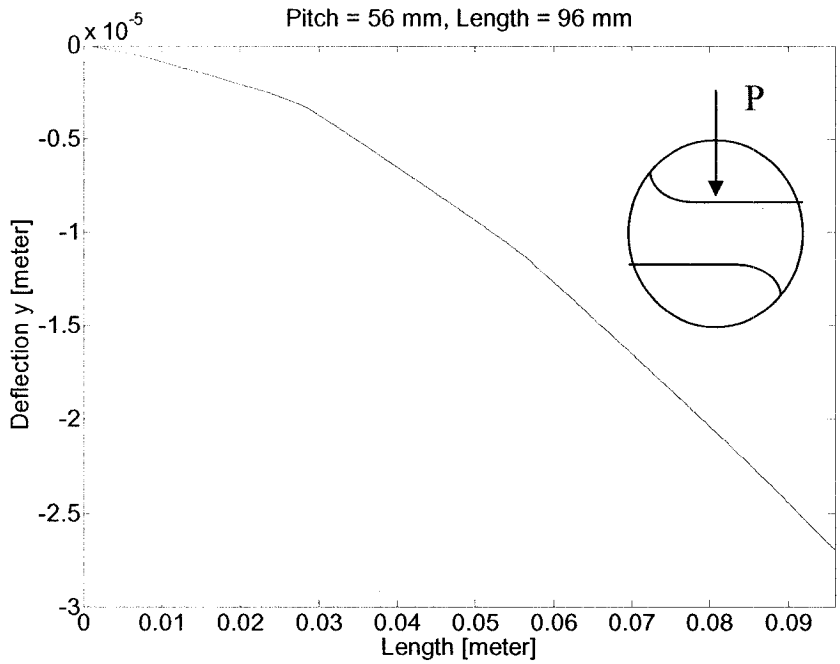

Figure 2.6: Deflection Curves for Twist Drill (Φ = 0 degree)
(Deflection at free end = - 2.6921 × 10^{-5} m = - 0.026921 mm)

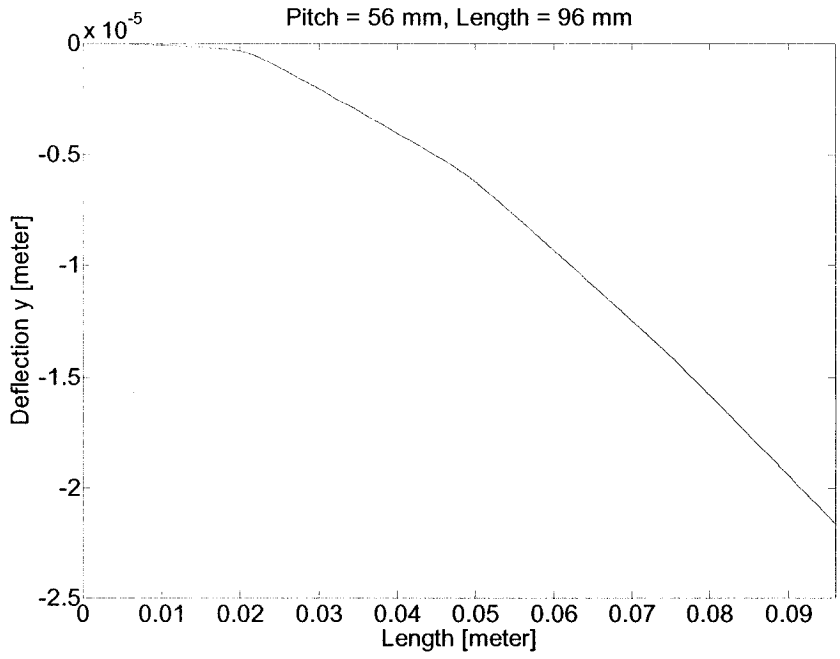

Figure 2.7: Deflection Curves for Twist Drill (Φ = 45 degree)
(Deflection at free end = - 2.1577 × 10^{-5} m = - 0.021577 mm)

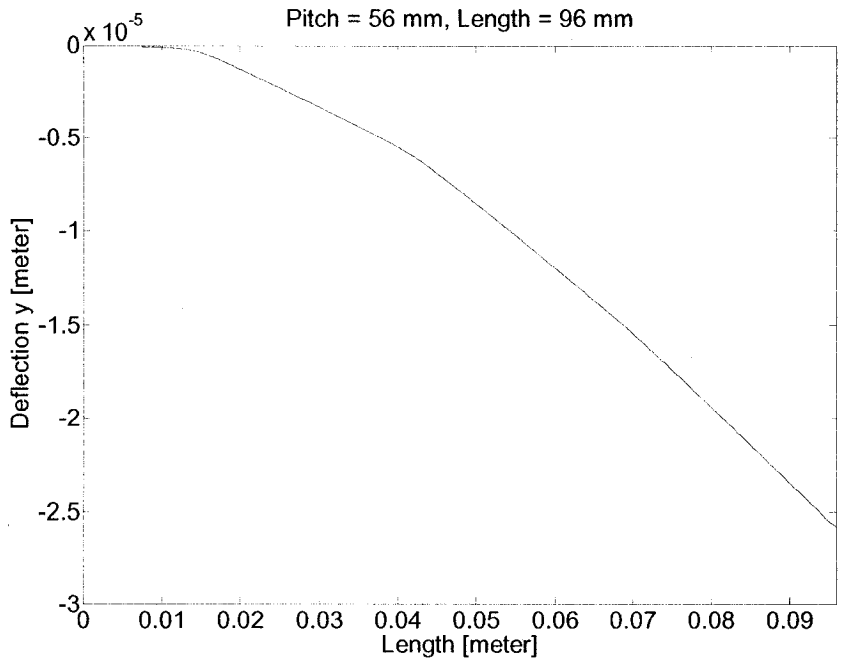

Figure 2.8: Deflection Curves for Twist Drill (Φ = 90 degree)
(Deflection at free end = - 2.5859 × 10^{-5} m = - 0.025859 mm)

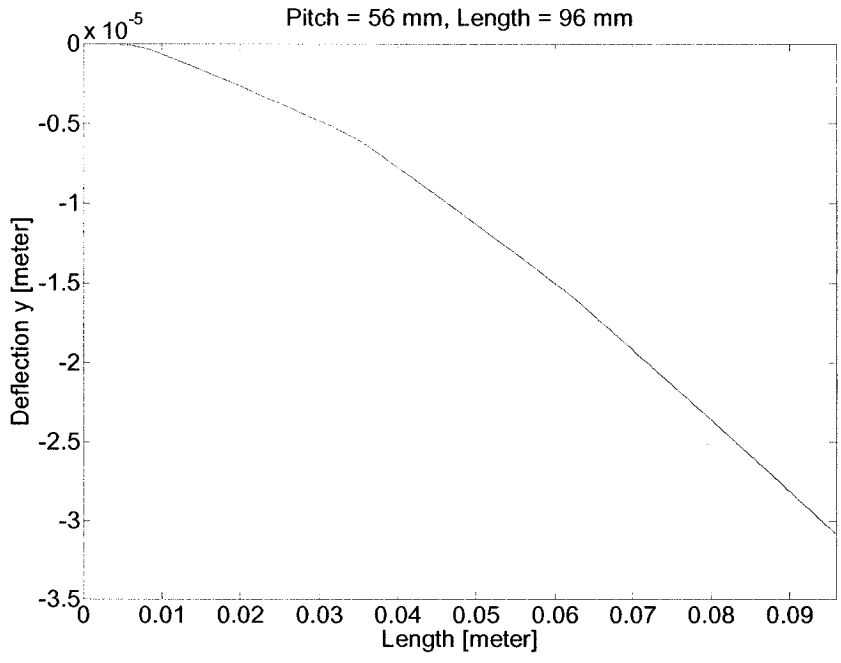

Figure 2.9: Deflection Curves for Twist Drill (Φ = 135 degree)
(Deflection at free end = - 3.0811 × 10^{-5} m = - 0.030811 mm)

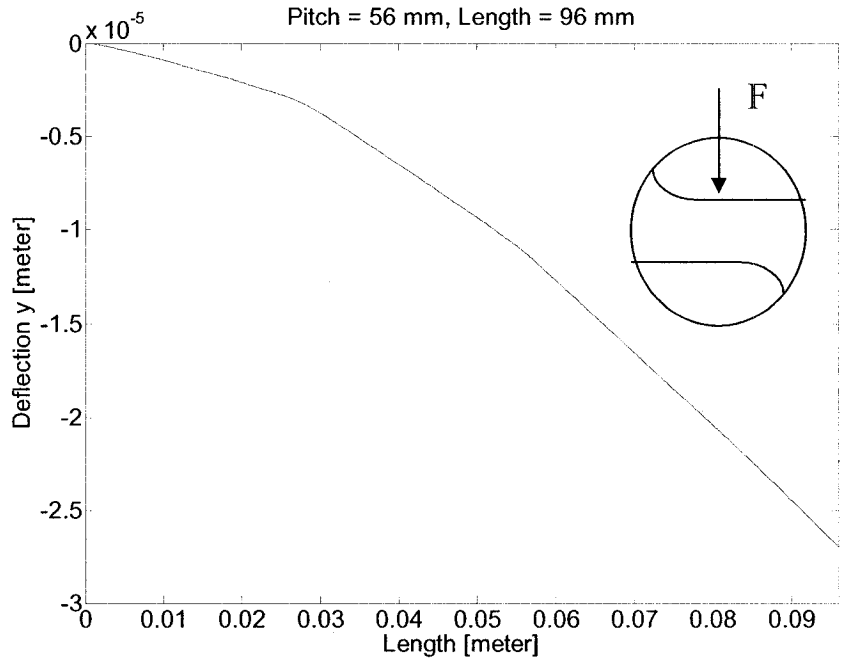

Figure 2.10: Deflection Curves for Twist Drill (Φ = 180 degree)
(Deflection at free end = - 2.6921 × 10^{-5} m = - 0.026921 mm)

Fig 2.11 shows variation in I_{zzx} along length 'x'. Since there are two flutes in this drill there are two cosine curves in the pitch length of 56 mm. Effect of variation in I_{zzx} is clearly reflected in the deflection curve by comparing figures 2.12 and 2.13, which show respectively the deflections of a twist drill and a rectangular beam. Unlike the deflection curve for strip of uniform rectangular cross-section shown in figure 2.13, for twist drill transition points are observed at the distances multiple of half pitch length along the length of drill where radius of curvature is comparatively smaller.

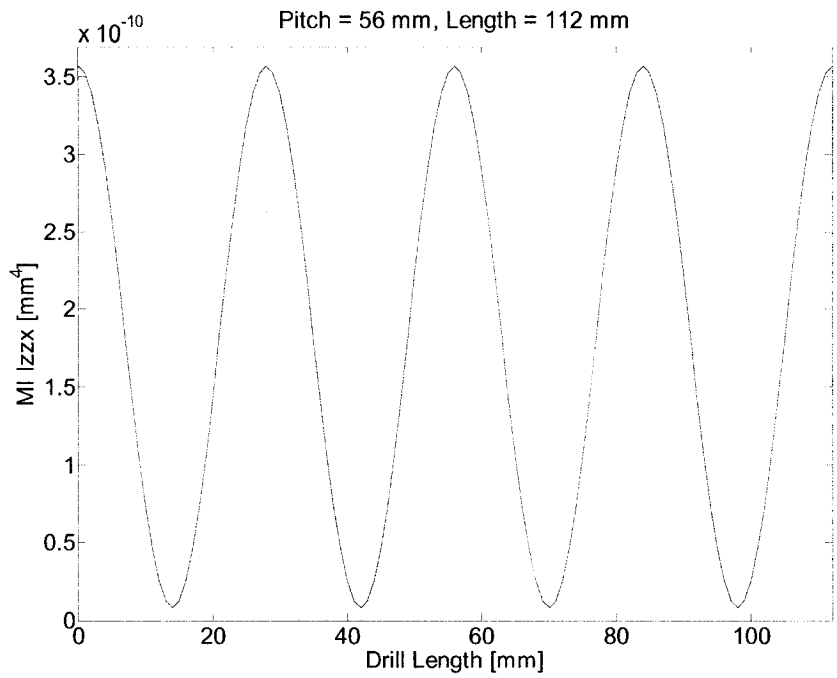

Figure 2.11: Area Moment of Inertia Variations along the Length of Twist Drill

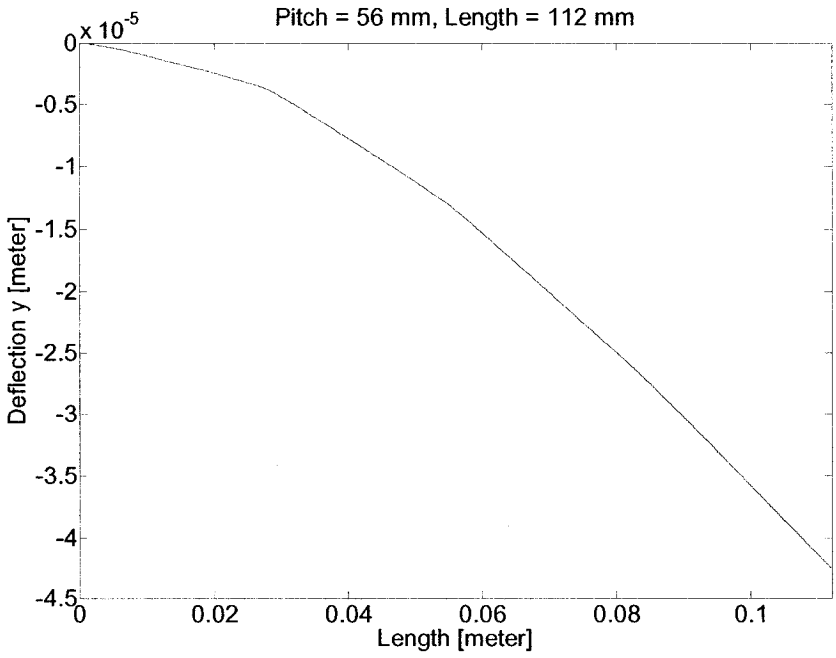

Figure 2.12: Deflection Curve for Twist Drill (Φ = 0 degree)

(Deflection at free end = - 4.2489 × 10^{-5} m = - 0.0425 mm)

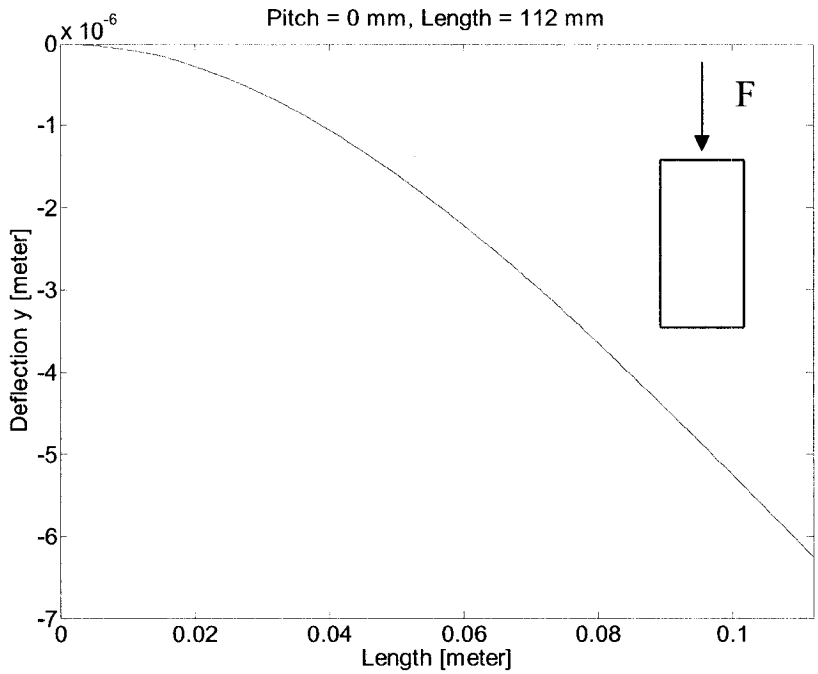

Figure 2.13: Deflection Curve for Rectangular Strip Placed Vertically
(Deflection at free end = - 6.2466 × 10^{-6} m = - 0.00625 mm)

Figures 2.14 and 2.15 are plots of slope ($\frac{dy}{dx}$) with respect to length for untwisted strip of uniform rectangular cross-section and twist drill, respectively. It is observed that slope variation pattern is repeated for every half pitch length for twist drill whereas for untwisted strip slope variation pattern is more uniform throughout the length.

Figures 2.16 and 2.17 are plots of curvature ($\frac{d^2y}{dx^2}$) with respect to length for untwisted strip of uniform rectangular cross-section and twist drill, respectively. Also the curvature values are higher (radius of curvature is smaller) around the points placed at distances which are multiple of half pitch length along the beam length as compared to the points spanned in-between these points. Again it is observed that as we move farther from fixed

end of drill the radius of curvature steadily increases whereas the curvature changes linearly for untwisted strip.

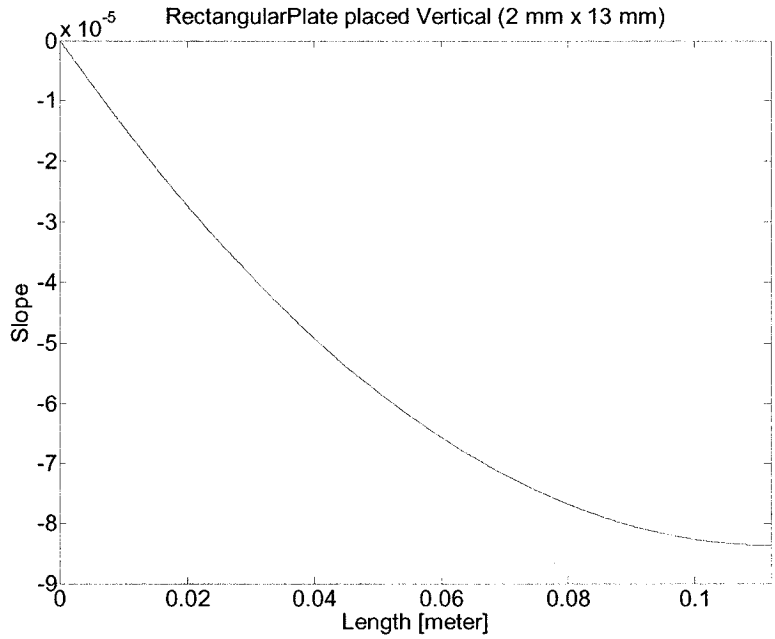

Figure 2.14: Slope variation curve for Rectangular Strip Placed Vertically

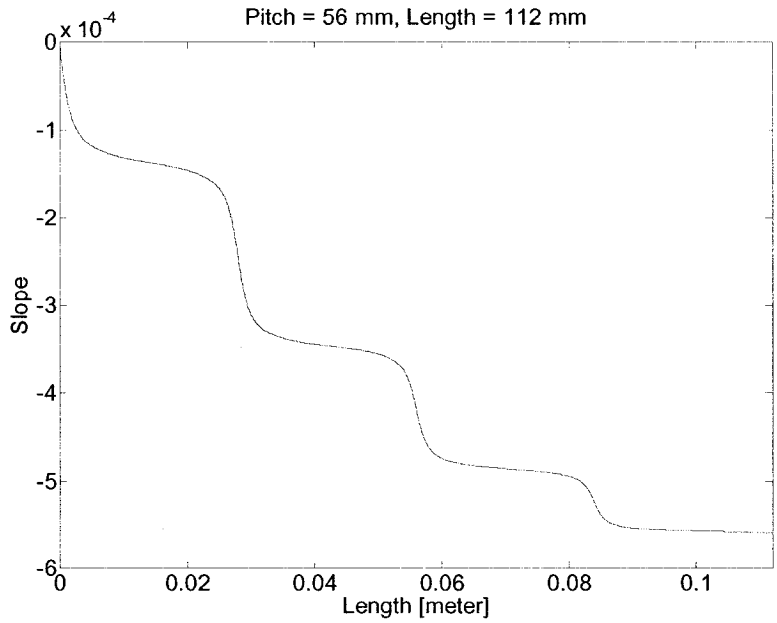

Figure 2.15: Slope Variation Curve for Twist Drill ($\Phi = 0$ degree)

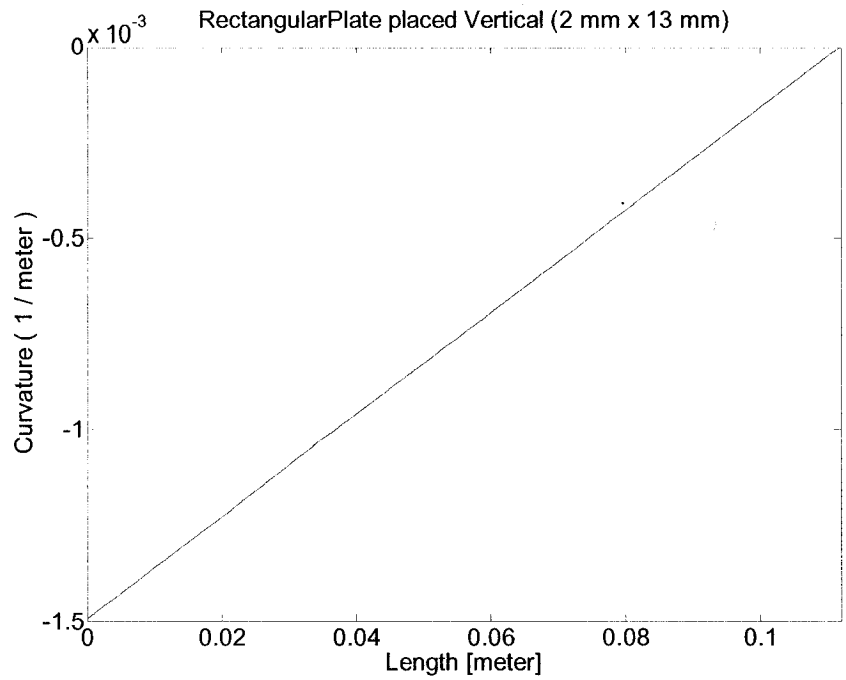

Figure 2.16: Curvature Variation Curve for Rectangular Strip Placed Vertically

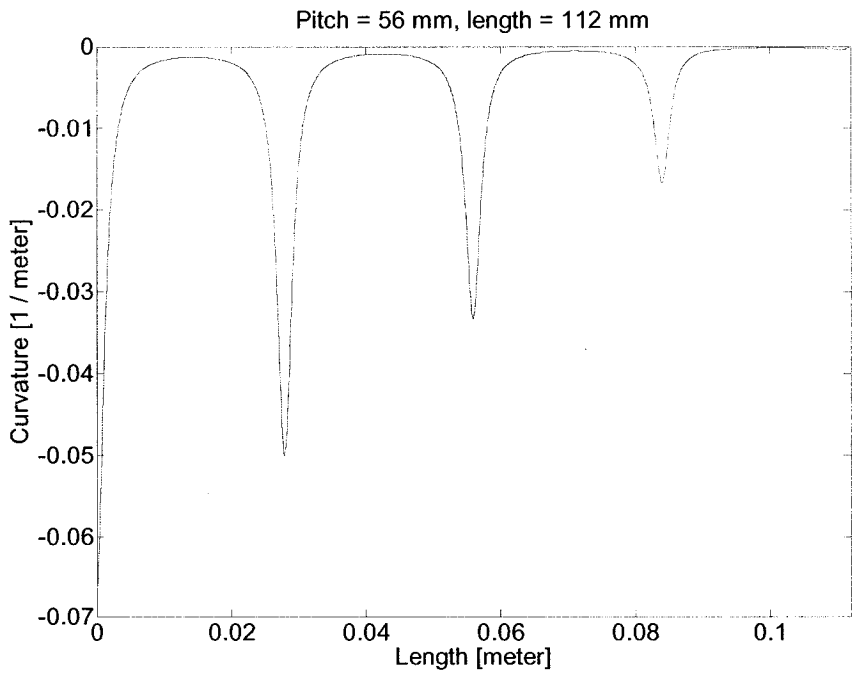

Figure 2.17: Curvature Variation Curve for Twist Drill (Φ = 0 degree)

Figures 2.18 to 2.24 are the plots of end deflection of a twist drill with respect to phase angle obtained for different values of pitch. Pitch is the indicator of degree of twist in the drill. When pitch is changed from smaller to higher values range of the end deflection is affected significantly. For smaller pitch drill the end deflection varies over a smaller range, indicating that lateral stiffness of drill does not vary much with the change in phase angle. On the other hand for higher pitch drill lateral stiffness vary significantly with the change in phase angle. Another observation is that the end deflection is found to be highest (lowest stiffness) in the small region around $\Phi = 72$ degree and lowest (highest stiffness) in the region around $\Phi = 112$ degree i.e. around circled points shown in figure 2.18.

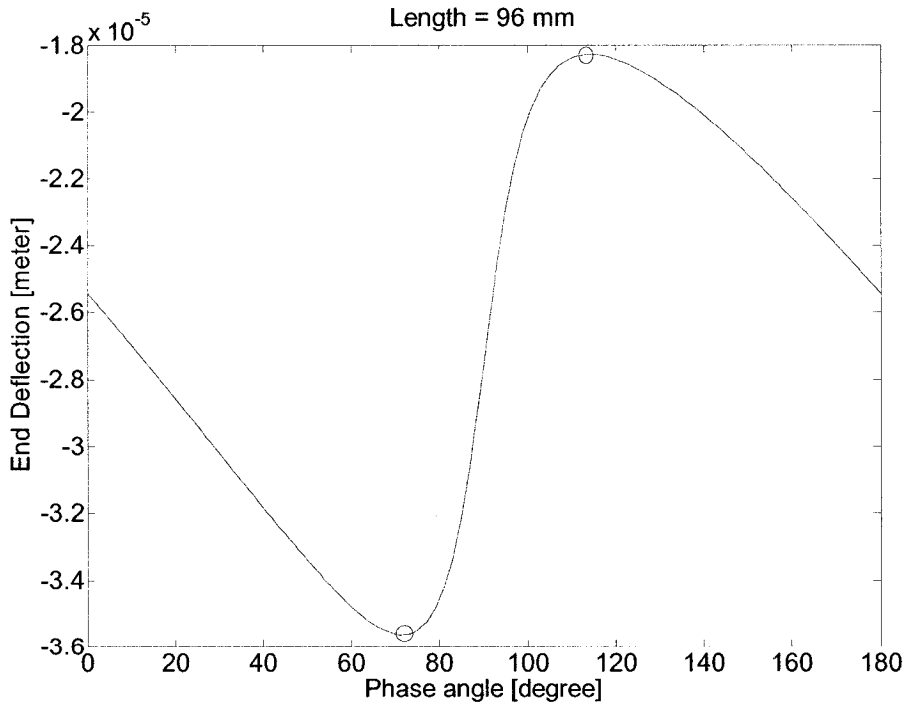

Figure 2.18: End Deflection Variation with Phase Angle (Pitch = 80 mm)

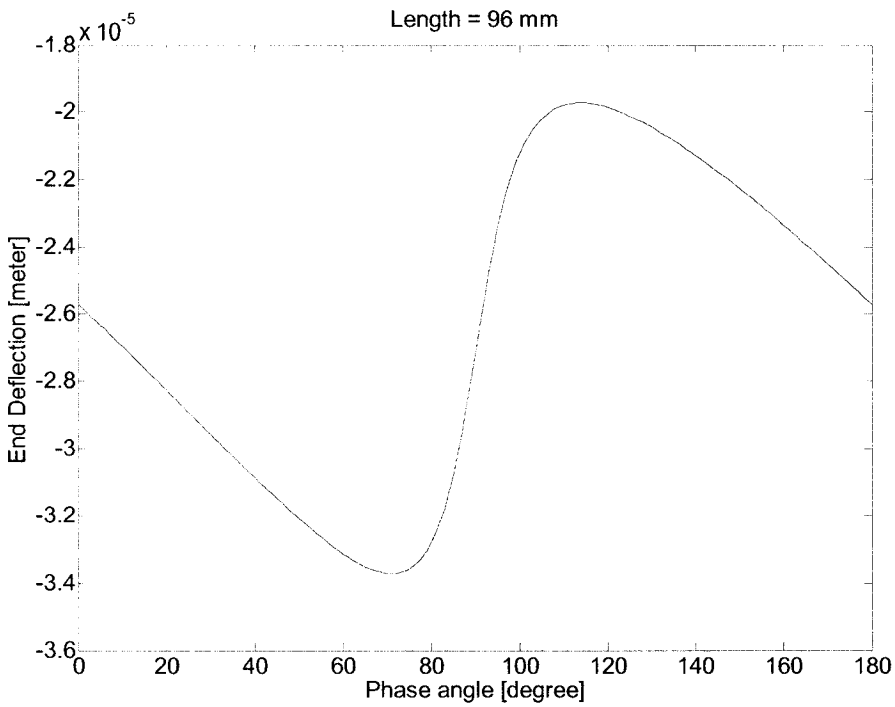

Figure 2.19: End Deflection Variation with Phase Angle (Pitch = 64 mm)

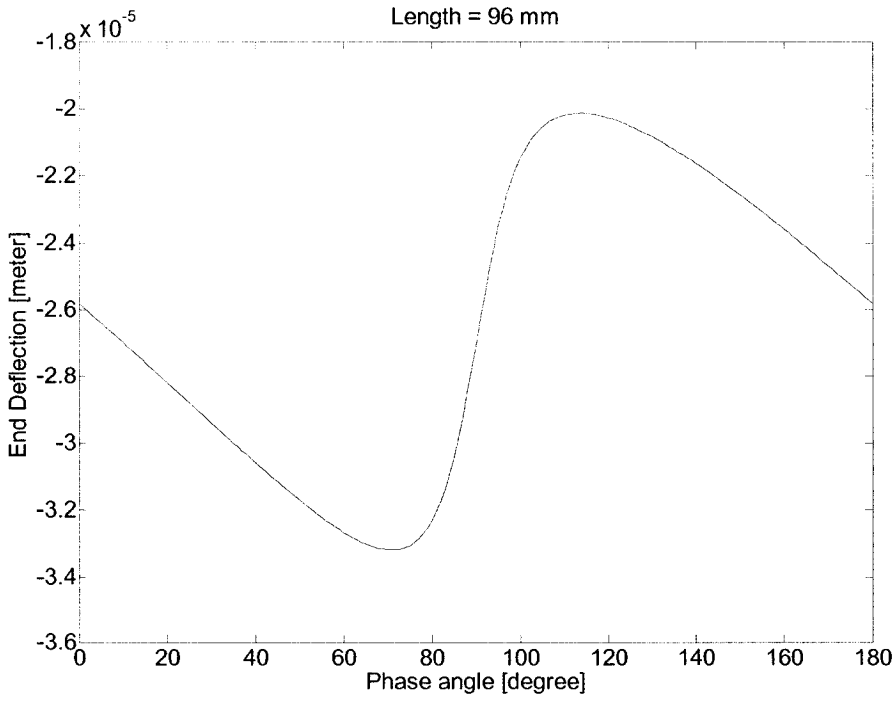

Figure 2.20: End Deflection Variation with Phase Angle (Pitch = 60 mm)

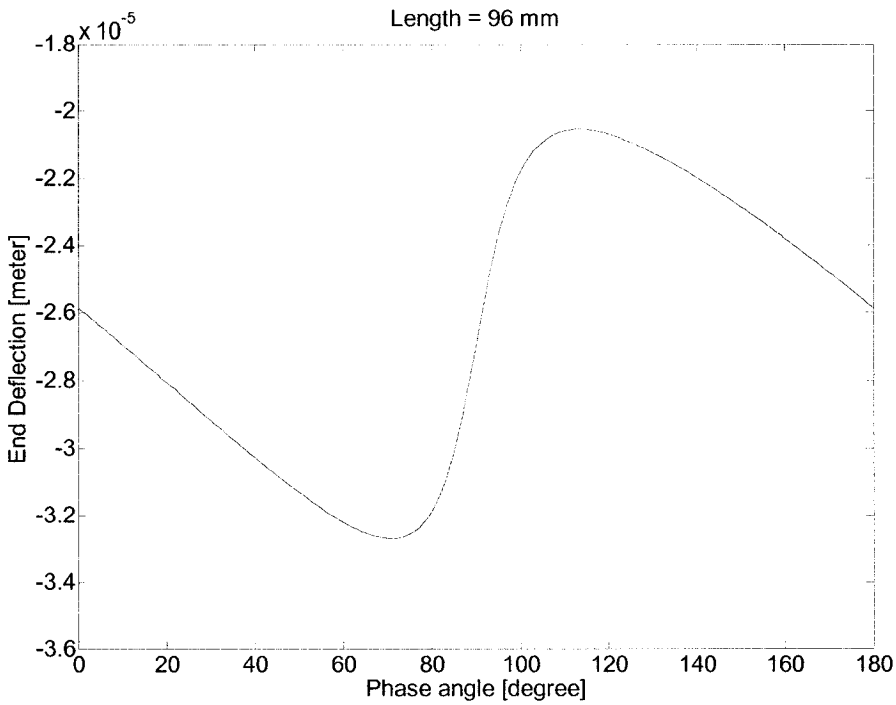

Figure 2.21: End Deflection Variation with Phase Angle (Pitch = 56mm)

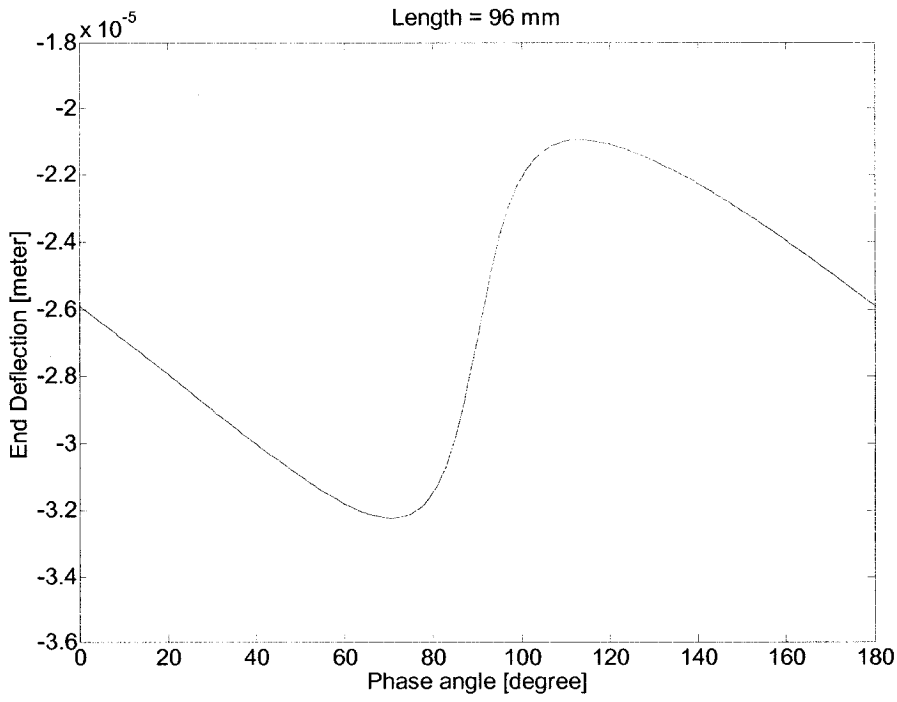

Figure 2.22: End Deflection Variation with Phase Angle (Pitch = 52mm)

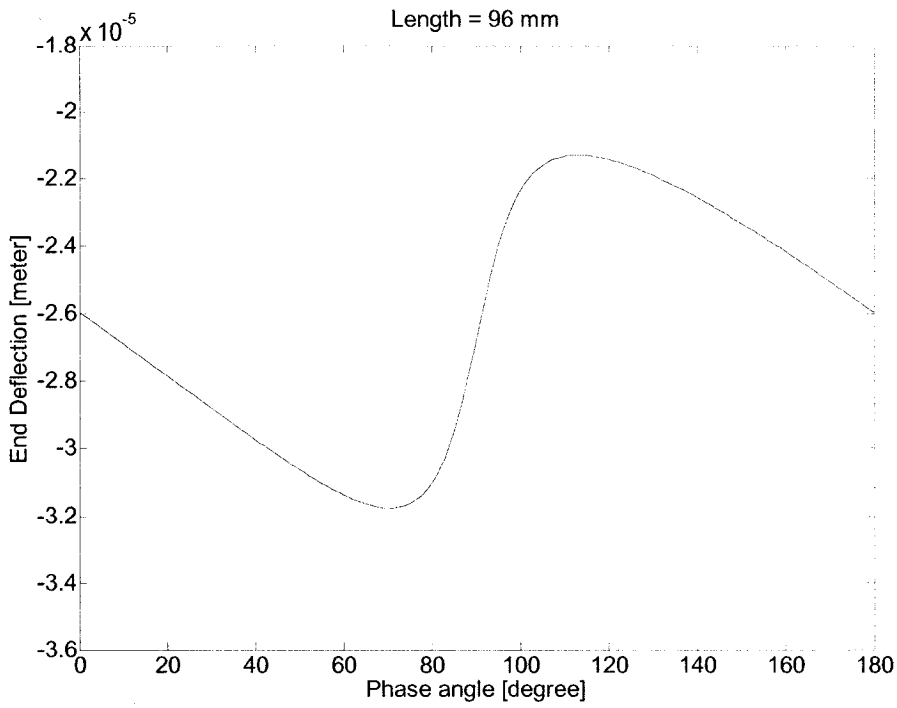

Figure 2.23: End Deflection Variation with Phase Angle (Pitch = 48 mm)

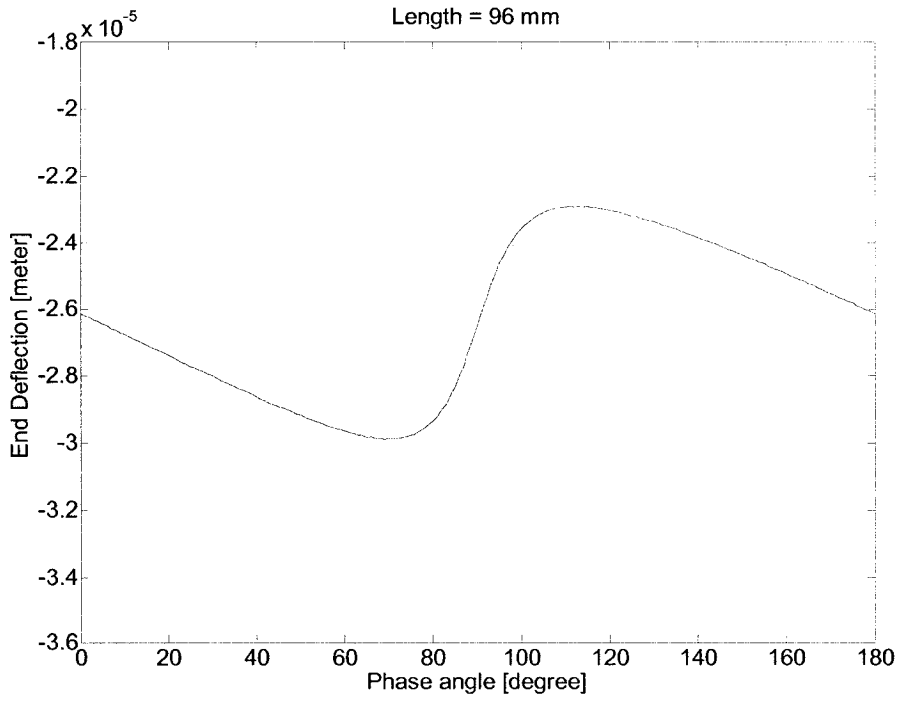

Figure 2.24: End Deflection Variation with Phase Angle (Pitch = 32 mm)

2.6 Significance of Phase Angle for Drilling using Twist Drills

Drill is required to be reground after a certain number of holes being drilled so as to restore the required geometry which ensures efficient cutting and maintain high accuracy. With each regrinding of drill, length is reduced by a small amount and in turn the phase angle also changes.

Axis of bi-symmetry 'ZZ' at the trill tip is parallel to cutting lips and perpendicular to line of action of cutting force whereas the axis of bisymmetry at root is assumed to be placed horizontal and is reference for measuring phase angle (Figure 2.25). Here root is the interface of fluted length and drill shank fixed to spindle and as already mentioned earlier shank is assumed to be rigid fixed end in our analysis. The phase angle is the acute angle between the axis of bi-symmetry at tip and at the root.

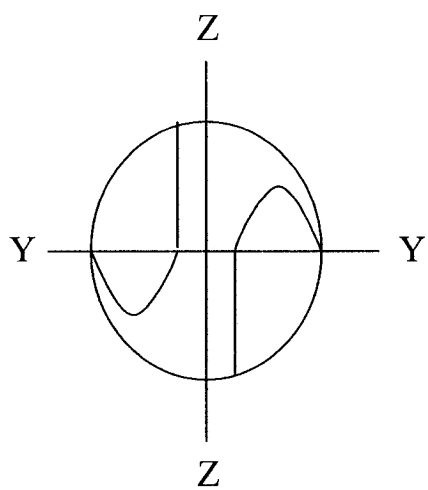

Figure 2.25: Schematic of Cross-section at Drill Tip

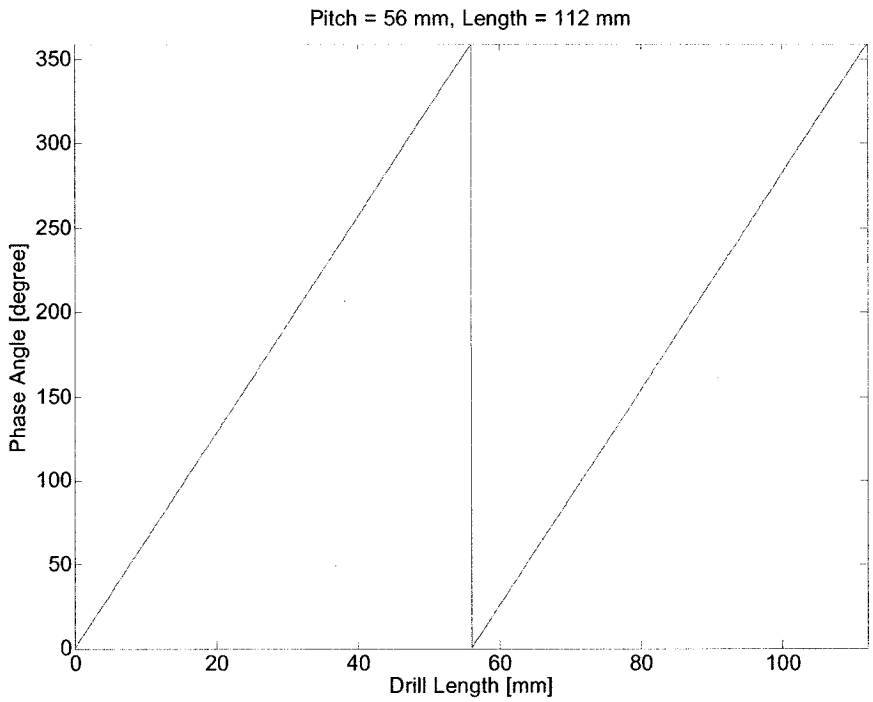

Figure 2.26: Variation of Phase Angle for Different Lengths of Twist Drill

Thus each different drill length has unique phase angle and phase angle for given length of a drill is defined here as characteristic phase angle for that drill length. The end deflections and corresponding characteristic phase angles are calculated for different drill lengths for standard drill geometry assumed in section 2.3 above. The characteristic phase angles of drill are plotted over a length of 300 mm as shown above (Figure 2.26).

In order to study the significance of characteristic phase angle, the end deflections for lengths between 0 – 56 mm (P = 56 mm) corresponding to characteristic phase angles are plotted versus drill lengths (Figure 2.27). Study of this plot revealed very important property of the twist drills by virtue of which the lateral stiffness of twist drill does not necessarily increase with decrease in length. In case of untwisted beams of uniform cross-

section the end deflection must always be smaller for smaller lengths and lateral stiffness increases with decrease in length. Transition zones are observed around a point at a distance of half pitch length and one pitch length from the fixed end wherein the amount of end deflection is found to be increasing with decrease in length. Two Critical Drill Lengths are observed in the zone; higher one is favorable for stable cutting because of higher lateral stiffness as compared to another smaller one which is unfavorable because of lower lateral stiffness.

For precision drilling applications, understanding of this typical stiffness characteristic observed in Twist Drills has tremendous significance because it enables to choose the safest drill length for assuring accuracy.

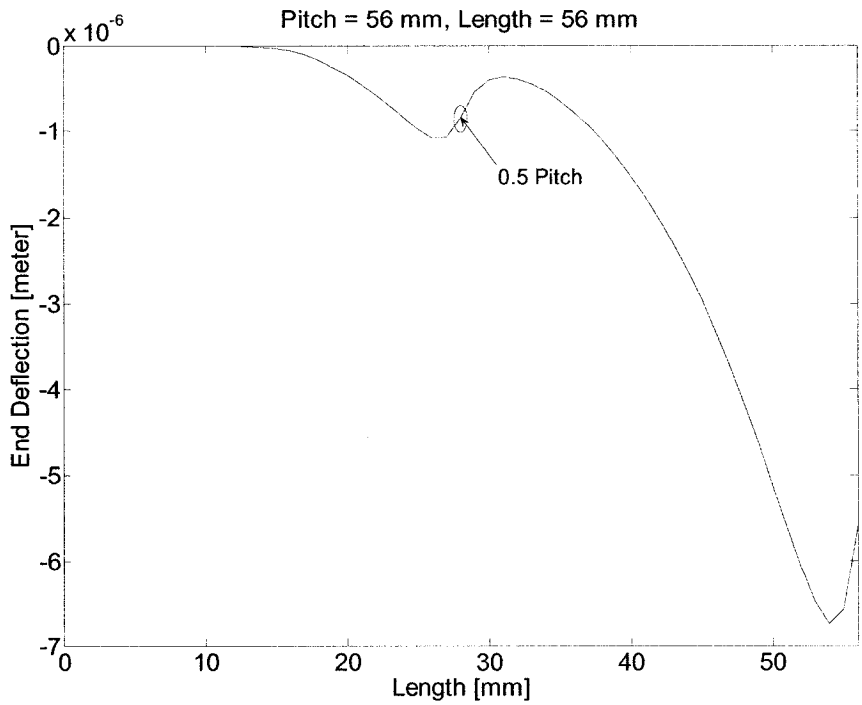

Figure 2.27: Characteristic End Deflection Curve for Twist drill

2.7 Summary

In the present chapter a continuous model to study static bending characteristics of twist drill is presented. Simulation results are presented and with the help of these results different aspects of static bending of twisted beams applied to twist drilling are discussed.

In the next chapter continuous model based on equation of motion for Euler-Bernoulli Beam is presented. Simulation results for sinusoidal force excitation are presented and first natural frequency of twist drill is identified.

CHAPTER 3

CONTINUOUS MODEL -EULER-BERNOULLI BEAM EQUATION APPLIED TO TWIST DRILLS

3.1 Introduction

In the previous chapter, effect of varying moment of inertia as a function of length on static bending characteristic of a fluted beam is studied and its application to twist drill is described. End deflections which represent the stiffness of the drill for different conditions are studied.

In this chapter equation of motion for twist drill as a continuous system is developed where moment of inertia term is the function of the length and the twist angle. Finally the equation is solved numerically for different forcing frequencies and fundamental natural frequency for 13 mm diameter drill is identified. Also deflection curves for first and second mode are presented.

Euler-Bernoulli Beam equation for lateral vibration analysis of beams with uniform cross-sections throughout the length is modified by replacing the constant moment of inertia term with varying values of moments of inertia for twisted beams as a function of length and twist angle. As a result a fourth order partial differential equation with trigonometric coefficients is obtained. In this equation the highest order space term is of

order four and the time term of order two. Unbalanced force term is function of both space and time. This partial differential equation can be solved either using numerical methods or finite element method to get the lateral deflection vectors in space and time domain.

The partial differential equation is converted to ordinary differential equation by assuming force and deflection variations with time to be sinusoidal. The equation is then simulated in Matlab over a range of forcing frequencies.

3.2 Continuous Form of Equation of Motion for Twist Drills

Euler Bernoulli Equation for lateral vibration of beams of uniform cross-section is given below, which is modified by substituting moment of inertia as a function of length 'x' for twisted beams [40].

$$m \cdot \frac{\partial^2 y}{\partial t^2} + E \cdot \frac{\partial^2}{\partial x^2}\left[I_{zzx} \cdot \frac{\partial^2 y}{\partial x^2} \right] = f(x,t)$$

Equation 3.1

From equation 2.14,

$$I_{zzx} = I_{zz} \cdot \cos^2(\beta \cdot x) + I_{yy} \cdot \sin^2(\beta \cdot x)$$

which can be represented as

$$I_{zzx} = \left(I_{yy} - I_{zz} \right) \cdot \cos^2(\beta \cdot x) + I_{yy}$$ **Equation 3.2**

Substituting in equation 3.1, we get,

$$m \cdot \frac{\partial^2 y}{\partial t^2} + E\left\{ \left(I_{zzx} \cdot \frac{\partial^4 y}{\partial x^4} \right) + \left(2 \cdot I'_{zzx} \cdot \frac{\partial^3 y}{\partial x^3} \right) + \left(I''_{zzx} \cdot \frac{\partial^2 y}{\partial x^2} \right) \right\} = f(x,t)$$

Equation 3.3

where,

I'_{ZZX} and I''_{ZZX} are first and second derivatives of moment of inertia function I_{ZZX}, and are written as,

$$I'_{ZZX} = \frac{\partial}{\partial x}\left(I_{ZZX}\right) = \beta \cdot \left(I_{yy} - I_{ZZ}\right) \cdot \sin(2 \cdot \beta \cdot x)$$

$$I''_{ZZX} = \frac{\partial^2}{\partial x^2}\left(I_{ZZX}\right) = 2 \cdot \beta^2 \cdot \left(I_{yy} - I_{ZZ}\right) \cdot \cos(2 \cdot \beta \cdot x) \qquad \textbf{Equation 3.4}$$

Denoting, $\left(I_{yy} - I_{ZZ}\right) = Q$, we can write the equation of motion as,

$$\left(\left(Q \cdot \cos^2(\beta \cdot x) + I_{yy}\right) \cdot \frac{\partial^4 y}{\partial x^4}\right) + \left(2 \cdot \beta \cdot Q \cdot \sin(2 \cdot \beta \cdot x) \cdot \frac{\partial^3 y}{\partial x^3}\right)$$

$$+ \left(2 \cdot \beta^2 \cdot Q \cdot \cos(2 \cdot \beta \cdot x) \cdot \frac{\partial^2 y}{\partial x^2}\right) + \left(\frac{m}{E} \cdot \frac{\partial^2 y}{\partial t^2}\right) - \left(\frac{f(x,t)}{E}\right) = 0$$

Equation 3.5

Above partial differential equation can be converted into an ordinary differential equation in space coordinate by assuming the time variation as below,

$$y(x,t) = Y(x) \cdot \cos(\omega \cdot t),$$

$$f(x,t) = F(x) \cdot \cos(\omega \cdot t) \qquad \textbf{Equation 3.6}$$

Hence,

$$\left(\left(Q\cdot\cos^2(\beta\cdot x)+I_{yy}\right)\cdot\frac{d^4y}{dx^4}\right)+\left(2\cdot\beta\cdot Q\cdot\sin(2\cdot\beta\cdot x)\cdot\frac{d^3y}{dx^3}\right)$$

$$+\left(2\cdot\beta^2\cdot Q\cdot\cos(2\cdot\beta\cdot x)\cdot\frac{d^2y}{dx^2}\right)-\left(\frac{m\cdot\omega^2}{E}\right)\cdot Y(x)-\left(\frac{F(x)}{E}\right)=0$$

Equation 3.7

Rewriting in the form,

$$\frac{d^4y}{dx^4}+\left(\frac{2\cdot\beta\cdot Q\cdot\sin(2\cdot\beta\cdot x)}{Q\cdot\cos^2(\beta\cdot x)+I_{yy}}\right)\cdot\frac{d^3y}{dx^3}+\left(\frac{2\cdot\beta^2\cdot Q\cdot\cos(2\cdot\beta\cdot x)}{Q\cdot\cos^2(\beta\cdot x)+I_{yy}}\right)\cdot\frac{d^2y}{dx^2}$$

$$-\left(\frac{m\cdot\omega^2}{E\cdot Q\cdot\cos^2(\beta\cdot x)+E\cdot I_{yy}}\right)\cdot Y(x)-\left(\frac{F(x)}{E\cdot Q\cdot\cos^2(\beta\cdot x)+E\cdot I_{yy}}\right)=0$$

Equation 3.8

Above equation can be rewritten in following compact form,

$$\frac{d^4y}{dx^4}+[j(x)]\cdot\frac{d^3y}{dx^3}+[g(x)]\cdot\frac{d^2y}{dx^2}$$

$$-\left(\frac{m\cdot\omega^2}{E}\right)\cdot[h(x)]\cdot Y(x)-\left(\frac{F(x)}{E}\right)\cdot[h(x)]=0$$

Equation 3.9

where,

$$j(x) = \left(\frac{2 \cdot \beta \cdot Q \cdot \sin(2 \cdot \beta \cdot x)}{Q \cdot \cos^2(\beta \cdot x) + I_{yy}} \right)$$

$$g(x) = \left(\frac{2 \cdot \beta^2 \cdot Q \cdot \cos(2 \cdot \beta \cdot x)}{Q \cdot \cos^2(\beta \cdot x) + I_{yy}} \right)$$

$$h(x) = \left(\frac{1}{Q \cdot \cos^2(\beta \cdot x) + I_{yy}} \right)$$

Equation 3.10

3.3 Simulation Results

3.3.1 Identification of Natural Frequencies :

Above differential can be solved using numerical solver in Matlab for Boundary Value Problems using four Boundary Conditions (BCs) for cantilever beam as follows.

A] At fixed end **x = 0**

$$y = 0, \qquad \frac{dy}{dx} = 0$$

B] At free end **x = L**

$$\frac{d^2y}{dx^2} = 0, \qquad \frac{d^3y}{dx^3} = F$$

Matlab program written to solve this equation is simulated in loop over a range of forcing frequencies and displacement amplitude vector obtained is plotted against corresponding forcing frequencies. First and second peaks of displacement amplitudes are located at forcing frequencies of 333 Hz and 1950 Hz. They correspond to first and second natural frequencies. Higher natural frequencies are extremely high which are usually not encountered in operation of the drill. Plot of Displacement Amplitude v/s forcing frequency obtained is presented below (Figure 3.1). This result is later used in Chapter 4 when lumped mass model is studied.

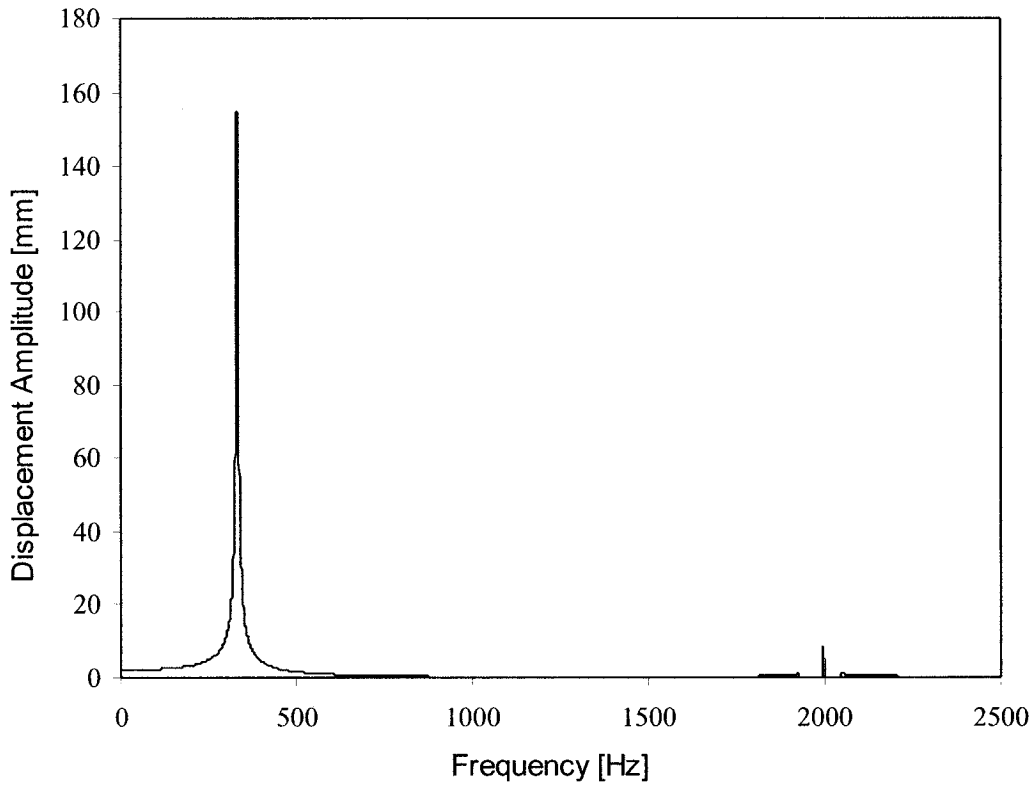

Figure 3.1: Displacement Amplitude v/s Forcing Frequency

(First Natural Frequency = 333.0 Hz, Second Natural Frequency = 1950.0 Hz)

3.3.2 Identification of Mode Shapes

The mode shapes of drill obtained by solving the continuous equation of motion (Equation 3.9) are presented below (Figures 3.2, 3.3). It must be noted that only the fluted part of the drill is considered in this case.

The first mode shape is found to be similar to static compliance of drill (Figures 2.6 to 2.10) obtained in second chapter by solving continuous form of static bending equation.

Analytical results for first and second mode shapes obtained by B. W. Huang [7] and experimental results for first and second mode shape obtained by M. Kohring [21] are found to be similar to our analytical results. Those results are presented below (Figures 3.4, 3.5) for comparison purpose. It is seen that the first mode shows significant bending in the fluted part of the drill.

Similar results for first and second mode are obtained by B. Dawson and W. Carnegie [5] which contains the mode shapes corresponding to first three natural frequencies. Another study by E. B. Magrab and D. E. Gilsinn [27] shows the mode shapes corresponding to first four natural frequencies.

All results presented here are the mode shapes corresponding to an unconstrained drill tip. These mode shapes reveal the presence of significant amount of vibrations in the rotating fluted body of the drill which are presumed to be responsible for drill breakage.

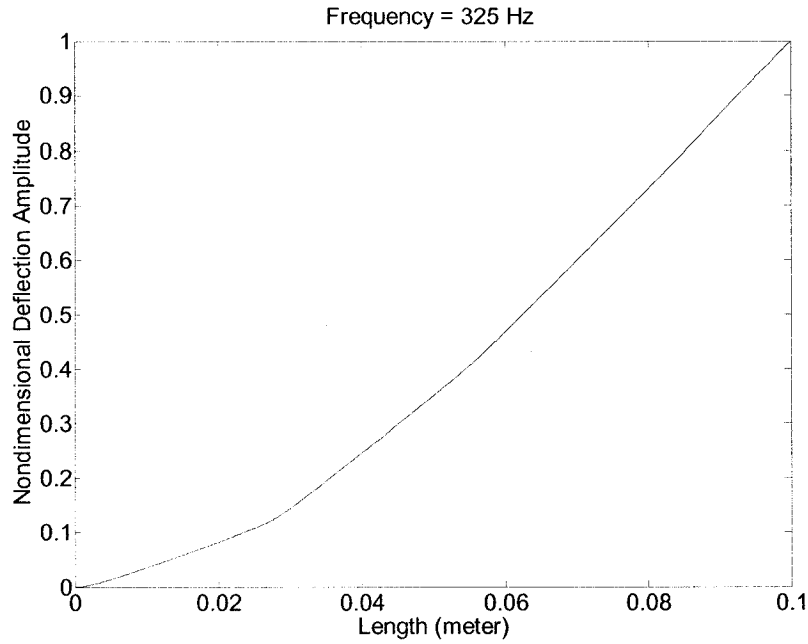

Figure 3.2: First Mode Shape for fluted drill (D = 13.0 mm, L = 100.0 mm)

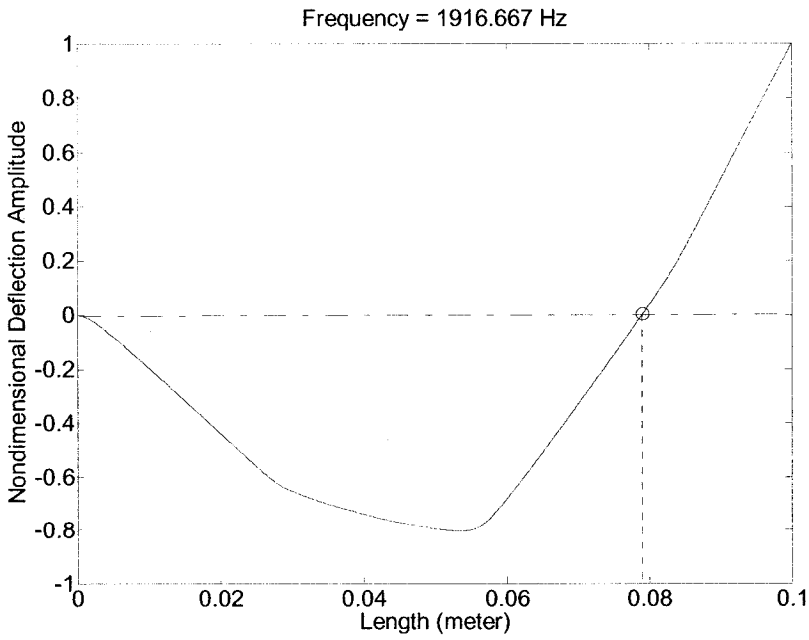

Figure 3.3: Second Mode Shape for fluted drill (D = 13.0 mm, L = 100.0 mm)

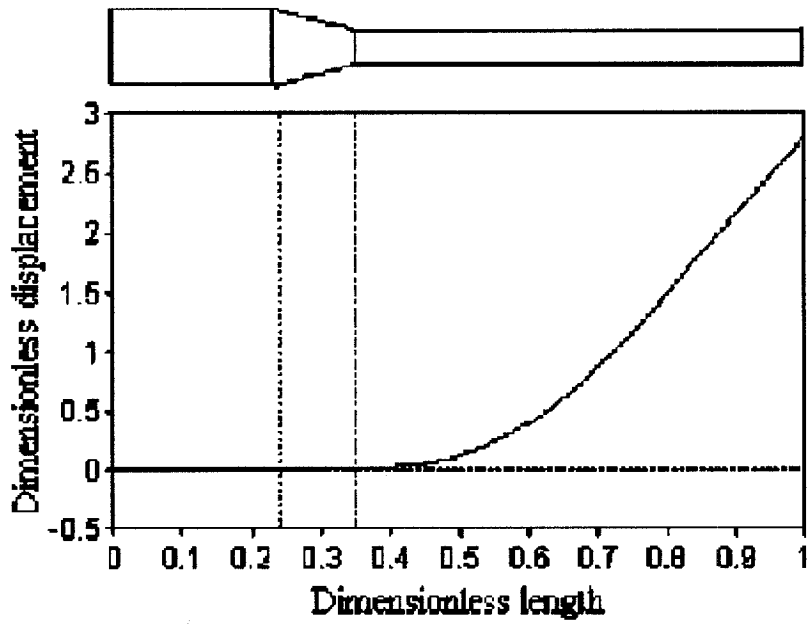

(a) the *i*th mode

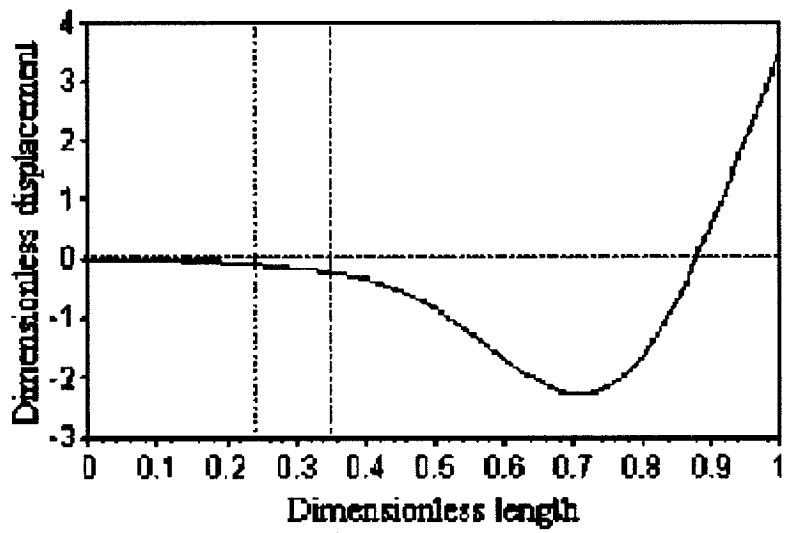

(b) the 2th mode

Figure 3.4: Analytical Mode Shapes for fluted micro-drill [6]

(Ds = 1.0 mm, Ls = 3.0 mm, D = 0.3 mm, L = 5.5 mm)

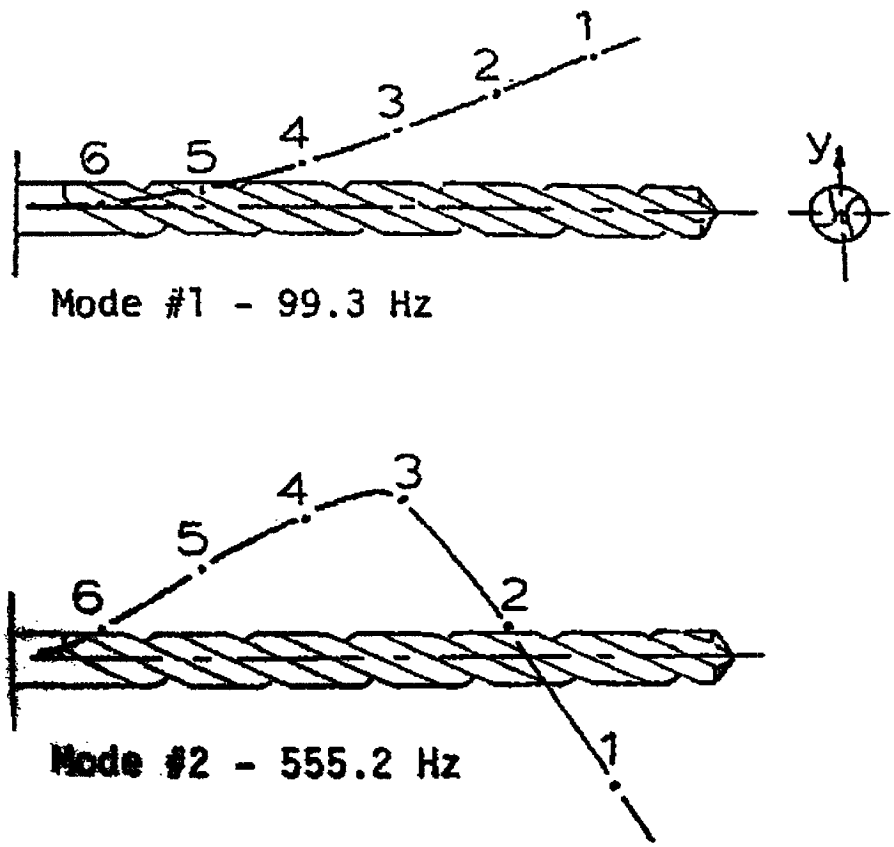

Figure 3.5: Experimental Mode Shapes for fluted drill [20]

(D = 19.05 mm, L = 305 mm)

3.4 Summary

In the present chapter continuous model based on equation of motion for Euler-Bernoulli Beam is presented and solved numerically in Matlab to identify fundamental and second natural frequencies of the twist drill. First and second mode shape diagrams obtained are compared with similar results in past research.

In the next chapter discrete model to study orbital dynamics of twist drill is presented. Simulation results are presented and with the help of these results parameters responsible for different types of drilled hole inaccuracies are identified.

CHAPTER 4

LUMPED MASS MODEL – ORBITAL DYNAMICS OF TWIST DRILLS

4.1 Introduction

In the previous chapter continuous form of equation of motion of twist drill is presented and solved numerically. First two natural frequencies are identified and corresponding mode shapes are obtained and compared with similar results in past literature.

In the present chapter lumped mass model of twist drill including the effect of drill work-piece interaction is presented. Results of simulation are analyzed to explain the influence of different parameters towards the drilling inaccuracies.

Several modeling efforts proposed in past describe discrete models for analyzing the lateral vibration behavior of twist drill. Some of them have stressed on drill chatter which occurs close to the natural frequencies. A few others have noted that the inaccuracies like lobed holes and position error are rather common at very low rotational speeds which however are far lower than the drill natural frequencies.

Drilling process generally can be segregated in different stages, most important being drill skidding and wandering. Drill skidding, is a random lateral movement of drill tip

which occurs at the start of drilling operation when drill interacts with work surface. Second one, drill wandering, is a vibratory motion of drill tip which when overlapped on the circular motion of drill axis produces out-of-round holes and sometimes center of these holes also deviate from axis of rotation.

Better understanding of dynamic behavior of twist drill during actual cutting action has demanded formulation of a two dimensional model which considers the complex phenomenon of drill-hole wall interaction. Model proposed in this chapter is similar to models proposed by Basel in [13]. The simulation parameters such as drill stiffness and fundamental natural frequency are calculated analytically for actual drill geometry i.e. twisted beam (Chapters 2 and 3). Another important difference is that selection of non-dimensional parameter 'α' i.e. ratio of work-stiffness to drill stiffness. The work stiffness is calculated from a new formulation developed as described later in this chapter.

Drill dynamics causing lobed and non-straight holes ultimately is influenced by many factors viz. unbalanced radial force, axial thrust force, rotating speed, eccentricity etc. Effort is made to explain the significance of different parameters and role of individual parameter on the occurrence of different kind of inaccuracies commonly evident in produced holes. Thus proposed model is an effort to elaborate the drill wandering phenomenon and factors influencing it, on the basis of realistically validated simulation parameters.

Only fluted body of the drill excluding the cylindrical shank portion is considered while calculating the lateral stiffness of drill. Spindle head supporting the drill is assumed to be rigid which is true in case of modern machine tools such as machining centers. Presence of oil grooves or coolant holes are neglected. Effect of rubbing action of land with drill and contribution of thrust force in lateral vibration are also not considered. The effects of centrifugal and gyroscopic actions are not considered in the model.

All the analytical calculations and simulation results presented are for two fluted twist drill of diameter D = 13 mm, length L = 96 mm and pitch P = 56 mm. Drill is assumed to be made by twisting a rectangular cross-section strip of size 13.0 mm x 2.0 mm.

4.2 Description of Mathematical Model

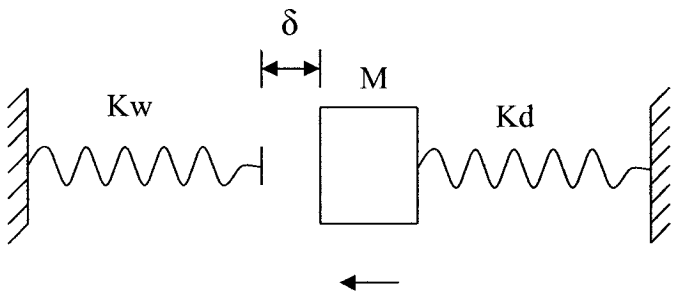

Figure 4.1: Schematic of Drill-Hole Wall Interface

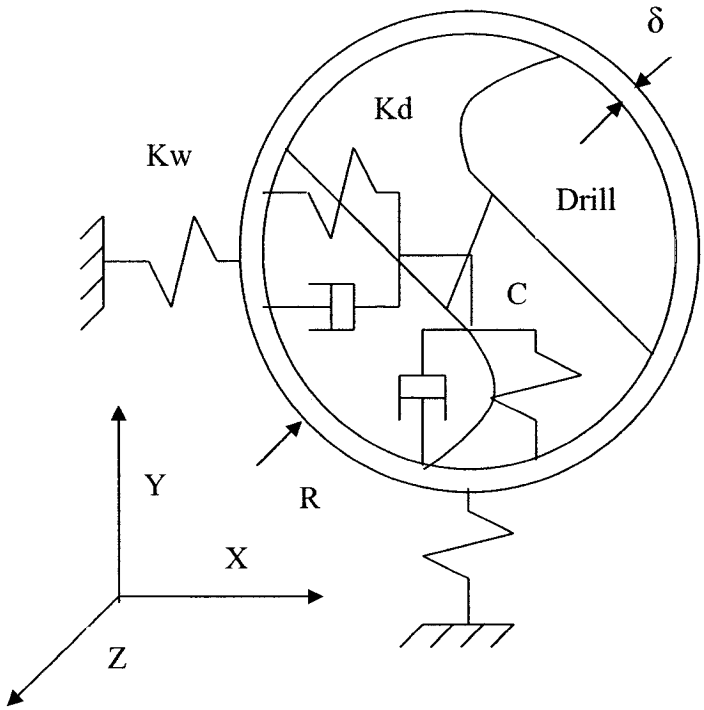

Figure 4.2: Schematic of Lumped Mass Model and Axes System

The two dimensional model described here represents the lateral vibration of a drill inside an oversize hole. Drilled holes are normally oversize by few micrometers by virtue of

which a thin film of coolant is maintained in between the precisely ground land of drill and hole-wall. Thus at any instant the drill tip is ideally assumed to be free to move by a distance equal to clearance gap (δ) under the action of unbalance force. When the drill tip displacement is more than the clearance gap, its motion experiences an additional resistance because of the stiffness of the work surface. Thus the overall system stiffness can be modeled as bilinear spring. This configuration is schematically represented in diagram (Figure 4.1).

For no contact between drill and the hole, the system stiffness is equal to the drill stiffness only. When the drill makes contact with hole both work surface and drill gets displaced by same amount. Consequently, drill and work stiffness act as system of parallel springs and the system stiffness is equal to sum of the stiffnesses of drill and work-piece.

Spindle support system is highly stiff compared to that of the drill. Drill acts as a massless cantilever beam and equivalent mass of the drill is assumed to be lumped at the tip. Lumped mass is assumed to be symmetrically supported by springs and rotating inside an oversize hole. The figure 4.2 is a schematic representation of the model, along with the axis system and forces acting on the system. Direction 'R' is always perpendicular to cutting lips and rotates with the drill. The unbalance forces are assumed to be acting in direction 'R'. The unbalanced forces arise as a result of unequal length of cutting lips, non-uniformities in material properties of work-piece, side forces generated due to alignment errors and other random forces generated in cutting process.

4.3 New Formulation for Work Stiffness (K_W)

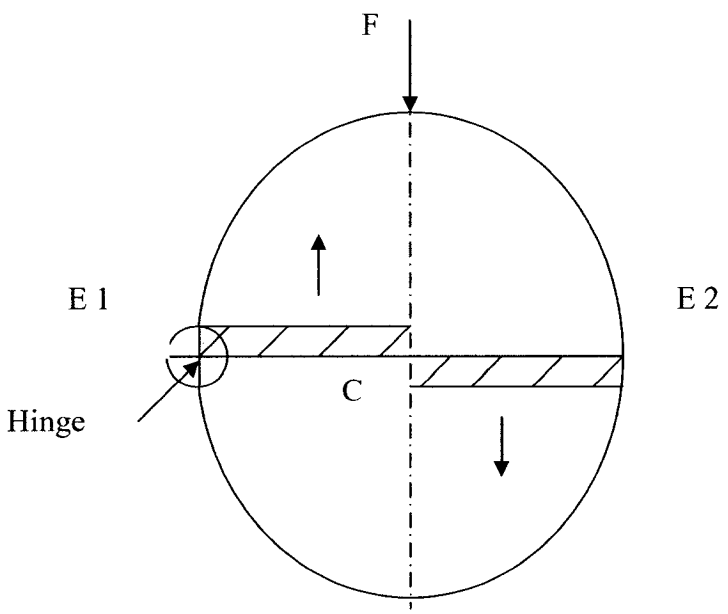

Figure 4.3: Cutting Lips Orientation- Top View

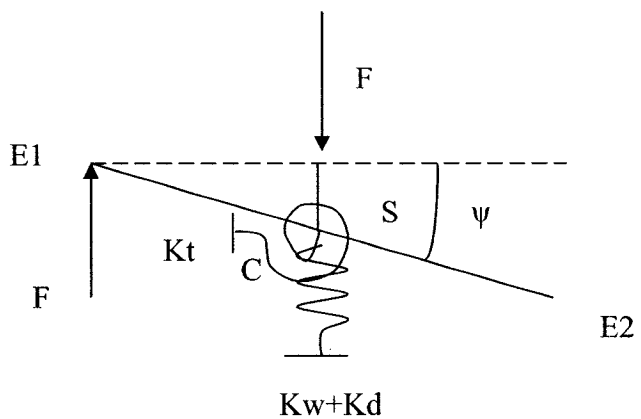

Figure 4.4: Cutting Lips in Displaced Position

Drill tip is a cone shaped end of the fluted body of the drill. Two straight cutting lips are formed as two flutes cut through the conical surface of the drill tip. To avoid rubbing of the tip surface against work surface those lips are relieved by providing end relief angle on the trailing surfaces. Two sharp cutting edges of the lips cut in opposite directions, with cutting edge E1-C cutting when lateral movement of drill tip is in upward direction and cutting edge E2-C cutting when the lateral movement is in downward direction as shown by arrows in diagram above (Figure 4.4).

Under the action of the unbalance force 'F' acting in downward direction the drill is displaced laterally by distance equal to 'S'. As the back face of the cutting lip E1-C is having a line contact with the matching conical surface work-piece at the bottom of the hole it can not cut through the material. But other cutting lip E2-C has its cutting edge facing the direction of lateral displacement and it cuts through the material. Consequently the line E1-C-E2 can be assumed to rotate by angle equal to 'ψ' and the point E1 rests against the work-piece and acts as the hinge point.

Thus the overall displacement under the action of unbalance force can be visualized as combination of linear displacement 'S' and angular twist 'ψ' of the drill tip as top end of the drill body is fixed to driving spindle. Angle 'ψ' is called Displacement Induced Twist. Hence drill is assumed to be a system combined of lateral and torsional springs. Bending and torsional stiffness of this system are represented schematically by the linear and torsional springs, respectively, as shown in diagram above (Figure 4.5).

The lateral stiffness of the system when drill tip is in contact with hole surface is sum of drill lateral stiffness and work stiffness as explained in section 4.2 above.

For this configuration we can write the equations for linear displacement and angular twist in terms of lateral and torsional stiffness of the system as given below.

$$K_t = \frac{T}{\psi} = \frac{F \cdot r}{\psi} = \frac{F \cdot r^2}{r \cdot \psi} = \frac{F \cdot r^2}{S} \qquad \textbf{Equation 4.1}$$

Also,

$$(K_w + K_d) \cdot S = F \qquad \textbf{Equation 4.2}$$

From above equations we get following two formulae for 'S'.

$$S = \frac{F \cdot r^2}{K_t} \qquad \textbf{Equation 4.3}$$

and,

$$S = \frac{F}{K_w + K_d} \qquad \textbf{Equation 4.4}$$

Equating both equations,

$$K_w + K_d = \frac{K_t}{r^2} \qquad \textbf{Equation 4.5}$$

Rearranging the equation, we get

$$K_w = \frac{K_t}{r^2} - K_d \qquad \textbf{Equation 4.6}$$

This is the new formulation for Work Stiffness in terms of radius of drill 'r', lateral stiffness of drill 'K_d' and torsional stiffness of drill 'K_t'.

4.4 Formulation of Equation of Motion

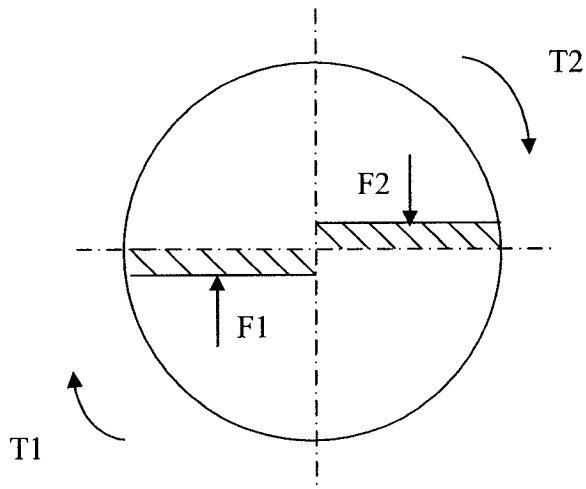

Figure 4.5.1: Cutting forces and torques on a twist drill

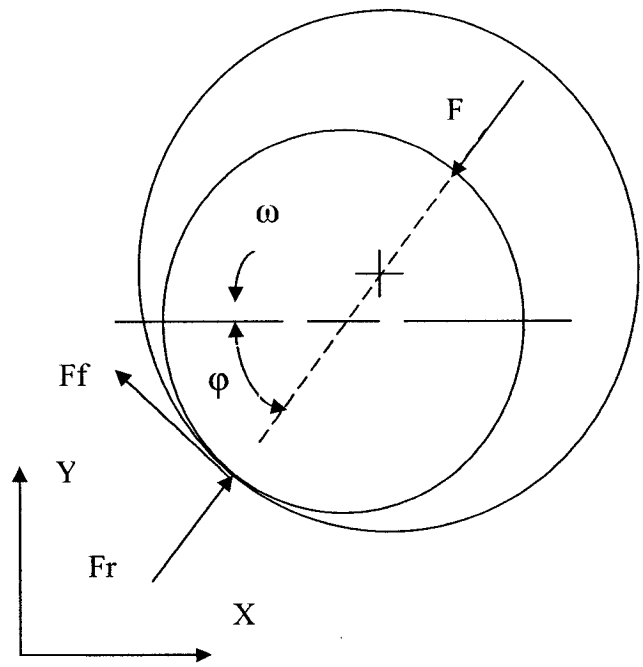

Figure 4.5.2: Free body diagram for drill's displaced position

Discrete form of equation of motion can be derived by following the same procedure followed in research paper by Dr S. A. Basile [13] and reference as follows.

The force diagram when drill is displaced by distance 'r' more than radial clearance 'δ' such that it makes contact with hole-wall is shown in diagram above (Figure 4.5). Drill is rotating in counter-clockwise direction with angular velocity 'ω'. When drill body is pressed against the hole-wall normal reaction 'F_r' will appear at the point of contact.

$$F_r = 0 \qquad \text{for} \qquad r < \delta$$

$$F_r = (r - \delta) \cdot K_w \qquad \text{for} \qquad r \geq \delta \qquad \textbf{Equation 4.7}$$

Because of the rubbing action at the point of contact, friction force 'F_f' is generated, the value of which depends on the coefficient of friction 'μ'.

$$F_f = \mu \cdot F_r$$

Substituting equation 4.7, we get

$$F_f = 0 \qquad \text{for} \qquad r < \delta$$

$$F_f = \mu \cdot (r - \delta) \cdot K_w \qquad \text{for} \qquad r \geq \delta \qquad \textbf{Equation 4.8}$$

Normal reaction force 'F_r' and frictional force 'F_f' appears only when radial displacement exceeds the radial clearance (i.e. when $r \geq \delta$).

This can be represented mathematically introducing Heaviside Unit-Step Function 'H(r – δ)' as follows,

$$H(r-\delta)=0 \quad \text{for} \quad (r-\delta)\leq 0$$
$$H(r-\delta)=1 \quad \text{for} \quad (r-\delta)\rangle 0 \qquad \textbf{Equation 4.9}$$

Equations 4.8 and 4.9 can be rewritten as follows,

$$F_r = [(r-\delta)\ K_w\ ]\ H(r-\delta) \qquad \textbf{Equation 4.10}$$

$$F_f = [\mu\ (r-\delta)\ K_w\ ]\ H(r-\delta) \qquad \textbf{Equation 4.11}$$

$$H(r-\delta) = H \qquad \textbf{Equation 4.12}$$

Ultimate purpose being the orbital motion analysis, the equation of motion can be written in both directions along co-ordinate axes 'X' and 'Y'. The components of forces ' F_x ' and ' F_y ' along axes 'X' and 'Y', respectively, are found out as given below. The acute angle between the horizontal direction and instantaneous position of axis of bisymmetry of twist drill is denoted by symbol 'φ' and called Instantaneous Position Angle.

$$F_x = F_r \cdot \cos\varphi - F_f \cdot \sin\varphi \qquad \textbf{Equation 4.13}$$

$$F_y = F_f \cdot \cos\varphi + F_r \cdot \sin\varphi \qquad \textbf{Equation 4.14}$$

If we refer figure 4.5, we get

$$\sin\ \varphi = \frac{Y}{r} \quad \text{and} \quad \cos\ \varphi = \frac{X}{r} \qquad \textbf{Equation 4.15}$$

Rewriting above equations, we get

$$F_x = \left(\frac{r-\delta}{r}\right) K_w (X - \mu.Y) H(r-\delta) \qquad \textbf{Equation 4.16}$$

$$F_y = \left(\frac{r-\delta}{r}\right) K_w (Y + \mu.X) H(r-\delta) \qquad \textbf{Equation 4.17}$$

Unbalance force component ' F ' acts in radial direction, perpendicular to the axis of bi-symmetry which is parallel to the cutting lips. It is combination of different forces arising during cutting process because of geometrical features of drill tip and other process parameters as discussed above in section 4.2. This force can be split in to components along co-ordinate axes.

According to S. A. Basile [13] these radial forces provide a good indication of drills orbital motion because of the radial displacement. Also there exists a factor called force amplitude modulation, which leads to formation of noncircular holes. S. A. Basile deduced by experimental measurements that the radial and thrust forces follow the same pattern as that of the oscillatory motion of drill and number of lobes of holes so produced is governed by the ratio of the number of oscillations exhibited by radial force to the drill rotational speed. And according to other researchers, Y. Gong et al. [12] drilled hole is usually polygon-shaped hole with an odd number of sides.

The components of unbalanced force before non-dimensionalization of equation of motion along co-ordinate directions F_{ix} and F_{iy} are selected such that they represent the above said effect of force amplitude modulation [13].

Following are the relations for the unbalanced force given by S. A. Basile [13] which are also used in the equation of motion formulated in next part of this section and equation of motion is simulated and corresponding results are shown in following section 4.5.

$$F_{bx*} = \frac{F_{imbx}}{k\delta} [1 - \lambda \sin(3\rho\tau)] [\cos(\rho\tau + \varphi)] \qquad \textbf{Equation 4.18}$$

$$F_{by*} = \frac{F_{imby}}{k\delta} [1 - \lambda \sin(3\rho\tau)] [\sin(\rho\tau + \varphi)] \qquad \textbf{Equation 4.19}$$

where,

λ = Amplitude Modulation Factor

$$F_{bx*} = \frac{F_{ix}}{k\delta}$$

$$F_{by*} = \frac{F_{iy}}{k\delta} \qquad \textbf{Equation 4.20}$$

Rest of the non-dimensional parameters 'k', 'ρ', 'τ' are explained in next stages. For simplification the rest of the random forces are neglected while formulating the equation of motion.

If 'M' is mass of a drill, 'K_d' and 'C_d' the stiffness and damping coefficient of the system, 'F_x' and 'F_{ix}' be the forces as described above then the simplified equations of motion in directions 'X' and 'Y' can be written as follows

$$M\ddot{X} + C_d\dot{X} + K_dX = F_x + F_{ix} \qquad \textbf{Equation 4.21}$$

$$M\ddot{Y} + C_d\dot{Y} + K_d Y = F_y + F_{iy} \qquad \textbf{Equation 4.22}$$

where,

$$\dot{X} = \frac{dX}{dt}, \qquad \ddot{X} = \frac{d^2X}{dt^2} \qquad \textbf{Equation 4.23}$$

$$\dot{Y} = \frac{dY}{dt}, \qquad \ddot{Y} = \frac{d^2y}{dt^2} \qquad \textbf{Equation 4.24}$$

Above equation of motion can be converted to the non-dimensional form. We can define non-dimensional parameters as given below.

Non-dimensional displacements 'x' and 'y',

$$\frac{X}{\delta} = x, \qquad \frac{Y}{\delta} = y \qquad \textbf{Equation 4.25}$$

frequency ratio 'ρ' and stiffness ratio 'α',

$$\rho = \frac{\omega}{\omega_n}, \qquad \alpha = \frac{K_w}{K_d} \qquad \textbf{Equation 4.26}$$

damping ratio 'ξ' and non-dimensional or equivalent stiffness 'k',

$$\xi = \frac{C_d}{2M\omega_n}, \quad k = \frac{4K_dK_w}{\left(\sqrt{K_d} + \sqrt{K_w}\right)^2} \qquad \textbf{Equation 4.27}$$

non-dimensional time 'τ'

$$\tau = \omega_n \cdot t \qquad \textbf{Equation 4.28}$$

Substituting equations 4.16, 4.18 and 4.20 in equation 4.21, we get

$$M\frac{d^2X}{dt^2}+C_d\frac{dX}{dt}+K_dX=-\left(\frac{r-\delta}{r}\right)K_w(X-\mu_xY)H\ (r-\delta)+F_{ix}$$

$$M\frac{d^2X}{dt^2}+C_d\frac{dX}{dt}+K_dX+HK_wX\left(1-\frac{\delta}{\sqrt{X^2+Y^2}}\right)-H\mu_xK_wY\left(1-\frac{\delta}{\sqrt{X^2+Y^2}}\right)=F_{ix}$$

Equation 4.29

We can write equation for natural frequency as

$$\frac{d\tau}{dt}=\omega_n$$ **Equation 4.30**

From equations 4.28 and 4.30, we get

$$\frac{dX}{dt}=\frac{dX}{d\tau}\omega_n$$ **Equation 4.31**

$$\frac{d^2X}{dt^2}=\frac{d^2X}{d\tau^2}\omega_n^2$$ **Equation 4.32**

Substituting equations 4.31 and 4.32 in equation 4.29, we get

$$M\omega_n^2\frac{d^2X}{d\tau^2}+C_d\omega_n\frac{dX}{d\tau}+K_dX+HK_wX\left(1-\frac{\delta}{\sqrt{X^2+Y^2}}\right)-H\mu_xK_wY\left(1-\frac{\delta}{\sqrt{X^2+Y^2}}\right)=F_{ix}$$

Equation 4.33

Rearranging above equation, we get

$$\frac{d^2X}{d\tau^2}+\frac{C_d\omega_n}{M\omega_n^2}\frac{dX}{d\tau}+\frac{K_dX}{M\omega_n^2}+\frac{HK_wX}{M\omega_n^2}\left(1-\frac{\delta}{\sqrt{X^2+Y^2}}\right)-\frac{H\mu_xK_wY}{M\omega_n^2}\left(1-\frac{\delta}{\sqrt{X^2+Y^2}}\right)=\frac{F_{ix}}{M\omega_n^2}$$

Equation 4.34

$$\frac{d^2\left(\frac{X}{\delta}\right)}{d\tau^2}+\frac{C_d\omega_n}{M\omega_n^2}\frac{d\left(\frac{X}{\delta}\right)}{d\tau}+\frac{K_d\left(\frac{X}{\delta}\right)}{M\omega_n^2}+\frac{HK_w\left(\frac{X}{\delta}\right)}{M\omega_n^2}\left(1-\frac{\delta}{\sqrt{X^2+Y^2}}\right)-\frac{H\mu_xK_w\left(\frac{Y}{\delta}\right)}{M\omega_n^2}\left(1-\frac{\delta}{\sqrt{X^2+Y^2}}\right)=\frac{F_{ix}}{M\omega_n^2\delta}$$

Equation 4.35

Substituting non-dimensional parameters from equations 4.25 to 4.27, new form of equation is obtained as follows.

$$\frac{d^2(x)}{d\tau^2}+2\xi\frac{d(x)}{d\tau}+\frac{K_d}{k}x+H\frac{K_w}{k}x\left(1-\frac{1}{\sqrt{x^2+y^2}}\right)-H\mu_x\frac{K_w}{k}y\left(1-\frac{1}{\sqrt{x^2+y^2}}\right)=\frac{F_{ix}}{k\delta}$$

Equation 4.36

From equations 4.26 and 4.27, we can write

$$\frac{K_d}{k}=\frac{\left(1+\sqrt{\alpha}\right)^2}{4\alpha},$$

Equation 4.37

$$\frac{K_w}{k}=\frac{\left(1+\sqrt{\alpha}\right)^2}{4}$$

Equation 4.38

If we assume the following notations,

$$\dot{x} = \frac{dx}{d\tau}, \qquad \ddot{x} = \frac{d^2x}{d\tau^2}$$

Equation 4.39

then, the equation of motion in its full non-dimensional form is written as follows.

$$\ddot{x} + 2\xi\dot{x} + \frac{\left(1+\sqrt{\alpha}\right)^2}{4\alpha}x + H\frac{\left(1+\sqrt{\alpha}\right)^2}{4}x\left(1-\frac{1}{\sqrt{x^2+y^2}}\right) - H\mu_x\frac{\left(1+\sqrt{\alpha}\right)^2}{4}y\left(1-\frac{1}{\sqrt{x^2+y^2}}\right) = \frac{F_{ix}}{k\delta}$$

Equation 4.40

Similarly for another direction 'Y', equation of motion in complete non-dimensional form can also be written as follows.

$$\ddot{y} + 2\xi\dot{y} + \frac{\left(1+\sqrt{\alpha}\right)^2}{4\alpha}y + H\frac{\left(1+\sqrt{\alpha}\right)^2}{4}y\left(1-\frac{1}{\sqrt{x^2+y^2}}\right) + H\mu_y\frac{\left(1+\sqrt{\alpha}\right)^2}{4}y\left(1-\frac{1}{\sqrt{x^2+y^2}}\right) = \frac{F_{iy}}{k\delta}$$

Equations 4.41

4.5 Calculation of Basic Simulation Parameters

Proper selections of simulation parameters can only guarantee the reliable results and subsequently leads to proper understanding of the process. Following is the list of all the basic simulation parameters.

1] Drill torsional stiffness (K_t)

2] Drill lateral stiffness (K_d)

3] Work stiffness (K_w)

4] Drill natural frequency (ω_n)

5] Forcing frequency (ω)

6] Radial clearance (δ)

7] Coefficient of friction (μ)

8] Amplitude Modulation Factor (λ)

9] Damping ratio (ξ)

All non-dimensional parameters appeared in the equations of motion derived above (Equations 4.40, 4.41) are in turn calculated from the basic parameters listed above.

4.5.1 Drill Torsional Stiffness (K_t)

Torsional stiffness value is selected from the experimental results explained in chapter 5 for experimental investigation of torsional stiffness of twist drills.

Figure 5.9 in chapter 5 shows the test result for 13.00 mm diameter drill for torsion test for the test torque in the direction of cutting torque.

Torsional stiffness of the drill

$$K_t = \text{Slope of the test curve}$$

$$= 5.6992 \ \frac{\text{Nm}}{\text{degree}}$$

$$K_t = 5.6992 \times \frac{180}{\pi}$$

$$K_t = 326.529 \frac{\text{Nm}}{\text{rad}}$$

Equations 4.42

4.5.2 Drill Lateral Stiffness (K_d)

Torsional stiffness is selected from the analytical results explained in chapter 2 for the analytical investigation of bending characteristics of twist drills.

Figure 2.4 in chapter 2 shows the test result for 13.00 mm diameter drill for bending of twist drill acting as a cantilever beam under the action of point load F = 1.0 N.

Lateral stiffness of drill

$$K_d = \frac{\text{Force}}{\text{End deflection}}$$

$$= \frac{1.0}{0.026921}$$

$$K_d = 37.1457 \ \frac{N}{mm} \qquad \textbf{Equations 4.43}$$

4.5.3 Work Stiffness (K_w)

Work stiffness value IS calculated from the new formulation proposed for estimation of work stiffness as discussed in section 4.3 of this chapter. The work stiffness is obtained from equation 4.7, as

$$K_w = \frac{K_t}{r^2} - K_d$$

Thus work stiffness for 13.00 mm diameter drill can be calculated substituting values of 'K_t' and 'K_d' from the equations 4.26 and 4.27 above.

$$K_w = \frac{326.529}{\left(6.5\times10^{-3}\right)^2} - \left(37.1457\times10^{3}\right)$$

$$= 7691.3513\times10^{3}\,\frac{N}{m} \qquad \textbf{Equations 4.44}$$

4.5.4 Drill Natural Frequency (ω_n)

Natural frequency is selected from the analytical results explained in chapter 3, where dynamic bending characteristics of twist drills are investigated.

Figure 3.1 in chapter 3 shows analytical result for 13.00 mm diameter drill for the force acting at the unconstrained drill tip obtained by solving continuous model in Matlab over a range of forcing frequencies.

Fundamental frequency of drill corresponding to the first peak in frequency plot is

$$\omega_n = 333.0 \quad \text{Hz}$$

$$= 333.0 \times (2\Pi) \quad \frac{\text{rad}}{\text{sec}}$$

$$\omega_n = 2092.3007 \quad \frac{\text{rad}}{\text{sec}} \qquad \textbf{Equations 4.45}$$

4.5.5 Other Parameters

Forcing frequency (ω) is proportional to the rotational speed of the drill and is equal to the angular velocity,

$$\omega = \frac{2\pi N}{60} \qquad \frac{\text{rad}}{\text{sec}}$$

where N is the rotational speed in revolutions per minute (rpm)

Simulations are done over a range of rotating speeds between 100 – 25000 rpm.

Radial clearance (δ) is usually very small and is selected to be equal to 40 micro-meters.

Coefficient of friction (μ) is chosen as 0.25.

Amplitude Modulation Factor (λ) is varird over a range between 0.2 – 2.5.

Damping ratio (ξ) is chosen as 0.07.

Stiffness ratio, $$\alpha = \frac{K_w}{K_d} = \frac{7691.3513 \times 10^3}{37.1457 \times 10^3} = 207.059$$ **Equations 4.46**

Equivalent stiffness, $$k = \frac{4K_d K_w}{\left(\sqrt{K_d} + \sqrt{K_w}\right)^2} = 129.9006 \quad \frac{N}{mm}$$ **Equations 4.47**

4.5.6 Final Simulation Parameters

Finally parameters selected for actual simulation are documented in tabular form and corresponding parameters selected by S. A. Basile are also listed for comparison purpose.

Simulation Parameters	**Value selected**	**Value: S. A. Basile (12)**
ξ	0.07	0.07
F_{imbx}, F_{imby}	0.2 – 3.0 N	-
$\frac{F_{imbx}}{k\delta}$, $\frac{F_{imby}}{k\delta}$	0.035 – 0.8956	0.2
α	200.0	4.6
k	129.9	329.0
δ	0.04 mm	1.0 mm
λ	0.2 – 5.0	1.3
μ	0.25	0.25
ω_n	2000.0 $(\frac{rad}{sec})$	507.1 $(\frac{rad}{sec})$
N	100 – 25000 (rpm)	-
ω	10.5 - 2620.0 $(\frac{rad}{sec})$	41.9 $(\frac{rad}{sec})$
PHI	0.0 (rad)	-0.13 (rad)

Table 4.1: Simulation Parameters

4.6 Simulation Results

Simulation results shown below are of two different categories.

First type of plot is a trajectory of the drill centerline obtained by plotting displacement vectors 'x' and 'y' on two dimensional domain (2-D). Same data is plotted on three dimensional domain (3-D) also with the third vector as time vector. This 3-D plot gives a clear picture of effect of these lateral oscillations as drill proceeds deeper inside the work-piece with time. Second type of plot is a locus of the outermost point on the cutting edge. The displacement vectors mentioned above are overlapped on the drills rotary motion to get the locus of outermost point of cutting edge. Drill is assumed to rotate at constant speed. Data is plotted on both 2-D and 3-D domain in a similar way as for the first type.

Series of 2-D and 3-D plots are obtained for different sets of parameters. Following are the simulation results obtained for three different sets of parameters.

For first case the unbalance forcing components 'F_{imbx}' and 'F_{imby}' are changed over a range of 0.2 N to 5.0 N.

For the second case the force amplitude modulation factor 'λ' is changed over a range of 1 to 5.

For the third case drill speed is changed over a range of 100 rpm to 20000 rpm.

4.6.1 Effect of Change in Unbalanced Force Components

Results of simulations for different magnitudes of unbalance force are presented below (figures 4.6 – 4.29). Smaller values for other variable parameters which are forcing frequency ' ω ' as function of rotating speed 'N' and amplitude modulation factor 'λ' are selected to keep the influence of these factors smaller so that the influence of imbalance force components F_{ix} and F_{iy} on hole inaccuracies is emphasized.

F_{ix}	=	F_{iy}	
	=	0.2 to 3.0	N
N	=	100	rpm
λ	=	1	

Rest of the simulation parameters listed in table as ξ , α, k, δ, μ, ω_n are held constant.

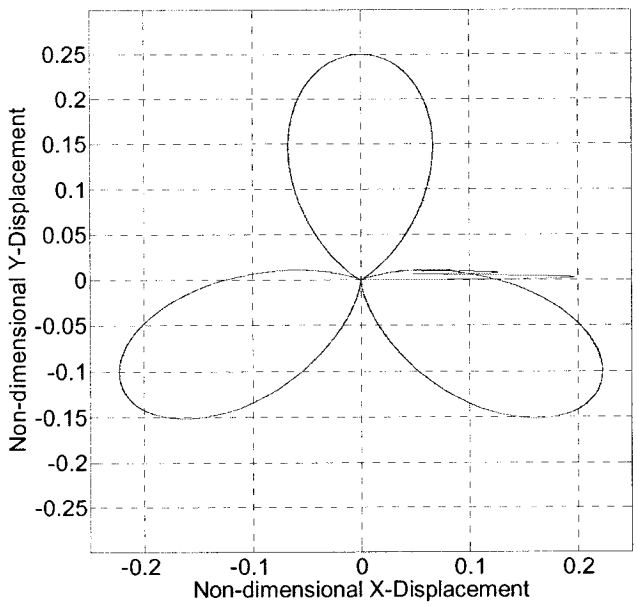

Figure 4.6: Trajectory of Drill Centerline (F_i = 0.2 N)

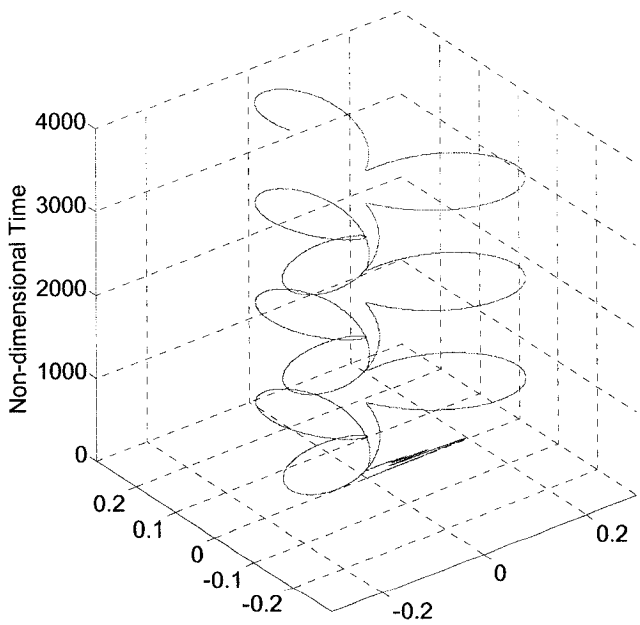

Figure 4.7: Trajectory of Drill Centerline on Time Scale (F_i = 0.2 N)

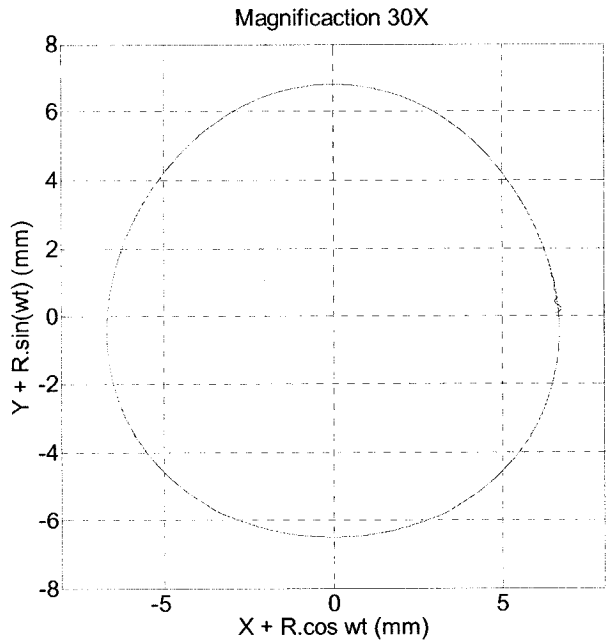

Figure 4.8: Locus of Outermost Point of Cutting Lip (F_i = 0.2 N)

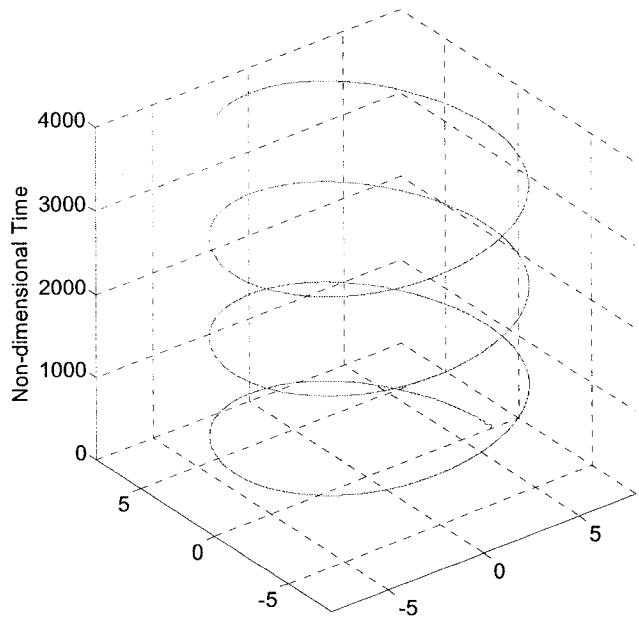

Figure 4.9: Locus of Outermost Point of Cutting Lip on Time Scale (F_i = 0.2 N)

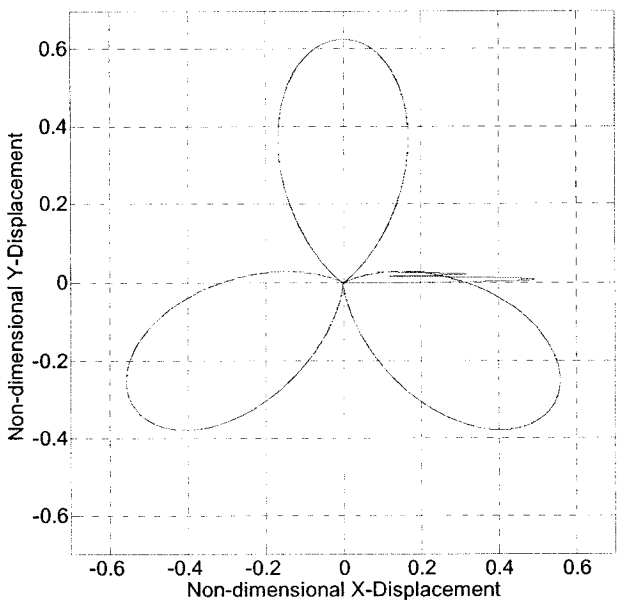

Figure 4.10: Trajectory of Drill Centerline (F_i = 0.5 N)

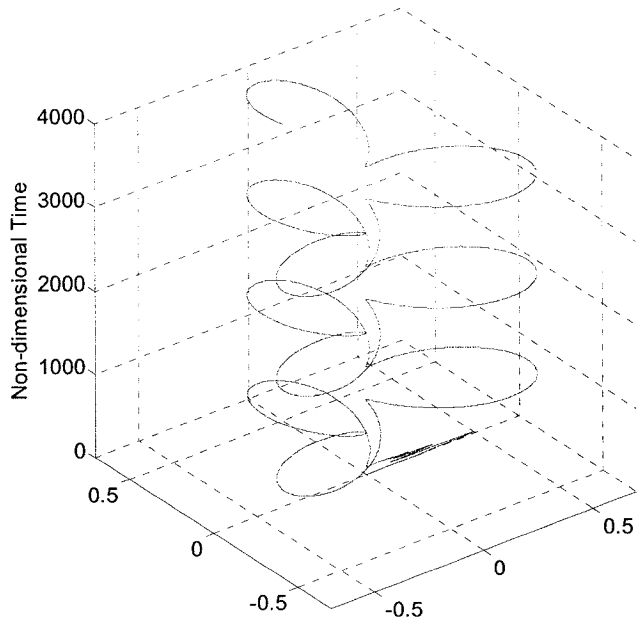

Figure 4.11: Trajectory of Drill Centerline on Time Scale (F_i = 0.5 N)

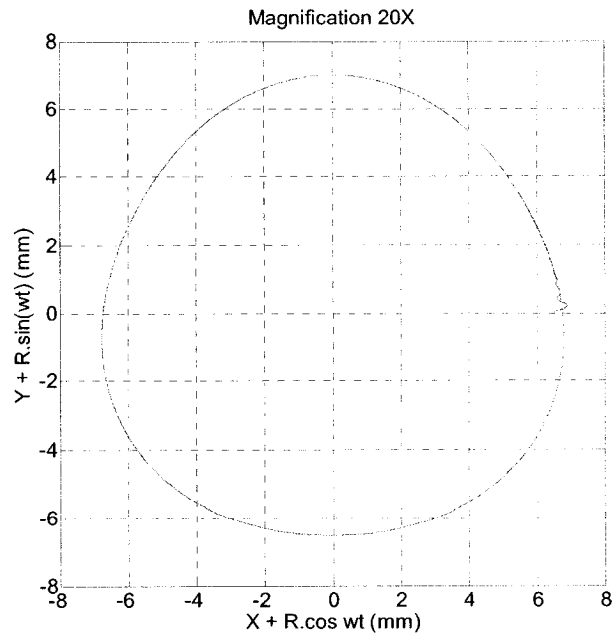

Figure 4.12: Locus of Outermost Point of Cutting Lip (F_i = 0.5 N)

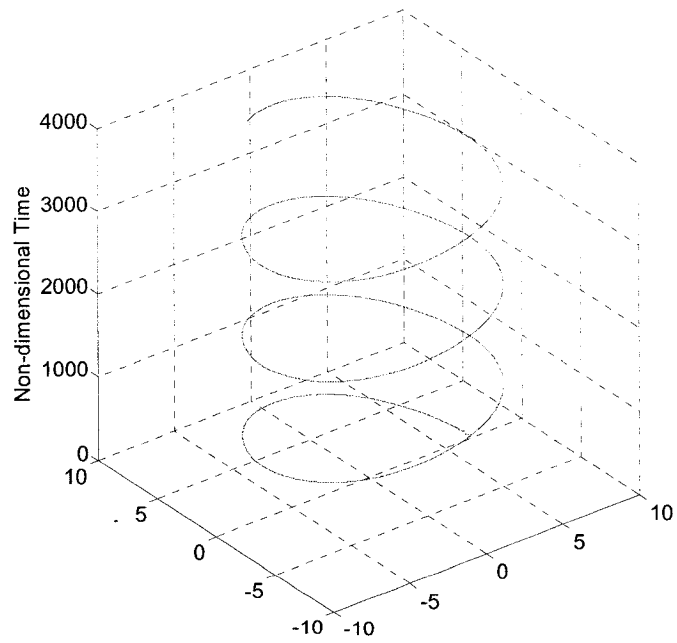

Figure 4.13: Locus of Outermost Point of Cutting Lip on Time Scale (F_i = 0.5 N)

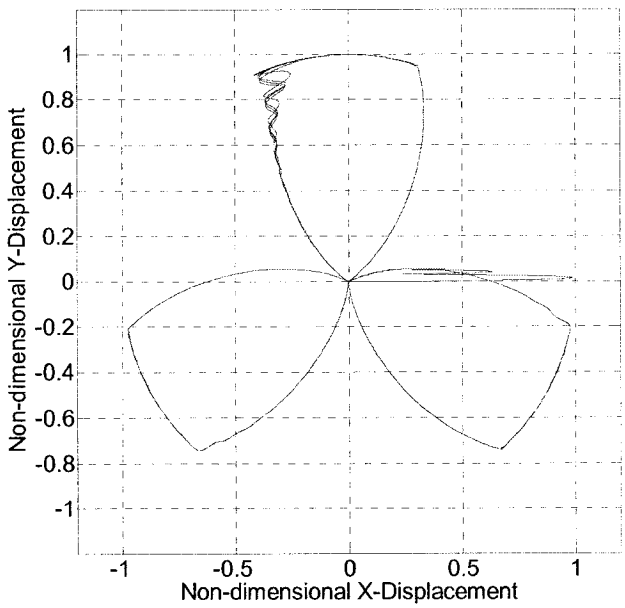

Figure 4.14: Trajectory of Drill Centerline (F_i = 1.0 N)

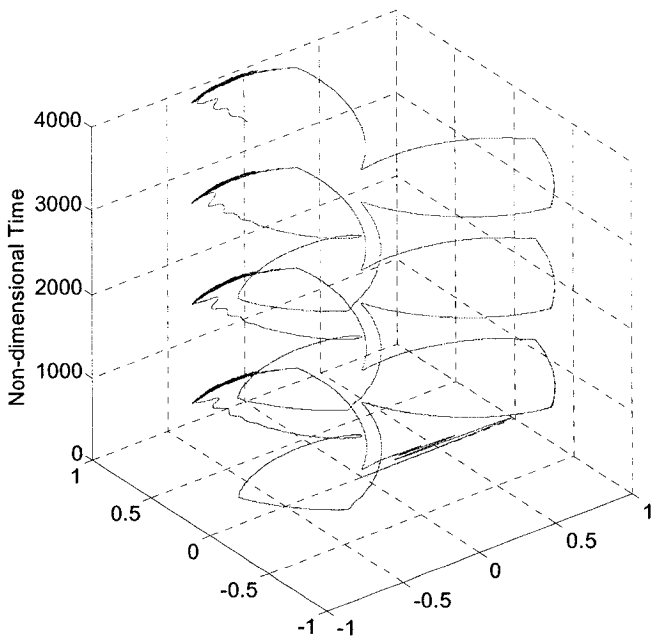

Figure 4.15: Trajectory of Drill Centerline on Time Scale (F_i = 1.0 N)

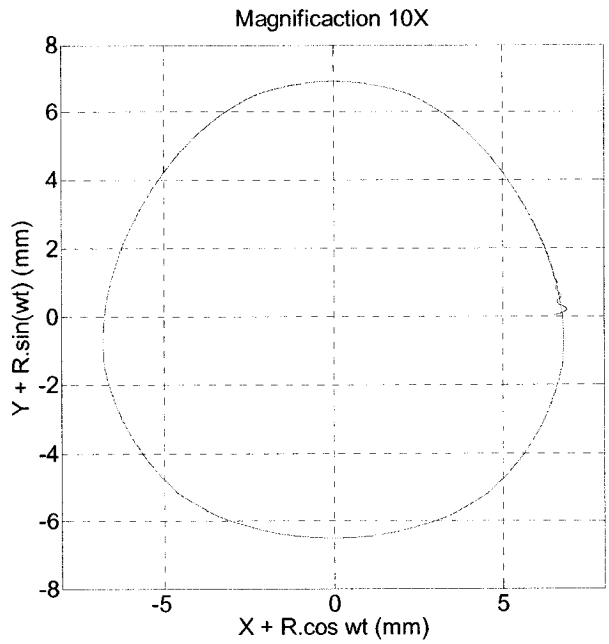

Figure 4.16: Locus of Outermost Point of Cutting Lip (F_i = 1.0 N)

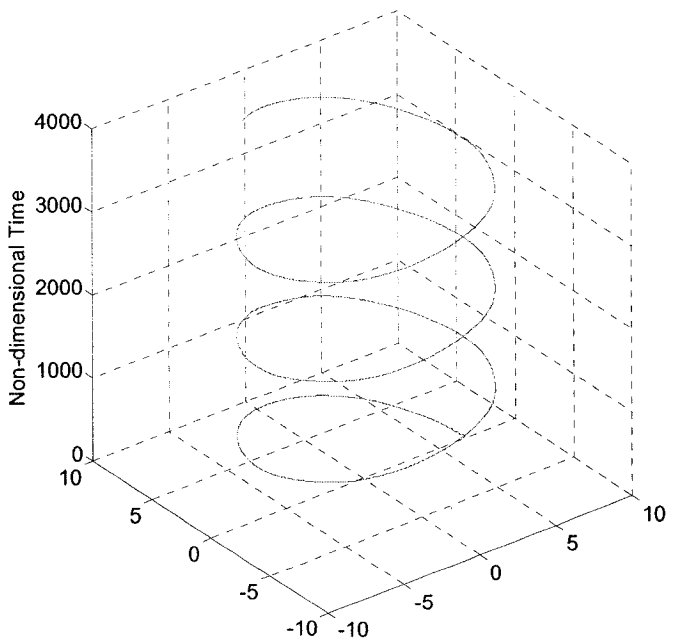

Figure 4.17: Locus of Outermost Point of Cutting Lip on Time Scale (F_i = 1.0 N)

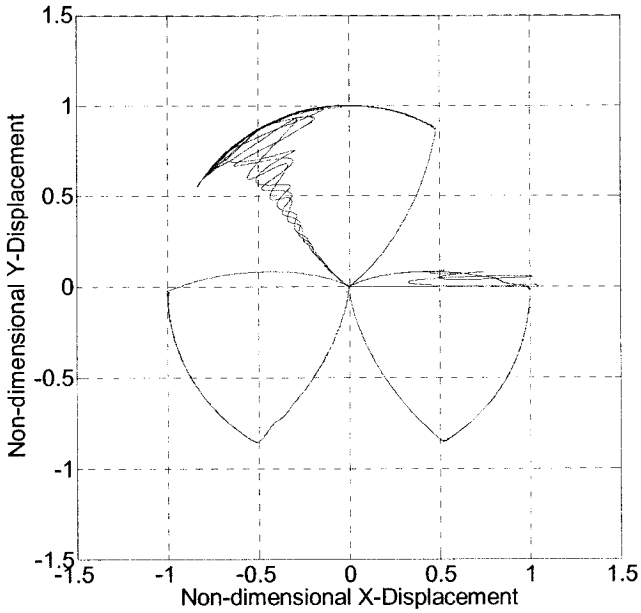

Figure 4.18: Trajectory of Drill Centerline (F_i = 1.5 N)

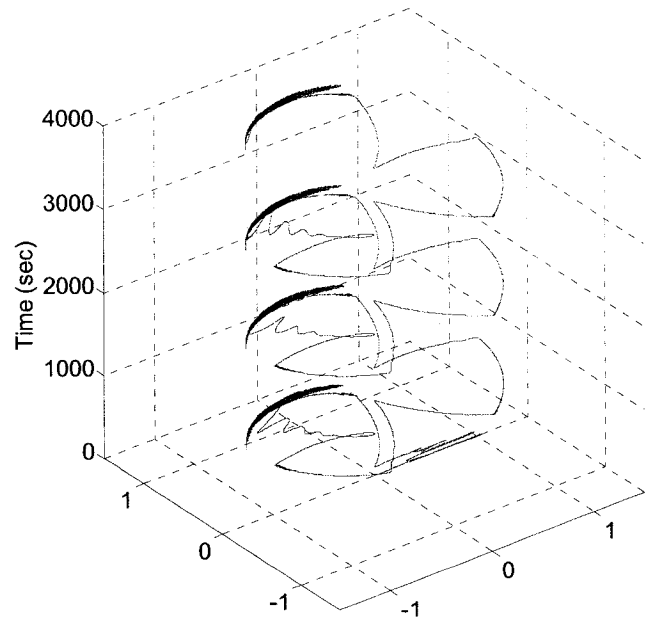

Figure 4.19: Trajectory of Drill Centerline on Time Scale (F_i = 1.5 N)

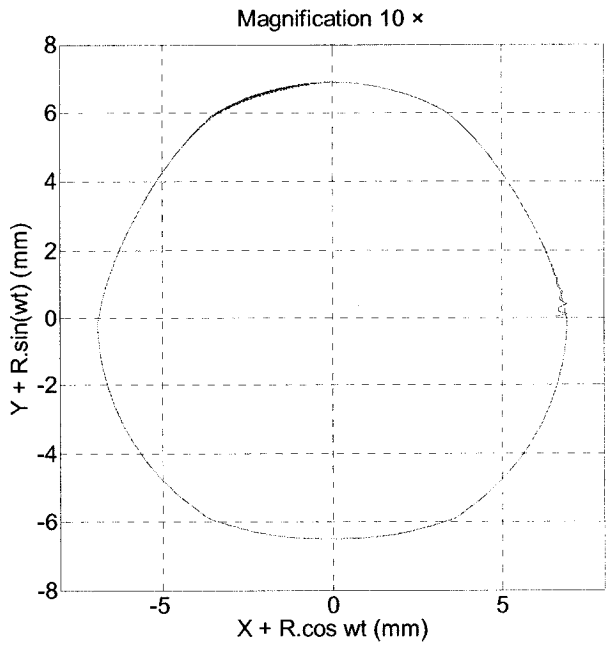

Figure 4.20: Locus of Outermost Point of Cutting Lip (F_i = 1.5 N)

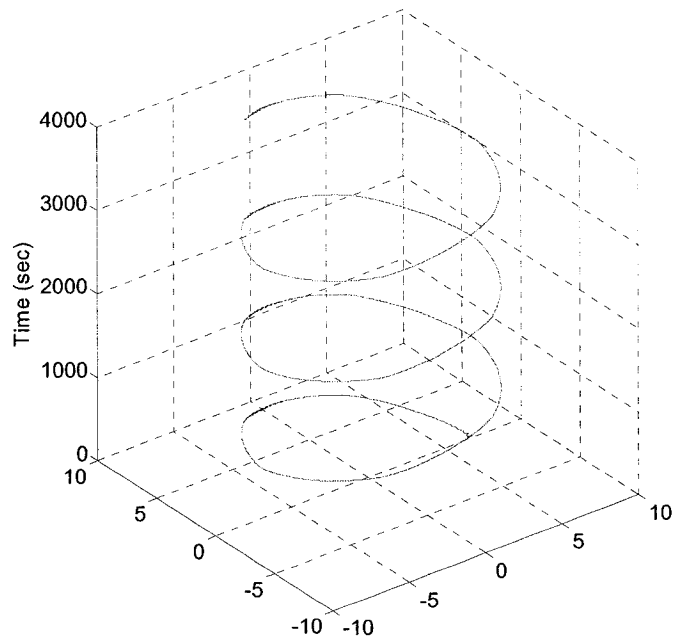

Figure 4.21: Locus of Outermost Point of Cutting Lip on Time Scale (F_i =1.5 N)

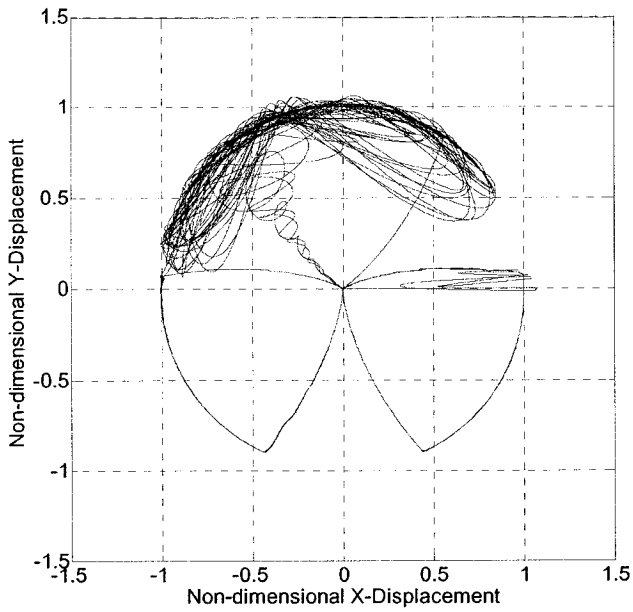

Figure 4.22: Trajectory of Drill Centerline (F_i = 2.0 N)

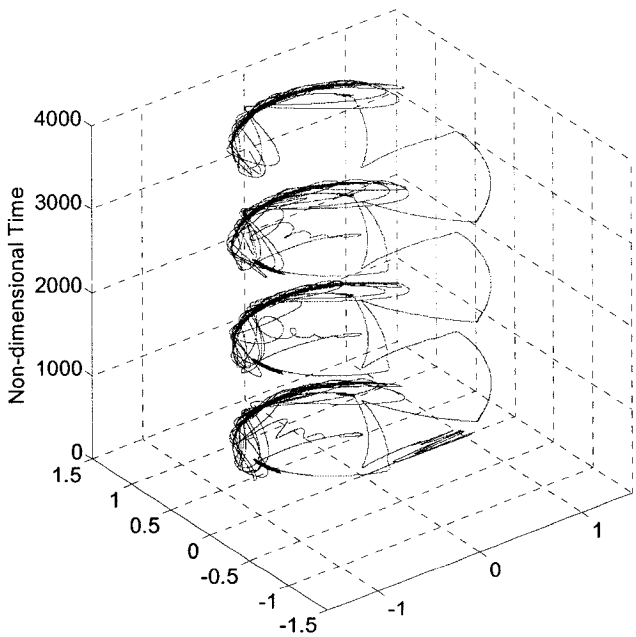

Figure 4.23: Trajectory of Drill Centerline on Time Scale (F_i = 2.0 N)

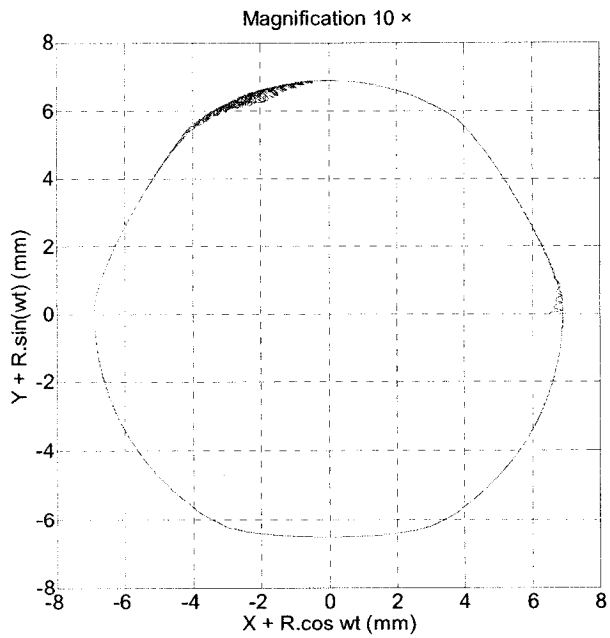

Figure 4.24: Locus of Outermost Point of Cutting Lip (F_i = 2.0 N)

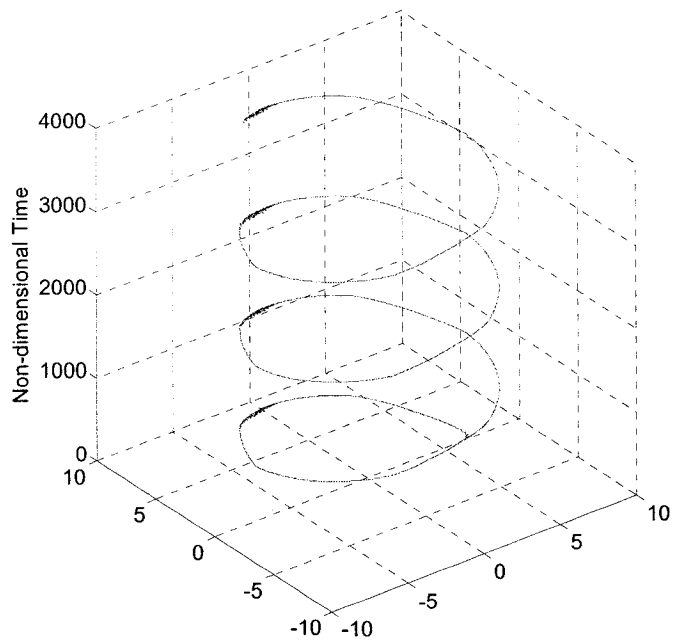

Figure 4.25: Locus of Outermost Point of Cutting Lip on Time Scale (F_i = 2.0 N)

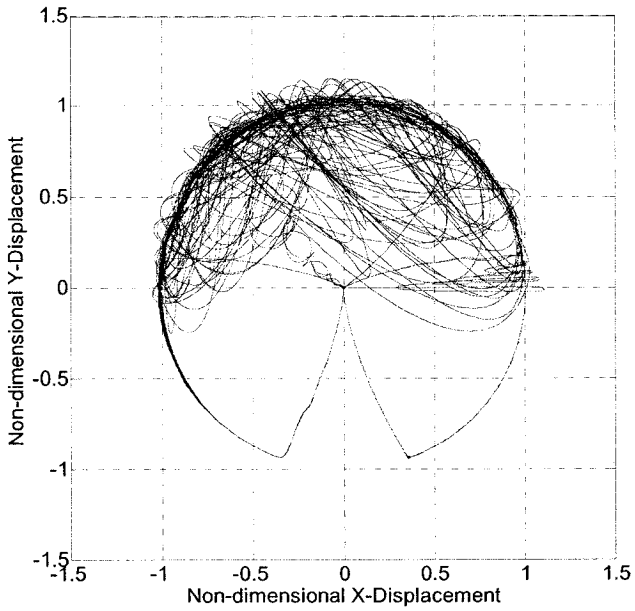

Figure 4.26: Trajectory of Drill Centerline (F_i = 3.0 N)

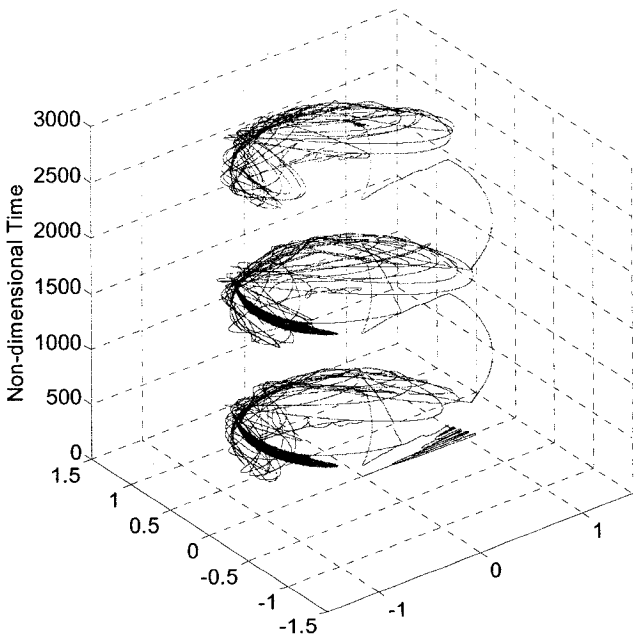

Figure 4.27: Trajectory of Drill Centerline on Time Scale (F_i = 3.0 N)

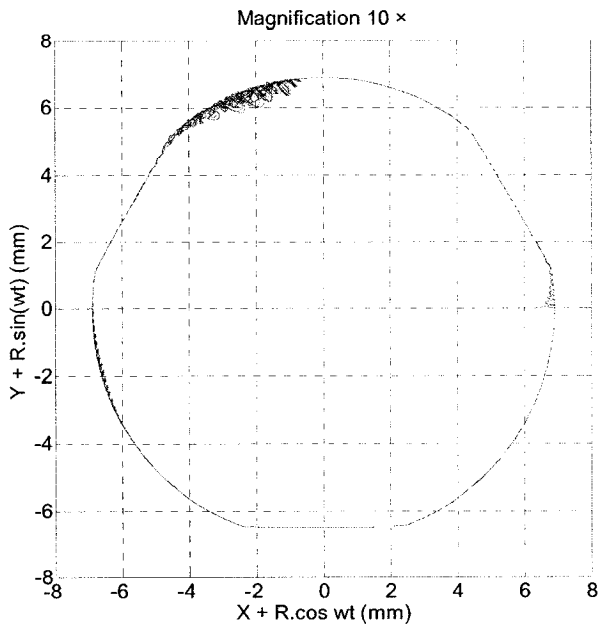

Figure 4.28: Locus of Outermost Point of Cutting Lip (F_i = 3.0 N)

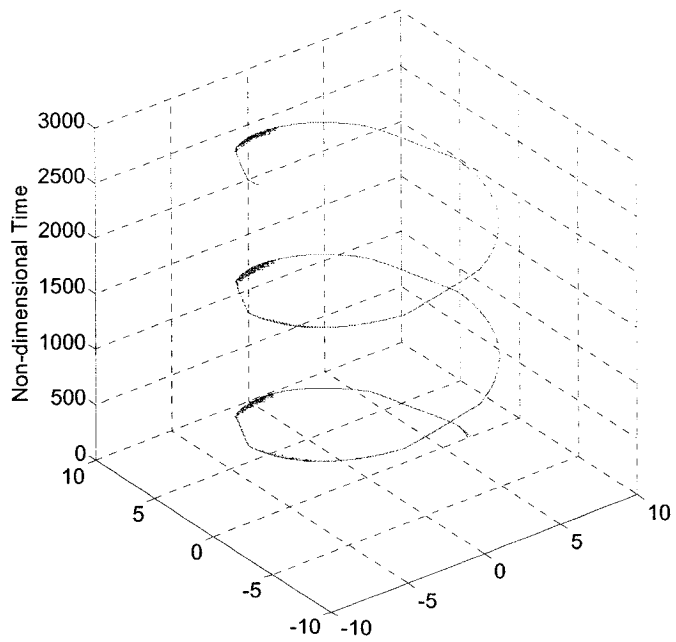

Figure 4.29: Locus of Outermost Point of Cutting Lip on Time Scale (F_i = 3.0 N)

4.6.2 Effect of Change in Force Amplitude Modulation Factor

Results of simulations for different magnitudes of amplitude modulation factor 'λ' are presented below (figures 4.6 – 4.29). Smaller values of other variable parameters which are forcing frequency 'ω' as function of rotating speed 'N' and force imbalance 'F_i' are selected to keep the influence of these factors smaller so that the influence of amplitude modulation factor on hole inaccuracies is emphasized.

F_{ix}	=	F_{iy}	
	=	0.2	N
N	=	100	rpm
λ	=	1 to 5	

Rest of the simulation parameters listed in table as ξ , α, k, δ, μ, ω_n are held constant for given system. Magnitudes of those parameters are given in table 4.1 above.

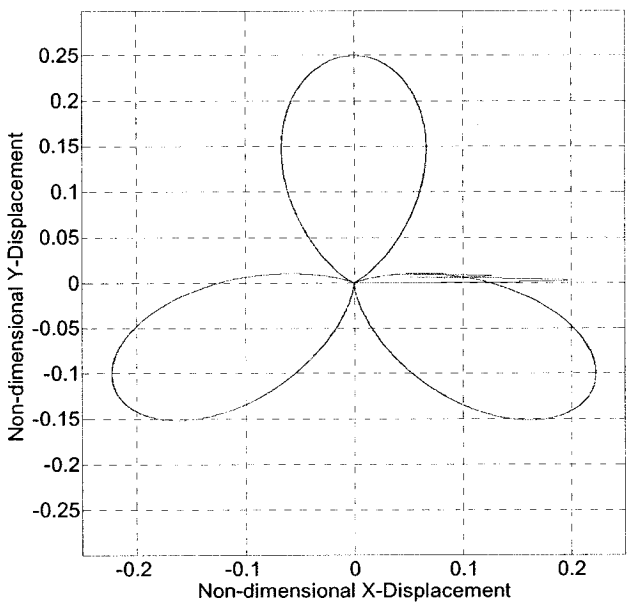

Figure 4.30: Trajectory of Drill Centerline (λ= 1)

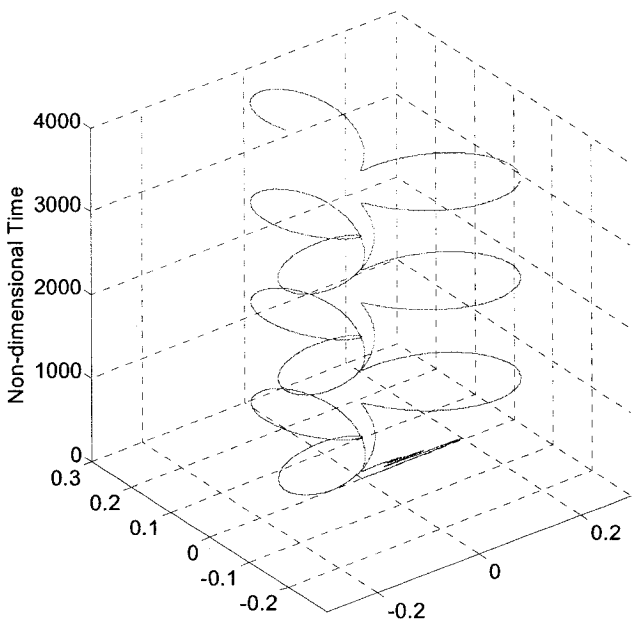

Figure 4.31: Trajectory of Drill Centerline on Time Scale (λ = 1)

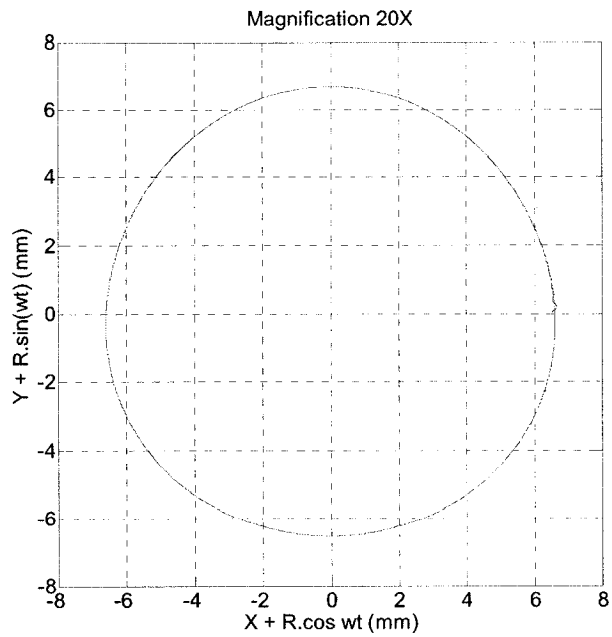

Figure 4.32: Locus of Outermost Point of Cutting Lip ($\lambda = 1$)

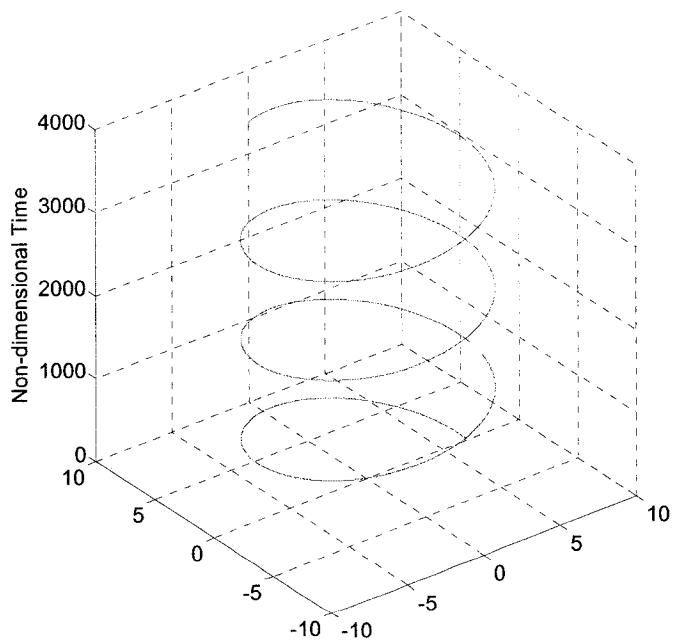

Figure 4.33: Locus of Outermost Point of Cutting Lip on Time Scale ($\lambda = 1$)

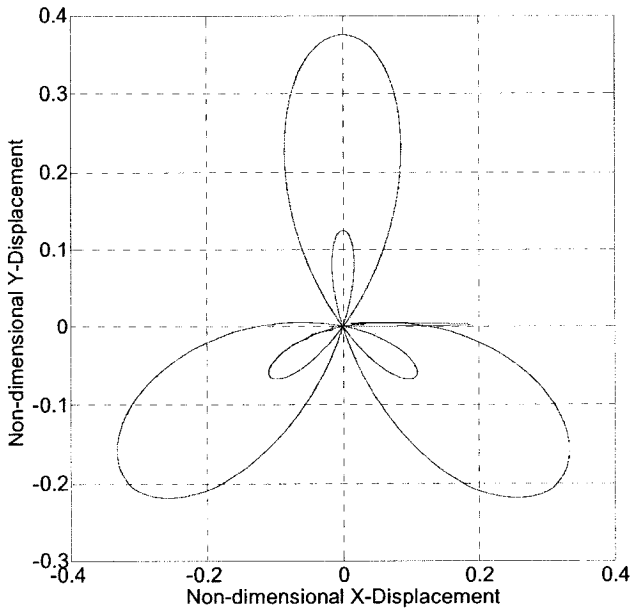

Figure 4.34: Trajectory of Drill Centerline ($\lambda = 2$)

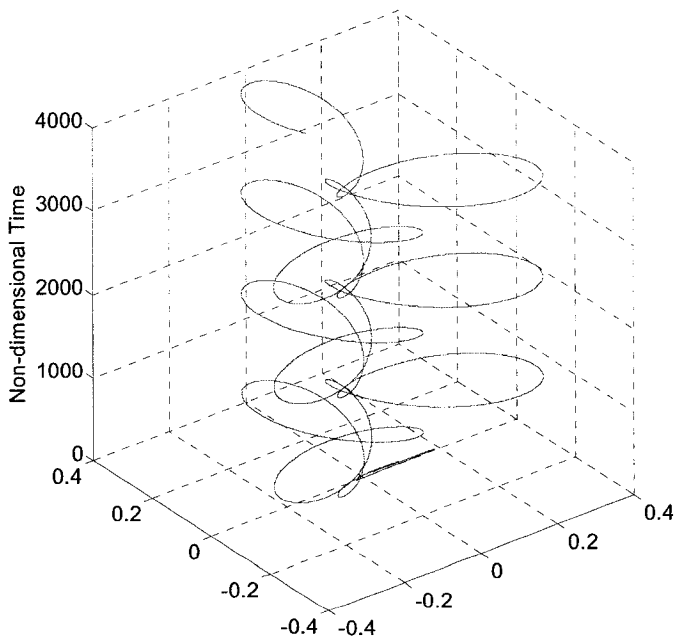

Figure 4.35: Trajectory of Drill Centerline on Time Scale ($\lambda = 2$)

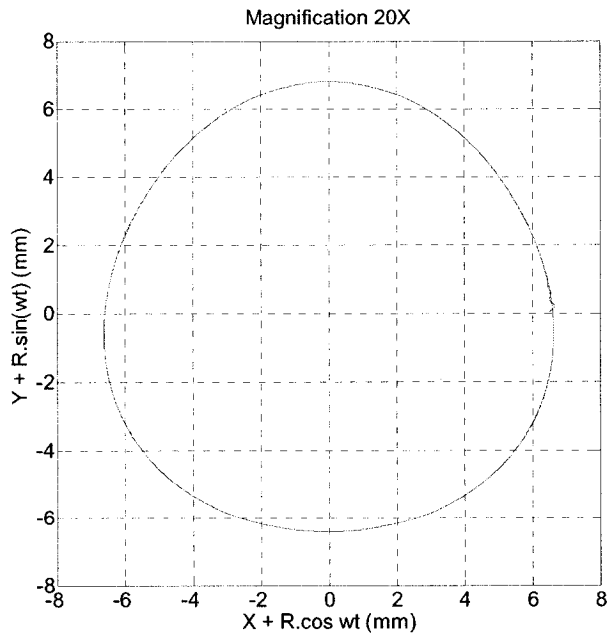

Figure 4.36: Locus of Outermost Point of Cutting Lip ($\lambda = 2$)

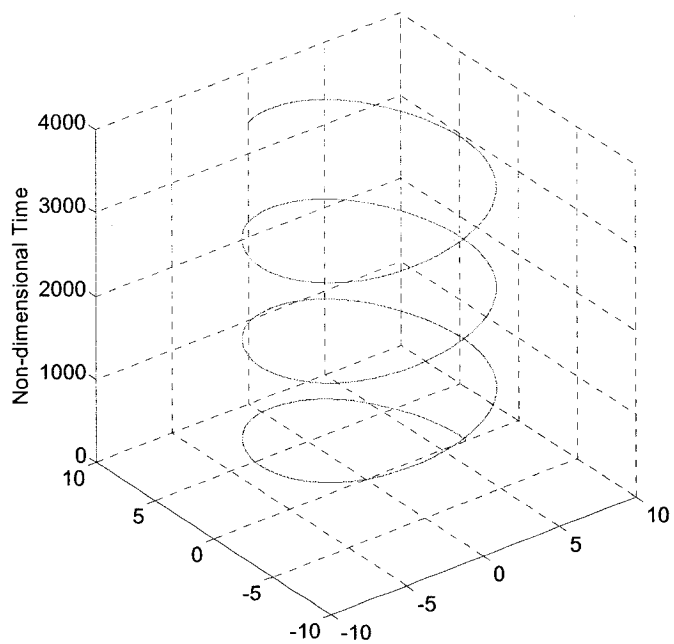

Figure 4.37: Locus of Outermost Point of Cutting Lip on Time Scale ($\lambda = 2$)

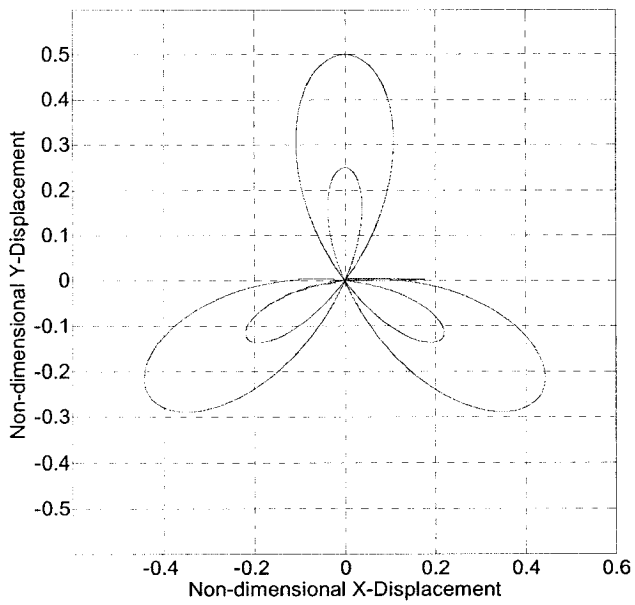

Figure 4.38: Trajectory of Drill Centerline ($\lambda = 3$)

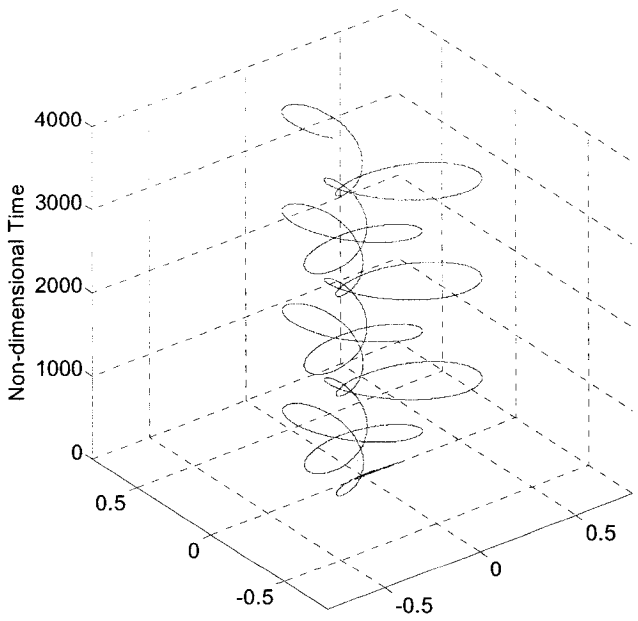

Figure 4.39: Trajectory of Drill Centerline on Time Scale ($\lambda = 3$)

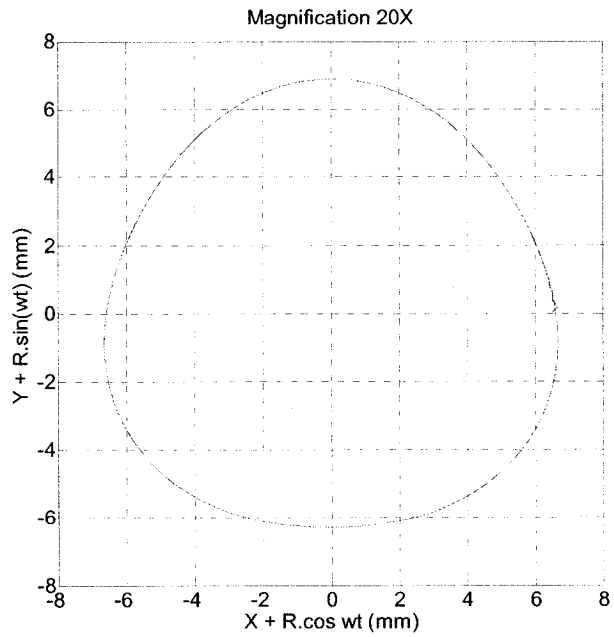

Figure 4.40: Locus of Outermost Point of Cutting Lip ($\lambda = 3$)

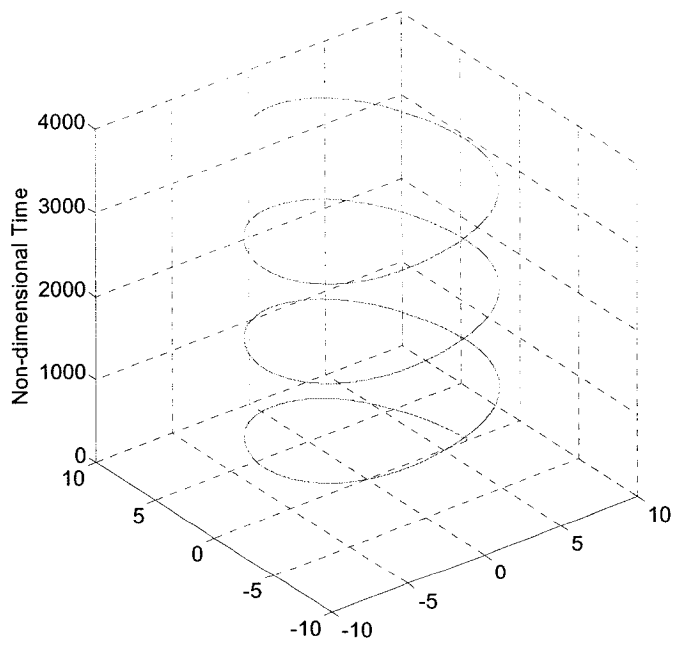

Figure 4.41: Locus of Outermost Point of Cutting Lip on Time Scale ($\lambda = 3$)

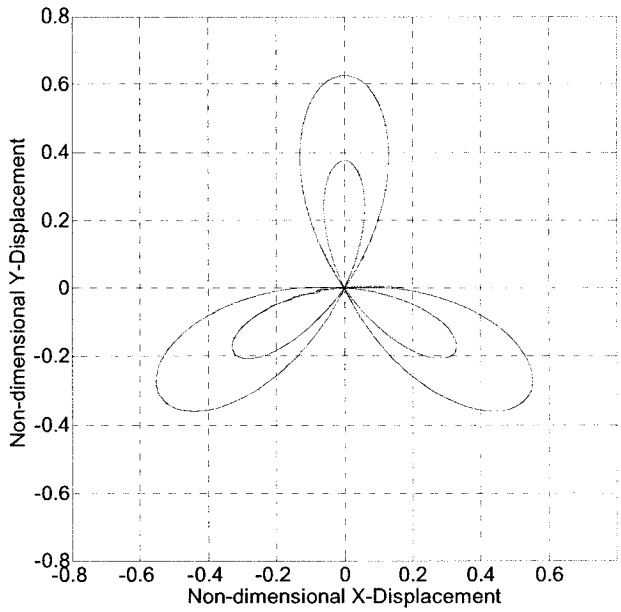

Figure 4.42: Trajectory of Drill Centerline ($\lambda = 4$)

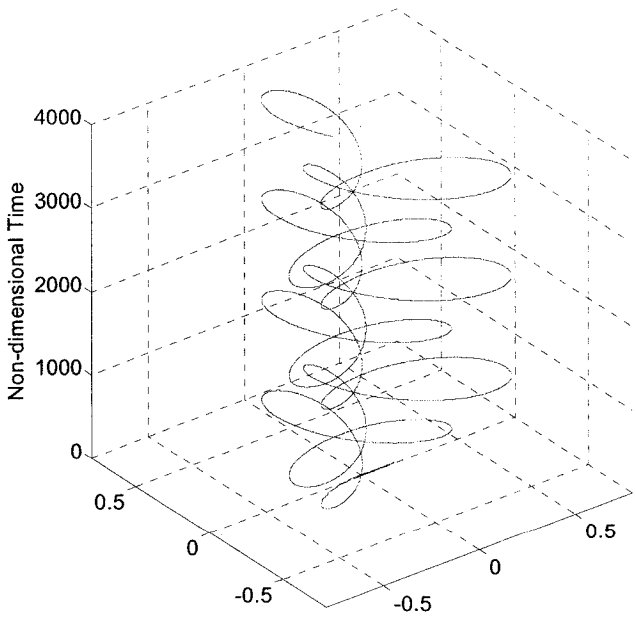

Figure 4.43: Trajectory of Drill Centerline on Time Scale ($\lambda = 4$)

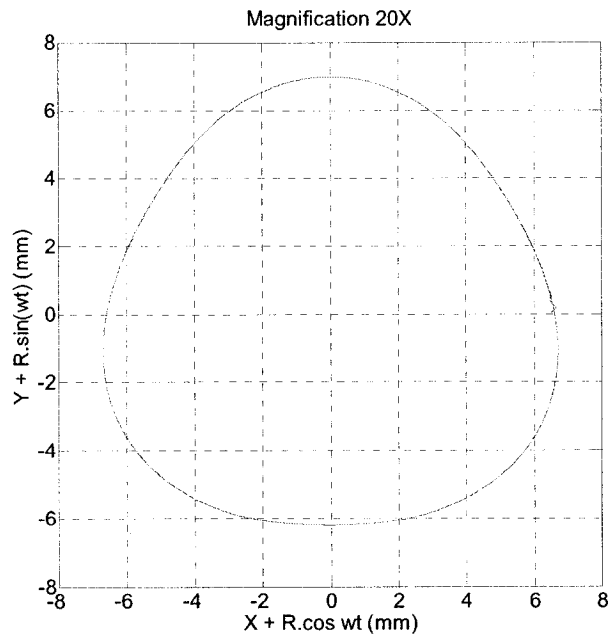

Figure 4.44: Locus of Outermost Point of Cutting Lip ($\lambda = 4$)

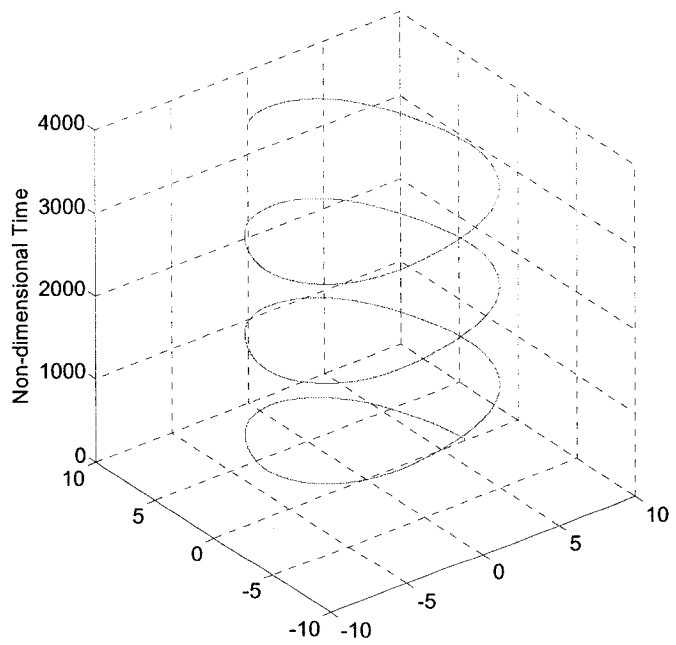

Figure 4.45: Locus of Outermost Point of Cutting Lip on Time Scale ($\lambda = 4$)

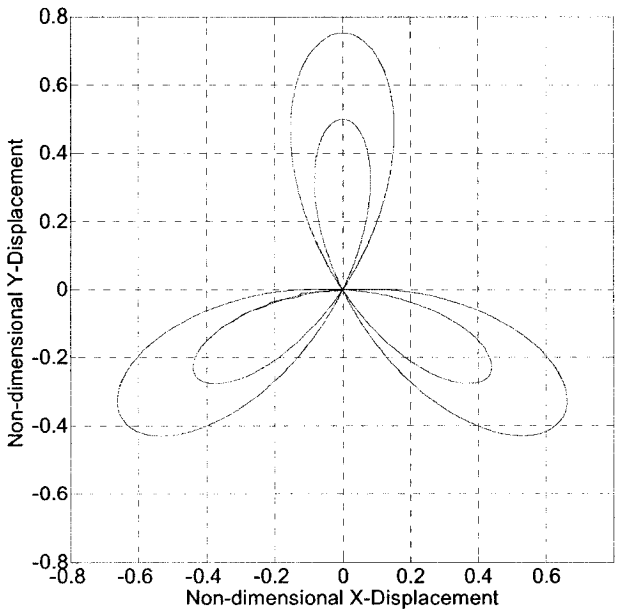

Figure 4.46: Trajectory of Drill Centerline ($\lambda = 5$)

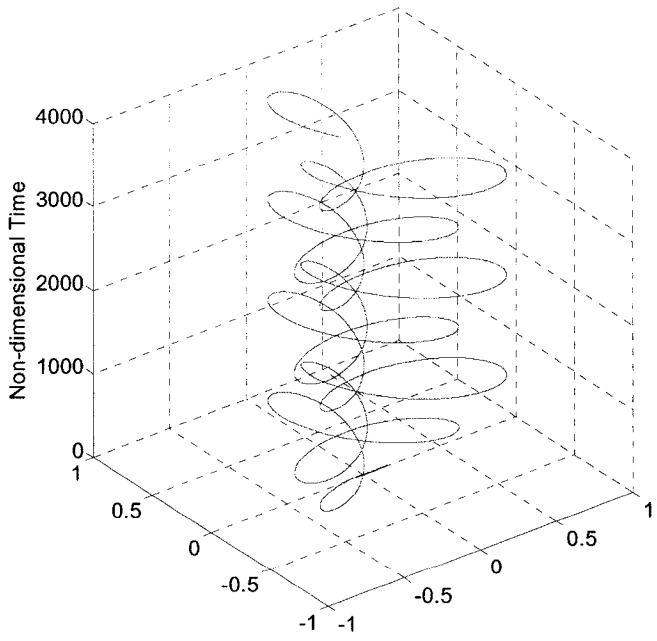

Figure 4.47: Trajectory of Drill Centerline on Time Scale ($\lambda = 5$)

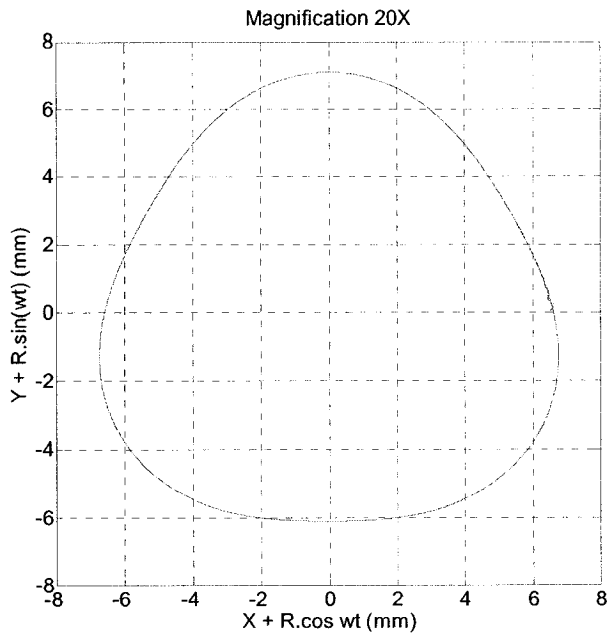

Figure 4.48: Locus of Outermost Point of Cutting Lip ($\lambda = 5$)

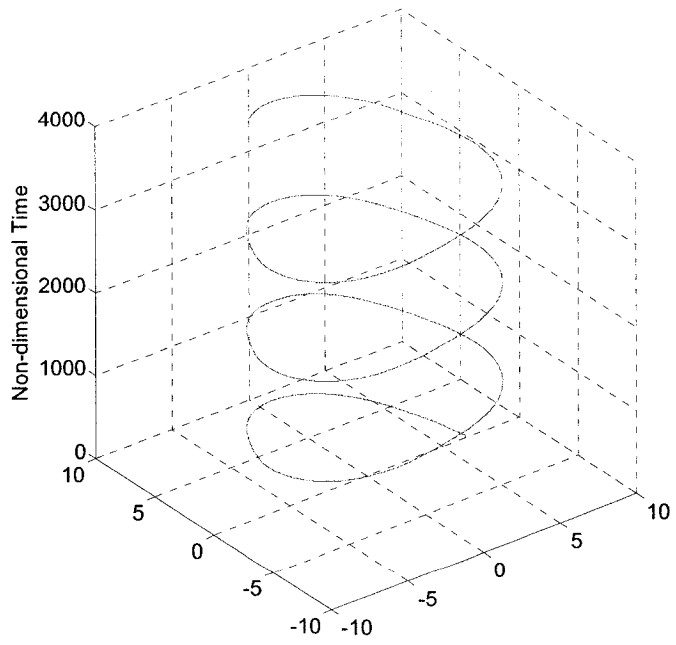

Figure 4.49: Locus of Outermost Point of Cutting Lip on Time Scale ($\lambda = 5$)

4.6.3 Combined Effect of Unbalance Force Components and Amplitude Modulation Factors

As mentioned in section 4.6.3 the influence of unbalance force components and amplitude modulation factors on drilled hole profile is different. Comparative study for combined effect of these parameters on hole profile will be more meaningful and will result in better understanding of factors responsible for formation of distinct hole profiles observed in actual practice.

Results of simulations for different combinations of magnitudes of amplitude modulation factor 'λ' and imbalance force F_i are presented below (figures 4.54 – 4.61). Small magnitude of forcing frequency 'ω' which is function of rotating speed 'N' is selected to emphasize on the influence of different combinations of amplitude modulation factor and force imbalance on hole inaccuracies.

N	=	100	rpm
λ	=	3	
F_{ix}	=	F_{iy}	
	=	0.4 to 1.0	N

Rest of the simulation parameters listed in table as ξ , α, k, δ, μ, ω_n are held constant for given system. Magnitudes of those parameters are given in table 4.1 above.

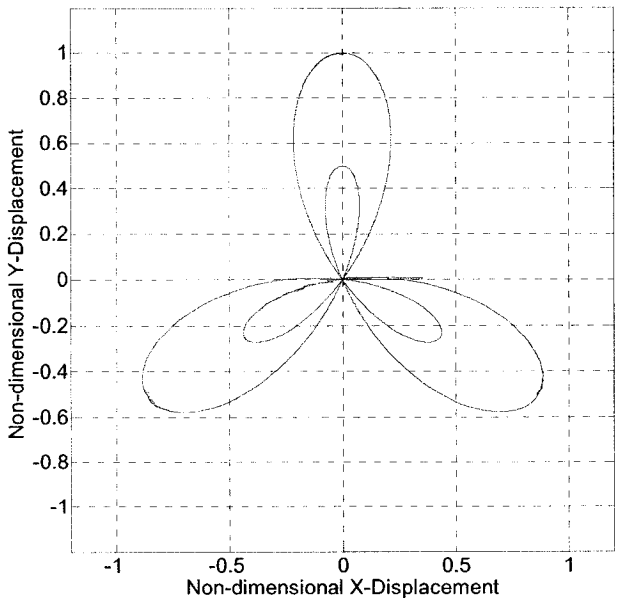

Figure 4.50: Trajectory of Drill Centerline ($\lambda = 3$, $F_i = 0.4$ N)

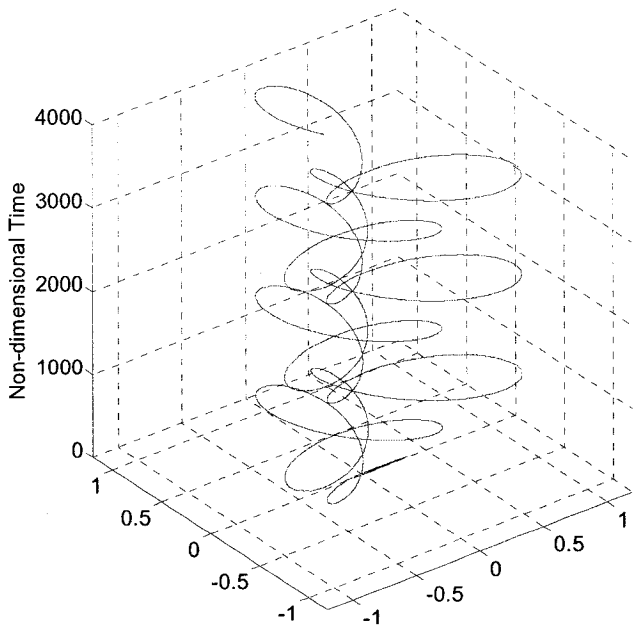

Figure 4.51: Trajectory of Drill Centerline on Time Scale ($\lambda = 3$, $F_i = 0.4$ N)

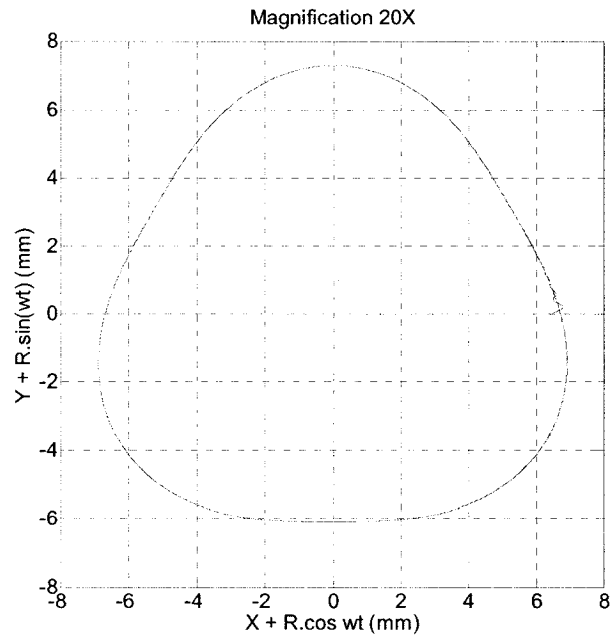

Figure 4.52: Locus of Outermost Point of Cutting Lip (λ= 3, F_i = 0.4 N)

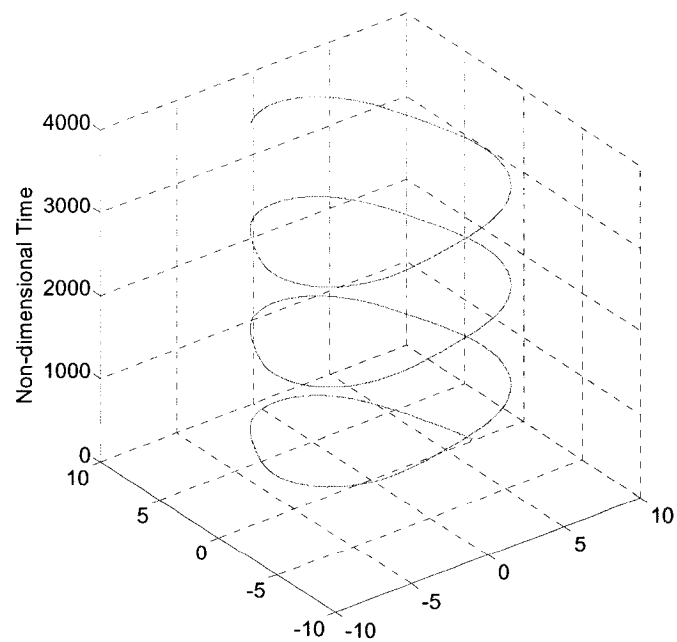

Figure 4.53: Locus of Outermost Point of Cutting Lip on Time Scale (λ= 3, F_i = 0.4 N)

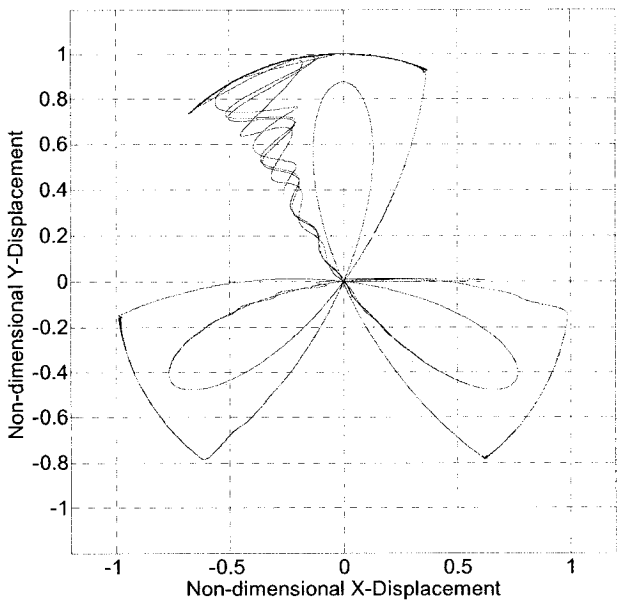

Figure 4.54: Trajectory of Drill Centerline ($\lambda = 3$, $F_i = 0.7$ N)

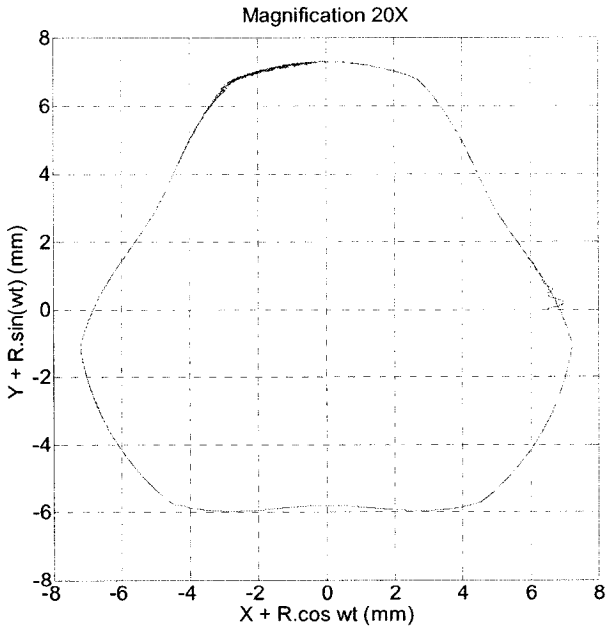

Figure 4.55: Locus of Outermost Point of Cutting Lip ($\lambda = 3$, $F_i = 0.7$ N)

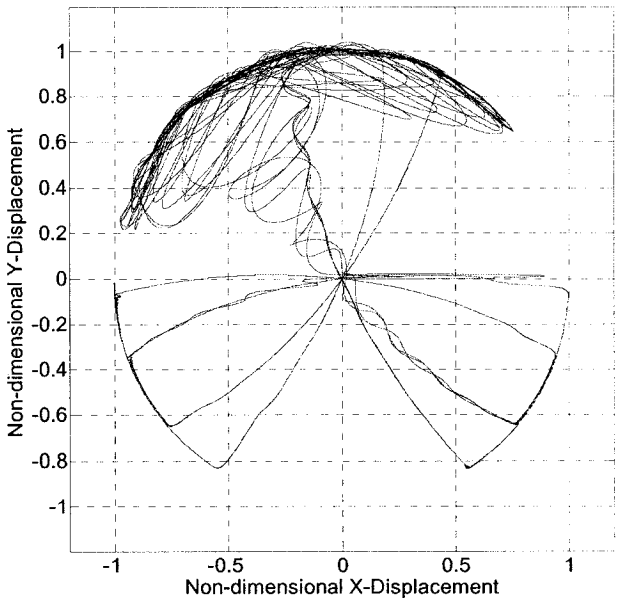

Figure 4.56: Trajectory of Drill Centerline ($\lambda = 3$, $F_i = 1.0$ N)

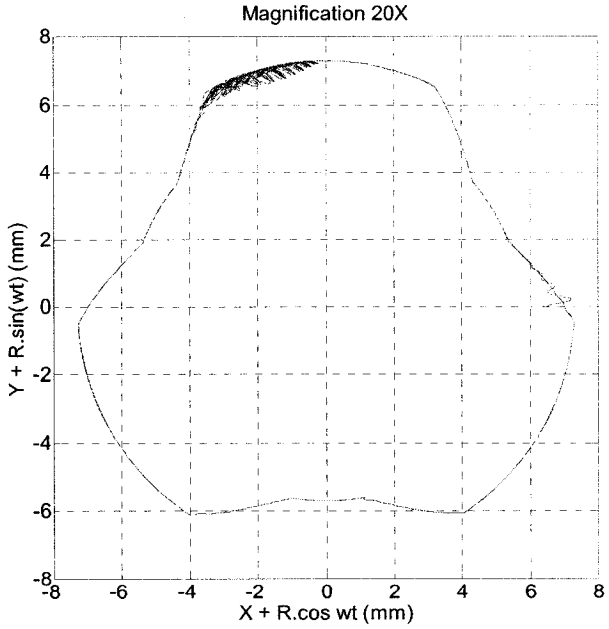

Figure 4.57: Locus of Outermost Point of Cutting Lip ($\lambda = 3$, $F_i = 1.0$ N)

4.6.4 Observations - 1

The predicted orbits for different magnitudes of force imbalance as shown in figures 4.8, 4.12, 4.16, 4.20, 4.24, 4.28 and for different magnitudes of amplitude modulation factor as shown in figures 4.32, 4.36, 4.40, 4.44, 4.48 clearly reveal contribution of these parameters in the formation of lobed holes. Influence of both the parameters on hole inaccuracies is almost similar. Higher the magnitudes of force imbalance components and amplitude modulation factor three lobed hole shape becomes more and more prominent.

There is significant difference in the trajectories of drill centerline as shown in figures 4.6, 4.10, 4.14, 4.18, 4.22, 4.26 and figures 4.30, 4.34, 4.38, 4.42, 4.46. This difference is reflected in the difference in the roughness of the corresponding predicted hole profiles.

Trajectory of drill centerline for higher values of amplitude modulation factor is more symmetric with higher and lower magnitude oscillations of same pattern repeated alternately making the three lobed shape of drilled hole more prominent.

Also influence of force imbalance on roughness of hole profile in addition to lobe formation is clearly evident from the predicted orbits (figures 4.50–4.57) shown in section 4.6.3 where combined effect of force imbalance and amplitude modulation factor on hole profiles inaccuracies is presented in the form of predicted orbits. It is observed that with increase in imbalance force the unevenness of hole profile increases.

4.6.5 Validation of Results – 1

In this section the results in literature in past literature similar to the numerical results obtained by simulation of lumped mass model developed in section 4.4 above are presented for the purpose of comparison and validation. Figure 4.58 below shows predicted and experimental hole shapes obtained by Y. Gong et al. [12].

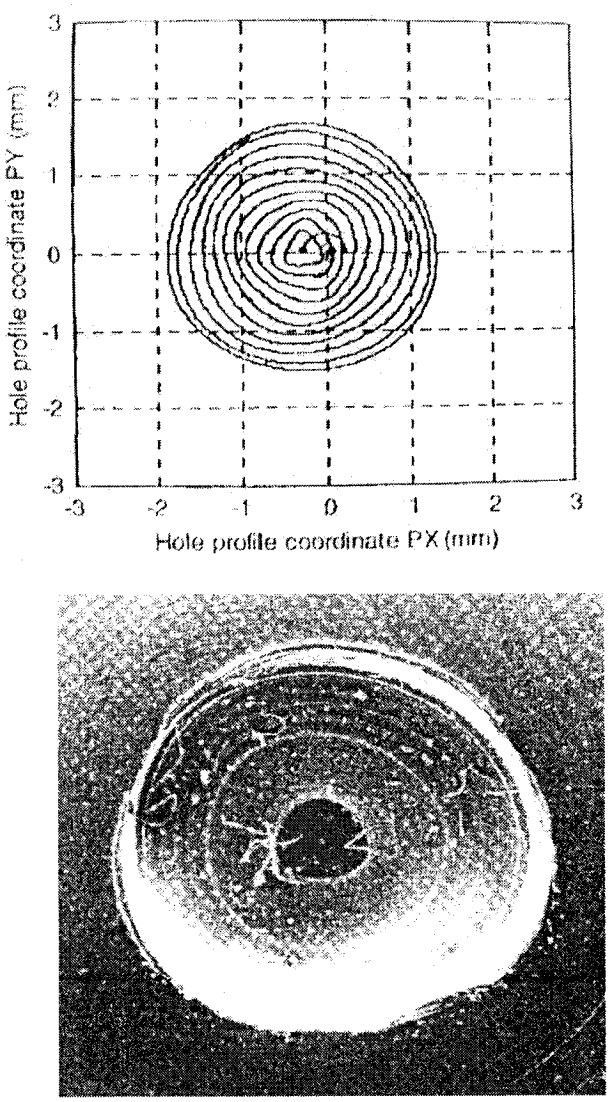

Figure 4.58: Simulated and Experimental Hole Profiles [12]

Figures 4.59 below shows predicted three lobed hole profiles obtained by P. V. Bayly et al. [17].

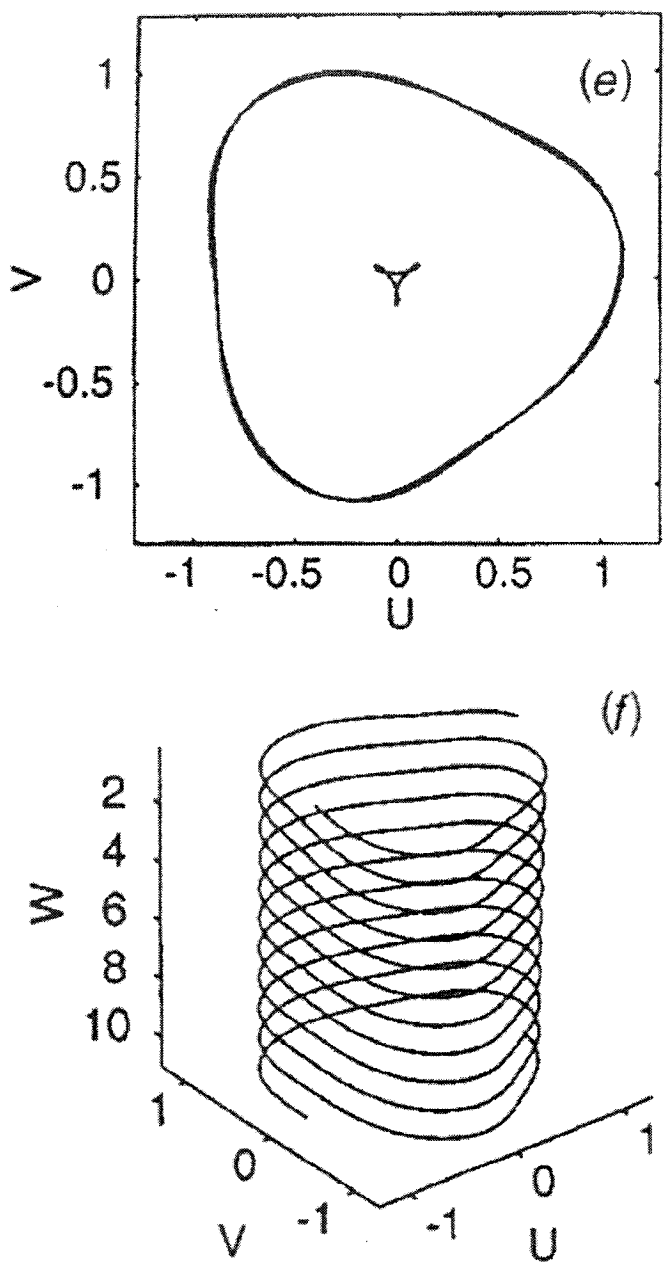

Figure 4.59: Predicted 3-Lobed Hole Profile [17]

Figures 4.60 below shows experimental hole profiles obtained by P. V. Bayly et al. [17].

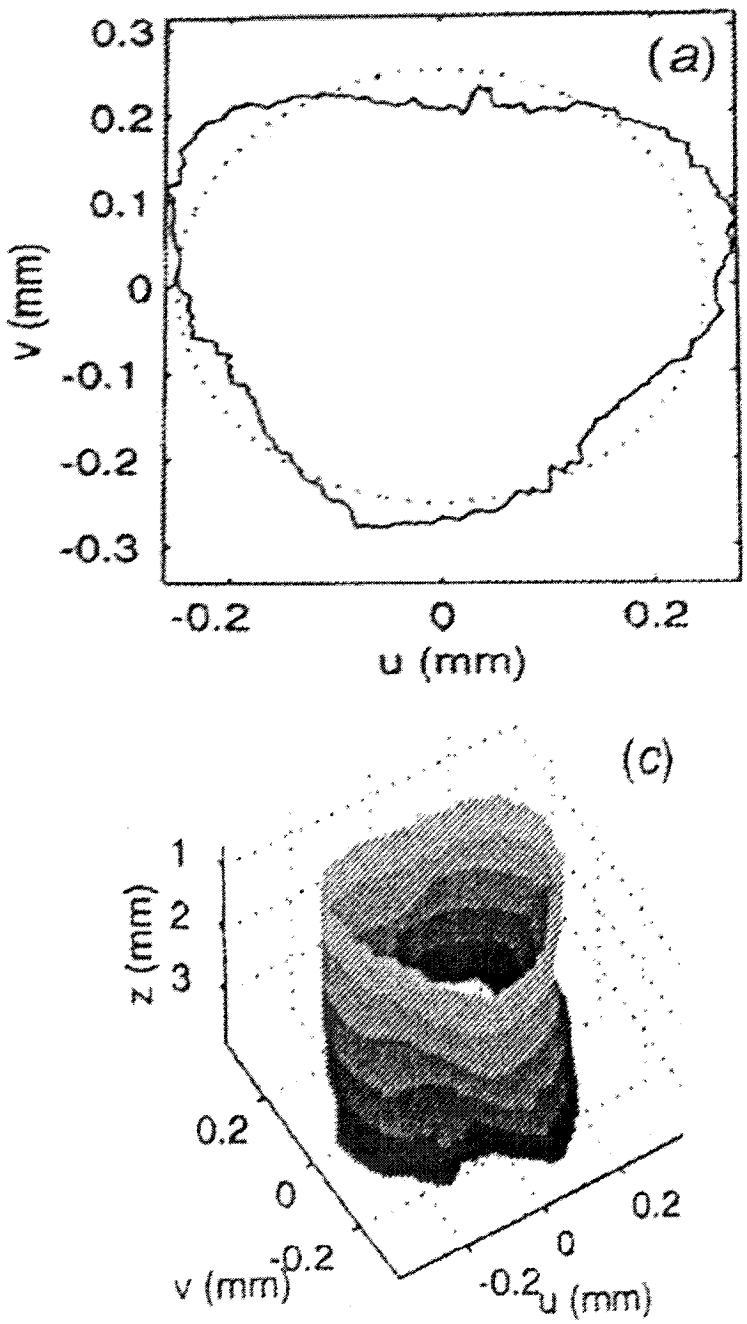

Figure 4.60: Experimental 3-Lobed Hole Profile [17]

Figures 4.61 below shows measured three lobed hole profiles and photograph obtained by P. V. Bayly et al. [17].

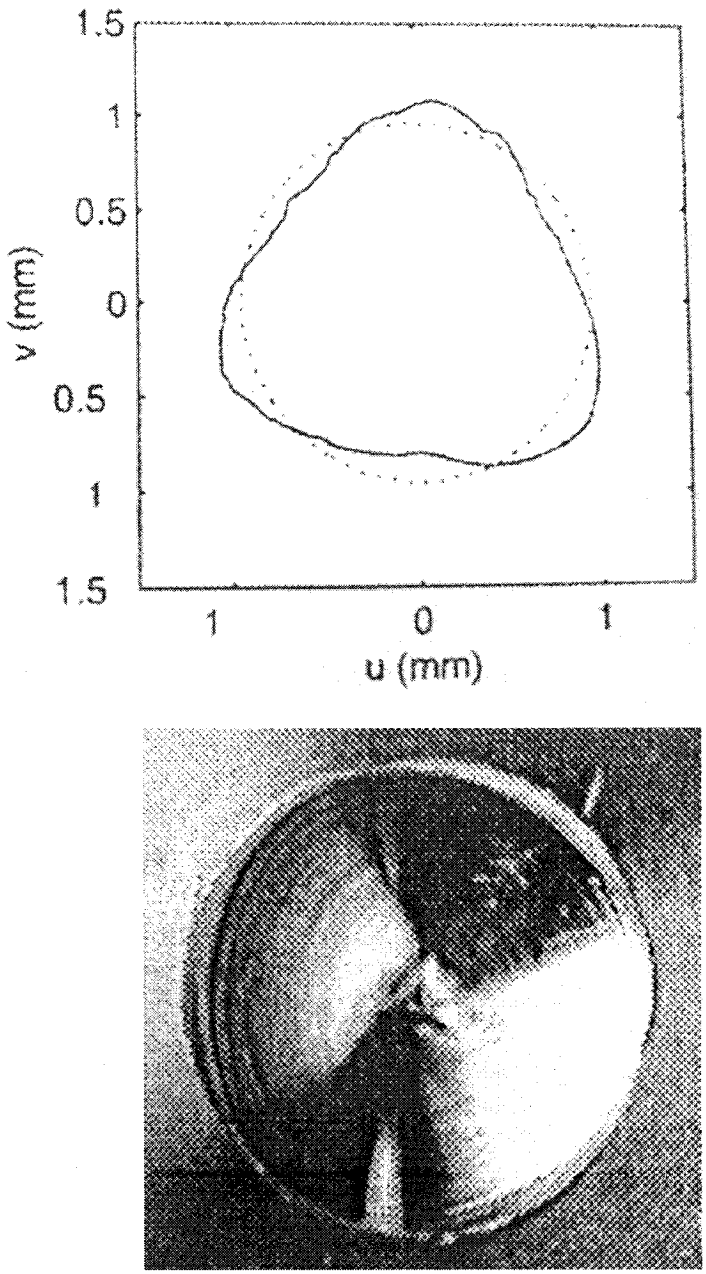

Figure 4.61: Measured Profile and Photograph of 3-Lobed Hole [17]

4.6.6 Effect of Change in Forcing Frequency

Results of simulations for different values of forcing frequency which is function of drill rotational speed 'N' are presented below (figures 4.62 – 4.81). Values of force imbalance 'F_i' and amplitude modulation factor 'λ' are kept constant for all simulations and influence of forcing frequency on hole inaccuracies is studied.

F_{ix} = F_{iy}

= 1.0 N

N = 100 to 25000 rpm

λ = 1.0

Rest of the simulation parameters listed in table as ξ , α, k, δ, μ, ω_n are held constant for given system. Magnitudes of those parameters are given in table 4.1 above.

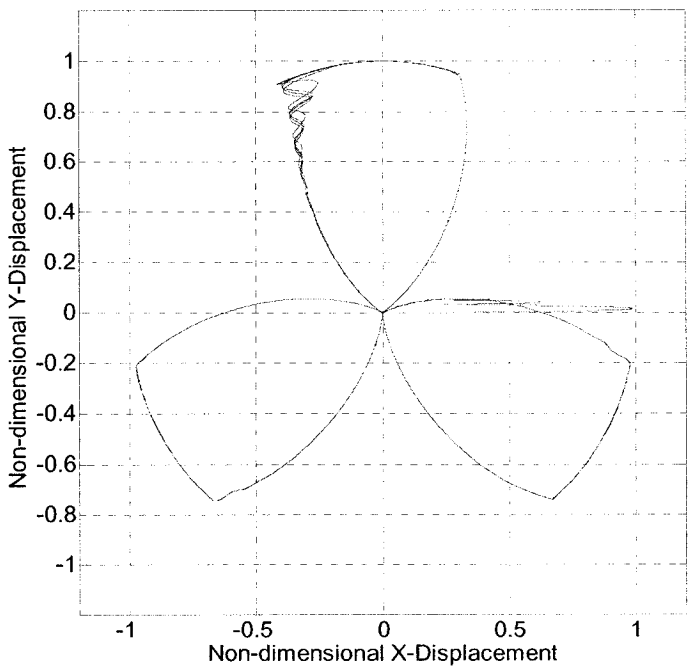

Figure 4.62: Trajectory of Drill Centerline (N = 100 rpm)

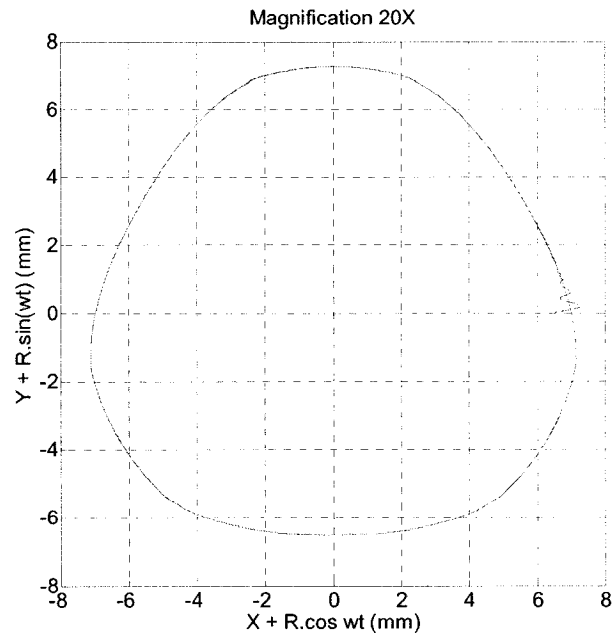

Figure 4.63: Locus of Outermost Point of Cutting Lip (N = 100 rpm)

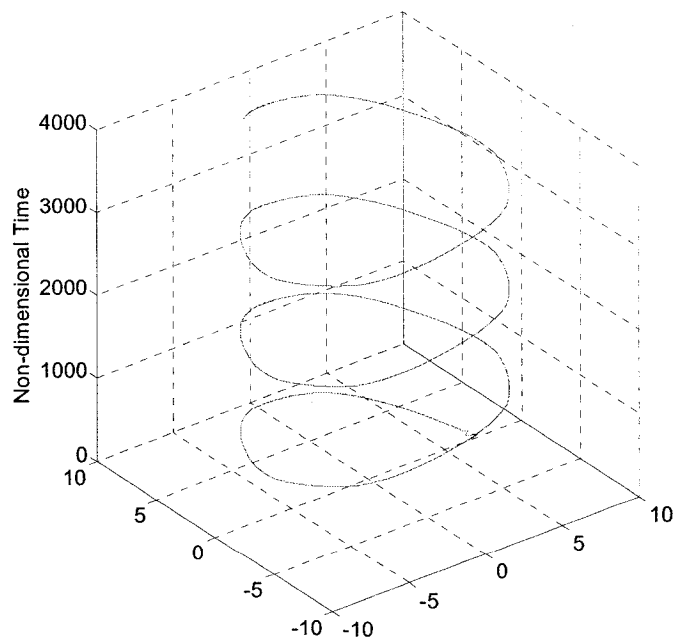

Figure 4.64: Locus of Outermost Point of Cutting Lip on Time Scale (N = 100 rpm)

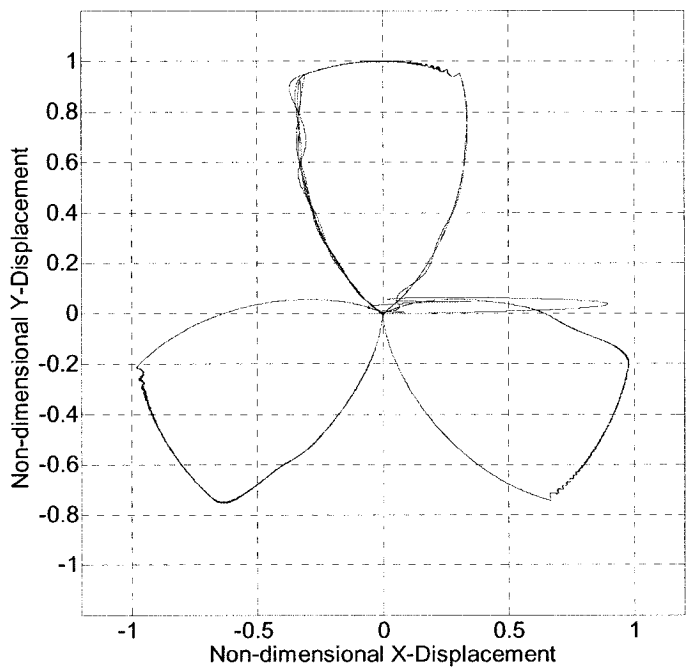

Figure 4.65: Trajectory of Drill Centerline (N = 300 rpm)

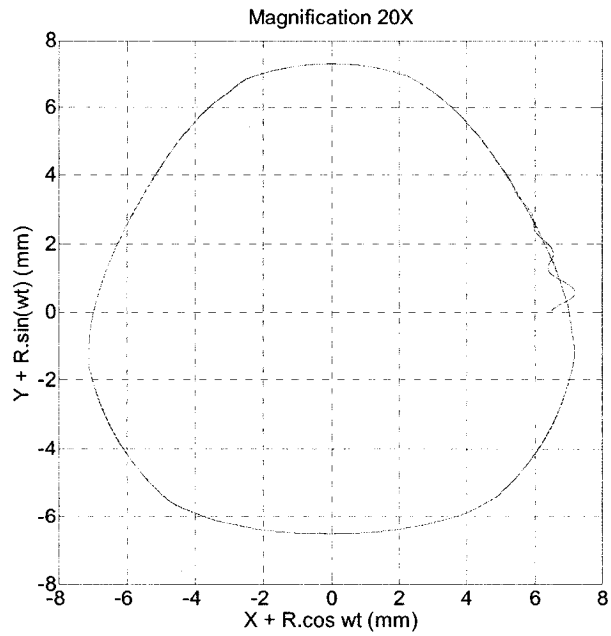

Figure 4.66: Locus of Outermost Point of Cutting Lip (N = 300 rpm)

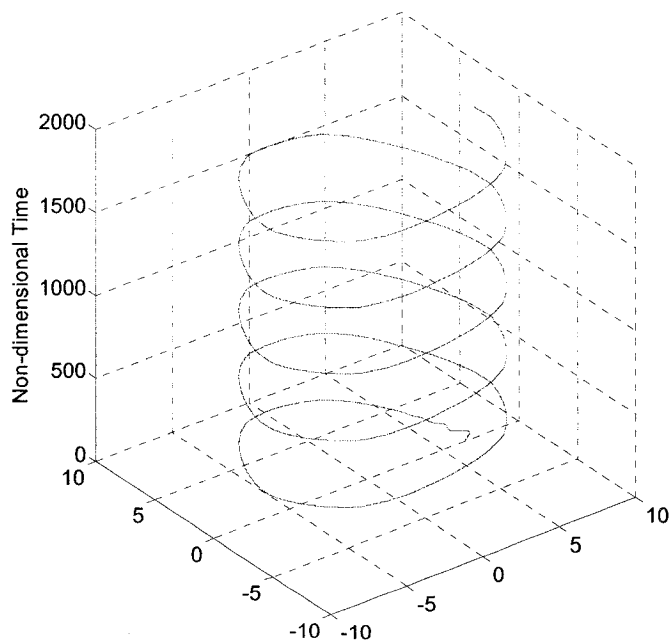

Figure 4.67: Locus of Outermost Point of Cutting Lip on Time Scale (N = 300 rpm)

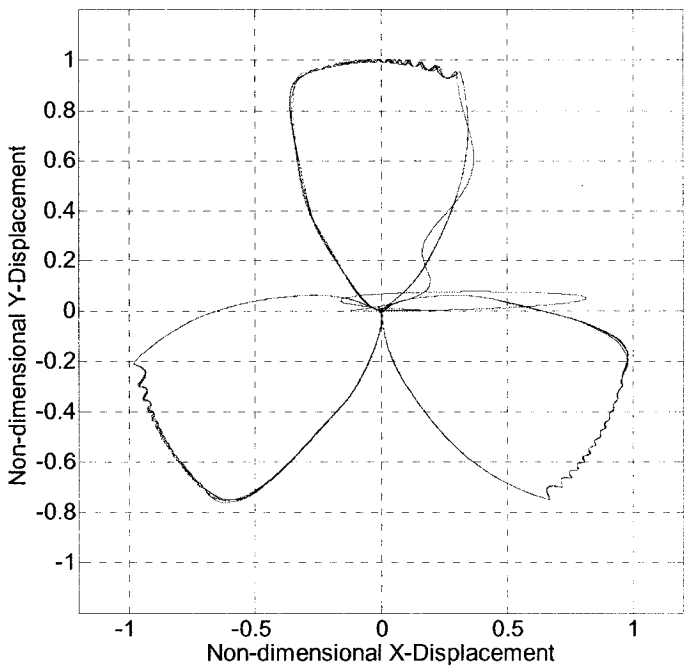

Figure 4.68: Trajectory of Drill Centerline (N = 500 rpm)

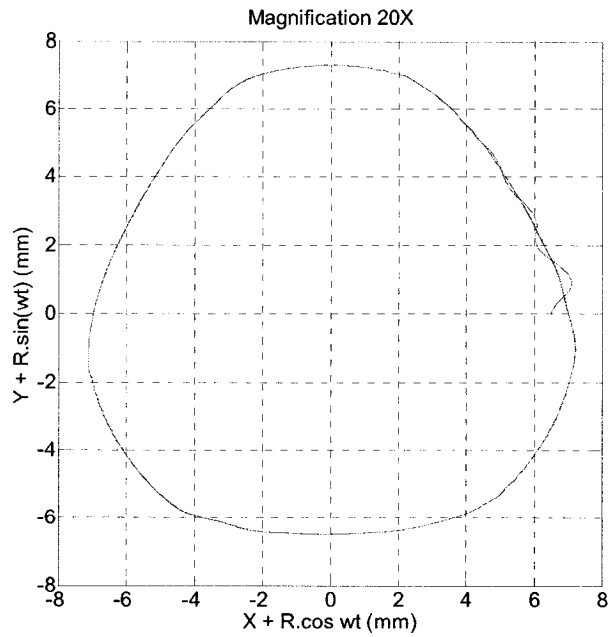

Figure 4.69: Locus of Outermost Point of Cutting Lip (N = 500 rpm)

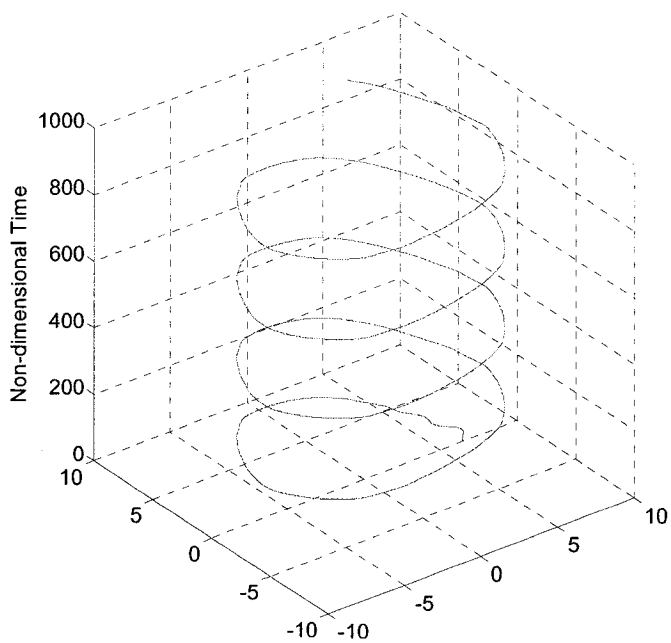

Figure 4.70: Locus of Outermost Point of Cutting Lip on Time Scale (N = 500 rpm)

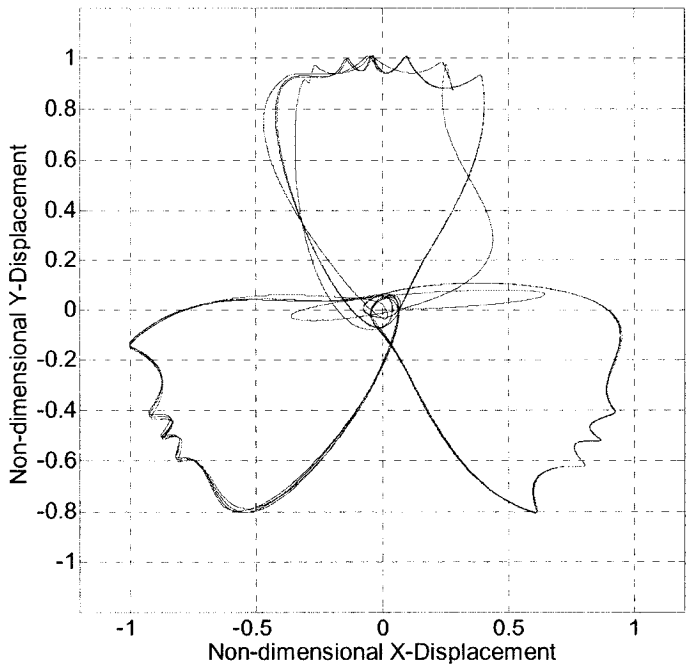

Figure 4.71: Trajectory of Drill Centerline (N = 1000 rpm)

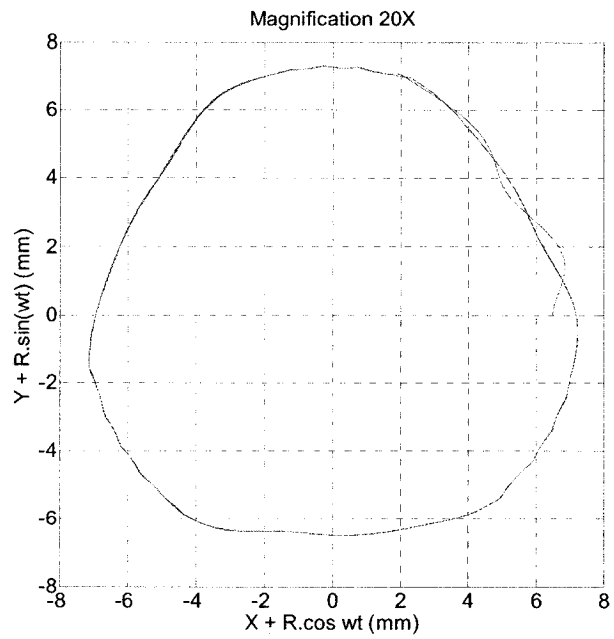

Figure 4.72: Locus of Outermost Point of Cutting Lip (N = 1000 rpm)

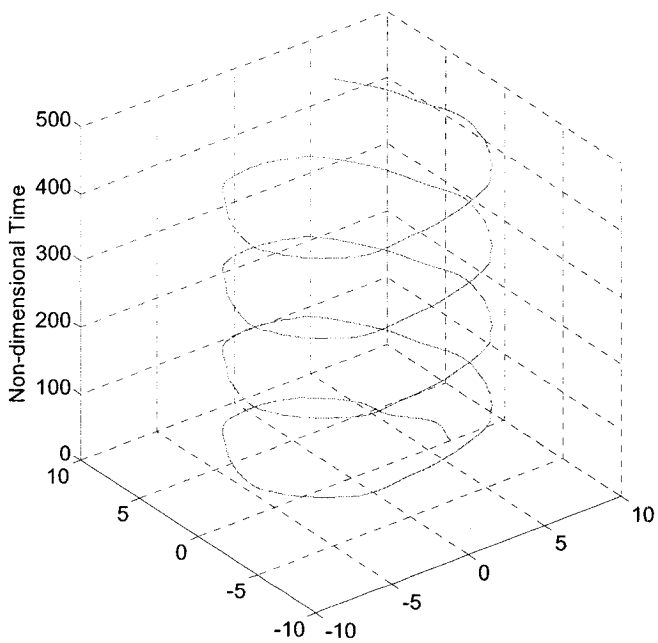

Figure 4.73: Locus of Outermost Point of Cutting Lip on Time Scale (N = 1000 rpm)

4.6.6.1 Observations - 2

Simulations results (Figures 4.62-4.73) again demonstrate formation of three lobed holes as a result of combined effect of force imbalance and amplitude modulation factor.

For lower speeds influence of rotational speed is not prominent. Effect of increase in rotational speed is evident in trajectories of drill centerline (Figures 4.62, 4.65, 4.68, 4.71) which results in an additional hole profile unevenness.

Thus force imbalance and amplitude modulation factor are major contributors in the formation of three lobed holes and unevenness of hole profile.

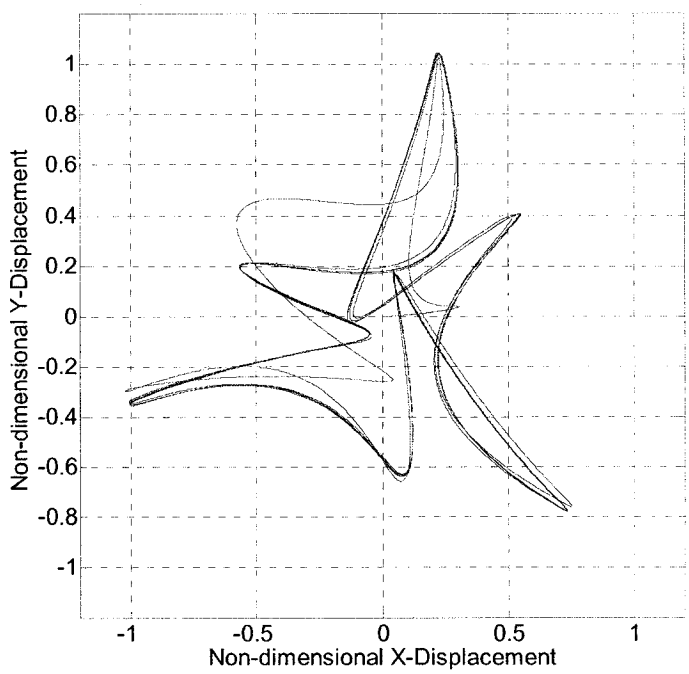

Figure 4.74: Trajectory of Drill Centerline (N =3000 rpm)

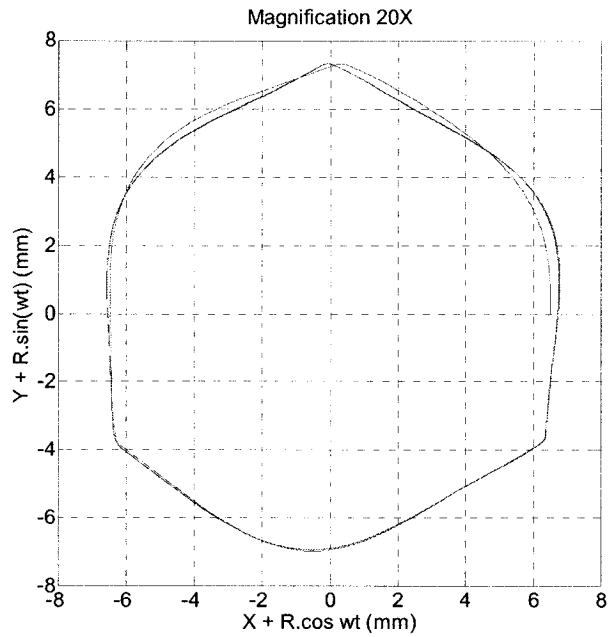

Figure 4.75: Locus of Outermost Point of Cutting Lip on Time Scale (N = 3000 rpm)

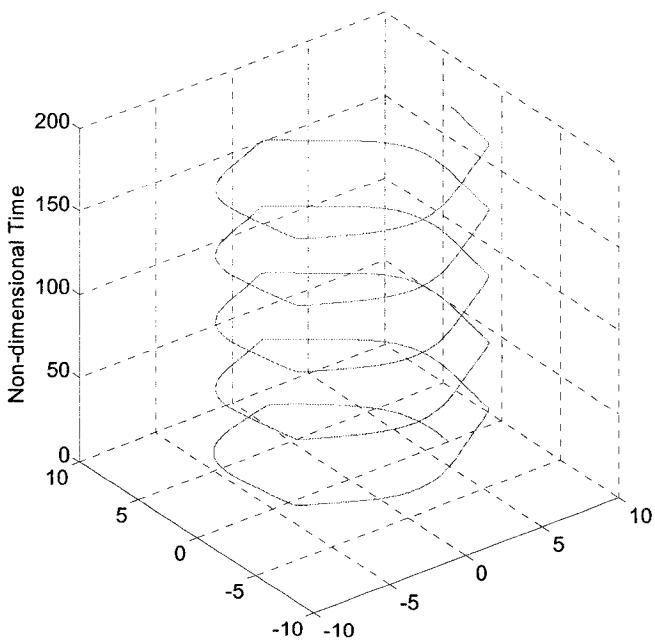

Figure 4.76: Locus of Outermost Point of Cutting Lip on Time Scale (N = 3000 rpm)

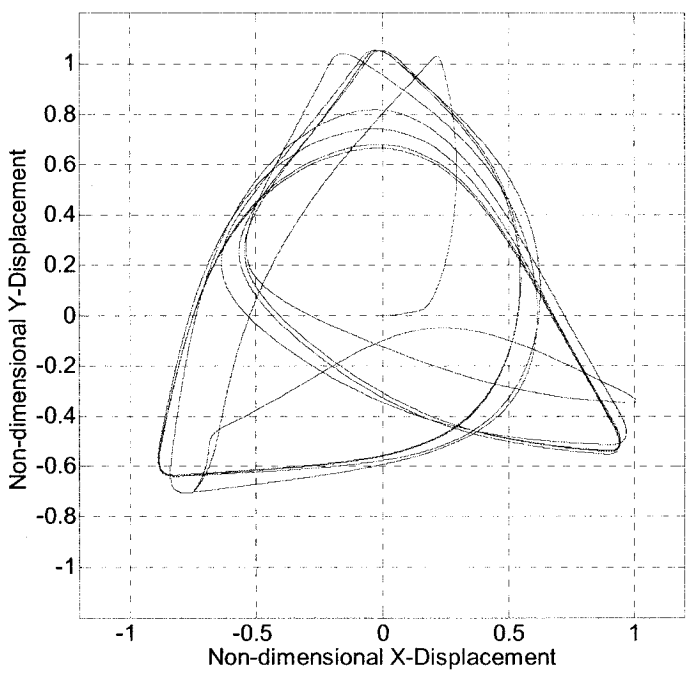

Figure 4.77: Trajectory of Drill Centerline (N = 6000 rpm)

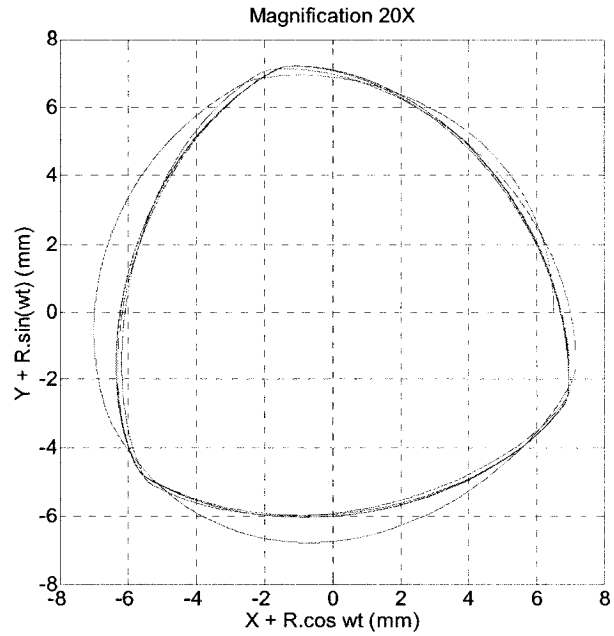

Figure 4.78: Locus of Outermost Point of Cutting Lip (N = 6000 rpm)

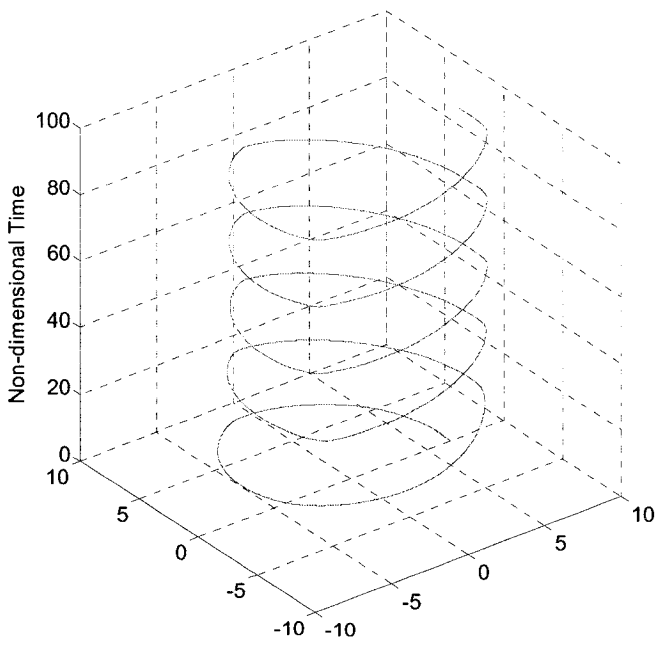

Figure 4.79: Locus of Outermost Point of Cutting Lip on Time Scale (N = 6000 rpm)

4.6.6.2 Observations - 3

Simulations results (Figures 4.74-4.79) demonstrate formation of polygonal and three lobed holes, respectively, as a result of combined effect of rotational speed, force imbalance and amplitude modulation factor.

Higher speeds are found to be influential and result in polygonal shaped hole profile. Effect of increase in rotational speed is evident in the trajectories of drill centerline (Figures 4.74 and 4.77), which results in an additional hole profile unevenness.

Thus rotational speed, force imbalance and amplitude modulation factor all together are responsible for formation of three lobed holes and unevenness of hole profile.

At lower speeds the lobes were more gradual and smooth, whereas the holes shapes at higher speeds as seen in figures 4.75 and 4.78 are more polygonal rather than smooth lobed profile.

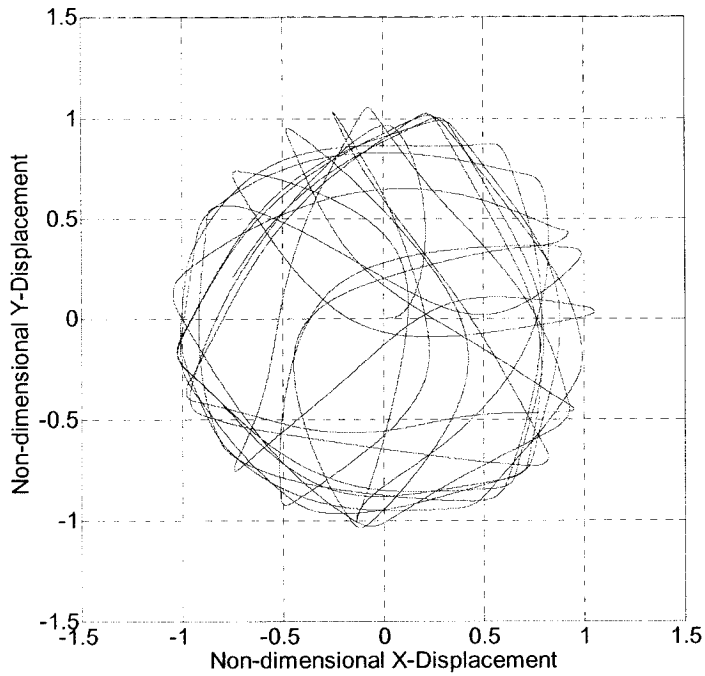

Figure 4.80: Trajectory of Drill Centerline (N = 10000 rpm)

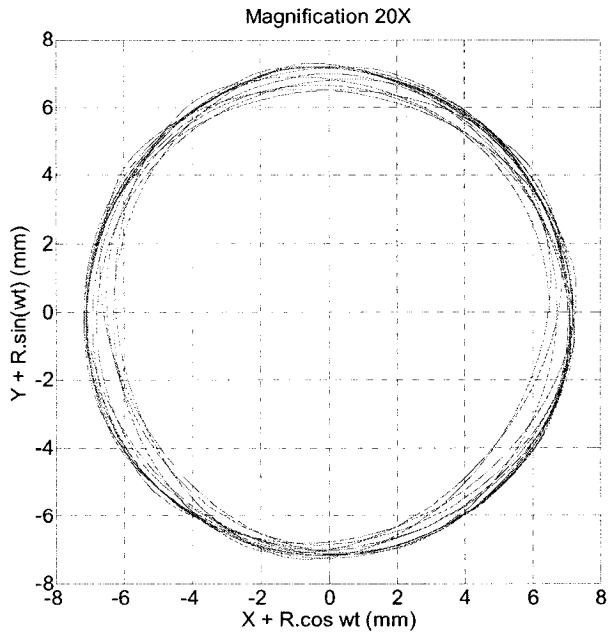

Figure 4.81: Locus of Outermost Point of Cutting Lip (N = 10000 rpm)

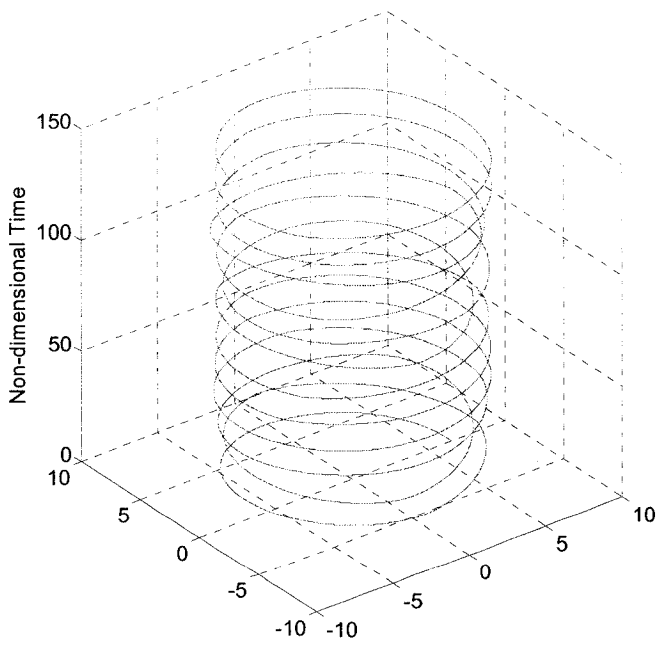

Figure 4.82: Locus of Outermost Point of Cutting Lip on Time Scale (N =10000 rpm)

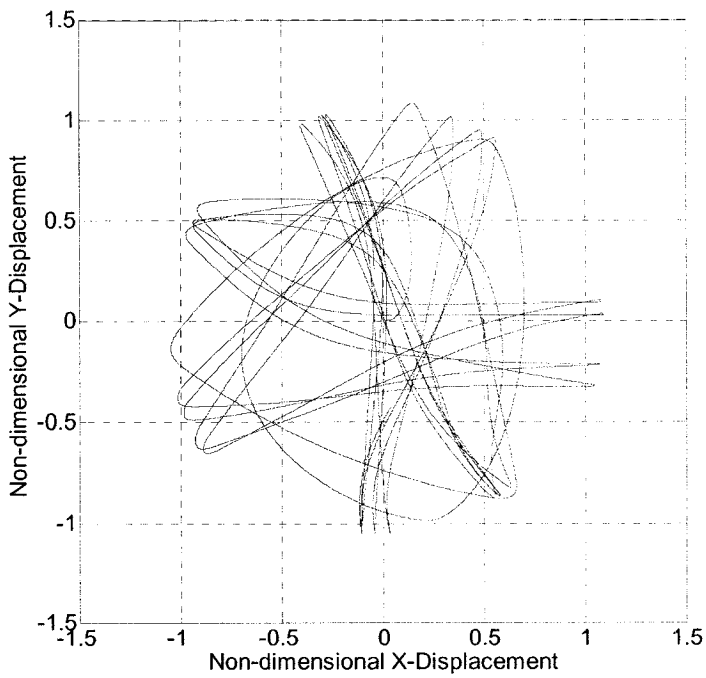

Figure 4.83: Trajectory of Drill Centerline (N = 14000 rpm)

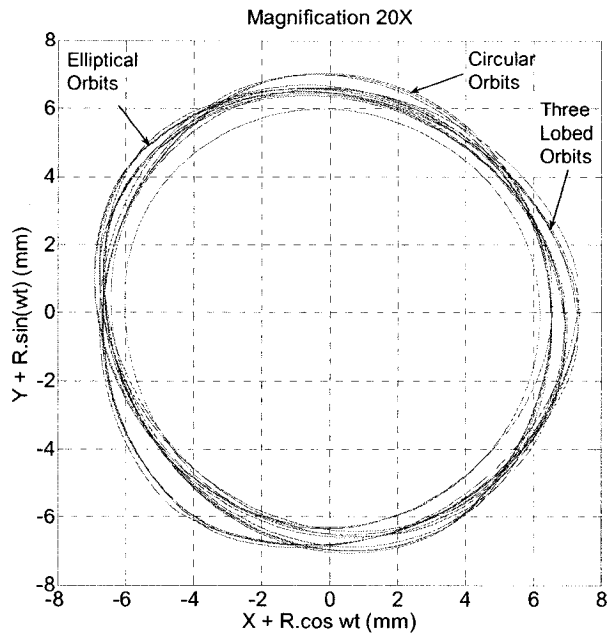

Figure 4.84: Locus of Outermost Point of Cutting Lip (N = 14000 rpm)

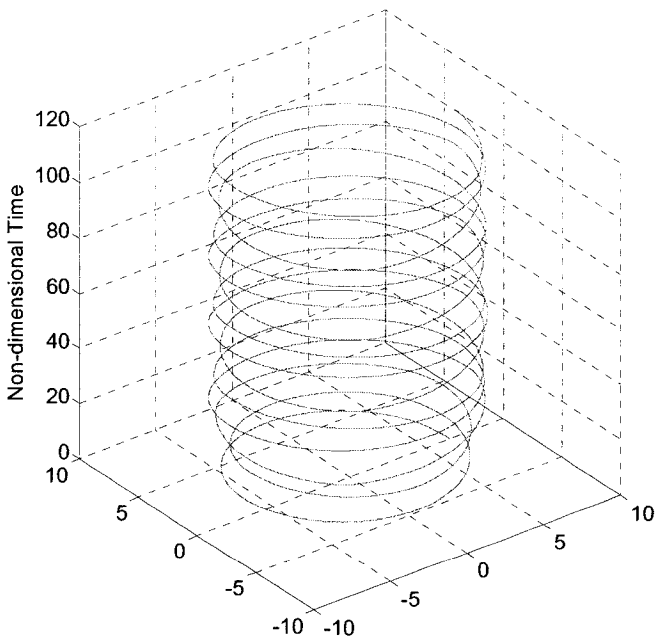

Figure 4.85: Locus of Outermost Point of Cutting Lip on Time Scale (N = 14000 rpm)

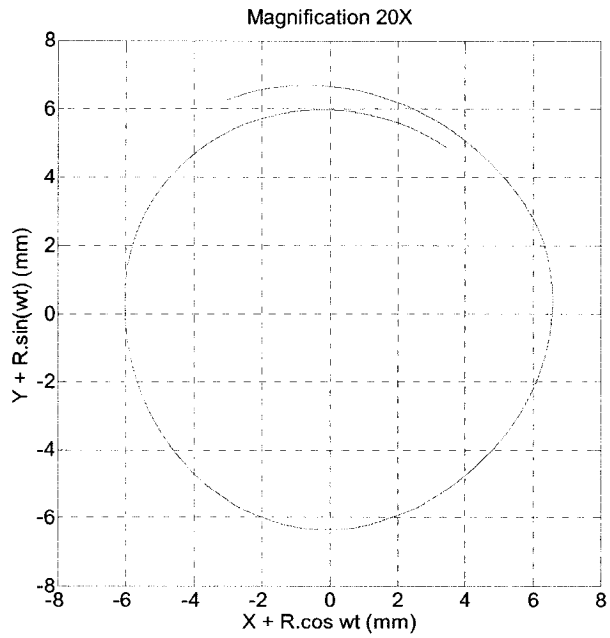

Figure 4.85.1: Circular Orbit (N = 14000 rpm, τ = 10-20)

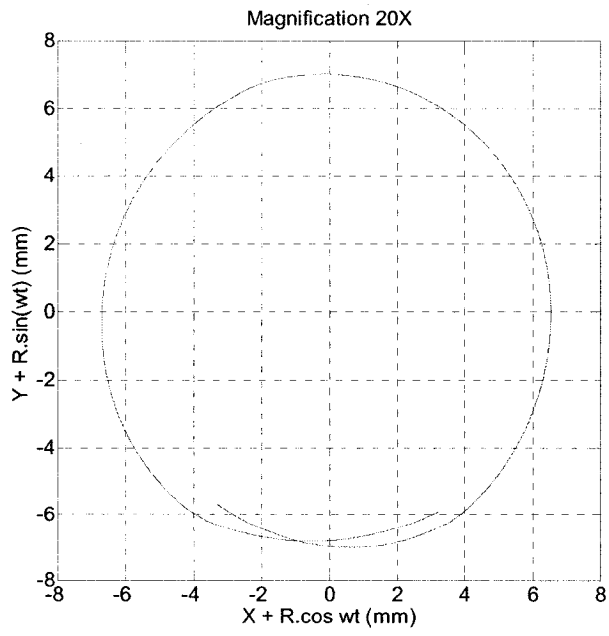

Figure 4.85.2: Circular Orbit (N = 14000 rpm, τ = 40-50)

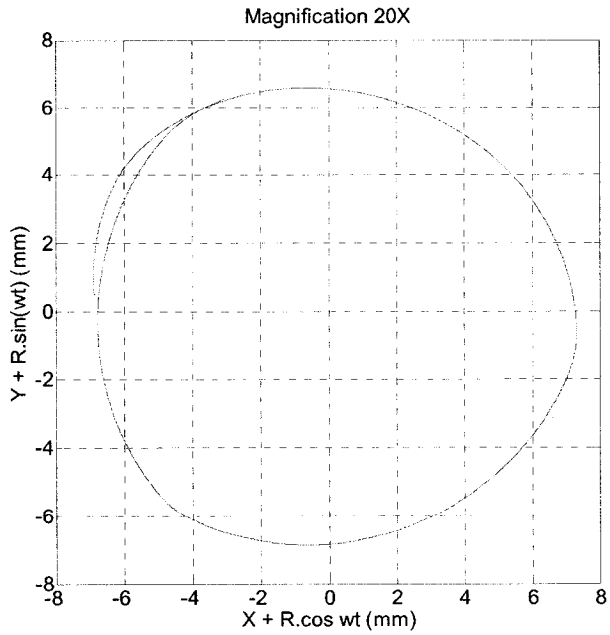

Figure 4.85.3: Three Lobed Orbit (N = 14000 rpm, τ = 20-30)

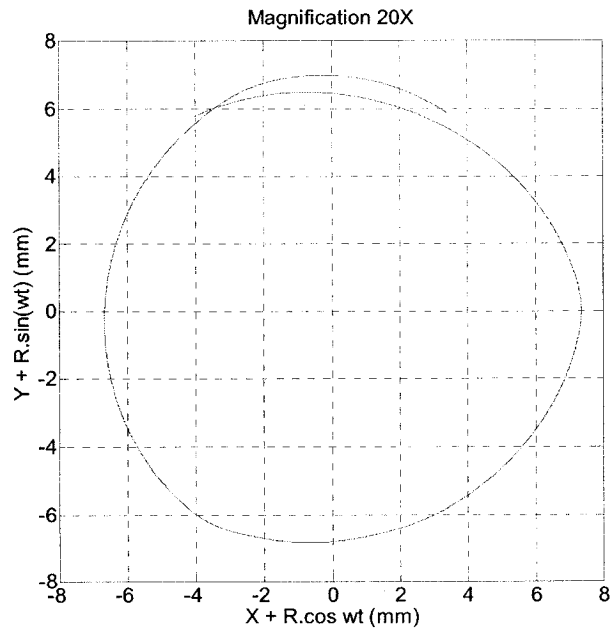

Figure 4.85.4: Three Lobed Orbit (N = 14000 rpm, τ = 70-80)

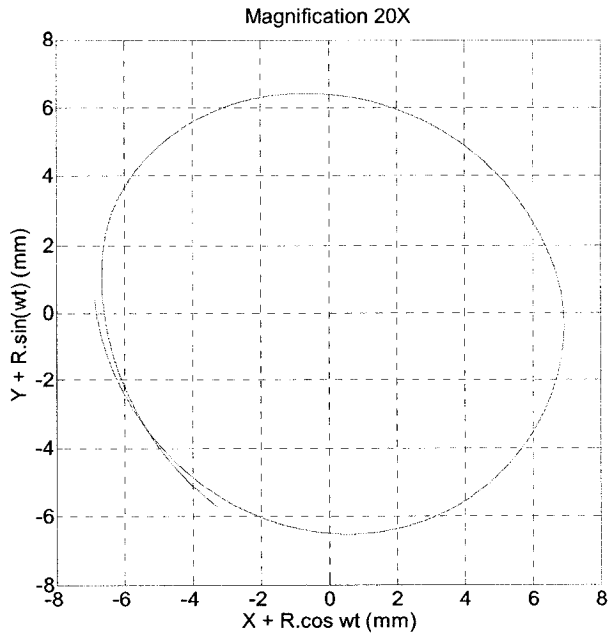

Figure 4.85.5: Elliptical Orbit (N = 14000 rpm, τ = 30-40)

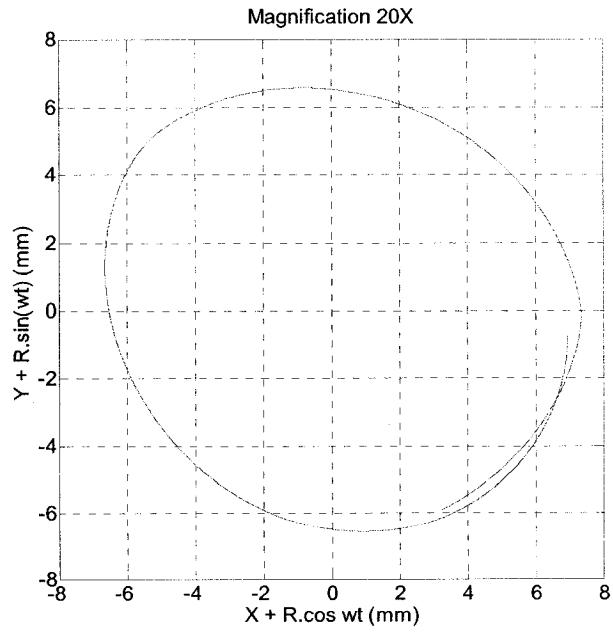

Figure 4.85.6: Elliptical Orbit (N = 14000 rpm, τ = 50-60)

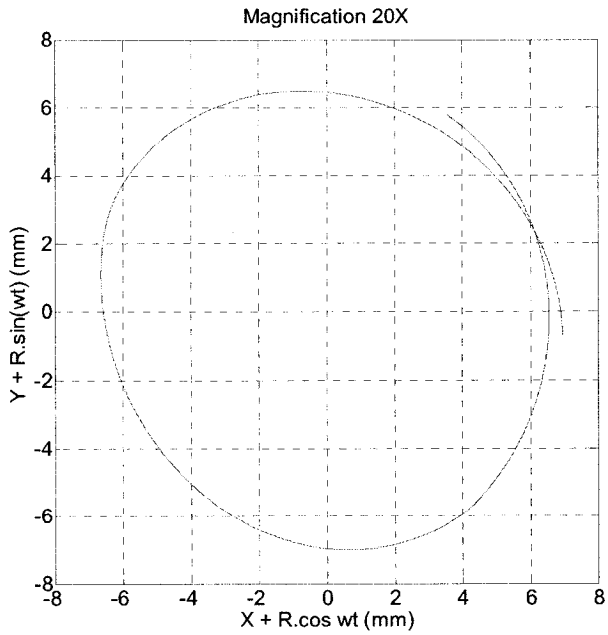

Figure 4.85.7: Elliptical Orbit (N = 14000 rpm, τ = 60-70)

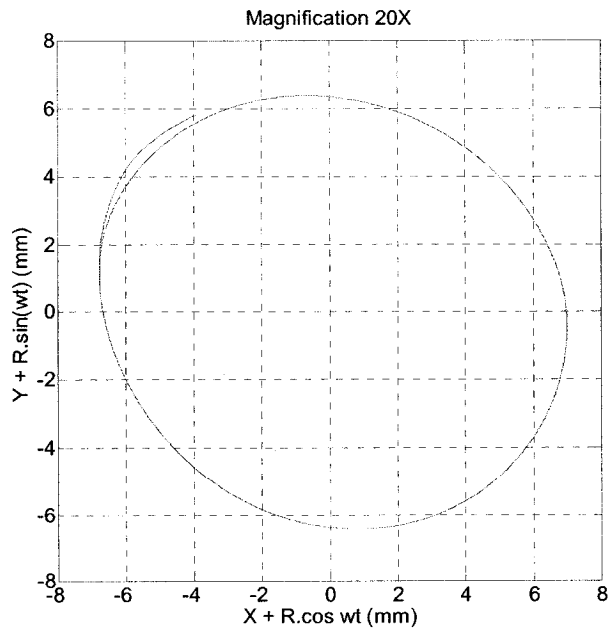

Figure 4.85.8: Elliptical Orbit (N = 14000 rpm, τ = 80-90)

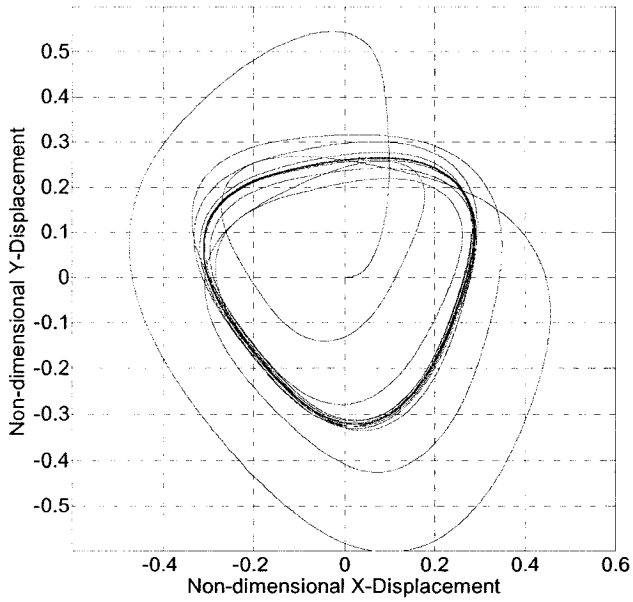

Figure 4.86: Trajectory of Drill Centerline (N = 18000 rpm)

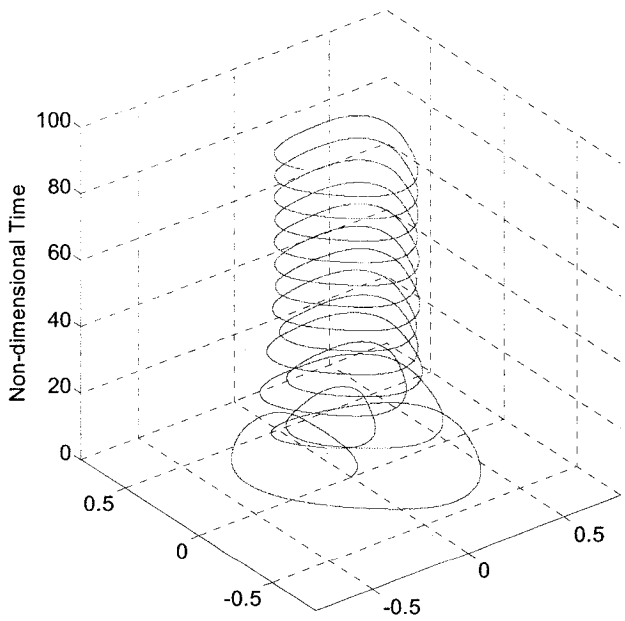

Figure 4.87: Trajectory of Drill Centerline on Time Scale (N = 18000 rpm)

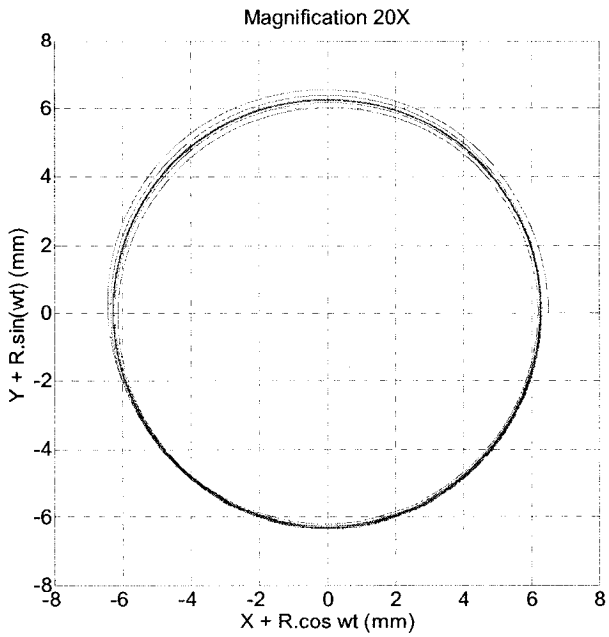

Figure 4.88: Locus of Outermost Point of Cutting Lip (N = 18000 rpm)

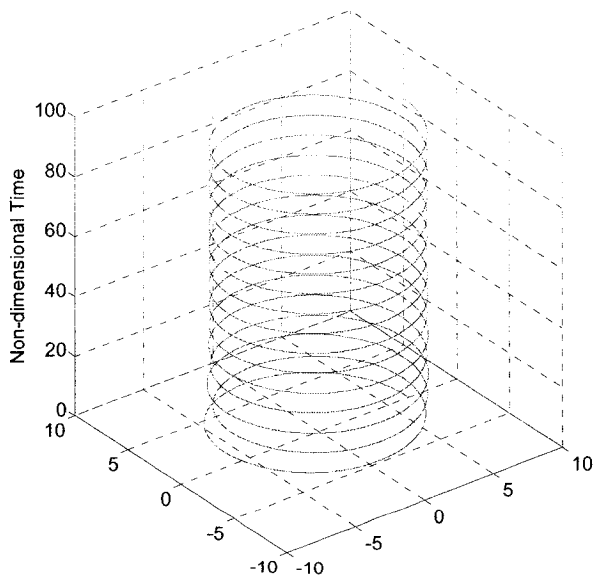

Figure 4.89: Locus of Outermost Point of Cutting Lip on Time Scale (N = 18000 rpm)

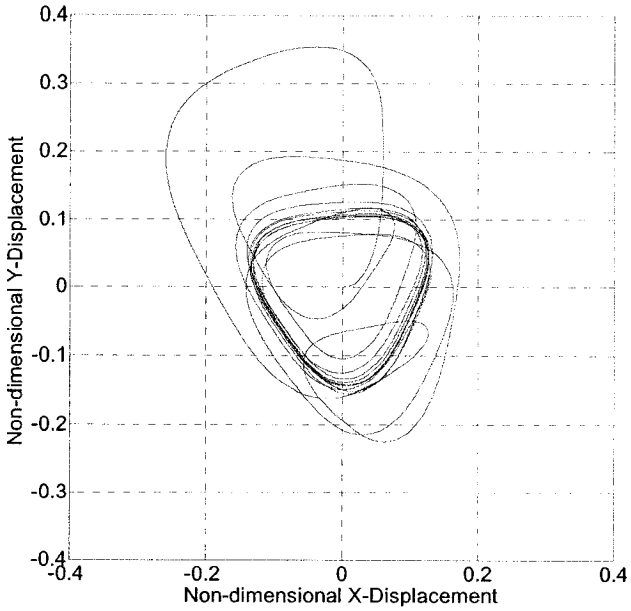

Figure 4.90: Trajectory of Drill Centerline (N = 18000 rpm)

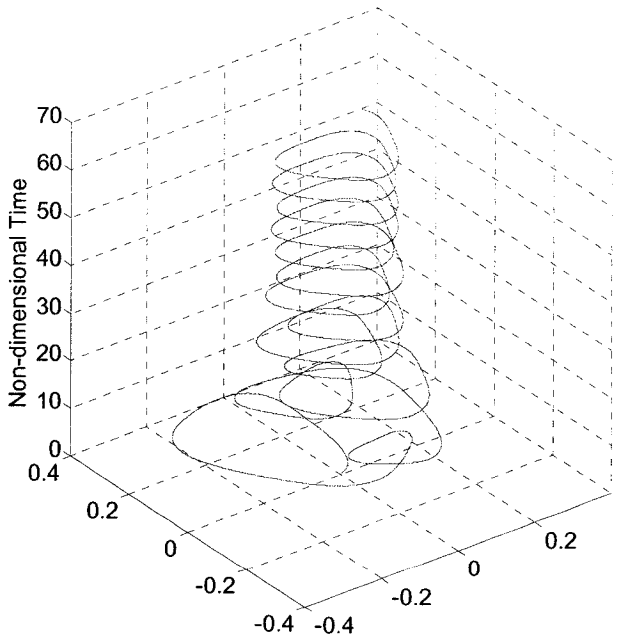

Figure 4.91: Trajectory of Drill Centerline on Time Scale (N = 25000 rpm)

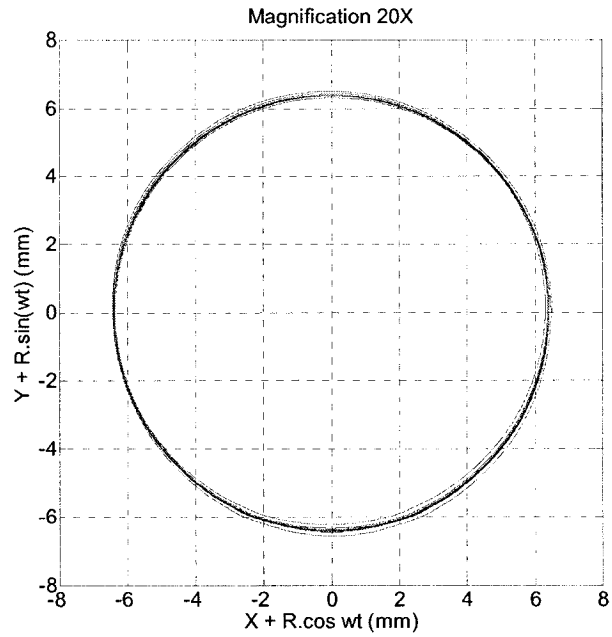

Figure 4.92: Locus of Outermost Point of Cutting Lip (N = 25000 rpm)

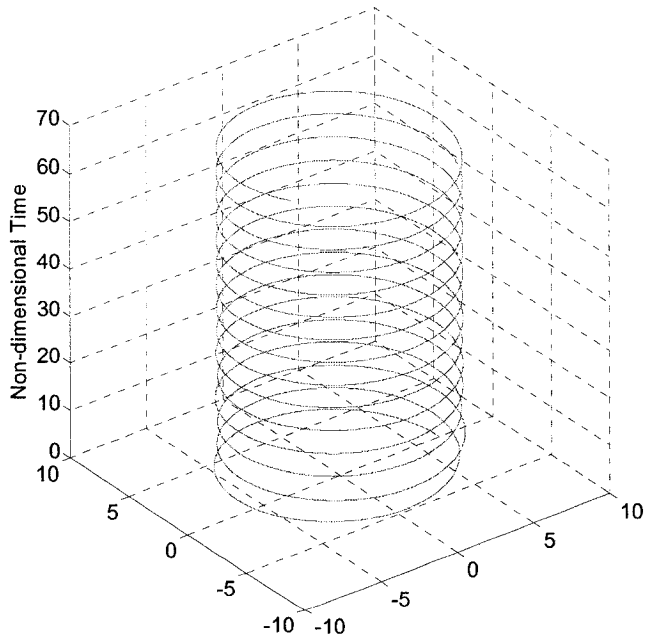

Figure 4.93: Locus of Outermost Point of Cutting Lip on Time Scale (N = 25000 rpm)

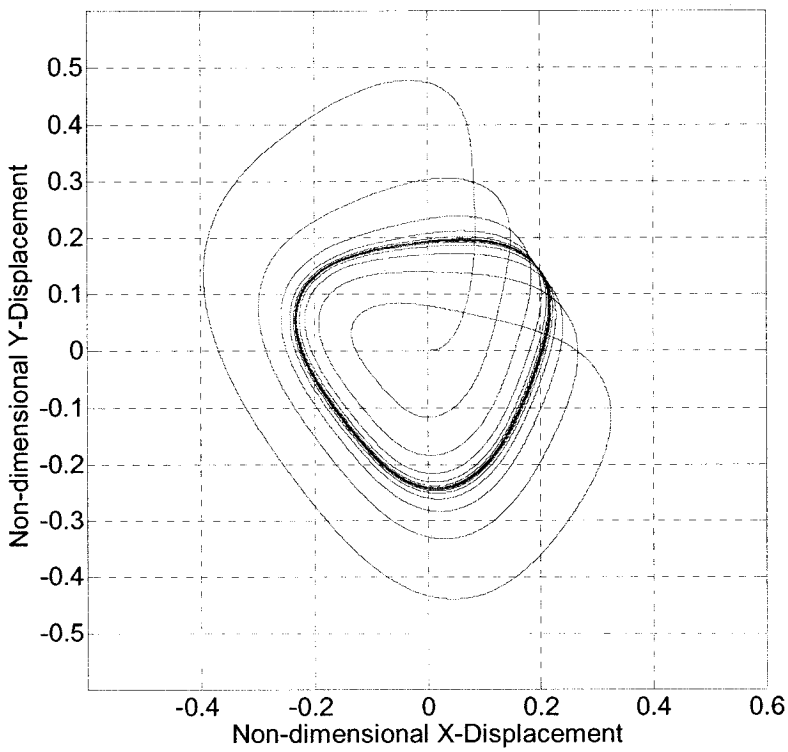

Figure 4.94: Trajectory of Drill Centerline (N = 20000 rpm)

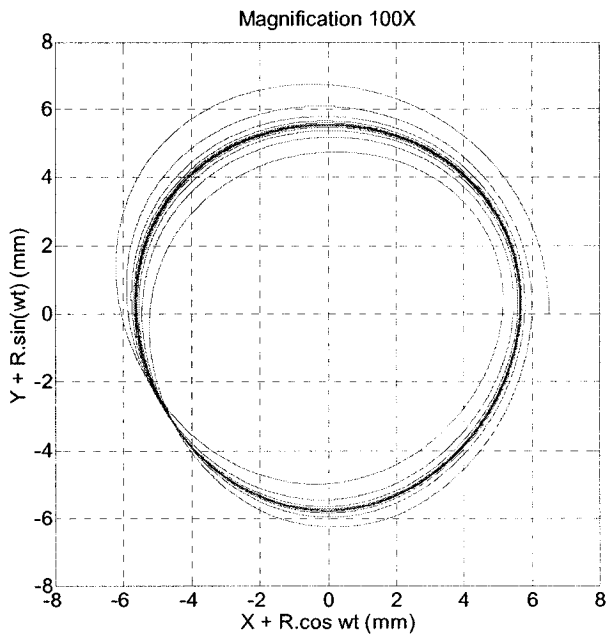

Figure 4.95: Locus of Outermost Point of Cutting Lip (N = 20000 rpm)

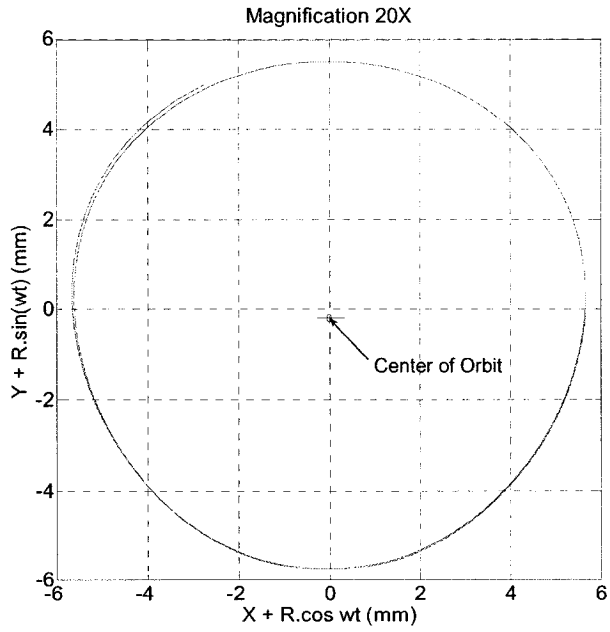

Figure 4.96: Three-Lobed Orbit (N = 20000 rpm, τ = 50-60)

4.6.6.3 Observations - 4

Simulations results (Figures 4.74-4.79) shown above demonstrate formation of elliptical holes or lobed hole profiles close to circular shape as a result of combined effect of rotational speed, force imbalance and amplitude modulation factor.

Higher speeds are found to be highly influential and result in smooth hole profiles more or less elliptical in shape. Effect of increase in rotational speed is evident in the trajectories of drill centerline (Figures 4.80, 4.83, 4.86, and 4.90) and predicted hole profiles (Figures 4.81, 4.82, 4.84, 4.85, 4.88, 4.89, 4.92 and 4.93) shown above.

Moreover at rotational speeds higher than 10000 rpm the holes shapes are found to be of different shapes at different depths as seen in figures 4.81, 4.82, 4.84 and 4.85. Different shapes of orbits at different hole depths are also shown in figures 4.85.1 to 4.85.8. Shape of the drilled orbits are close to either circular, three lobed or elliptical shapes and is changed instantaneously as drill moves deeper and deeper.

In figures 4.82 and 4.85 it is observed that the size of drill orbit also changes instantaneously as drill moves deeper and deeper. The difference in the size of drill orbits at different times is easily noticed when we compare the orbits shown in figures 4.85.1 and 4.85.2 for different times.

In figures 4.86, 4.90 and 4.94 showing trajectories of drill centerline it is observed that center of the drill orbit change its location continuously along with time which can be

referred as Speed Induced Wandering. In figure 4.96 showing an drill orbit at certain time for rotational speed of 20000 rpm, shift of the center of orbit from drill's geometric center is seen clearly. This type of phenomenon leads to straightness error because of which the mating shaft will not pass through the hole even if both the shaft and drilled hole sizes are within required tolerance limits.

Thus rotational speed, force imbalance and amplitude modulation factor all together are responsible for drilling errors such as shape, size, straightness and surface finish errors, all of them being the primary measures for defining drilling accuracy.

4.6.7 Validation of Results – 2

In this section again the analytically or numerically predicted or experimentally obtained orbital plots found in past research work for twist drill are compared with the numerical results obtained by simulation of lumped mass model developed in section 4.4 above for the purpose of comparison and validation.

Figure 4.97 below shows experimental three lobed drill orbit found in research paper by Z. Katz et al. [14] for N = 710 rpm, D = 10 mm, L = 87 mm, b = 1.5 mm. Similar orbit is also shown in figure 4.61 above. These results can be compared with the predicted orbit (Figure 4.98) obtained by simulating lumped model developed in section 4.4 above for N = 1200 rpm, D = 13 mm, L = 96 mm and b = 2 mm.

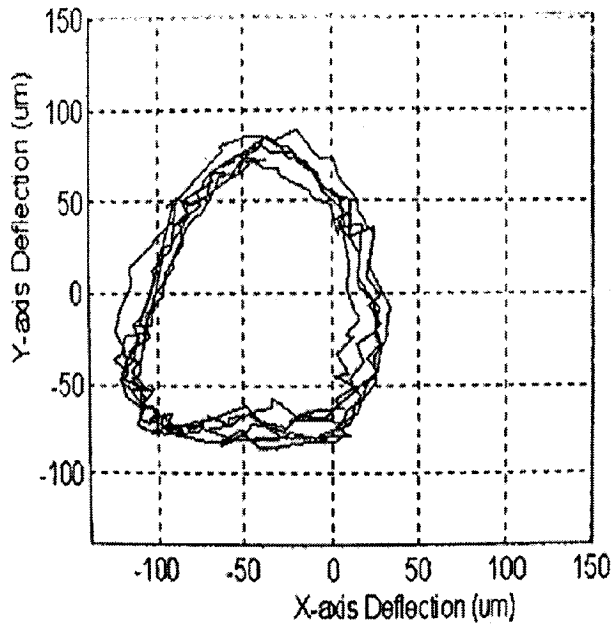

Figure 4.97: Experimental Three-Lobed Orbit [9]

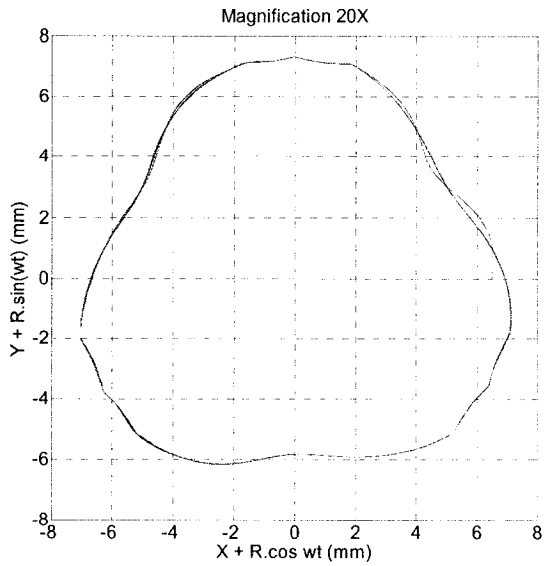

Figure 4.98: Experimental Three-Lobed Orbit [9]

Figure 4.99 below shows experimental elliptical drill orbit obtained by A. C. Wijeyewickrema et al. [9] for N = 710 rpm, D = 9.525 mm, L = 101.6 mm.

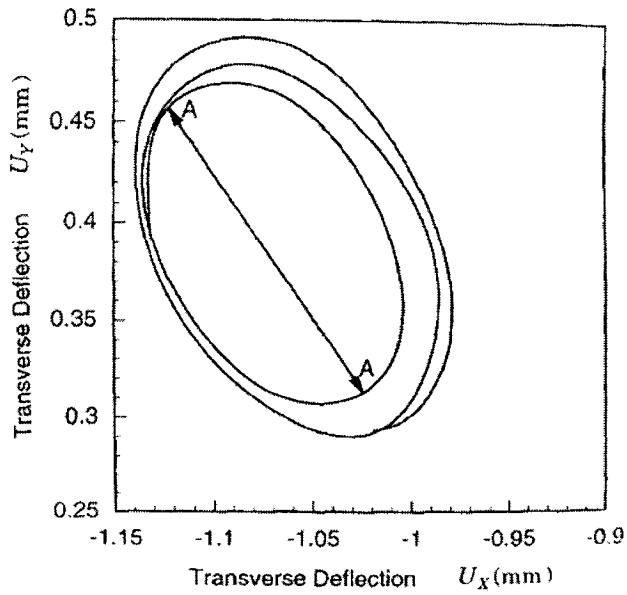

Figure 4.99: Experimental Elliptical Orbit [9]

Predicted drill orbits (Figure 4.100) for harmonic imbalance force obtained using finite element methods as presented by A. C. Wijeyewickrema et al. [9] for N = 10000 rpm, D = 9.525 mm, L = 101.6 mm are in close agreement with our numerically predicted drill orbits for similar harmonic force imbalance and N = 14000 rpm (Figures 4.84-4.85.8).

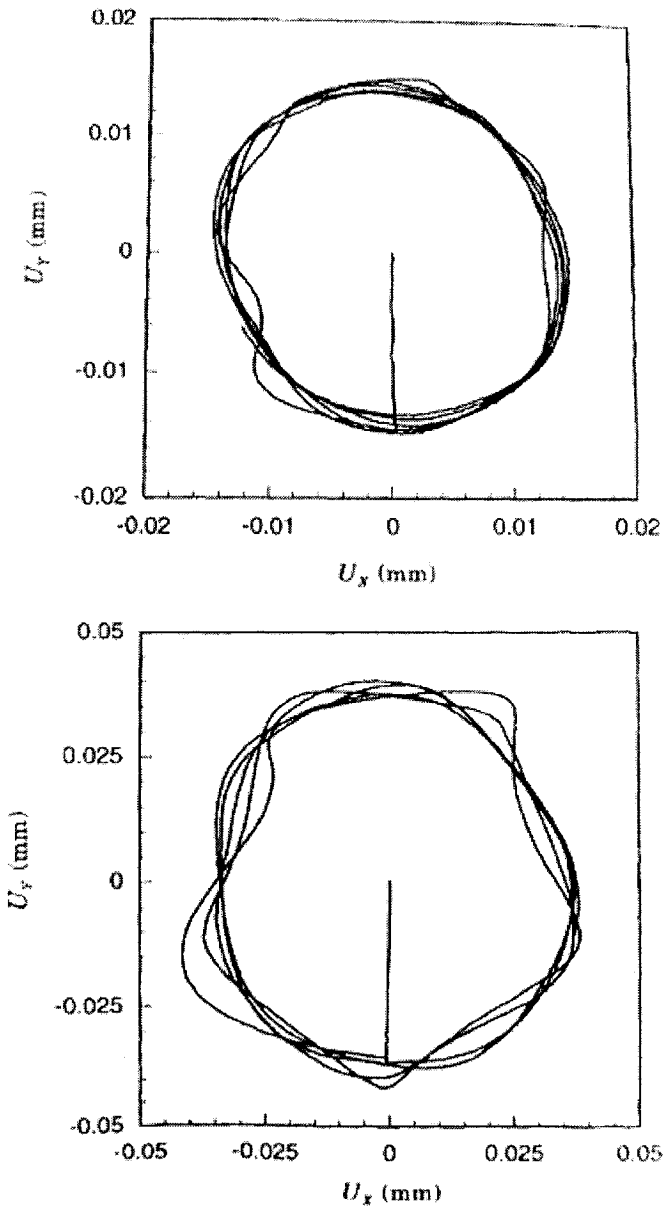

Figure 4.100: Drill Orbits Predicted using Finite Element [9]

Nature of imbalance cutting force decides the shape of drill orbit. Predicted orbits (Figure 4.101) presented by A. C. Wijeyewickrema et al. [9] for experimentally prescribed imbalance force and N = 10000 rpm, D = 9.525 mm, L = 101.6 mm follow the same pattern observed for imbalance force.

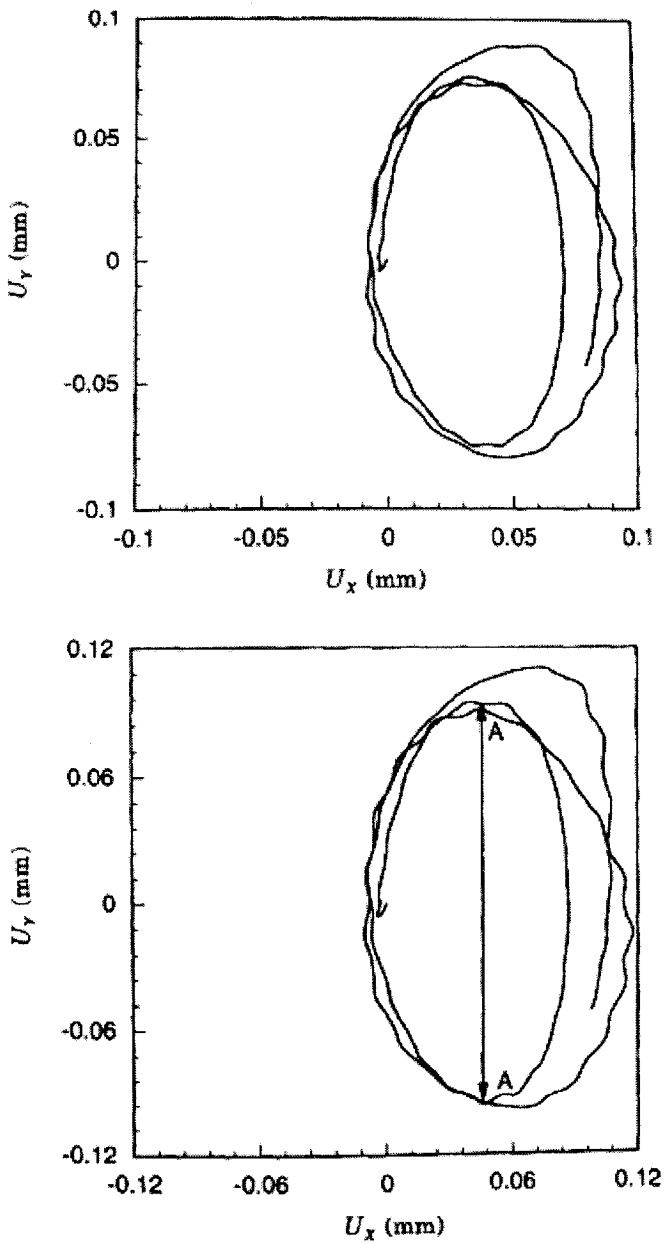

Figure 4.101: Experimental Elliptical Orbit [9]

4.7 Summary

In the present chapter discrete model to study orbital dynamics of twist drill is presented and the simulation results obtained by numerically solving the model in Matlab are analyzed and contribution of different parameters in different kinds drilling inaccuracies like size error, shape error, straightness error, surface roughness are explained.

In the next chapter torsional stiffness of drills of different sizes in the direction of cutting torque and opposite direction are measured experimentally and compared for variations.

CHAPTER 5

EXPERIMENTAL INVESTIGATION OF TORSIONAL STIFFNESS SYMMETRY OF TWIST DRILLS

5.1 Introduction

In the previous chapter discrete model considering the effect of drill work-piece interaction is presented and orbital dynamics of twist drill is discussed in relation to the influence of various parameters on different drilling errors.

The orbital dynamics in the last chapter considered only the transverse bending vibration of the twist drill. However, the cutting loads will apply a time varying torque on the drill and will cause torsional vibrations also. Since the cutting loads introduce both transverse and torsional vibrations the two types of vibrations are coupled in nature.

This chapter describes the experimental investigations of the effect of twisted nature of the twist drill on its torsional stiffness in the direction of cutting torque and in the opposite direction.

5.2 Experimental Set-up

Initially drill of diameter 12.7 is subjected to torsion test in cutting direction on a Universal Testing Machine (UTM). Details of the test set-up on UTM i.e. mounting of fixtures and drill are shown in picture (Figure 5.1) below. UTM facilitates torsion test only in one direction. Hence new Test Fixture is designed to test the drills of diameters ranging between 8.0 – 20 mm. All the parts of the set-up are designed considering the maximum possible cutting torque (60.0 Nm) for highest size of drill to be tested.

Test Fixture has following parts,

Support plate: This is a flat rectangular plate of mild steel with machined bottom face and has arrangement to mount it on T-table with bolts.

Bearing Pillars: These are two mild steel strips welded on the top of support plate and carry two concentric in line holes to carry the aluminum sleeve type bearings. The sleeve bearings are press fitted into the holes in the pillars and their inside diameter accommodates a clearance fit for the cylindrical shank and fluted body of the drill. One of the pillars giving support to shank of drill has threaded holes. Bolts are tightened against the flat ground on the cylindrical shank of drill for arresting the rotation when torque is applied on the drill tip.

Torque arm: This is a mild steel strip with a hole machined on one end and arrangement to hang dead weights on other end. Again the hole carries the aluminum sleeve type

bearings. The sleeve bearings are press fitted into the holes in the pillars and inside has a clearance fit with fluted body of drill. The arm has threaded holes to fix two bolts one from top and the other from bottom which pass through threaded holes and bearing sleeves. When those bolts are tightened the hemispherical tips of the bolts rest inside the drill flutes and arrest the relative rotation between torque arm and drill tip when the torque is applied on the drill tip.

Details of the designed Test Fixture and drill mounted for actual test are shown in picture (Figure 5.2) below. At the time of test, the drill is supported by bearing pillars. Shank of the drill is fixed by tightening the bolts and the torque arm is mounted on drill tip in horizontal direction. Then overhanging side of arm is loaded with dead weights progressively starting with very small weight, and the downward deflection of the arm is noted down every time. Torque is exerted on drill tip and drill gets twisted and arm makes angular motion. A micron dial indicator is used to measure the vertical movement of arm. Angular twist is calculated by dividing the downward displacements by effective length of the arm. Torque is calculated by product of gravitational force corresponding to dead weight and effective length of the arm.

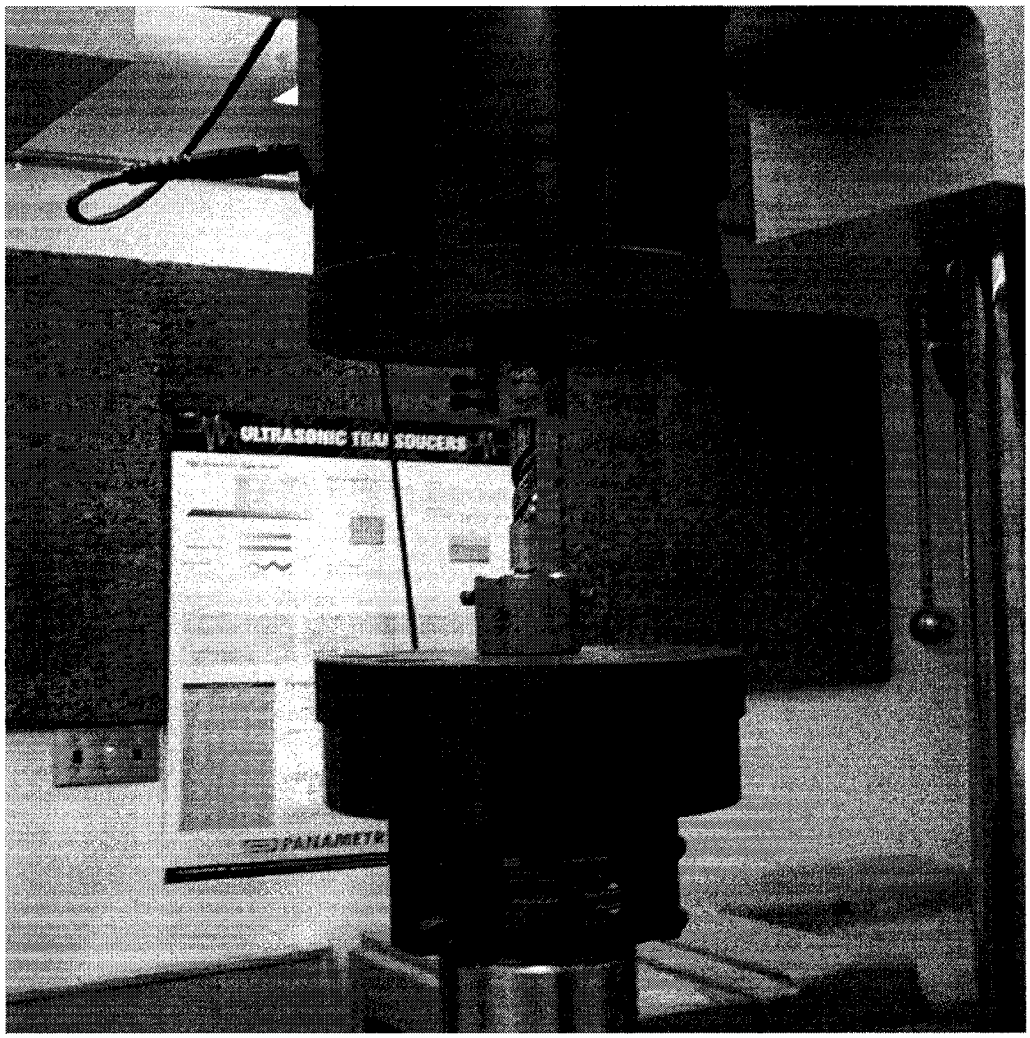

Figure 5.1: Torsion Test on UTM (D = 12.7 mm, Cutting Direction)

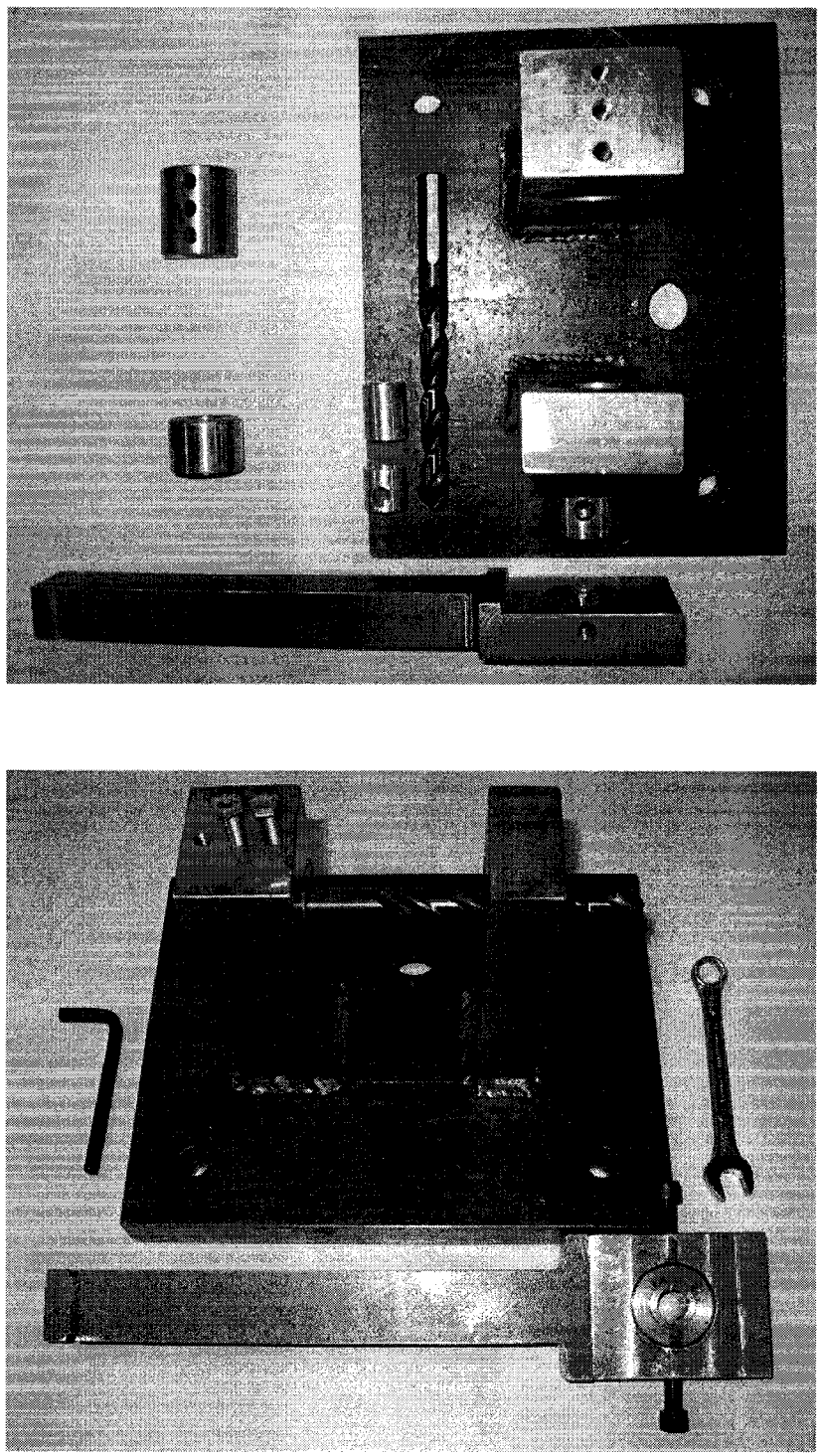

Figure 5.2: Torsion Test Fixture Components

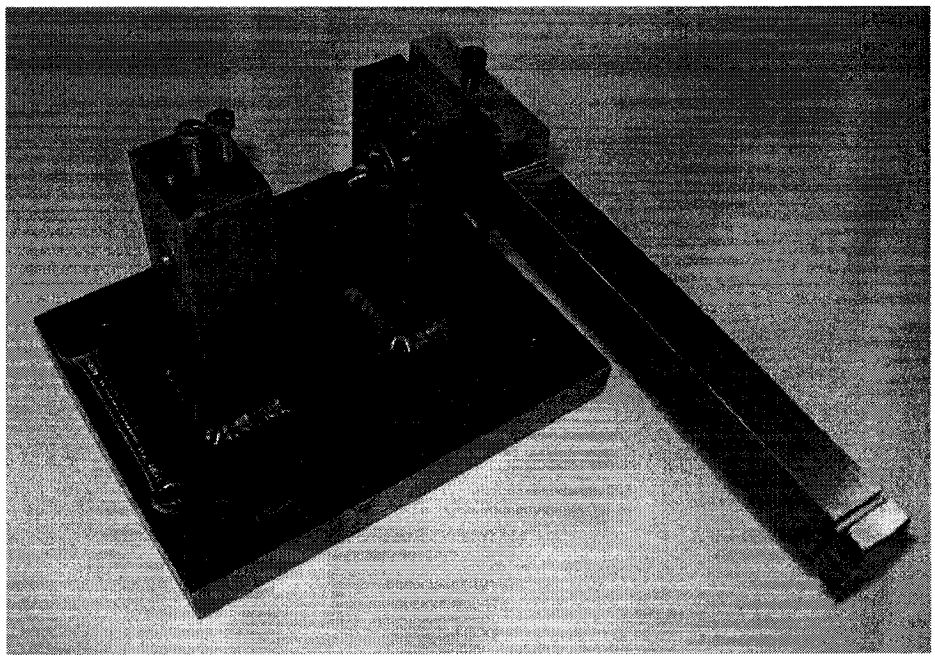

Figure 5.3: Test set –up for Torsion Test on Twist Drills

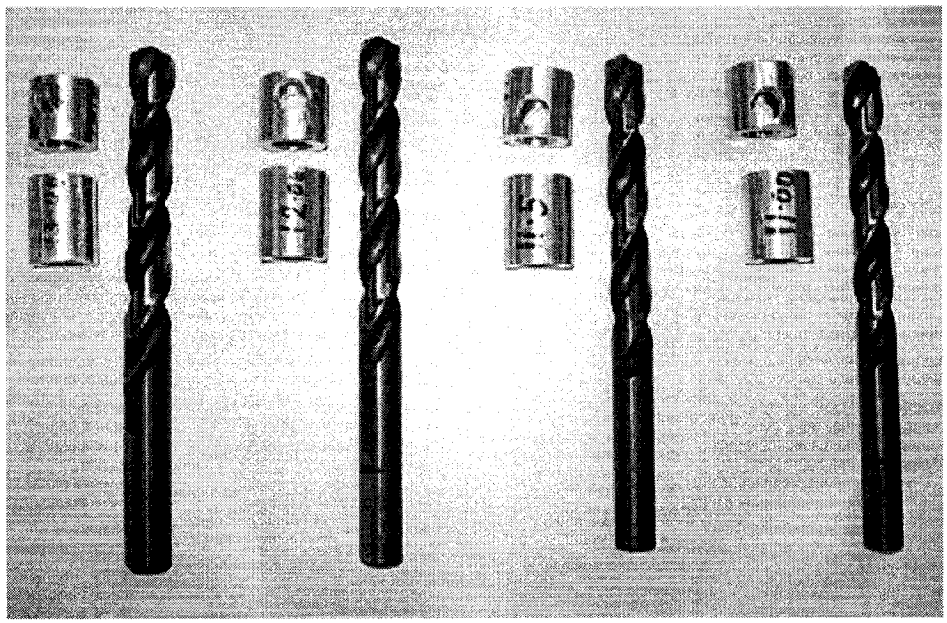

Figure 5.4: Twist Drills Tested on Torsion Test Fixture

5.2 Test Results and Conclusion

Tests are conducted for four different sized drills, 10.5 mm, 11.0 mm, 12.0 mm and 13.0 mm diameter. Two tests for each of the drills on in clockwise direction and other in anticlockwise direction are done. Test data is plotted in Microsoft Office Excel Corresponding plots of the Torque v/s Twist Angle and are shown in figures 5.3 to 5.10. The slopes of those plots give the torsional stiffness values. Following are the torsional stiffness values obtained from the experimental results.

For 10.5 mm drill

1] $K_t\ (10.5\ \text{mm}) = 2.7579 \times \frac{180}{\pi} = 158.016\ \frac{\text{Nm}}{\text{rad}}$ (Cutting Direction)

2] $K_t\ (10.5\ \text{mm}) = 2.8339 \times \frac{180}{\pi} = 162.372\ \frac{\text{Nm}}{\text{rad}}$ (Opposite Cutting Direction)

Equations 5.1

Difference between two stiffness values is + 2.76 %.

For 11.0 mm drill

1] $K_t(11.0\ \text{mm}) = 3.8205 \times \frac{180}{\pi} = 218.899\ \frac{\text{Nm}}{\text{rad}}$ (Cutting Direction)

2] $K_t\ (11.0\ \text{mm}) = 3.8439 \times \frac{180}{\pi} = 220.239\ \frac{\text{Nm}}{\text{rad}}$ (Opposite Cutting Direction)

Equations 5.2

Difference between two stiffness values is + 0.61 %.

For 12.0 mm drill

1] $K_t\ (12.0\ mm) = 4.3138 \times \frac{180}{\pi} = 247.163 \frac{Nm}{rad}$ (Cutting Direction)

2] $K_t\ (12.0\ mm) = 4.3428 \times \frac{180}{\pi} = 248.824 \frac{Nm}{rad}$ (Opposite Cutting Direction)

Equations 5.3

Difference between two stiffness values is + 0.67 %.

For 13.0 mm drill

1] $K_t\ (13.0\ mm) = 5.6992 \times \frac{180}{\pi} = 326.540 \frac{Nm}{rad}$ (Cutting Direction)

2] $K_t\ (13.0\ mm) = 5.5840 \times \frac{180}{\pi} = 319.940 \frac{Nm}{rad}$ (Opposite Cutting Direction)

Equations 5.4

Difference between two stiffness values is - 2.14 %.

From the above calculations it is clear that the value of the torsional stiffness in clockwise twisting and anticlockwise twisting does not differ much, the difference being within + 2.67 % to – 2.14 %.

It can be concluded that the small difference in values of stiffness in two directions is because of either manual reading errors or calibration error of dial indicator used. Thus experimental results validate the symmetry in torsional stiffness of the twist drills.

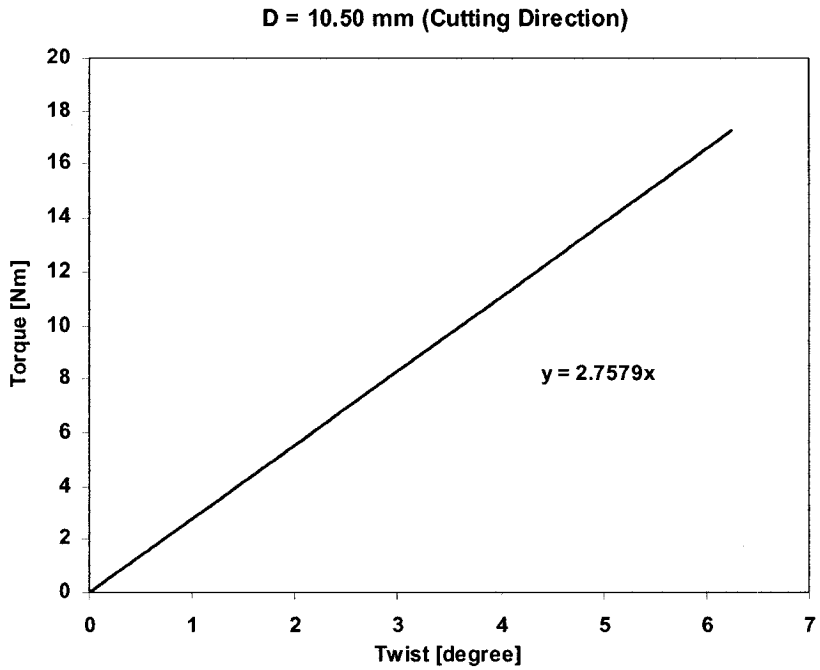

Figure 5.5: Plot of Torque v/s Twist Angle (D = 10.5 mm, Cutting Direction)

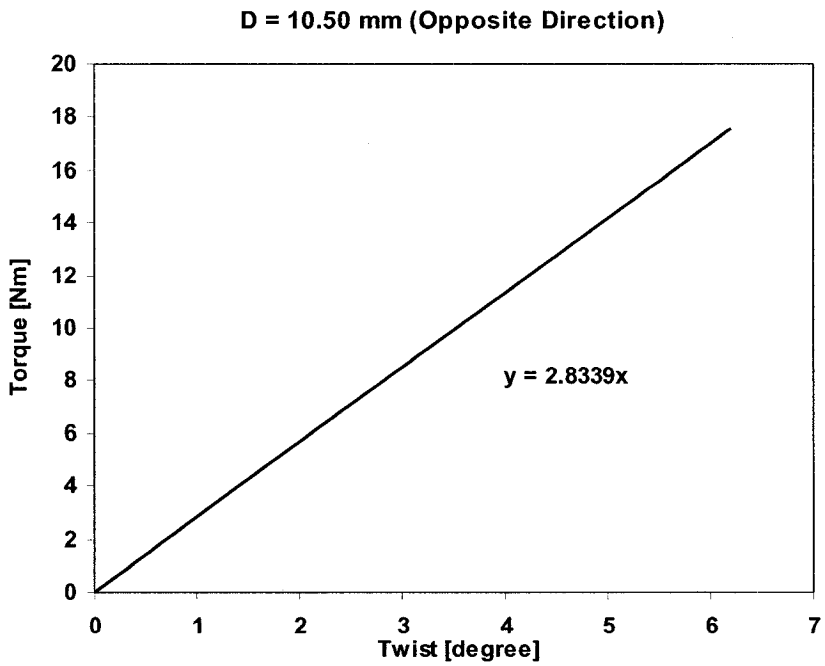

Figure 5.6: Plot of Torque v/s Twist Angle (D = 10.5 mm, Opposite Cutting Direction)

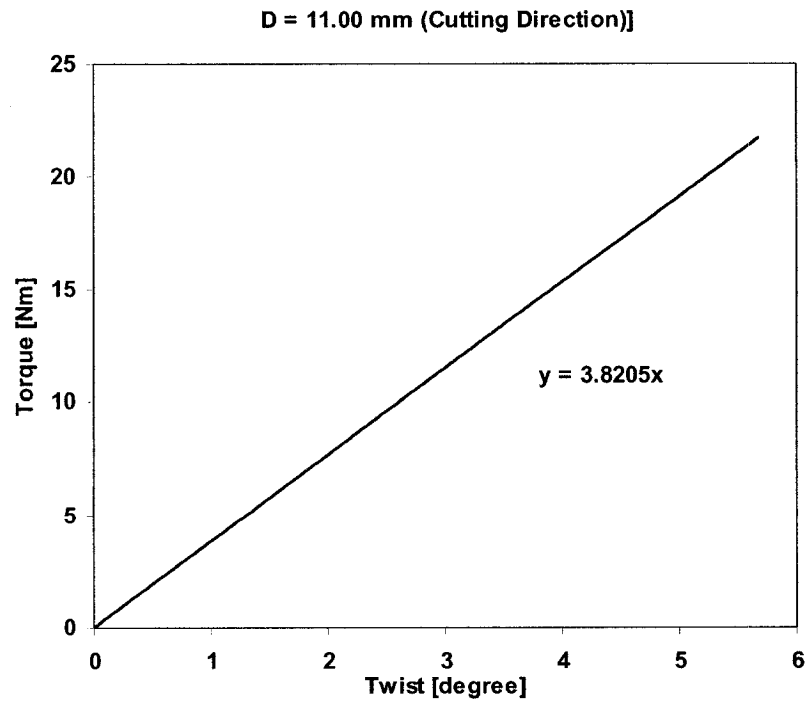

Figure 5.7: Plot of Torque v/s Twist Angle (D = 11.0 mm, Cutting Direction)

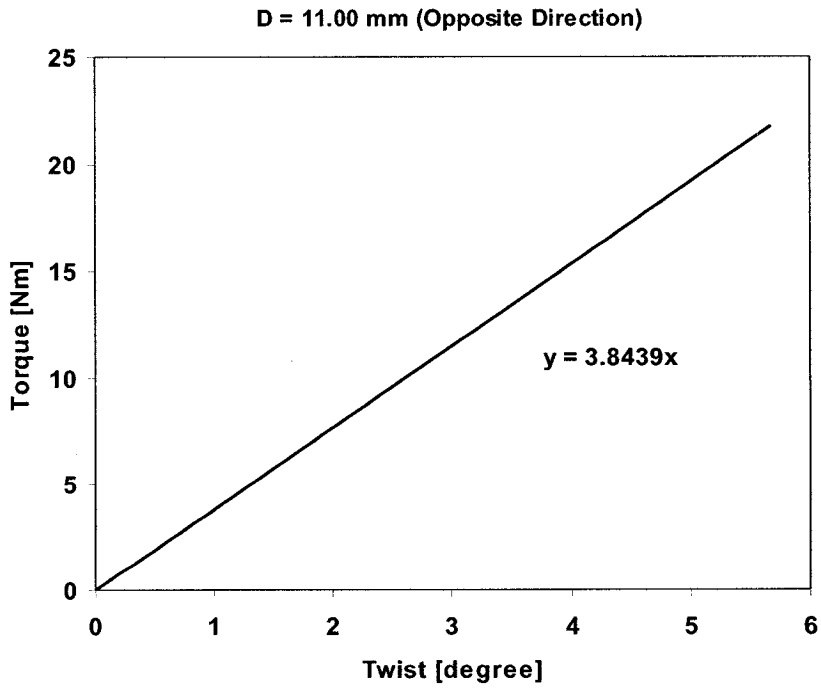

Figure 5.8: Plot of Torque v/s Twist Angle (D = 11.0 mm, Opposite Cutting Direction)

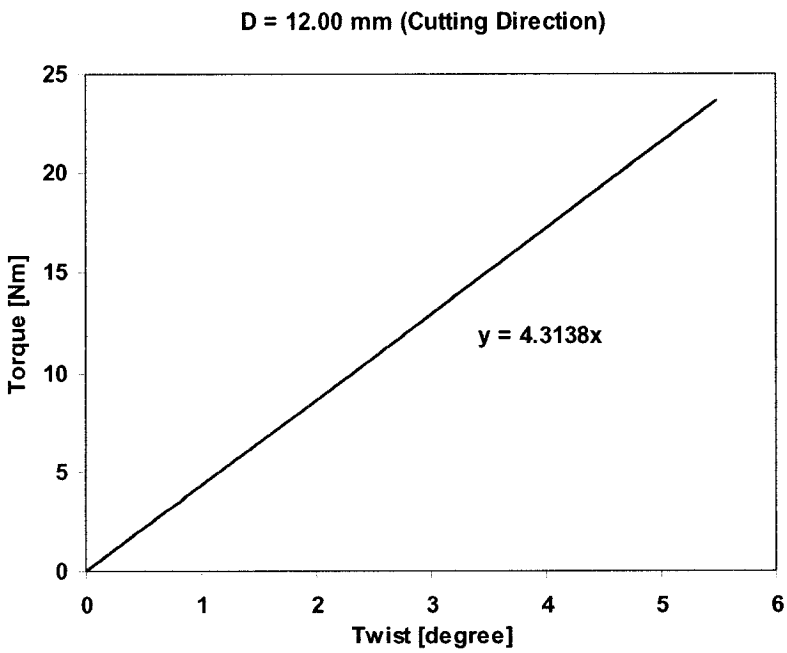

Figure 5.9: Plot of Torque v/s Twist Angle (D =12.0 mm, Cutting Direction)

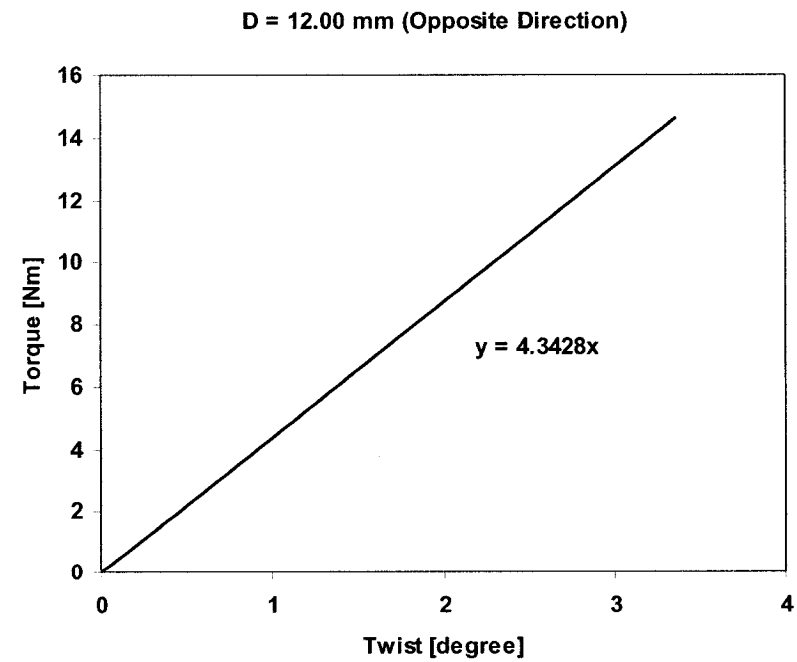

Figure 5.10: Plot of Torque v/s Twist Angle (D =12.0 mm, Opposite Cutting Direction)

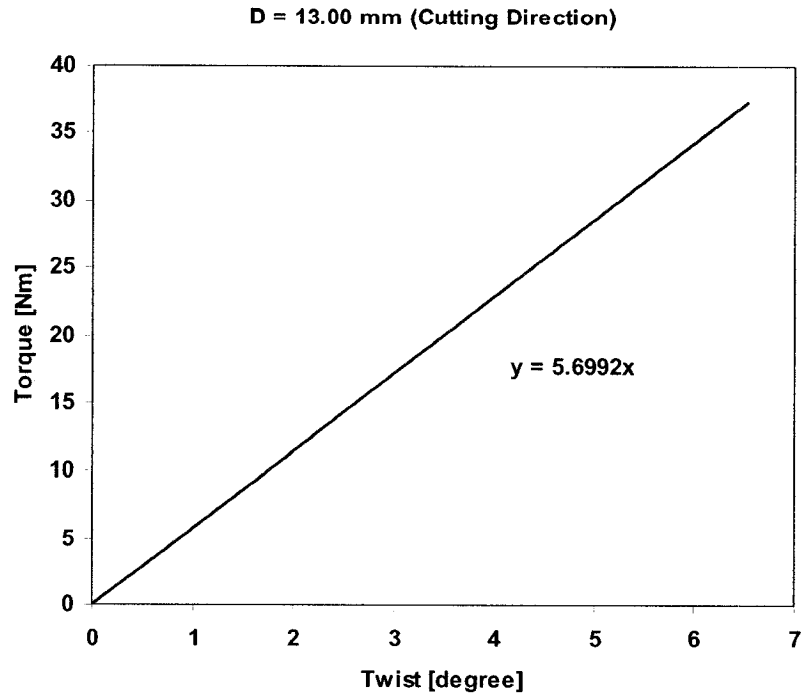

Figure 5.11: Plot of Torque v/s Twist Angle (D=13.0 mm, Cutting Direction)

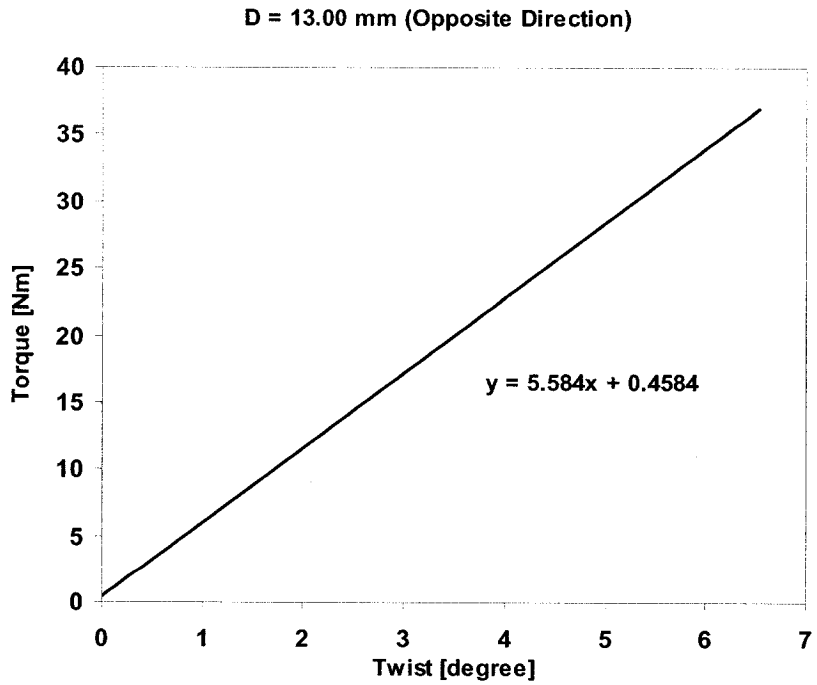

Figure 5.12: Plot of Torque v/s Twist Angle (D = 13.0 mm, Opposite Cutting Direction)

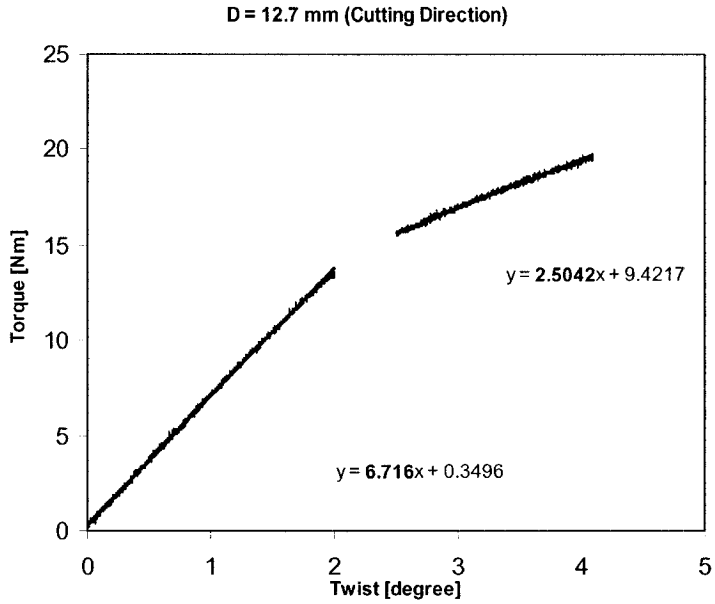

Figure 5.13: Plot of Torque v/s Twist Angle

(UTM Test, D = 12.7 mm, Cutting Direction)

5.4 Summary

In the present chapter torsional stiffness of drills of different sizes in the direction of cutting torque and opposite direction are measured experimentally and compared for variations. The difference in stiffness in the cutting direction and opposite direction is found to be within + 2.67 % to – 2.14 %, for four different size drills and assumed to be negligible.

In the next chapter discrete model is presented to study the effect of time dependent cyclic variations of the torsional stiffness of twist drill due to the cutting resistance appearing when twist direction coincide with cutting direction on torsional vibration behavior of twist drill. Another lumped mass model to study the Bending-Torsional Coupling is developed and analyzed to study its significance on torsional vibration of twist drill.

CHAPTER 6

LUMPED MASS MODEL - BENDING TORSIONAL COUPLING DYNAMICS OF TWIST DRILLS

6.1 Introduction

In previous chapter torsional stiffness variations of twist drill in cutting direction and the opposite were investigated experimentally. Twist drill is unique in itself among all types of cutting tools because of its fluted structure, which resembles the pre-twisted beams. Influence of this geometrical characteristic on static and dynamic behavior of twist drills is investigated in previous chapters.

In this chapter discrete torsional model is developed considering time dependent cyclic variations of the torsional stiffness of twist drill when cutting through the work-piece material. Such stiffness variations are caused by the addition of work stiffness in the cutting direction. Model is simulated in Matlab for harmonic torque imbalance and results are presented. Another lumped mass model to study the bending-torsional coupling is developed. Simulation results are analyzed and the influence of this coupling on torsional vibration of twist drill is investigated.

As discussed before the two cutting lips of drill cut in opposite directions as drill rotates, and the cutting forces acting on them form a couple and drill is twisted about its center

line as other end of the drill is fixed in the drive spindle. When drill is cutting through the material at uniform rate the mean cutting torque twists the drill by fixed amount which is called the initial displacement and the torque variations about the mean value of torque cause torsional vibrations.

Another important phenomenon is axial-torsional coupling. When drill is fed in the work tremendous thrust force acts at the tip of drill in upward direction. Because of the twisted geometry of the drill, the fluctuations in upward thrust lead to alternate twisting and untwisting of drill. Inversely the fluctuations in cutting torque also leads to twisting and untwisting of drill which alternately increases or decreases the length of drill affecting the instantaneous feed rates.

The concept of work stiffness was discussed in section 4.3 of chapter 4. The lateral displacement of drill tip when in contact with work-piece is accompanied by an angular twist and an increase in drill stiffness. The overall movement of the drill tip is represented as combination of linear displacement of drill tip center 'S' and angular displacement 'ψ'. Twisting of drill because of the lateral displacement of drill tip results in bending-torsion coupling.

From this discussion it is clear that the torsional vibration analysis is very important as is lateral vibration analysis in understanding the reasons for drilling inaccuracies. Following sections discuss effect of nonlinearities in torsional stiffness and bending torsional coupling on torsional response of twist drill.

6.2 Nonlinear Torsional Stiffness Models

As explained above in section 6.1, when twist direction of vibrating drill coincide the cutting direction, the rate of cutting increases momentarily with corresponding increase in cutting resistance. Consequently, the torsional stiffness of the drill increases.

In presence of the additional cutting resistance the resulting drill twist is less than that under free end condition without the cutting load. Thus it is clear that during drilling through the work-piece material the torsional stiffness of drill in cutting direction is different from that in the opposite direction and the torsional stiffness is essentially nonlinear.

The variations in the torsional stiffness can be represented by different simplified models as explained in following sections.

6.2.1 Bilinear Torsional Stiffness

When the direction of drill torsional vibration is opposite to the cutting direction the torsional behavior of the twist drill will be decided by torsional stiffness of drill alone. When the direction of drill torsional vibration coincide the cutting direction the drill twist will be smaller since the equivalent stiffness of the system, represented below (Figure 6.1), will be higher than the torsional stiffness of drill alone.

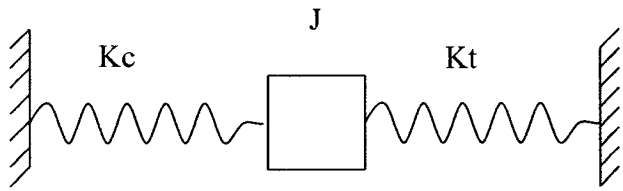

Figure 6.1: Schematic of Drill Torsional Stiffness in Cutting Direction

From equation 5.4, torsional stiffness for 13 mm drill is, $K_t = 326.540 \frac{Nm}{rad}$

Let the additional work stiffness due to cutting be, $K_c = 100.00 \frac{Nm}{rad}$

Equations 6.1

Let 'K_s' be the overall system stiffness at any time, K_{snc} be the system stiffness for the opposite cutting direction and K_{sc} be the system stiffness for cutting direction.

The overall system stiffness over the one complete cycle is given as follows,

$$K_s = K_{snc} = 326.54 \frac{Nm}{rad} \quad \text{for} \quad 0 < \theta \leq \pi$$

Equations 6.2

$$K_s = K_{sc} = 426.54 \frac{Nm}{rad} \quad \text{for} \quad \pi < \theta \leq 2\pi$$

Equations 6.3

The variation in system stiffness along time is shown in figure 6.2

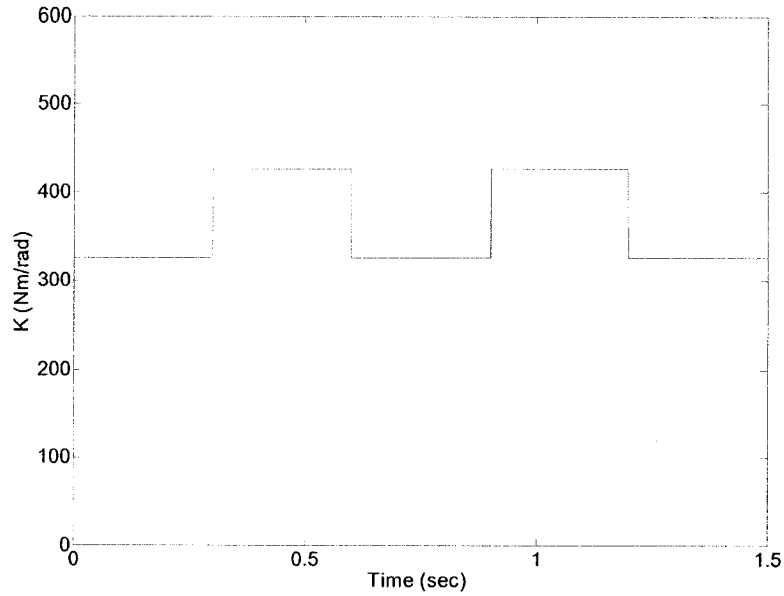

Figure 6.2: System Torsional Stiffness v/s Time (N = 100 rpm)

6.2.2 Combined Linear Sinusoidal Torsional Stiffness

Bi-Linear torsional stiffness model represents the nonlinearity in the system. In order to understand the behavior of the nonlinear system, the stiffness variation is assumed to be gradual instead of the sharp rectangular variations. The gradual increase in stiffness can be represented by a half-sinusoidal curve.

The torsional stiffness for 13 mm drill is, $K_t = 326.540 \frac{Nm}{rad}$

The additional stiffness due to cutting is taken as, $K_c = 100.00 \frac{Nm}{rad}$

Let 'K_s' be the overall system stiffness at any time, K_{snc} be the system stiffness for the opposite cutting direction and K_{sc} be the system stiffness for cutting direction.

The overall system stiffness over the one complete cycle are given as follows,

$$K_s = K_{snc} = 326.54 \frac{Nm}{rad} \qquad \text{for } 0 < \theta \leq \pi$$

Equations 6.4

$$K_s = K_{sc} = K_t + K_c \sin \omega t \qquad \text{for } \pi < \theta \leq 2\pi$$

$$= (326.54 + 100.00 \sin \omega t) \frac{Nm}{rad}$$

Equations 6.5

The variation in system stiffness along time is shown in figure 6.3 below

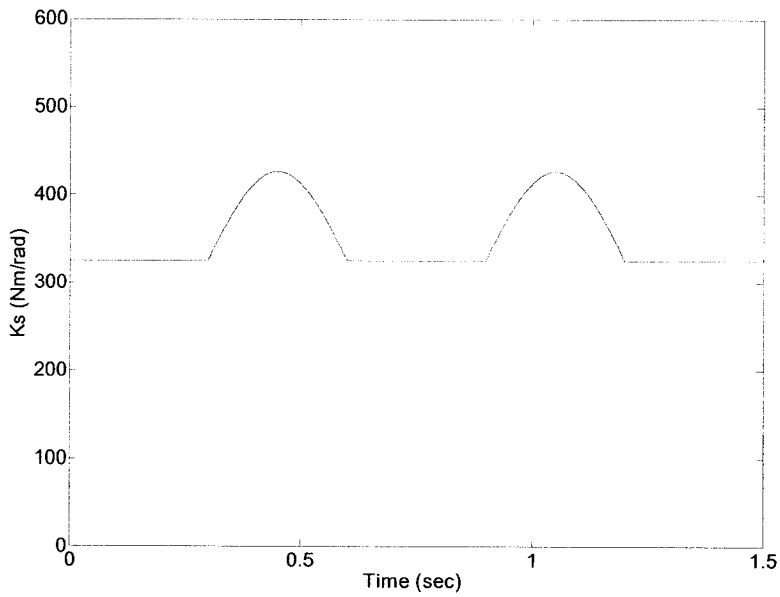

Figure 6.3: System Torsional Stiffness v/s Time (N = 100 rpm)

6.3 Discrete Model- Nonlinear Torsional Stiffness

Two different models representing nonlinear torsional stiffness are explained in sections 6.2.1 and 6.2.2 above. Equation of motion for Torsional Vibration of a drill based on these models can be written as follows,

$$J\ddot{\theta} + C_d\dot{\theta} + K_s\theta = T(1 - \lambda \sin\ \omega t) \qquad \textbf{Equation 6.6}$$

where,

$$K_s = K_{snc} \quad \text{for} \quad 0 < \theta \leq \pi$$

$$= K_t$$

$$K_s = K_{sc} \quad \text{for} \quad \pi < \theta \leq 2\pi$$

$$= K_t + K_c \sin \omega t$$

(As discussed in sections 6.2.2 above) **Equations 6.7**

and

J = Mass Moment of Inertia of twist drill,

C_d = Coefficient of Damping,

K_s = Non-Linear Torsional Stiffness of the system,

λ = Amplitude Modulation Factor as described in chapter 4,

T = Torque Amplitude

6.4 Simulation Results 1

Discrete Torsional model developed above considering the nonlinearity in Torsional stiffness is simulated in Matlab and results are presented. Deflection time plots for constant linear stiffness are also presented for comparison with results of above model.

Two different sets of results are presented for different types of torque variations. Two different types of torque fluctuations Type A and Type B, used for simulation are shown in figures 6.4 and 6.5. For Type A the torque fluctuations about mean torque are higher and for Type B the torque fluctuations about mean torque are lower.

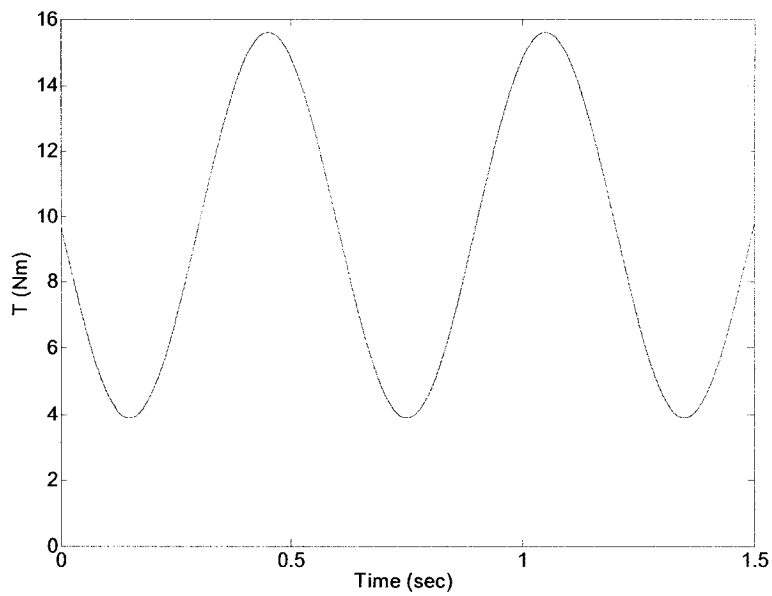

Figure 6.4: Torque v/s Time –Type A (N = 100 rpm)

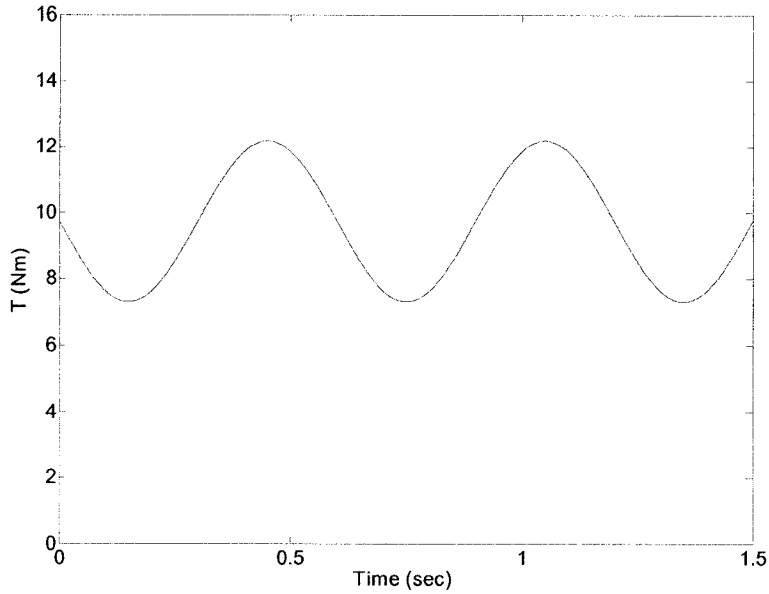

Figure 6.5: Torque v/s Time – Type B (N = 100 rpm)

Torsional responses for the two different types of input torques when system stiffness is constant and equal to torsional stiffness of drill ($K_s = K_t = 326.54 \frac{Nm}{rad}$), are shown in figures 6.6 and 6.8.

Torsional responses when system stiffness is nonlinear along time as explained in section 6.2.2 above for the two different types of input torques are shown in figures 6.7 and 6.9. Peaks in those plots are suppressed gradually because the stiffness increases gradually during second half of each cycle. Small amount of phase lag with respect to input torque seen in all these torsional responses is result of the viscous damping considered in the model.

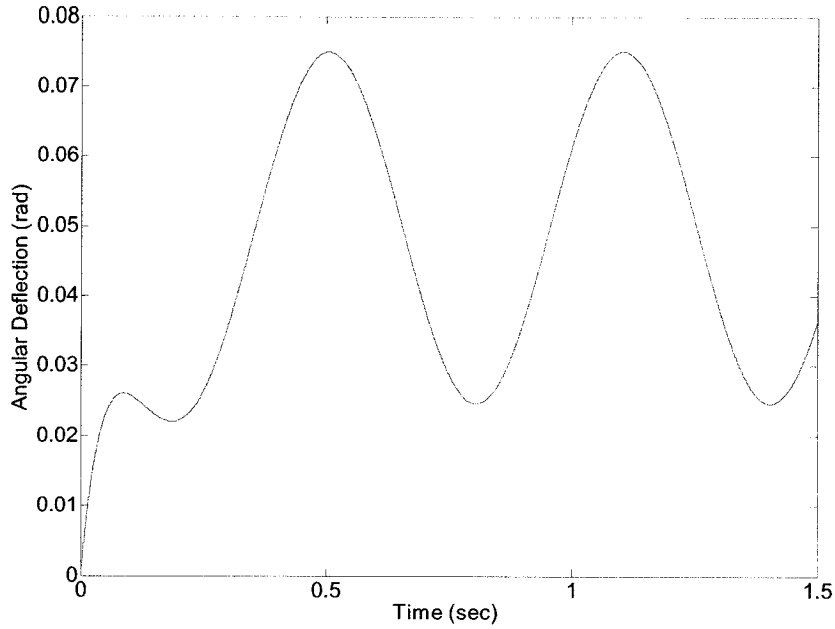

Figure 6.6: Angular Displacement v/s Time
(Torque Type A, Stiffness Linear, N = 100 rpm)

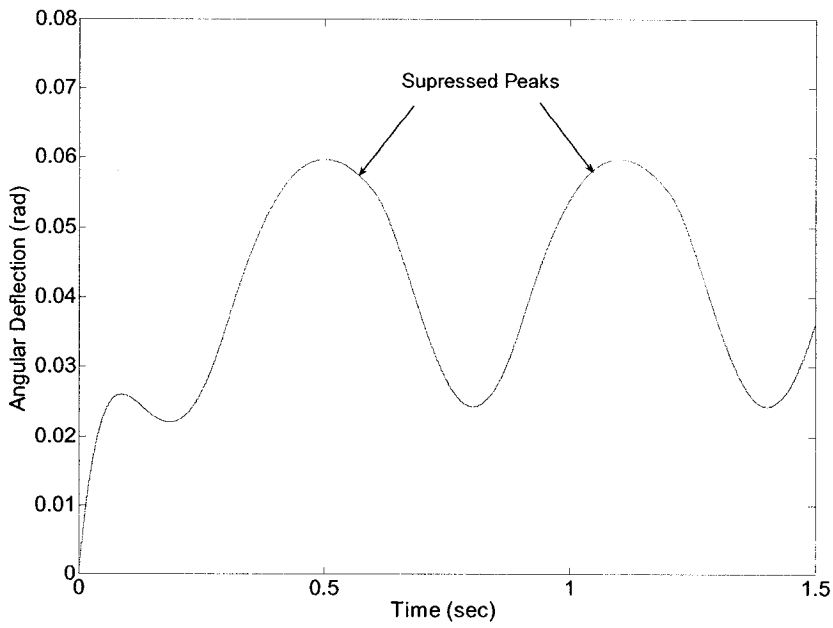

Figure 6.7: Angular Displacement v/s Time
(Torque Type A, Stiffness Non-Linear, N = 100 rpm)

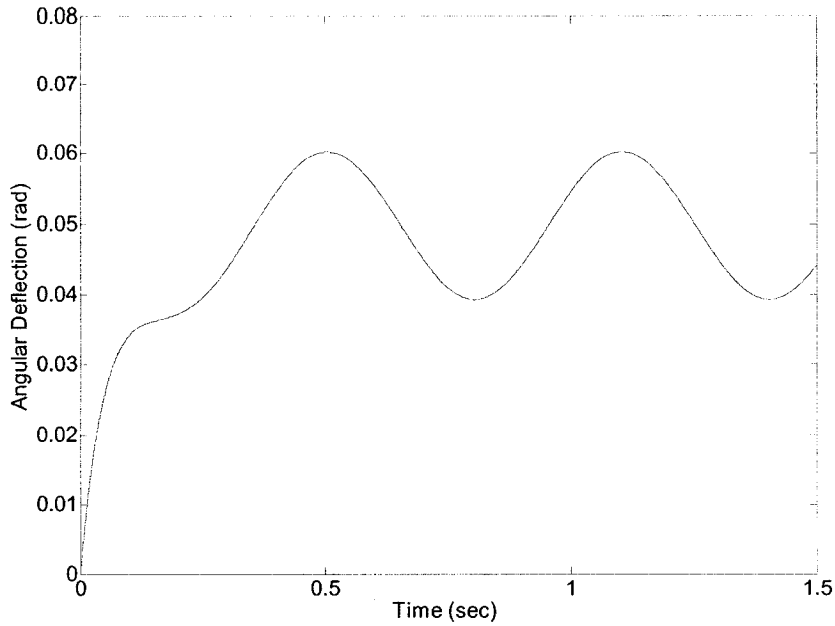

Figure 6.8: Angular Displacement v/s Time
(Torque Type B, Stiffness Linear, N = 100 rpm)

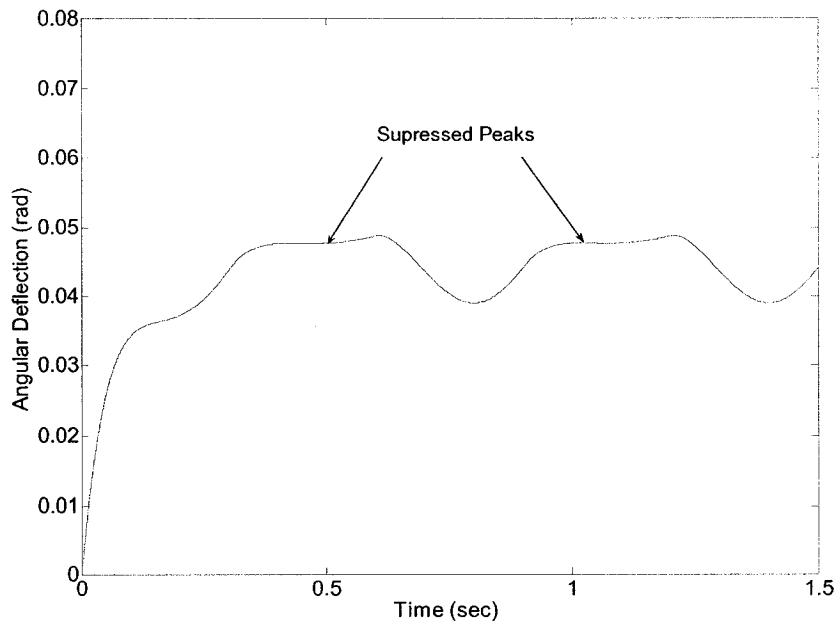

Figure 6.9: Angular Displacement v/s Time
(Torque Type B, Stiffness Non-Linear, N = 100 rpm)

6.5 Discrete Model for Bending-Torsional Coupling

In this section the lumped mass model explained in section 4.4 for lateral vibration of drill and the discrete torsional model based on nonlinear torsional stiffness explained in section 6.2.3 above are combined to study the effect of bending-torsional coupling on torsional response of twist drill.

Although this coupling is not as significant as that of torsion-axial coupling it would be rather interesting to study this phenomenon in more detail.

Equation 4.29 derived in section 4.4 of chapter 4 is the equation of motion in X direction of drill mass lumped at the tip of drill and rotating in clearance hole.

$$m\frac{d^2X}{dt^2}+C_d\frac{dX}{dt}+K_dX+HXK_w\left(1-\frac{\delta}{\sqrt{X^2+Y^2}}\right)-HY\mu_xK_w\left(1-\frac{\delta}{\sqrt{X^2+Y^2}}\right)=F_{ix}$$

Equation of motion in Y direction can be written as follows,

$$m\frac{d^2Y}{dt^2}+C_d\frac{dY}{dt}+K_dY+HYK_w\left(1-\frac{\delta}{\sqrt{X^2+Y^2}}\right)-HX\mu_xK_w\left(1-\frac{\delta}{\sqrt{X^2+Y^2}}\right)=F_{iy}$$

Equation 6.8

The equation of motion for torsional vibration of a drill (Equation 6.6) does not consist of the coupling because of the bending induced twist referred while discussing the concept of work stiffness in chapter 4.

That equation can be modified to include the effect of coupling. Lateral displacement 'S' of a drill tip as described in chapter 4 (Refer Section 4.3, Figure 4.4) is nothing but radial displacement as a result of displacements X and Y in respective directions and can be written as,

$$S = \sqrt{X^2 + Y^2}$$

Equation 6.9

And angular twist induced is given by,

$$\theta_c = \frac{\sqrt{X^2 + Y^2}}{R}$$

Equation 6.10

Adding this term to equation 6.6 above, we get

$$J \cdot \ddot{\theta} + C_d \cdot \dot{\theta} + K_s \cdot \theta + K_s \theta_c = T(1 - \lambda \cdot \sin\ \omega t)$$

Equation 6.11

where,

$$K_s = K_{snc} = K_t \quad \text{for} \quad 0 < \theta \leq \pi$$

$$K_s = K_{sc} = K_t + K_c \sin \omega t \quad \text{for} \quad \pi < \theta \leq 2\pi$$

Equation 6.12

Rearranging the equation

$$J\cdot\ddot{\theta}+C_d\cdot\dot{\theta}+K_t\cdot\theta+(K_c\sin\omega t)\cdot\theta_c\cdot H_\theta+K_t\cdot\theta_c+(K_c\sin\omega t)\cdot(\theta_c)\cdot H_\theta$$

$$= \quad T(1-\lambda\cdot\sin\ \omega\cdot t)$$

Equation 6.13

where,

$$H_\theta = 0 \qquad 0<\theta\ \leq\pi$$

$$H_\theta = 1 \qquad \pi<\theta\leq 2\pi$$

Equation 6.14

'H_θ' is unit step function similar to 'H(r-δ)' introduced in section 4.4 earlier.

Equations 4.29, 6.8 and 6.13 are three coupled equations of motion. First two are equations of motion for lateral vibration of drill in two orthogonal directions along co-ordinate axes. Third equation is equation of motion for torsional vibration for nonlinear torsional stiffness.

6.6 Simulation Results 2

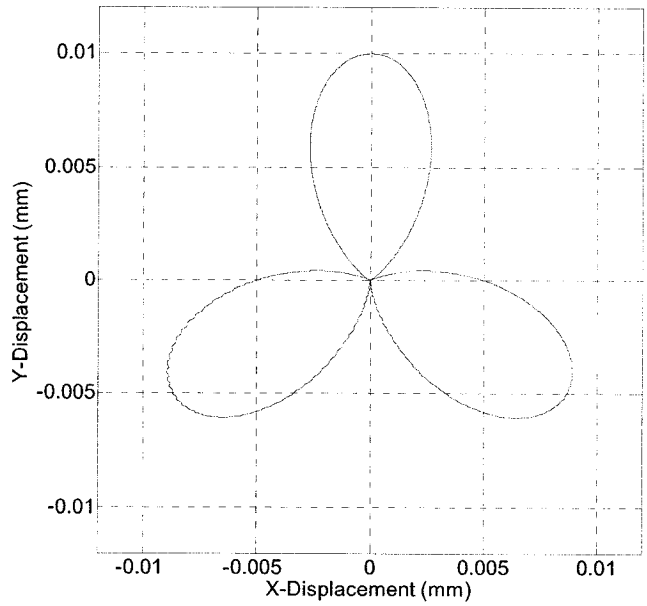

Figure 6.10: Trajectory of Drill Centerline (N = 100 rpm, F_i = 0.2 N, λ = 1)

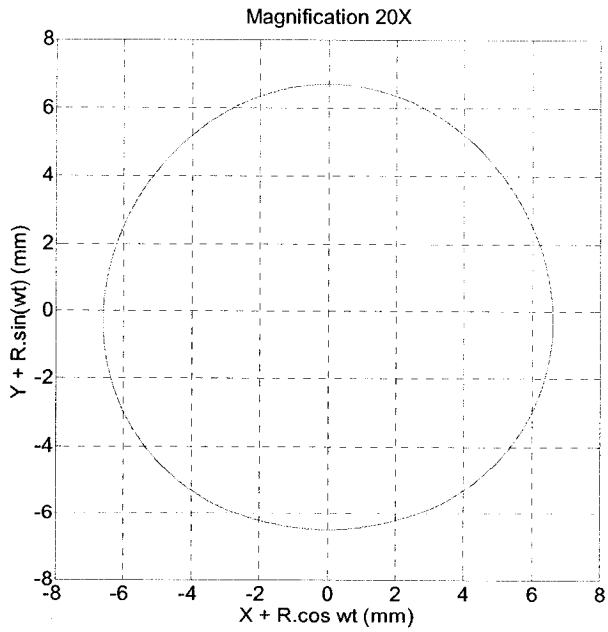

Figure 6.11: Locus of Outermost Point of Cutting Lip (N = 100 rpm, F_i = 0.2 N, λ = 1)

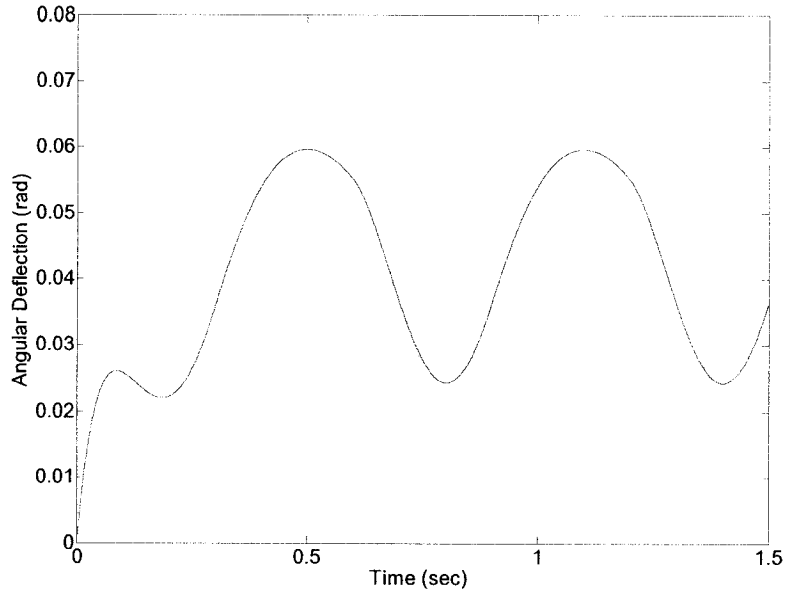

Figure 6.12: Angular Displacement v/s Time without Coupling
(Torque Type A, Stiffness Non-Linear, N = 100 rpm)

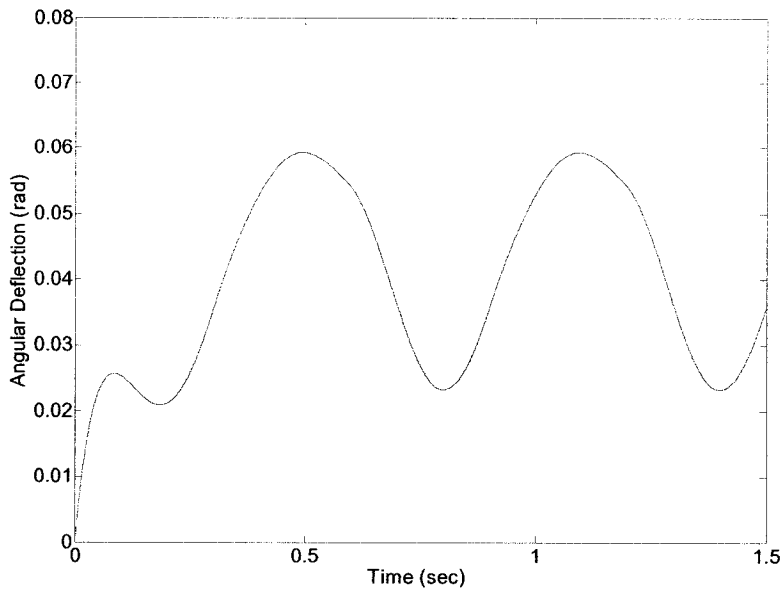

Figure 6.13: Angular Displacement v/s Time with Coupling
(Torque Type A, Stiffness Non-Linear, N = 100 rpm)

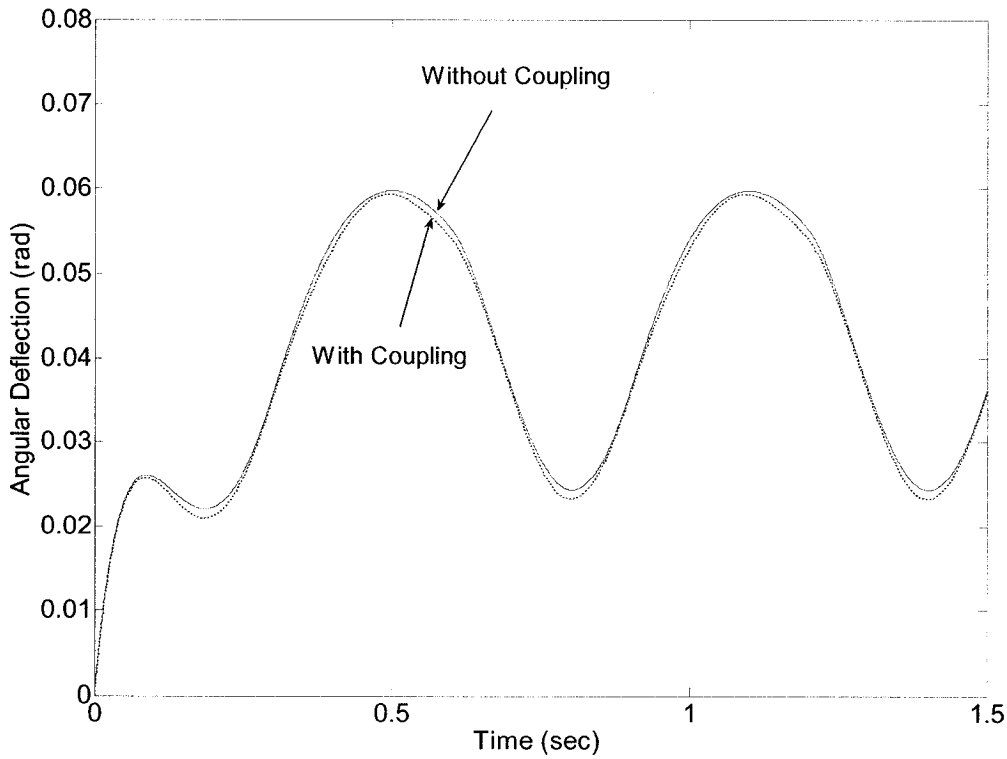

Figure 6.14: Coupled and Uncoupled Angular Displacements Overlapped

(N = 100 rpm, F_1 = 0.2 N, λ = 1)

The set of three ordinary equations presented in previous section are solved simultaneously in Matlab to get the torsional time response and corresponding orbital motion of the drill tip. Results of simulations are shown in figures 6.10 to 6.14. Simulations are carried out at rotational speed of 100 rpm. Other simulation parameters are as listed in table 4.1 in chapter 4.

Figure 6.10 and 6.11 are trajectory of drill center line and locus of outermost point on cutting lip respectively. Figure 6.12 and Figure 6.13 are angular displacement time responses of drill without effect of coupling and with effect of coupling, respectively. Plots also show the effect of nonlinear torsional stiffness which is function of time and represented by combination of linear and half-sinusoidal stiffness variations over each cycle as discussed in section 6.2.2 earlier. Figure 6.14 shows displacement plots in figures 6.12 and 6.13 overlapped on each other to visualize effect of coupling on torsional response of the drill. Close observation of these plots reveals the difference in angular displacement magnitudes along time as a result of bending-torsional coupling as explained earlier.

For further investigation of the coupling effect some more simulation results are presented below for different sets of parameters.

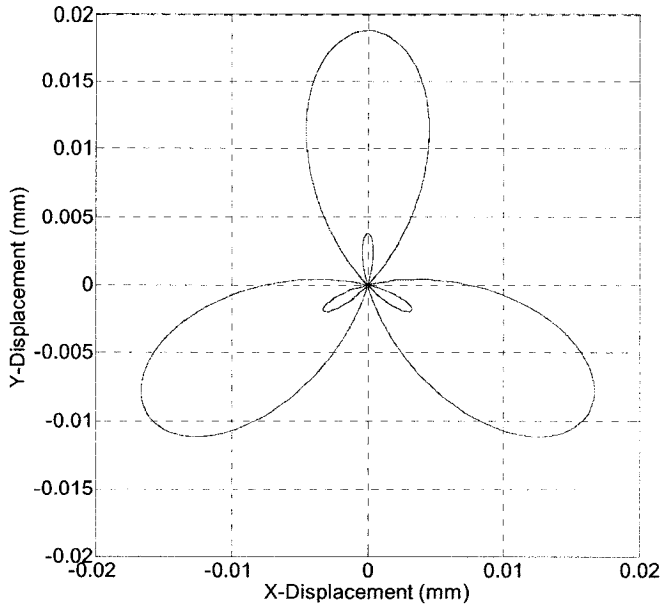

Figure 6.15: Trajectory of Drill Centerline (N = 200 rpm, F_i = 0.3 N, λ = 1.5)

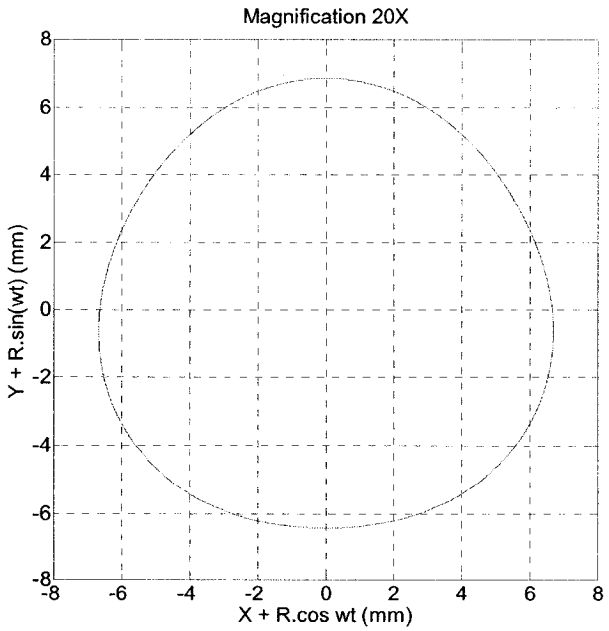

Figure 6.16: Locus of Outermost Point of Cutting Lip (N = 200 rpm, F_i = 0.3 N, λ = 1.5)

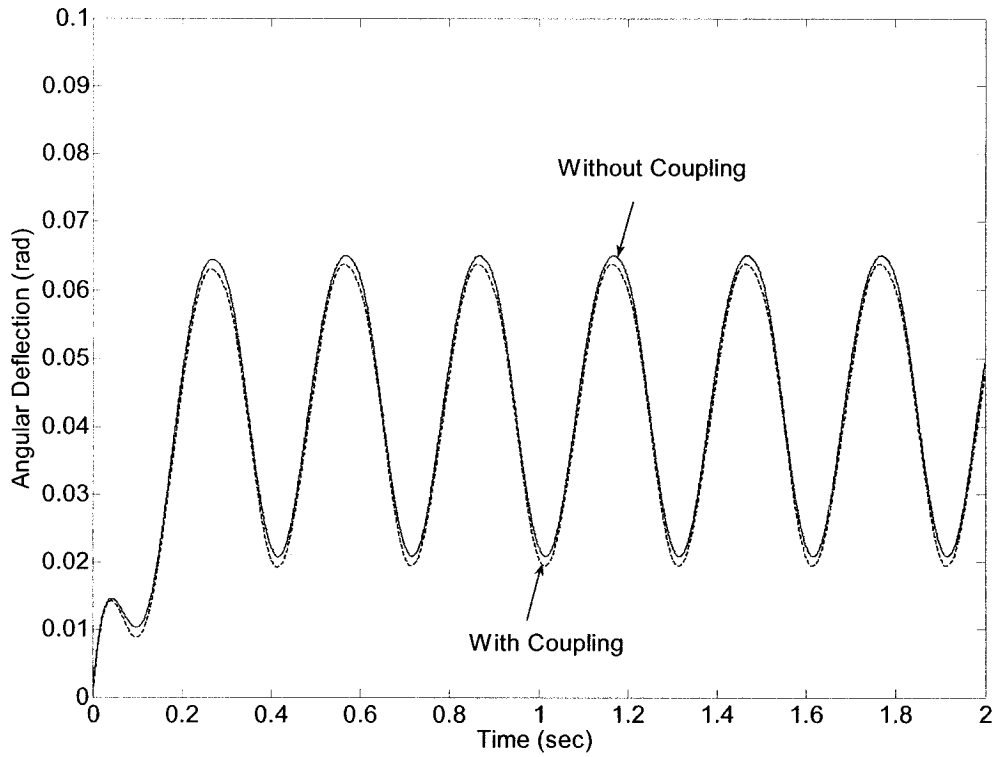

Figure 6.17: Coupled and Uncoupled Angular Displacements Overlapped, (N = 200 rpm, F_1 = 0.3 N, λ = 1.5)

Results shown above (Figures 6.15 – 6.17) are obtained by increasing all of the parameters viz. speed, imbalance force and amplitude modulation factor. Like figure 6.14 the figure 6.17 also clearly shows change in magnitudes of angular deflections at different times as an effect of coupling.

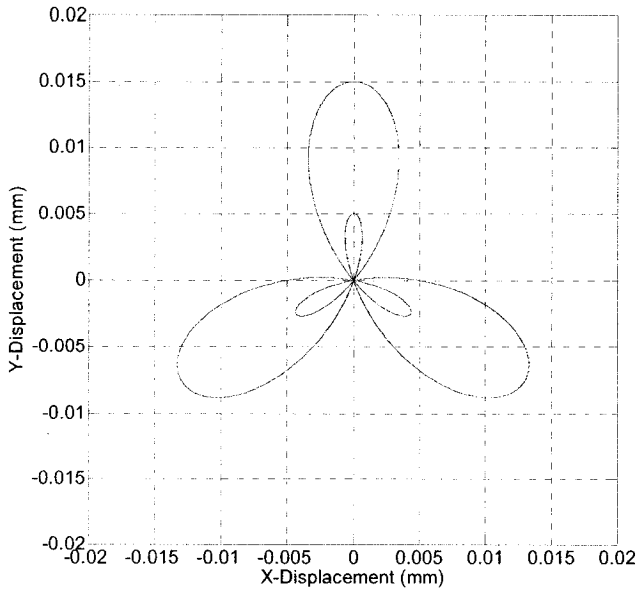

Figure 6.18: Trajectory of Drill Centerline (N = 200 rpm, F_i = 0.2 N, λ = 2)

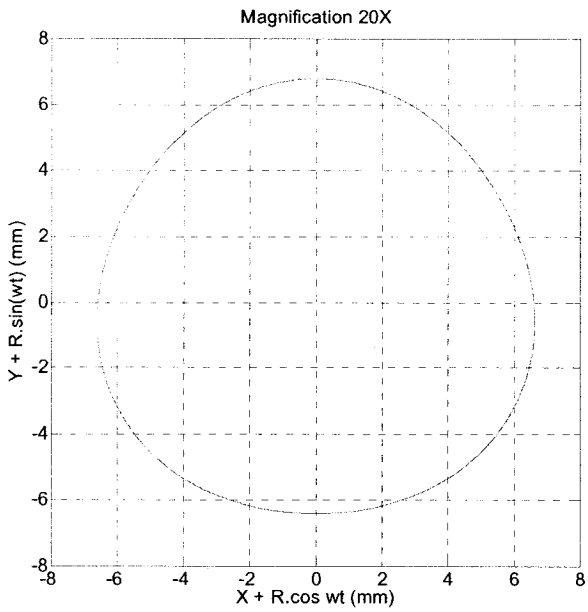

Figure 6.19: Locus of Outermost Point of Cutting Lip (N = 200 rpm, F_i = 0.2 N, λ = 2)

Drill centerline trajectory and orbital plot shown above (Figures 6.18, 6.19) are found to follow the same pattern as shown in chapter 4 while discussing effects of different parameters on drill profile in details. The trajectory and orbital plots are same as obtained in chapter 4 because the coupling we discussed here is unidirectional i.e. twisting does not induce any additional lateral displacement as bending does.

Figure 6.20 below is corresponding displacement time plots for coupled and uncoupled cases overlapped for comparison. Figure 6.21 is similar plot obtained for higher amplitude modulation factor and other parameters kept constant.

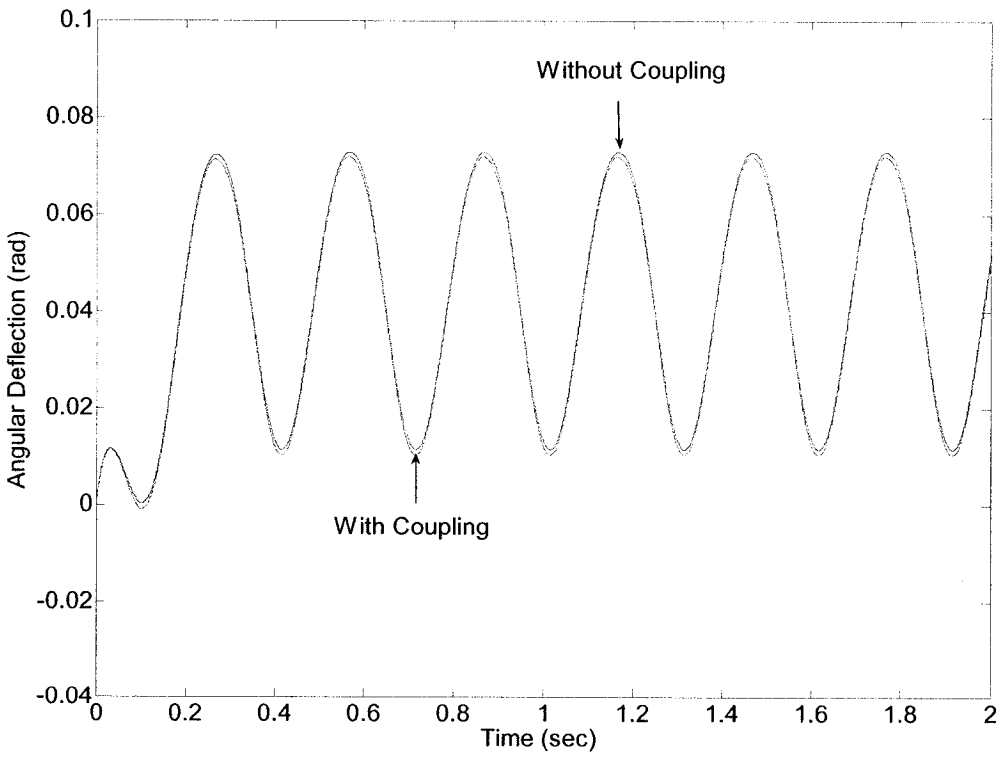

Figure 6.20: Coupled and Uncoupled Angular Displacements Overlapped, (N = 200 rpm, F_i = 0.2 N, λ = 2)

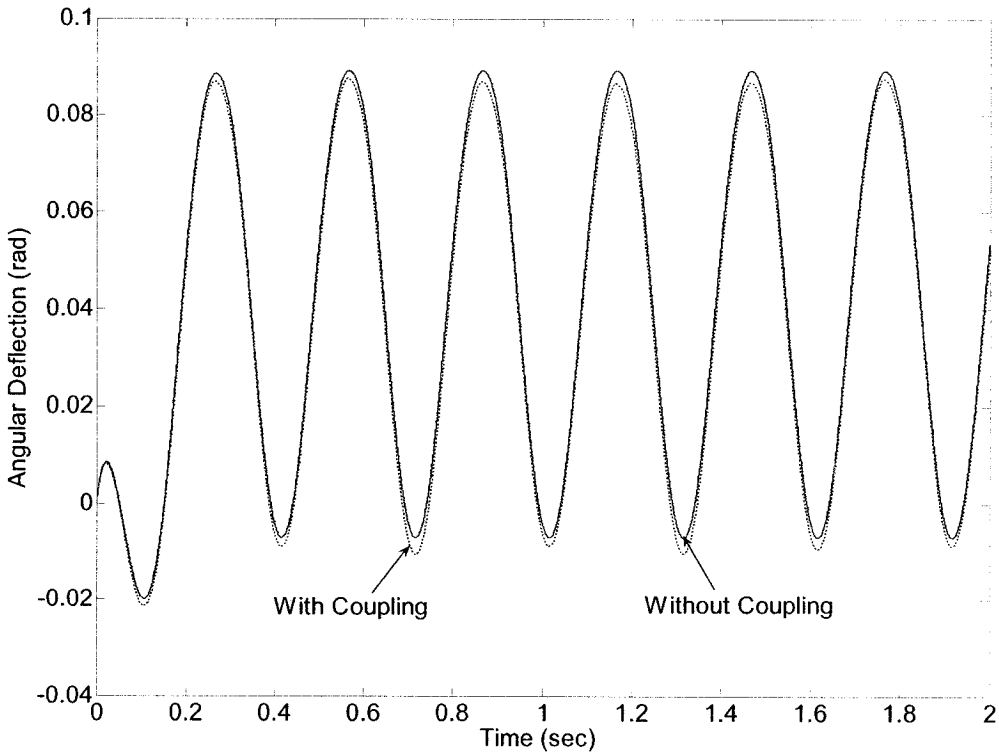

Figure 6.21: Coupled and Uncoupled Angular Displacements Overlapped,

(N = 200 rpm, F_i = 0.2 N, λ = 3)

6.7 Observations

The effect of nonlinear torsional stiffness is that the peaks in the displacement time response of twist drill for harmonic torque excitation are suppressed. In other words the torsional displacements for nonlinear stiffness are smaller as compared to that for linear stiffness.

After we analyze the displacement time plots in figures 6.14, 6.17, 6.20 and 6.21, it is noticed that the angular displacements for coupled case are always smaller than that for uncoupled case. Explanation for this is as follows.

The small amounts of additional angular displacements induced by lateral displacements of drill tip must always be in the direction of angular velocity as shown in figure 6.22 below. The static twist of drill corresponding to mean cutting torque is always in the direction opposite to direction of rotation, whereas the direction of the angular displacement in response to the torque fluctuation about the mean torque changes its direction from clockwise to counterclockwise from time to time.

Thus the overall effect is that the displacement time plot is shifted downward by small amount as seen in figures 6.14, 6.17, 6.20 and 6.21. In other words the overall angular displacement is reduced by small amount as a result of bending-torsional coupling.

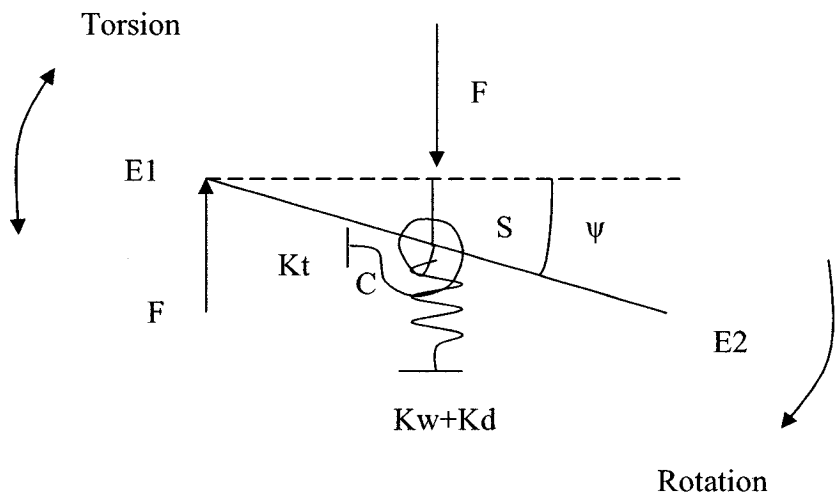

Figure 6.22: Schematic of Bending-Torsion Coupling

6.7 Summary

Two most important aspects of torsional vibration of drill are nonlinearity in torsional stiffness and bending induced torsion of drill.

Torsional model representing the time dependent cyclic variations of torsional stiffness depending upon the instantaneous direction of angular displacement in simplified mathematical form is developed and simulation results are discussed.

Simplified torsional model representing the bending–torsional coupling and torsional stiffness nonlinearity is developed and simulation results are discussed.

CHAPTER 7

CONCLUSIONS AND FUTURE RECOMMENDATIONS

7.1. Summary and Conclusions

This thesis work is a systematic study of the static and dynamic behavior of twist drill. Results of numerical analysis of proposed models are analyzed and are followed by observations and explanations. Ultimate aim is to earn global understanding of the dynamic behavior of the twist drill and investigate the relation between the drilling inaccuracies and lateral and torsional vibration behavior of the twist drill.

Summary of the work described in different chapters of the thesis and conclusions drawn are given below.

I. Continuous static bending model was developed and static behavior analyzed to understand the influence of fluted geometry on drill lateral stiffness. This understanding is very important in design of twist drills as well as in drill selections for various drilling application.

   Web thickness, length of fluted body of drill and rate of twisting (helix angle or pitch) are crucial elements of design of the twist drill. Stiffness of the drill for given drill cross-section depends on both pitch and length of drill.

II. Continuous model based on Euler-Bernoulli beam theory was developed and analyzed to locate first two natural frequencies and respective mode shapes.

Although the first natural frequency of the drill is quite higher as compared to the spindle speed in common practice, the technological developments in cutting tool materials and use of robust modern machine tool spindles, those seemingly higher speeds are reachable; whereas the second natural frequency is too high to reach. Other valuable information earned is the first and second mode shapes. Reasons for drill breakage common in machining operation can be found from deflection data for whole length of drill obtained from the modal analysis.

III. Discrete model for drill rotating in clearance hole is an approach closer to actual drilling process. Harmonic forcing function used for excitation of model was taken from the Dr Basile's study. Contribution of different combinations of simulation parameters in occurrence of out of round and non-straight holes is studied.

Selection of forcing function used for excitation of model defines the accuracy of the predicted orbital patterns. Force excitation model based on experimentally measured data can guarantee that the predictions will be closer to practically observed holes shapes. Modulated forcing excitation is responsible for the lobed holes and rough surface finish; whereas speed in

combination with modulated forcing excitation is mainly responsible for straightness error caused by wandering of drill center line and hole size variations along the length.

IV. Experimental investigation carried out for torsional stiffness of drill revealed that the twisted nature of drill does not have any impact on the drill's torsional stiffness in clockwise and anticlockwise directions and those are equal.

Thus the cutting resistance appearing intermittently when angular deflection of vibrating drill tip coincide the direction cutting direction is the important factor responsible for the time dependent nonlinear behavior of the torsional stiffness of drill while cutting holes.

V. Discrete torsional vibration model is presented to represent the effect of the time dependent non-linearity of torsional stiffness and bending-torsional coupling both resulting from the interaction of vibrating cutting lips with the work-piece, on torsional time response of drill.

Overall angular displacements are smaller because of intermittent increase in torsional stiffness due to cutting resistance and reverse twisting of drill tip due to the interaction of drill with work-piece.

7.2. Recommendations for Future Work

I. The partial differential equation presented in chapter 3 can be modified by introducing effect of boundary conditions representing the interaction of cutting lips with work-piece material. This equation can be solved numerically to get the time and space domain response and drilled hole profiles and can be predicted more precisely.

II. Discrete model studied in chapter 4 can be validated by experimental measurements of drilled hole profiles. Validation of predicted orbital plots for high speeds can be done by drilling tests on the robust machine tool like CNC Machining Center.

III. Bending-Torsional model can be validated by comparing the simulation results with the experimental measurements for actual cutting process.

IV. Bending-Torsional coupling model presented in chapter 6 can be modified to include effect of Axial-Torsional coupling and new comprehensive Axial-Torsional-Bending model can be developed.

LIST OF REFERENCES

1. H. Choudhary, S. K. Bose, "Elements of Workshop Technology – Vol I, II", 1988, Asia Publishing House, Mumbai, India
2. Sujatha, S. V. Muthukrishna, "Twist Drill Deformation and Optimum Drill Geometry", Computers and Structures, 1995, Vol. 57-5, pp 903-914
3. D. M. Rincon, A. G. Ulsoy, "Complex Geometry, Rotary Inertia and Gyroscopic Moment Effects on Drill", Journal of Sound and Vibration, 1995, 188(5), pp 701-715
4. B. W. Huang, "Dynamic Characteristics of a Drill in the Drilling", Proc. Instn. Mech. Engrs. Vol. 217 (B), Engineering Manufacture, 2003, pp 161-167
5. B. Dawson, W. Carnegie, "Model Curves of Pre - Twisted Beams of Rectangular Cross – Section", Journal of Mechanical Engineering Science, 1969, Vol. II (1), pp 1-13
6. O. Tekinalp, A. G. Ulsoy, "Modeling and Finite Element Analysis of Drill Bit Vibration", Transactions of ASME, 1989, Vol. 111, pp148-155
7. B. W. Huang, "The Drilling Vibration Behavior of a Twisted Micro-drill", Journal of Manufacturing and Engineering, 2004, Vol. 126, pp 719-726
8. A. C. Wijeyewickrema, L. M. Keer, "Critical Speeds and Buckling Loads of a Pre-Twisted Rotors", Journal of Sound and Vibration, 1995, Vol. 179 (5), pp 109-129
9. A. C. Wijeyewickrema, L. M. Keer, K. F. Ehman, "Drill Wandering Motion. Experiment and Analysis", International Journal of Mechanical Sciences, Vol. 37 - 5, May 1995, pp 495-509

10. S. J. Lee, K. F. Eman, S. M. Wu, "An Analysis of Drill Wandering Motion", Journal of Engineering for Industry, 1987, Vol. 109, pp 297-305

11. Y. Gong, C. Lin, K. F. Ehmann, "Dynamics of Initial Penetration in Drilling: Part 1 – Mechanistic Model for Dynamic Forces ", Journal of Manufacturing Science and Engineering, 2005, Vol. 127, pp 281-288

12. Y. Gong, C. Lin, K. F. Ehmann, "Dynamics of Initial Penetration in Drilling: Part 2 – Motion Models for Drill Skidding and Wandering with Experimental Verification ", Journal of Manufacturing Science and Engineering, 2005, Vol. 127, pp 289-297

13. S. A. Basile, "Modeling Transverse Motions of a Drill Bit for Process Understanding", Precision Engineering, 1993, Vol. 15 (4), pp 258-265

14. A. Poustie, Z Katz, "On the hole Quality and Drill Wandering Relationship", International Journal of Advanced Manufacturing Technology, 2001, Vol. 17, pp 233-237

15. K. Gupta, O. B. Ozdoganlar, S. G. Kapoor, R. E. Devor, "Modeling and Prediction of Hole Profile in Drilling, Part 1: Modeling Drill Dynamics in the Presence of Drill Alignment Errors", Transactions of ASME, 2003, Vol.125, pp 6-13

16. K. Gupta, O. B. Ozdoganlar, S. G. Kapoor, R. E. Devor, "Modeling and Prediction of Hole Profile in Drilling, Part 2: Modeling Hole Profile", Transactions of ASME, 2003, Vol.125, pp 14-20

17. P. V. Bayly, M. T. Lamar, S. G. Calvert, "Low-Frequency Regenerative Vibration and the Formation of Lobed Holes in Drilling", ASME Journal of Manufacturing Science and Engineering, 2002, Vol. 124, pp 275-285

18. P. G. Reinhall, D. W. Storti, "Modeling and Analysis of the Dynamics of a Drill Penetrating a Thin Plate", Transactions of the ASME, Journal of Applied Mechanics, 1986, Vol. 53, pp 691-694

19. C. H. Kahng, I. Ham, "Dynamic Behavior of Drill Bit- Hole Profile Errors and Improvements", Annals of the CIRP, 1975, Vol. 24, pp 27-32

20. D. F. Galloway, "Some Experiments on the Influence of Various Factors on Drill Performance", Transactions of ASME, 1957, pp 191-231

21. M. Kohring, C. Johnson, "Modal Analysis of Twist Drills", Proceedings of Third International Model Analysis Conference, 1985, Vol. 2, pp 1171-1177

22. A. G. Ulsoy, "A Lumped Parameter Model for the Transverse Vibration of Drill Bits", ASME Journal of Engineering for Industry, Vol. 10, pp 15-25

23. H. Fujii, E. Marui, S. Ema, "Whirling Vibration in Drilling. Part 1: Cause of Vibration and Role of Chisel Edge", Journal of Engineering for Industry, 1986, Vol. 108, pp 157-162

24. H. Fujii, E. Marui, S. Ema, "Whirling Vibration in Drilling, Part 2: Influence of Drill Geometries, Particularly of the Drill Flank, on the Initiation of Vibration", Journal of Engineering for Industry, 1986, Vol. 108, pp 163-168

25. H. Fujii, E. Marui, S. Ema, "Whirling Vibration in Drilling, Part 3: Vibration Analysis in Drilling Work-piece with a Pilot Hole", Journal of Engineering for Industry, 1988, Vol. 110, pp 315-321

26. D. M. Rincon, A. G. Ulsoy, "Effect of Drill Vibration on Cutting Forces and Torque", Annals of the CIRP, 1994, Vol. 42, pp 59-62

27. E. B. Magrab, D. E. Gilsinn, "Buckling Loads and Natural Frequencies of Drill Bits and Fluted Cutters", Transactions of the ASME, Journal of Engineering for Industry, 1984, Vol. 106, pp 196-204

28. Y. S. Tarng, T. C. Li, "Detection and Suppression of Drilling Chatter", ASME Journal of Dynamic Systems, Measurement, Control, 1994, Vol. 116, pp 729-734

29. E. Marui, S. Ema, "Suppression of Chatter Vibration in Drilling.", ASME Journal of Manufacturing Science and Engineering, 1998, Vol. 120, pp 200-202

30. H. Fujii, E. Marui, S. Ema, "Chatter Vibration in Drilling", Journal of Engineering for Industry, 1988, Vol. 110, pp 309-314

31. A. Askari, E. Stone, "Nonlinear Model of Chatter in Drilling process", Taylor and Francis- Dynamic Systems, 2002, Vol. 17-1, pp 65-85

32. A. G. Rehorn, J. Jiang, P. E. Orban, E. Bordatchev, "Modeling and Experimental Investigation of Spindle and Cutter Dynamics for a High-Precision Machining Center", International Journal of Advanced Manufacturing Technology, 2004 Online

33. W. C. Chen, "Applying the Final Element Method to Drill Design Based on Drill Deformations", ELSEVIER- Finite Elements in Analysis and Design, 1997, Vol. 26, pp 57-81

34. P. V. Bayly, S. A. Metzler, A. J. Schaut, K. A. Young, "Theory of Torsional Chatter in Twist Drills: Model, Stability Analysis and Composition to Test", Transactions of the ASME, Nov 2001, Vol. 123, pp 552-561

35. D. H. Hodges, "Torsion of Pretwisted Beam Due to Axial Loading", ASME Journal of Applied Mechanics, 1980, Vol. 47, pp 393-397

36. T. Arvajeh, F. Ismail, "Machining Stability in High Speed Drilling- Part 2: Time Domain Simulation of a Bending-Torsional model and experimental Validations", ELSEVIER- International Journal of Machine Tools and Manufacture, 2006, Vol. 46, pp 1573-1581

37. A. J. Schaut, D. N. Dilley, P. V. Bayly, "Effect of Chisel Edge on the Chatter Frequency in Drilling", Journal of Sound and Vibration, 2005, Vol. 281, pp 423-438

38. K. V. Nagrajan, "Dynamic Behavior of Drill-Shaft-Drive Assembly Subjected to Cutting Loads", M.A.Sc Thesis, Concordia University, Montreal, Canada, 2005

39. W. T. Thomson, M. D. Dahleh, "Theory of Vibration with Applications", 2003, Pearson Education, Inc., New Jersey, USA

40. S. S. Rao, "Mechanical Vibrations", 2005, Pearson Education Inc., New Jersey, USA

41. S. Ramamurtham, "Strength of Materials", 1998, Dhanpat Rai Publications, New Delhi, India

42. R. Pratap, "Getting Started with Matlab- A Quick Introduction for Scientists and Engineers", 2004, Oxford University Press, UK